Ultrafast Dynamics in Transition Metal Dichalcogenides and their Hybrid Structures

by Tim Völzer

CUMULATIVE DISSERTATION

Submitted to the Faculty of Mathematics and Natural Sciences
of the University of Rostock

in fulfillment of the requirements for the degree
doctor rerum naturalium (Dr. rer. nat.)

Rostock, 14.05.2025

https://doi.org/10.18453/rosdok_id00005051

Supervisors:

1. Prof. Dr. Stefan Lochbrunner, University of Rostock
2. Prof. Dr. Tobias Korn, University of Rostock

Referees:

1. Prof. Dr. Stefan Lochbrunner, University of Rostock
2. Prof. Dr. Peter Baum, University of Konstanz
3. Prof. Dr. Josef Wachtveitl, Goethe University Frankfurt

Date of the official thesis defense:
10.10.2025

Abstract

The unique features of monolayer transition metal dichalcogenides (1L-TMDCs) have drawn substantial interest of fundamental science. Likewise, they serve as key materials in optoelectronic applications, both in their pristine form and in combination with molecular coatings, referred to as hybrid structures. From either perspective, certain basic phenomena crucially determine their properties and performance. Most notably, electron-phonon coupling and the recombination dynamics of electronically excited species in TMDCs as well as interfacial charge transfer within the hybrids play a major role. To shed light on these processes, we conducted transient absorption (TA) spectroscopy and microscopic emission measurements in the framework of this thesis. Right after the optical excitation of 1L-TMDCs, we observe coherent lattice vibrations with a dominant contribution of the A_1' Raman mode. It undergoes a softening at higher excitation densities and causes a spectrally broad imprint on the TA signal, revealing fundamental deviations from theoretically predicted signatures. On top, we note an unprecedented oscillation feature matching the E′ mode. Subsequently, we unveil the cascade-like cooling of the excited specimens, *i.e.* an equilibrium of bound electrons and free carriers. This process successively involves an interelectronic thermalization and the step-wise coupling to different phonon species. For the last stage of the dynamics, namely the recombination of the excited specimens, we find a pivotal role of crystal defects in general, but fundamentally differing mechanisms in the 1L *versus* bulk material. In the latter case, the population decay proceeds *via* a density-dependent Auger scattering of carriers, as opposed to a geminate exciton-based recombination for the former. Finally, we investigate hybrids of 1L-TMDCs coated with monomeric Perylene Orange molecules. Here, we discover massive quenching of the dye fluorescence, hinting at an efficient charge separation.

Kurzzusammenfassung

Die einzigartigen Eigenschaften von Einzellagen-Übergangsmetall-Dichalkogeniden (1L-TMDCs) haben im besonderen Maße die Aufmerksamkeit der Grundlagenforschung auf sich gezogen. Gleichermaßen dienen sie als Schlüsselmaterialien für optoelektronische Anwendungen, sowohl in ihrer blanken Form als auch in Kombination mit molekularen Beschichtungen, sogenannten Hybridstrukturen. Aus beiden Perspektiven bestimmen grundlegende Phänomene die Eigenschaften und Funktion. Besonders Elektron-Phonon-Kopplung und die Rekombinationsdynamik in TMDCs sowie Ladungstransfer an der Grenzfläche innerhalb der Hybride spielen eine vorrangige Rolle. Um diese Prozesse aufzuklären, haben wir transiente Absorptionsspektroskopie (TA) und mikroskopische Emissionsmessungen im Rahmen dieser Arbeit durchgeführt. Direkt nach der optischen Anregung der 1L-TMDCs beobachten wir kohärente Gitterschwingungen mit einem vorwiegenden Beitrag der A_1'-Mode. Sie durchläuft eine Aufweichung bei hohen Anregungsdichten und verursacht einen spektral breiten Abdruck auf dem TA-Signal. Dieser weist fundamentale Abweichungen zu theoretisch vorhergesagten Signaturen auf. Obendrein beobachten wir eine bisher unbekannte Oszillation, die sich mit der E′-Mode deckt. Anschließend enthüllen wir die kaskadenartige Abkühlung der angeregten Spezies, einem Gleichgewicht aus gebundenen Exzitonen und freien Ladungsträgern. Dieser Vorgang beinhaltet eine interelektronische Thermalisierung und die schrittweise Kopplung an unterschiedliche Phononentypen. Für den letzten Abschnitt der Dynamik, die Rekombination der angeregten Spezies, ergibt sich im Allgemeinen eine zentrale Rolle von Kristalldefekten. Allerdings zeigen sich grundlegend verschiedene Mechanismen in der Monolage gegenüber dem Volumenkristall. In letzteren Fall zerfällt die Population über eine dichteabhängige Auger-Streuung, im Gegensatz zur paarweisen, innerexzitonischen Rekombination für erstere. Zum Schluss untersuchen wir Hybride aus mit Perylen Orange beschichteten 1L-TMDCs. Hier entdecken wir eine massive Fluoreszenzauslöschung auf Seite des Farbstoffs, was auf eine effiziente Ladungstrennung hinweist.

Index of abbreviations

1L	monolayer
2D	two-dimensional
BGR	band gap renormalization
CBM	conduction band minimum
CT	charge transfer
DAS	decay-associated amplitude spectrum
DECP	displacive excitation of coherent phonons
eT	electron transfer
ET	energy transfer
FFT	fast Fourier transform
FLIM	fluorescence lifetime imaging microscopy
hBN	hexagonal boron nitride
HOMO	highest occupied molecular orbital
hT	hole transfer
ISRS	impulsive stimulated Raman scattering
LED	light-emitting diode
LUMO	lowest unoccupied molecular orbital
µPL	photoluminescence microscopy
NOPA	noncollinear optical parametric amplifier
PDI	perylene diimide
PDMS	polydimethylsiloxane
PL	photoluminescence
PO	Perylene Orange (N,N'-bis(2,6-diisopropylphenyl)-3,4,9,10-perylenetetracarboxylic diimide)
QY	quantum yield
TA	transient absorption
THz	terahertz
TMDC	transition metal dichalcogenide
TVD	thermal vapor deposition
VBM	valence band maximum

Table of contents

1 Introduction

Ever since the Nobel Prize-winning discovery of graphene[1], two-dimensional (2D) crystals have risen as novel materials[2,3]. Among them, the semiconducting transition metal dichalcogenides (TMDCs) have emerged as one of the most promising classes for both fundamental research[4,5] as well as specific applications such as in electronics[6] or as catalysts[7–9].

Owing to their layered structure bound by van der Waals forces, one can fabricate ultrathin films of TMDCs, down to the atomic limit of so-called monolayers (1Ls). In this extreme case, quantum confinement effects and the absence of adjacent layers that would form a dielectric environment fundamentally change the physics of 1L-TMDCs compared to their bulk counterparts. Most notably, the constraint to two dimensions drastically reduces the screening of the Coulomb interaction within bound pairs of electron and hole, *i.e.* excitons. As a direct consequence, the exciton binding energy soars to unprecedented values of several 100 meV [4,10–12], one to two orders of magnitude above the range for conventional semiconductors[13–18]. Hence, stable excitons persist even at room temperature. Aside from 1L-TMDCs, this applies only to even lower-dimensional systems such as 0D molecules and quantum dots or 1D nanotubes.[16] However, in 2D, the electron-hole pairs exhibit high mobilities and diffusion lengths[19–21], thus unfolding their full potential in mediating energy transport.

Furthermore, the thickness reduction from bulk crystal to 1L is accompanied by a transition from an indirect to a direct band gap semiconductor for many TMDCs[10,22]. This leads to an emerging monolayer photoluminescence (PL), while the bulk material does not emit[23,24]. In combination with their strong light-matter interactions, manifesting in reasonable light absorption even for monolayers[25–27], these properties open a plethora of optoelectronic applications.

Indeed, numerous devices based on TMDCs have been fabricated so far[6], including light-emitting diodes (LEDs)[28], photodetectors[29,30], and solar cells[31,32]. The basic idea of the latter two is the conversion of photons into an electric current. This process, which proceeds reversely in LEDs, may be boiled down to the following steps. First, absorbing a photon creates a (Coulomb-bound) electron-hole pair. Subsequently, these charges must separate, in order for them to be drawn towards the different contacts, generating the intended current flow.

Typically, the charge separation is facilitated by combining two different layers with a staggered band gap, commonly denoted as a type II energy alignment. This term describes that the band gaps of the two materials are essentially offset with respect to each other. Hence, the electrons energetically favor the one material while the holes prefer the opposite one, thus resulting in charge transfer (CT). Under this scope, corresponding heterostructure systems of two or more different, stacked TMDCs have been and still are intensively studied[33–35]. Corresponding studies typically either focus on the PL of interlayer excitons as a spectral signature of separated charges[36,37] or investigate the dynamics of the CT[38–42].

However, the combination of TMDCs with molecular layers to form hybrid structures has gained less attention, although it offers some promising advantages. First of all, large-area coating methods like thermal vapor deposition (TVD) are well-established for dye films[43,44]. This simple and reproducible technique paves the way for potential device fabrication on an industrial scale. Second, chemical modification of organic molecules allows for tuning of their energy levels as well as their aggregation and layer growth behavior.[45,46] Ergo, a huge variety of systems appears possible. Finally, from an experimental point of view, the high fluorescence quantum yield (QY) of dye molecules

facilitates emission spectroscopy experiments. Numerous representatives of this material class score near-unity values[46] as opposed to typically subpercent photoluminescence yields of 1L-TMDCs[24,47,48]. It is owing to these characteristics that dye molecules on their own also serve as building blocks for organic LEDs[49,50] and solar cells[51,52].

Nevertheless, the unique properties of TMDCs can be exploited as well, leading to outstanding device characteristics. The vertical stacking of atomically thin layers preserves the quasi-2D geometry, thus minimizing the required out-of-plane diffusion path of excited specimens. Accordingly, corresponding photodetectors demonstrated photoresponse times of only a few picoseconds[30,53–55], therefore paving the way for operation in the terahertz (THz) regime in the long term. Simultaneously, TMDCs represent promising candidates for THz electronics in the sense of modulators[56–58], emitters[59] and detectors[60] for corresponding radiation.[61] However, characteristic vibrational modes of the crystal lattice, their quanta denoted as phonons, fall in this frequency region as well[62–68] and might interfere with the designed function. Moreover, recent studies have demonstrated that sufficiently short laser pulses can excite these phonons coherently[69–72]. As a consequence, the whole lattice vibrates in phase, which in turn modulates its optical and electronic characteristics. With regard to optimizing the discussed devices, further understanding of these effects is required. Beyond the concrete application, this also offers a unique opportunity to study the interplay between the lattice, the electromagnetic radiation, and the electronic response of the material.

The devices' efficiency is determined by multiple factors that correspond to the different steps of the principal process and relate to fundamental physical processes. At any stage, recombination and trapping of excited species limit their lifetime and thus partially prevents them from participating in the intended process. Understanding these loss channels as well as the mechanisms at play constitutes the prerequisite to controlling them and to optimizing the device performance. From this perspective, a key characteristic of TMDCs is that excitons are expected to dominate in thin films, most notably the 1L, while free carriers prevail in bulk systems. Ergo, this different nature of excited species suggests different behaviors. Additionally, the recombination dynamics provide valuable insight into the excited species' diffusion[20,73] and reveal a pivotal importance of crystal defects[74–78]. Therefore, the device performance might be hindered by trapping.

In hybrids or heterostructures, the rate of the CT equally competes with these loss channels, lowering the respective yield. As the separation of the oppositely charged carriers takes place as a purely interfacial process, it sheds light on the interactions between the different materials. *Vice versa*, a strong coupling of the layers forms the basis for a rapid and therefore efficient CT. Eventually, the mobility governs the diffusion of excited species as well as the drainage of the separated carriers towards the electrodes. These transport properties are largely defined by scattering with phonons[79,80], ergo depend crucially on the coupling between the electronic and the phononic system. On top of that, this coupling also represents a major energy distribution mechanism and thus determines the cooling of the electronic system, especially after optical excitation above the band gap. Thereby, it influences how long the excess energy is available for the electronically excited species. This may either facilitate thermally activated charge separation or, in contrast, cause undesired backward transfer. From this point of view, investigating the cooling dynamics unravels the electron-phonon coupling in return.

Regarding these pivotal processes, a comprehensive understanding is still missing, likewise leaving room for device optimization. Hence, following the significance of TMDCs in optoelectronics along with the underlying physical mechanisms, this thesis seeks to answer four fundamental research questions:

1. **Coupling of the electronic and phononic system:**
   How does it affect the dynamics, especially the thermalization of the electronic system? How long is the excess energy above the band gap preserved?
2. **Recombination dynamics:**
   How long do the excited species in TMDCs, *i.e.* excitons and free carriers, live and how do they recombine? How does this process depend on the layer thickness and which effects is it governed by?
3. **Coherent phonons:**
   Which vibrational modes can be excited? How do they affect the optical and electronic properties and by which experimental parameters are they influenced?
4. **Charge transfer in hybrid structures:**
   How fast and efficient does charge separation proceed in hybrid structures?

In this work, I tackle these questions by spectroscopic means, employing time-resolved emission as well as ultrafast transient absorption (TA) measurements. The latter maps the temporal evolution of the absorption characteristics of pristine TMDC layers after optical excitation. In this respect, suitable analyses allow for the disentanglement of various consecutive processes, *e.g.* the thermalization of the electronic system and its interaction with the lattice as well as the recombination of the excited species [P1][P3]. On top, particularly short laser pulses coherently excite phonon modes, which in turn leave an oscillating mark onto the transient signal [P3]. Time-resolved emission microscopy for its part is applied to track down charge transfer in dye/1L-TMDC hybrid structures indirectly *via* the quenching of the molecular fluorescence [P2].

The presented thesis is structured in the following way. Chapter 2 introduces TMDCs, dye molecules and hybrid materials composed of the former two. It connects their structure on the atomic level to their unique electronic and optical properties. Part 3 sketches the experimental methods employed to prepare 2D flakes and hybrids thereof, as well as to shed light on the ultrafast dynamics taking place in these samples after light absorption. From this point, I expound the results of my studies, beginning with chapter 4 on the electronic thermalization and phonon-driven cooling process in 1L-TMDCs. The subsequent part 5 deals with the different charge recombination kinetics in the bulk material compared to the monolayer. Afterwards, in chapter 6 we study the nature of coherently excited phonons and how they interact with the optical properties of 1L-TMDCs. As the last part with reference to the experimental results, chapter 7 tracks down interfacial interactions in PO/TMDC hybrid structures. Finally, a summary of the main body concludes this dissertation.

2 Characteristics of low-dimensional materials

TMDCs and their hybrid structures owe the vast scientific attention to their unique electronic and optical properties, triggering both fundamental research[4] and specific applications[6]. In the following, I will provide an overview of their most outstanding characteristics. To lay the foundation, we start with the structure and properties of the pristine TMDCs. Afterwards, we deal with the counterpart, *i.e.* dye molecules, and ultimately combine these two building blocks to form their hybrid structures and wrap up their features.

2.1 Transition metal dichalcogenides - From monolayer to bulk material

2.1.1 Lattice and electronic structure

From a general perspective, TMDCs are layered crystals consisting of transition metal and chalcogen atoms in a 1:2 stoichiometry. In principle, the possible combinations unfold a huge variety of materials, even with differing electronic properties[81]. In a narrower sense, however, the majority of research focuses on molybdenum-based and tungsten-based sulfides and selenides, which behave similarly in all aspects discussed in this section.

First of all, these materials share the same crystal structure[82], see figure 2.1 (a). Their lattice is built up by triatomic, so-called monolayers, forming the smallest crystal unit in vertical direction. They consist of one metal plane encased between two chalcogen layers, each of the three following a 2D trigonal lattice arrangement of its atoms. When viewed from above, as in panel (b), the metal and chalcogen positions do not lie on top of each other but are horizontally displaced with respect to each other. They are located in such a way that each metal atom resides in the middle of its six symmetrically arranged, nearest chalcogen neighbors, leading to a hexagonal pattern in top view. The metal forms covalent bonds with these three atoms on each side, holding the individual planes of the monolayer strongly together. As opposed to this, the layers bond to each other comparably weakly *via* van der Waals interactions. This pronounced imbalance between intralayer and interlayer forces facilitates the separation of single monolayers from thick crystals, *i.e.* in a top-down approach. Several techniques are frequently used[83,84]. Most originally, mechanical exfoliation[85], see section 3.1.1, yields individual 1Ls of several 10 µm in lateral size. Liquid-phase ultrasonication or intercalation methods[86] may be scaled, but provide an ensemble of flakes with varying thickness and size. *Vice versa*, chemical vapor deposition follows a bottom-up concept[87–89]. It can in principle provide larger sample areas, yet still suffers from inferior quality of the resulting crystals[90]. Despite their particularities, all these approaches rely on the heterogeneity of the forces within the lattice with strong intralayer *versus* weak interlayer bonds.

Moreover, the distinctive hexagonal arrangement of the atoms translates into an equally shaped Brillouin zone of the reciprocal lattice, as displayed in figure 2.1 (c). Here, following the symmetry axes in the $k_z = 0$ plane sketches the essential features of the band structure of a typical TMDC monolayer *versus* bulk material, which in turn is shown in panel (d). The principle direct and therefore optically relevant transitions for the monolayer are illustrated by the vertical arrows and also appear in the absorption spectrum in panel (g). The energetically lowest features A and B result from the excitation of bound electron-hole pairs, named excitons, around the K point of the

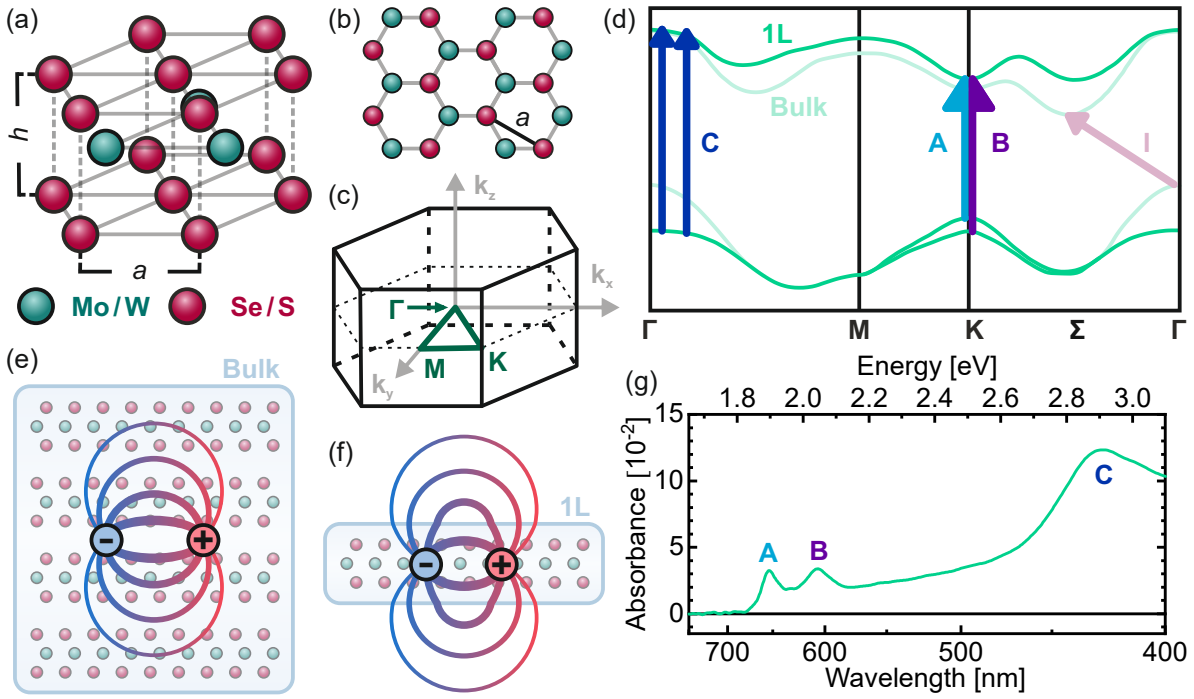

Figure 2.1: (a) Intralayer lattice structure and (b) top view of typical TMDCs. The geometric constants predominantly depend on the chalcogen, in the range of $a = 3.18\,\text{Å} - 3.32\,\text{Å}$ and $h = 3.13\,\text{Å} - 3.36\,\text{Å}$[81,82]. (c) Hexagonal Brillouin zone of the reciprocal lattice. The pivotal high-symmetry points are marked, their direct connections (dark green lines) constitute the x-axis in panel (d). (d) Schematic, typical band structure of monolayer and bulk TMDCs, based on[91]. The arrows mark the essential direct band transitions that manifest in the absorption peaks (A, B, and C) in panel (g), plus the indirect gap (I) for bulk materials. (e,f) Exciton binding situation in bulk (e) and 1L (f), based on[11]. While the field lines propagate continuously in the bulk, they are refracted at the monolayer surface. (g) Absorption spectrum of 1L-MoS_2, showing three peaks corresponding to the excitonic transitions (A and B) as well as the region of the band nesting (C) in panel (c).

Brillouin zone[4,92–94]. Here, both the conduction band minimum (CBM) and valence band maximum (VBM) are located, constituting a direct gap. Furthermore, the broken inversion symmetry within each crystal layer causes the valence band to split up into two spin states[4,95–97], yielding the two distinct transitions. *Vice versa*, the bound carrier pairs, which rapidly relax to the band extrema, into the A exciton state, can recombine radiatively. Their emission emerges as a prominent photoluminescence peak close to the A absorption band[23,24]. A third, energetically broader transition occurs around the Γ point. As opposed to the excitonic peaks A and B, this one is caused by band nesting[94,98]. In this region, the valence and the conduction band run almost parallel. Consequently, a large amount of density of states accumulates for similar transition energies, giving rise to the C peak at shorter wavelengths. These three characteristic absorption bands can be found in all of the common 1L-TMDCs[26].

Stacking these monolayers upon each other creates a bulk crystal, where interlayer interactions cause certain changes in the band structure. This effect essentially depends on the spatial extent of the contributing orbitals[4,99,100]. Near the Γ and Σ points, the p_z orbitals of the chalcogen atoms and the d_{z^2} ones from the transition metal predominantly feed the density of states. Their strong out-of-plane components mediate

coupling between the layers, thus shrinking the energetic band distance in the bulk and forming an indirect gap from the VBM at Γ to the CBM at Σ. The bands around the K point, in contrast, are mostly associated with orbitals in the metal plane plus a small component from the chalcogen p_x and p_y. They are all oriented in plane and hence barely respond to the addition of adjacent layers. Ergo, the K point gap remains relatively constant, making the indirect Γ-Σ transition the energetically lowest one in the bulk material. Striving for the minimization of their potential energy, excited electrons and holes will relax to CBM and VBM, respectively. In this case, however, these two reside at different points in reciprocal space. Hence, their recombination requires the compensation of their momentum mismatch, *e.g.* by phonons, which drastically suppresses radiative decay channels. As a consequence, relevant PL occurs mainly in 1L-TMDCs[23,24].

Aside from band changes, the transition from bulk crystal to monolayer is also accompanied by a drastic increase of the exciton binding energy. As figure 2.1 (e) shows, a bound pair of electron and hole in the bulk material is completely embedded in a dielectric environment. This substantially screens the Coulomb interactions between the opposite charges, leading to a weak binding in the order of several 10 meV[101–104]. A different situation presents itself in the monolayer (panel (f)) with virtually no surrounding dielectric material in the out-of-plane direction. Accordingly, the electrostatic potentials are drastically less screened, manifesting in binding energies of some 100 meV[4,10–12,81,93,96,103,105]. Consequently, excitons persist even at room temperature and largely determine the electronic response and dynamics of 1L-TMDCs.

2.1.2 Vibrational modes of the lattice

The crystal structure does not only influence the electronic states but defines the possible motions of the lattice itself, which can be quantized in terms of phonons[63]. Their different modes are distributed all over the Brillouin zone as well, however, those at the Γ point - in other words with a wave vector $\vec{k}$ of zero - bear particular importance. They are excitable *via* interactions with light, since photons carry vanishing momenta compared to particles with finite mass. The most prominent examples in 1L are the out-of-plane mode A_1' and the in-plane mode E′, illustrated in figure 2.2 (a) and (b), respectively. It shall be noted that alternatively, two phonons with opposite, canceling wavevectors can be created under optical excitation, which also satisfies momentum conservation.

Yet, the $\vec{k} = 0$ modes play the most important role for instance in Raman spectroscopy, which is widely used for characterization of TMDCs. Here, due to interlayer coupling[106], the frequencies of A_1' and E′ shift with increasing layer number[63,107,108]. However, their frequency changes are of opposite sign, with the out-of-plane mode speeding up and the in-plane mode decelerating for thicker crystals. This behavior is frequently exploited to discriminate flake thicknesses in the mono- and few-layer regime. In addition to the aforementioned dependence, the mode frequencies are sensitive to doping, strain[109] and temperature[63,66] as well. This emphasizes their importance as fingerprints used for *in-situ* flake characterization by means of Raman spectroscopy.

Beyond this classic technique, such lattice vibrations can also be excited by laser pulses used for example in time-resolved spectroscopy. If the pulse duration is sufficiently short - in the order of magnitude of or below half of the mode period - it is able to trigger largely coherent phononic motions, which in turn leave their time-periodic mark on the material properties. For this optical excitation of coherent phonons, two different mechanisms seem conceivable[110]. On the one hand, impulsive stimulated Raman scattering (ISRS), see figure 2.2 (d), is based on the same inelastic collisions as the standard Raman spectroscopy. In this process, a part of the photons energy is transferred to the atomic nuclei, initiating

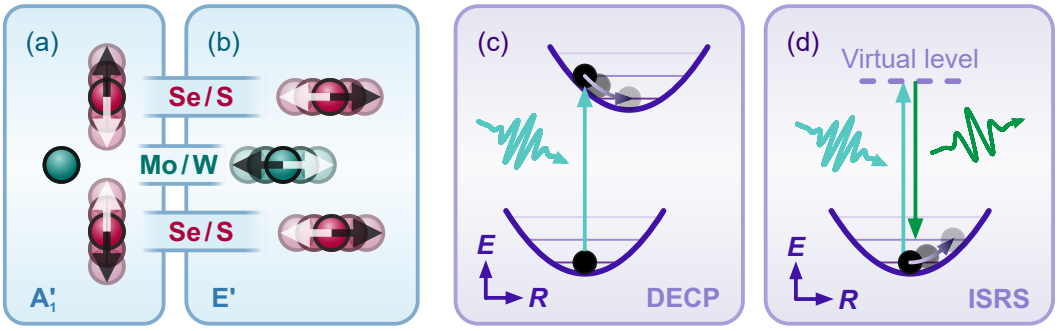

Figure 2.2: Characteristic Raman modes in 1L-TMDCs and their optical excitation. (a,b) Real space illustration of the nuclear motion according to the prominent modes A_1' (a) and E′ (b), adapted from [P3]. The black and white arrows indicate the signed direction of the atom displacement. (c,d) Light-based phonon excitation mechanisms. The blue parabolas depict the potential energy curve in dependence of a generalized nuclear coordinate R with the horizontal lines representing the vibrational levels. Accordingly, the black dot does not stand for a real particle, but rather boils down the complex spatial configuration of the nuclei within the lattice to one parameter. In DECP (c), the minimum of the harmonic potential is shifted by an electronic excitation, triggering nuclear motion around the new equilibrium, but starting from the original position. In ISRS (d), a scattering process *via* a virtual level transfers a part of the photon energy to the phononic system, fueling the initial velocity of the atomic nuclei and red-shifting the outgoing photon's frequency.

their motion, while the scattered light is red-shifted with respect to its original wavelength. On the other hand, in the picture of displacive excitation of coherent phonons (DECP), panel (c), the photon is absorbed to lift the system into an electronically excited state. This alters the balance of the chemical bonds, leading to a displacement of the minimum of the potential energy surface. In other words, the favorable equilibrium constellation of the atoms changes, while their actual positions cannot follow as quickly. Ergo, after the optical excitation, the nuclei positions lie off their energetic optimum, naturally producing an oscillating motion along the potential surface around the equilibrium constellation.

All in all, TMDCs exhibit a layered structure that facilitates the isolation of a single monolayer. These stand out from thicker flakes owing to extraordinarily high exciton binding energies and a direct band gap. The optical characterization of such samples produces specific absorption and Raman spectra, facilitating the application of more sophisticated spectroscopic techniques.

2.2 Dye molecules as bright and characteristic emitters

To create hybrid structures based on TMDC layers in hybrid structures, we choose dye molecules as their counterpart, which have been equally studied by means of spectroscopy. The latter favors substances with a strong emission. Among them, the group of perylene diimides (PDIs) offers stable and well-studied materials applied in organic photovoltaics. On top of that, chemical modifications within the range of PDIs facilitate a targeted tuning of the dye's properties. In this thesis, we focus on the representative N,N'-bis(2,6-diisopropylphenyl)-3,4,9,10-perylenetetracarboxylic diimide, widely known as Perylene Orange (PO). As a commercially available dye, it applies for organic optoelectronics[111] and luminescent dye concentrators[112,113].

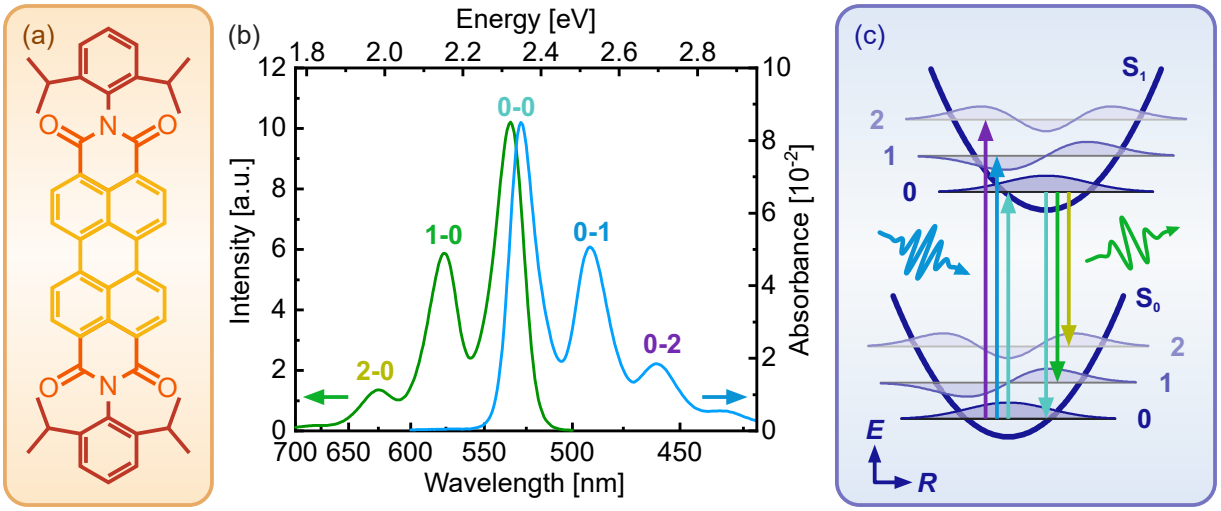

Figure 2.3: (a) Structural formula for PO molecule, consisting of the perylene core (yellow), the imide groups (orange) and the diisopropylphenyl substituents (dark red). (b) Static absorption and emission spectrum of dilute (1 µM) solution of PO in chloroform, measured by Erik von der Oelsnitz. They exhibit a clear symmetry and each consist of a series of individual peaks. (c) Shifted harmonic oscillator model explaining the spectral shapes in (b). The potentials of S_0 and S_1 are slightly displaced with respect to the nuclear coordinate R. The three lowest vibrational levels (0, 1, 2) are represented by their wave functions of the corresponding eigenstates. Vertical arrows mark the vibronic transitions labeled in (b).

The molecular structure of PO breaks down into three major components, as figure 2.3 (a) indicates, which influence different properties of the molecule[45,46,114]. The system is based on a perylene core. Together with an imide group at each of the two sides, it forms the optically active part of the molecule, the chromophore. It predominantly determines the two relevant electronic states, the highest occupied molecular orbital (HOMO) and lowest unoccupied molecular orbital (LUMO). These two both bear a conjugated π-system delocalized over the whole chromophore. This results in a large transition dipole to the first electronically excited state S_1 that follows the long symmetry axis. However, as an important peculiarity, HOMO and LUMO are characterized by wavefunction nodes, in other words probability depletion, at the nitrogen atoms. Thus, any functional groups added here, referred to as imide substituents are electronically fairly isolated from the chromophore and barely alter the optical properties. The latter include a prominent fluorescence with a conveniently long lifetime of about 4 ns and excellent QYs above 90 %. At this point, the addition of two diisopropylphenyl groups at the nitrogen atoms completes the PO molecule. In contrast to the 2D sketch, the substituents are actually rotated out of the plane of the perylene. Lying outermost and as the sole part reaching out into the third dimension, they mainly govern the interactions with the environment. On the one hand, this provides a good solubility and a low tendency to form aggregates compared to the bare chromophore. On the other hand, it prevents the formation of ordered films on substrates, which, on the contrary, can be achieved using completely flat organic dyes[44,115–117].

The monomer, however, already exhibits a characteristic absorption and emission spectrum in the visible range. As figure 2.3 (b) depicts, they bear a symmetry with respect to each other, both of them showing three major peaks. These shape features can be explained by the model of a shifted harmonic oscillator[118], see panel (c). It illustrates

the potential energy surface of the electronic ground state S_0 and the first excited one S_1. The x-axis represents the nuclear coordinate R belonging to the dominant optically active vibrational normal mode. These two curves are assumed as identical apart from their offset in energy and their displacement in R. The latter arises from the weakened chemical bonds in the electronically excited state. In addition, the first three energy levels of the major mode are indicated in each harmonic potential. Here, the typical vibrational energy quanta lie in the order of 170 meV[111]. At room temperature, consequently, the molecule resides in the ground state with reference to the electronic system as well as the according vibration. This constitutes the initial state for any absorption processes.

Lifting the electronic system from S_0 into S_1 can lead to a higher vibrational state as well, which is referred to as a vibronic transition. This access to excited vibrational levels produces additional absorption peaks at higher energies. However, similar to the lattice atoms in the DECP mechanism in the previous section, the nuclear constellation in figure 2.3 (c) does not change instantaneously upon electronic excitation. In formal terms of the potential energy diagram, this signifies that all transitions from S_0 to S_1 proceed vertically[119]. Accordingly, the probability of ending up in a particular vibrational level follows from the overlap integral of the initial and final states' nuclear wavefunctions, which are depicted in the illustration. These transition-specific coefficients are denoted as the Frank-Condon factors[120]. In the case of PO with a relatively small offset of the mode coordinate between S_0 and S_1, they decrease monotonously with higher quantum numbers of the final vibrational level. Hence, the absorption bands shrink towards the blue spectral region.

The fluorescence spectrum essentially reflects the reverse process. Even after the transition into higher vibrational levels of the electronically excited state, this excess energy will be rapidly redistributed into other modes of lower frequency. Thus, in analogy to the absorption process, the starting point for any emission is again the vibrational ground state. The target states within S_0, in contrast, may involve a higher level. Hence, this reduces the energy distance between the initial and final energy by an integer multiple of the vibrational quantum. Consequently, this gives rise to peaks further in the red spectral region, as opposed to the equivalent absorption features occurring at shorter wavelengths. On top, the probabilities and resulting amplitudes for the fluorescence peaks follow the same rules as for the absorption signal, ergo producing a spectrum mirror-symmetric to the latter.

Consequently, PO dye molecules produce a signature spectral fingerprint in both absorption and fluorescence. On top, the latter's high yield and slow decay facilitate emission measurements to discriminate between isolated molecules and those affected by the interaction with other materials.

2.3 Interfacial energy alignment in hybrid structures

After the characterization of TMDCs and PO as individual substances, we now dive into their combination in the form of hybrid structures. In the case of such composite materials, their properties and the possibility of CT or energy transfer (ET) processes crucially depend on energy level alignment of their components. To illustrate this, we compare the HOMO and LUMO energies of PO to the band extrema of the most relevant TMDCs in figure 2.4 (a). The former result from electrochemical and optical measurements, whereas the latter stem from density functional theory calculations. As a reference material, hexagonal boron nitride (hBN) is included on top, due to its isolating properties while exhibiting a similar surface structure. Note that these calculations were each performed

for the individual materials without any environment. Therefore, the specific values may differ in the actual hybrid owing to interfacial interactions, the altered dielectric surroundings *et cetera*[121]. Nevertheless, we use the diagram for a rough estimate of the possible processes.

For all TMDCs, the VBM or CBM appear to lie in between the PO orbital energies, while the latter are completely comprised by the hBN gap. The consequences of this alignment are illustrated for the example of PO/WSe_2 in panel (b) of figure 2.4. It presents a staggered gap, denoted as type II, where exactly one of the two levels of each material falls into the gap of the opposite one. In other words, the bands on the two sides are basically offset with respect to each other, whereas in a type I alignment, the larger gap completely encases the smaller one. Generally, electrons always strive towards lower energies, whereas holes move energetically upwards. Ergo, after optical excitation of a type II hybrid, electron transfer (eT) from the TMDC to the dye and hole transfer (hT) in the opposite direction can take place. Independent of whether the excited specimens are initially created in the molecule or the semiconductor, this results in charge separation. The latter in turn forms a prerequisite for the functionality of many optoelectronic devices, *e.g.* in solar cells or photodetectors.

Interestingly, the transfers in both directions bear a profound asymmetry regarding their tempos. CT from the TMDC to the molecular layer occur on a picosecond time scale[124,129,132–137], as opposed to a few 100 ps or even several 10 ps in the reverse direction[132–134,136,138,139]. The reason for this imbalance lies in the large size of a typical organic dye molecule compared to a 1L-TMDC unit cell, while both of them usually accommodate one excitation at the maximum. In physical terms, the density of states in the crystal greatly exceeds that of the organic layer. The more states are available, the faster the transfer proceeds. For thicker dye coatings, however, the diffusion of molecular

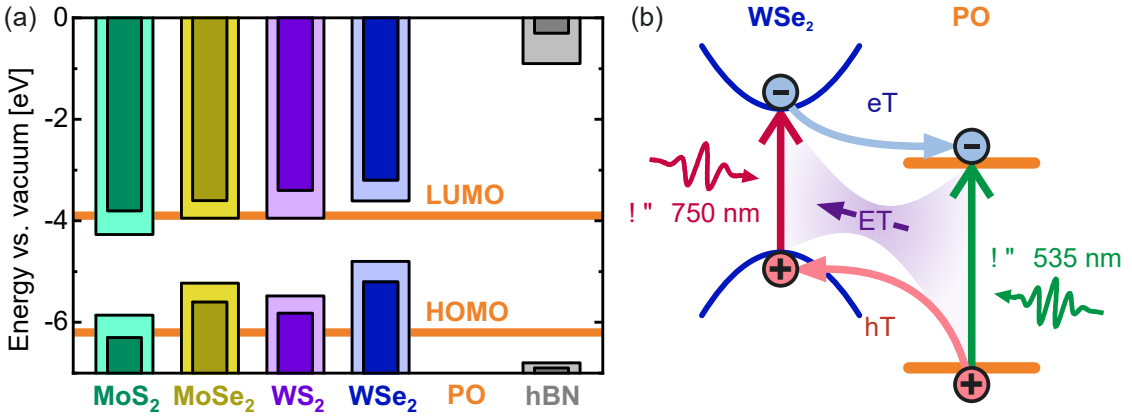

Figure 2.4: (a) Energy level alignment in hybrid structures of PO and 2D materials. The horizontal lines represent the energies of HOMO and LUMO of the isolated molecule[122]. Upper and lower bars show the CBM and VBM energies of the crystals, respectively. The pale and dark sections mark the variance between the values taken from different studies that used density functional theory without taking excitonic effects into account. (1L-TMDCs: MoS_2[123–127], $MoSe_2$[123,124,126–128], WS_2[125–127,129,130], WSe_2[123,126,127]; hBN[131]) For each of the TMDCs, at least one band extremum resides within the HOMO-LUMO gap of PO. The hBN bands, in contrast, lie far outside the molecular energy levels. (b) Charge and energy transfer processes in a PO/WSe_2 hybrid. Given the type II band alignment, hT proceeds from PO to WSe_2, while electrons from the conduction band migrate in the opposite direction (eT). On top, ET may occur, where the whole exciton moves to the material with the smaller band gap, in this case from dye to TMDC.

excitons to the interface may slow down the CT rate[132]. The opposite extreme case of thin coatings in the monomer limit, in contrast, has not been studied up to this point. Here, owing to its particularly low density of states, the molecular side will not cause any relevant changes in the TMDC. From the dye perspective, on the other hand, one can investigate the pure interaction with the flake, as the molecules all reside at the interface and they do not interact with each other. Thus, this scenario provides an opportunity to evaluate the true CT dynamics.

One experimentally observable consequence of such CT is the quenching of the emission of the hybrid's individual components. The charge separation tears their excitons apart, hence preventing their radiative recombination. However, if electrons and holes are able to retain their bound state over the layer distance, they form interlayer excitons. If these recombine radiatively, their emission emerges red-shifted with respect to those of the separate materials, providing unambiguous evidence of charge separation[129,140–142].

Alternatively to CT, Förster type ET[142–144] might occur also in a type II alignment, moving the whole exciton from PO to WSe_2. This quenches the fluorescence of dye as well, hindering a distinction of charge and energy transfer based solely on the dye's emission. Still, following from the energetic alignment, one would expect a subsequent eT back to the PO, eventually leading to an identical situation of separated charges.

Contrary to the PO/TMDC hybrids, none of these processes should occur in PO/hBN structures. On the one hand, the band gap of hBN spans too large to allow for optical excitation in the visible range. When excitons are created in PO, on the other hand, neither CT nor ET are energetically possible. Thus, the dye can emit its fluorescence without any impairment. At the same time, the hBN surface structure resembles that of the TMDCs, suggesting a similar arrangement of the molecules on top. Ergo, we use the PO/hBN system as a reference sample without quenching to compare the TMDC-based hybrids to.

Summing up, the possible processes in PO/TMDC hybrid structures are determined by the relative position of the individual components' energy levels. The typical case of a type II alignment enables charge transfer of both electrons and holes, which leads to the experimental observation of emission quenching.

3 How to investigate ultrafast dynamics in 2D systems

3.1 Preparation of atomically thin layers

This thesis aims at the investigation of aforementioned 1L-TMDCs as well their hybrid structures in combination with PO. To fabricate these samples, the following section explains the isolation of atomically thin layers from a TMDC bulk crystal. As a second part, we describe the deposition of molecular coatings.

3.1.1 Exfoliation and deterministic transfer of TMDC flakes

TMDCs unfold their most characteristic properties when thinned down to monolayers. Owing to their layered structure hold together by relatively weak van der Waals forces, the separation of atomically thin films can be achieved by means of mechanical cleaving[85]. Starting from a bulky crystal, one attaches and then pulls off a standard adhesive tape, thereby ripping off a submillimeter TMDC film. The repetition of this procedure successively reduces the thickness. Once a suitable regime is reached, one conducts a final exfoliation, this time using a polydimethylsiloxane (PDMS) film as the target substrate. After this last step, the examination using an optical microscope identifies monolayer regions. Their thin-film interference creates a reflection contrast with reference to the surrounding substrate[145,146], see also figure 7.1 (a,d). If a flake of sufficient size and quality is found, one transfers it to the final substrate[147,148], for instance silicon wafers or transparent glass slides. To that end, the PDMS stamp with the flake on top is carefully brought into contact with the target. Next, one removes the silicone even slower and more smoothly, allowing the viscoelastic characteristics of the PDMS to take full effect. At sufficiently low speed, the material will virtually flow off the target, leaving the flake behind.

This mechanical exfoliation with subsequent stamping offers a versatile tool to prepare atomically thin flakes from layered crystals and transfer them to a desired substrate at will. Yet, a disadvantage arises from residual PDMS on the final layer[149], which may impair the contact to subsequently added layers. In this light, chemical vapor deposition offers an alternative[87–89]. However, it remains challenging to obtain large and uniform monolayers using this method, plus the crystal quality usually suffers from high defect concentrations[90].

3.1.2 Thermal vapor deposition of molecular films

Several key applications of TMDCs presuppose their combination with other materials like molecules to enable interactions such as charge transfer. In this work, I implemented a coating procedure based on TVD to obtain homogeneous PO films with a adjustable thickness down to the monomeric regime[43,44]. Figure 3.1 depicts the scheme of the developed apparatus. The whole deposition process takes place in a vacuum chamber at approximately 1×10^{-2} mbar. Two copper blocks form the basis of the interior, each equipped with heating cartridges and a thermal sensor connected to a temperature controller (Model 321, Lake Shore Cryonics). The precursor PO powder is placed in a small well on the upper side of the lower block. It is heated to about 430 K to 450 K for a standard monomeric coating, depending on the current filling of the dye reservoir.

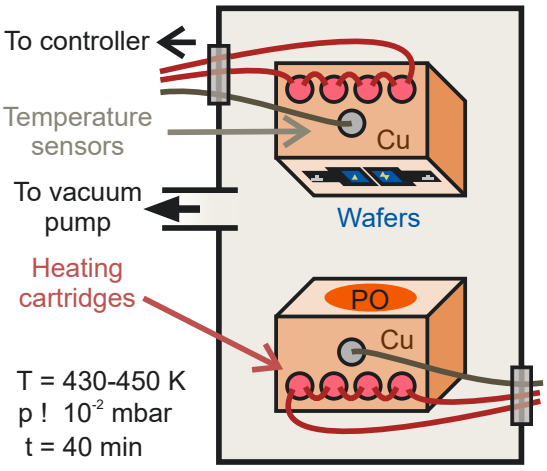

Figure 3.1: Vacuum TVD chamber for evaporating dye molecules and bringing them onto a target substrate. PO powder is located in a reservoir on top of the lower copper block, which is heated to drive the transition into the gas phase. The opposite block remains roughly at room temperature and holds the wafers with the exfoliated flakes upside down. Heating cartridges provide the thermal energy and Pt100 sensors check the current temperature, all of which is regulated by a connected controller.

At these temperatures, the molecules start to sublimate, diffuse through the gas phase and deposit onto the target substrate, which remains roughly at room temperature. After 40 min, approximately 15 of which are taken up by the thermal ramp-up, the heating is turned off and the vacuum is broken to stop the evaporation. Now, the resulting coatings can be characterized using static absorption and fluorescence spectroscopy. Comparing the former to the extinction coefficient of PO[150], we are able to estimate the molecule density deposited onto the surface. Under these conditions, the created dye film contains roughly one molecule per 40 nm^2, which corresponds to about $^1/_{30}$ of a perfectly covering PO monolayer, as derived in the supporting information of [P2].

In alternative approaches to dye deposition, we tested spin coating and stamping as well, although the obtained films were strongly inhomogeneous. Hence, TVD remains the method of choice for all following experiments.

3.2 Microscopic emission measurements

Emission microscopy techniques play a pivotal role in the characterization and investigation of TMDC flakes, dye films as well as hybrids combining the two of them. The high fluorescence QYs of dye molecules and the emerging photoluminescence of 1L-TMDCs ensure sufficiently strong signals. A reduced emission, on the other hand, usually hints at quenching caused by interfacial or intermolecular interactions. With this in mind, a spatially resolved emission map of the sample allows for a comparison with the flake topography to identify regions of stronger or weaker signals, respectively.

In the framework of this thesis, we employed photoluminescence microscopy (µPL), Raman microscopy, and fluorescence lifetime imaging microscopy (FLIM), which may be boiled down to the general principle illustrated in figure 3.2. The light of an excitation laser is focused onto the sample *via* an objective, achieving spatial resolutions of about 1 µm. The sample is moved in x- and y-direction in order for the laser focus to scan the area of interest. The emitted or scattered light is collected and recollimated by the same optic. A beam splitter separates the outgoing from the incoming radiation. Finally, spectral filters block the elastically scattered pump light and may select specific wavelength ranges to pass towards the detection.

At this point, the major peculiarities of the different setups come into play. For µPL and Raman measurements, a spectrometer provides spectral resolution. Thus, one essentially obtains a 3D data set $I(x, y, \lambda)$, containing the measured intensity in dependence of the

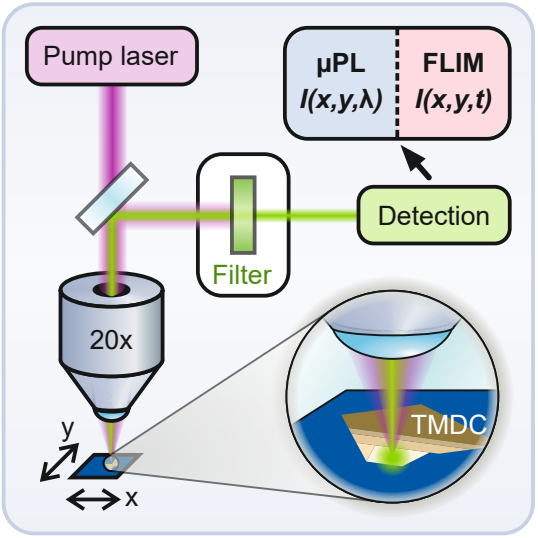

Figure 3.2: Generalized setup for emission microscopy. The excitation light passes though an objective to yield a spatially fixed spot, while the sample moves to obtain a scan of the latter. Next, the emitted light is collected and spectrally filtered. The exact detection mode depends on the method applied, yielding spectrally resolved data for µPL and Raman spectroscopy as opposed to time traces for FLIM. The zoomed-in region schematically illustrates the focusing of the pump beam onto a model flake and the collection of the emitted light.

two in-plane coordinates and of the wavelength. For FLIM, a pulsed laser is required. In contrast to the previous techniques, this facilitates the detection *via* time-correlated single-photon counting, providing temporal resolution of approximately 100 ps. Ergo, the resulting 3D array $I(x, y, t)$ is defined by the x-, y- and time axes.

Evaluation of the 3D data typically implies the averaging or integration over one or multiple of these axes or parts of them. For instance, integrating over the time axis in $I(x, y, t)$ or $I(x, y, \lambda)$ over a certain spectral region leads to 2D intensity maps that reflect the flake topography and might indicate quenching. Averaging over areas of interest, in turn yields emission spectra or time traces with an enhanced signal-to-noise ratio that bear information about the involved species and their dynamics.

In addition to the truly emission-based techniques, one can also use the µPL setup to perform Raman spectroscopy, which relies on inelastic scattering of the pump light. Since the resulting wavelengths lie much closer to the excitation energy than for typical luminescence scenarios, one has to adapt the filtering before and the dispersion within the spectrometer.

3.3 Ultrafast transient absorption spectroscopy

Since most of the electronic and phononic dynamics in TMDCs and their hybrids happens on femtosecond to picosecond time scales, their investigation requires a correspondingly fast spectroscopic technique. Here, ultrafast TA spectroscopy provides the means to investigate light-induced changes of a material's absorption properties. Assigning spectral signatures to specific excited species or quantities in turn enables the identification and monitoring of the underlying physical processes.

3.3.1 Experimental implementation in a referenced pump-probe scheme

Figure 3.3 shows an exemplary sketch of the TA setup. It mainly follows the typical pump-probe scheme for such optical apparatuses[151,152], aside from a few improvements to obtain the high sensitivity and time resolution required for the investigation of atomically thin samples. These changes will be discussed in detail later in this section. To begin with, we focus on the general layout of the setup and the basic functions of its parts.

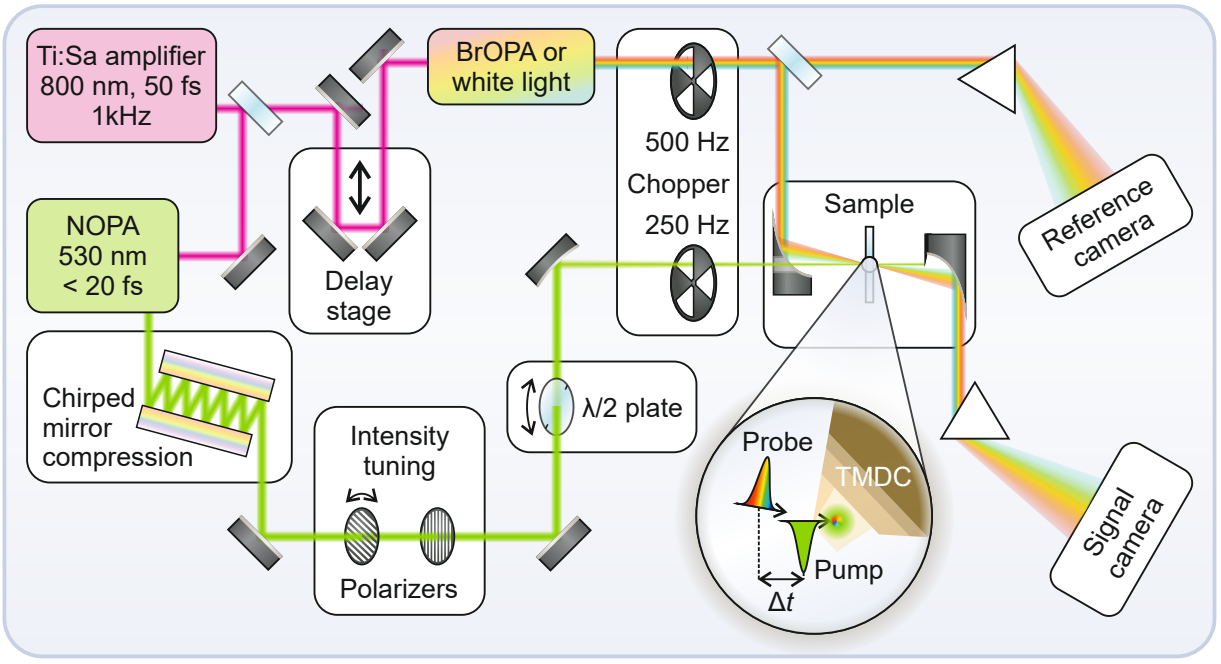

Figure 3.3: Setup for TA spectroscopy. Note that the NOPA can be operated at different output wavelengths or replaced by the plain second harmonic generation. The pump pulse compression may alternatively be performed using a prism compressor or is completely omitted. The spectrally broad probe light can be generated using a broadband noncollinear optical parametric amplifier (NOPA) or a standard supercontinuum generation. Adapted from [P3]

A titanium:sapphire amplifier (Spitfire Ace, Spectra Physics) emits pulses with a center wavelength of 800 nm and a duration of ≈ 50 fs at a repetition rate of 1 kHz. This fundamental beam is split up to feed the branches for pumping and probing separately. For the former, a NOPA converts the fundamental near-infrared pulses into visible ones with a tunable wavelength and - if properly compressed - an even shorter duration[153]. To achieve the latter, either chirped mirrors or a prism compressor compensate for the chirp accumulated in the NOPA and during the following beam path. This way, one typically reaches a temporal resolution of a few 10 fs. As an alternative pump source, the second harmonic at 400 nm suits the absorption range of most samples, but provides a worse time resolution. In the next step, the pulse energy can be tuned *via* the combination of two wire grid polarizers, by the first of them being rotated. Subsequently, a half-wave ($\lambda/2$) plate turns the linear polarization of the excitation as desired, before the pulses are focused onto the sample. Absorbed pump photons deposit energy in the system and create excited specimens, thereby triggering dynamic processes. The transmitted part of the excitation beam, on the other hand, is blocked.

The second portion of the fundamental beam is designated as the probe. First, it travels both ways over a stage with a linearly movable retroreflector to tune the delay t of the probe pulses with respect to the pump at the sample position. Second, it is converted into spectrally broad light using a broadband NOPA[154] or supercontinuum generation[155]. Finally, the probe beam is focused onto the sample as well to measure its absorption properties. The transmitted light is recollimated, dispersed by a fused silica prism and directed to the detection (signal) camera. In standard TA setups, the pump beam is chopped at half of the laser repetition rate, resulting in an alternating on-off pattern. This facilitates the direct comparison of the absorption characteristics of the sample with

versus without preceding excitation by comparing consecutive laser shots. Here, the TA signal in terms of the wavelength-resolved change in absorbance ΔA is calculated from the spectral intensities $I(\lambda)$ transmitted through the (un)excited sample:

$$\Delta A(\lambda, t) = A^*(\lambda, t) - A_0(\lambda, t) = -\log_{10} \frac{I^*(\lambda, t)}{I_0(\lambda, t)} \tag{3.1}$$

where $A^*(\lambda, t)$ and $A_0(\lambda, t)$ stand for the sample absorbance, while $I^*(\lambda, t)$ and $I_0(\lambda, t)$ denote the intensities at the signal camera, in each case with $(^*)$ and without $(_0)$ preceding pump pulse, respectively.

At this point, the modifications of this setup with respect to the standard one come into play. Here, the probe beam is split up into a signal and a reference portion. While the former proceeds to the sample as usual, the latter is directly dispersed onto a second camera. By this means, any fluctuations of the probe spectrum can be monitored in this undisturbed beam and are corrected for in the signal probe intensities in equation (3.1). This greatly improves the sensitivity, an essential prerequisite for the investigation of ultrathin samples like 1L-TMDCs. Additionally, two choppers operating at one half and one quarter of the laser repetition rate are placed in the probe and pump beam, respectively. This creates a four-shot pattern that not only allows for the comparison of the transmission of the excited *versus* the unexcited sample but also enables real-time monitoring of the dark current as well as of the scattered excitation light that reaches the camera. A final peculiarity of this setup is the tight focus down to about 10 µm by employing off-axis parabolic mirrors. Typical 1L-TMDC flake sizes range around a few 10 µm, thus demanding a high spatial resolution.

Overall, this setup is capable of measuring the transient absorption of samples after excitation at tunable wavelengths. It provides a high sensitivity as well as an excellent time and spacial resolution, all of which are required to investigate the ultrafast dynamics in TMDCs and their hybrid structures.

3.3.2 Disentanglement of dynamic processes and extraction of their spectral imprint

For the analysis of the 2D data set $\Delta A(\lambda, t)$, one typically conducts a global fitting procedure to separate consecutive processes and to characterize them in terms of their inherent spectral signal changes[156]. In this approach, the temporal evolution of the data is modeled using generic multiexponential functions or even specific rate equations. The former case reflects the most broadly applicable scenario, where one aims at the basic distinction of multiple steps and their time scales in a cascade of dynamics. On the downside, one pays the price that certain processes such as peak shifts and broadenings or nonexponential kinetics cannot be mapped in a quantitatively exact fashion. Nevertheless, even qualitative results usually suffice to identify the underlying mechanisms that determine the spectral shape and time evolution of the signal. In the end, each of the input exponentials yields a so-called decay-associated amplitude spectrum (DAS) that embodies the signal changes occurring on the according time scale.

The shape of the DAS encodes characteristic modifications of the sample's optical properties. For TMDCs, photoexcitation typically causes the alteration of absorption bands, in particular of their spectral position and width. Consequently, this creates specific signatures in the TA spectra, which are schematically illustrated by synthetic Gaussian profiles in figure 3.4. Part (a) shows the effect of a red shift with different magnitudes. It results in a pair of a negative peak at the original band position and

a positive one at lower energies. As the shift grows larger, the negative transient remains relatively constant, while the positive feature moves further to the red spectral region. Panel (b) depicts the influence of a band broadening, causing a reduction of the absorbance - *i.e.* a negative TA signal - in the center of the peak and a symmetric increase at the flanks. Here, a stronger broadening mostly yields a growth of the negative TA band. At the same time, the positive features initially rise as well but for a significant stretching of the original peak width, they predominantly extend spectrally while maintaining their amplitude. Finally, we combine a constant shift with an increasing broadening in figure 3.4 (c). Again, we find a pair of a positive and a negative peak. The latter barely changes with the magnitude of the broadening, while the former becomes gradually wider and its maximum shifts slightly to the red.

In total, TA spectroscopy provides a powerful tool to investigate ultrafast processes by means of their impact on the absorption properties of the sample material. This technique can resolve phenomena down to a few 10 fs. Moreover, a global analysis can separate individual, consecutive processes from the data, extracting their time constants and amplitude spectra. These possibilities make TA spectroscopy an indispensable method to monitor electronic and phononic dynamics.

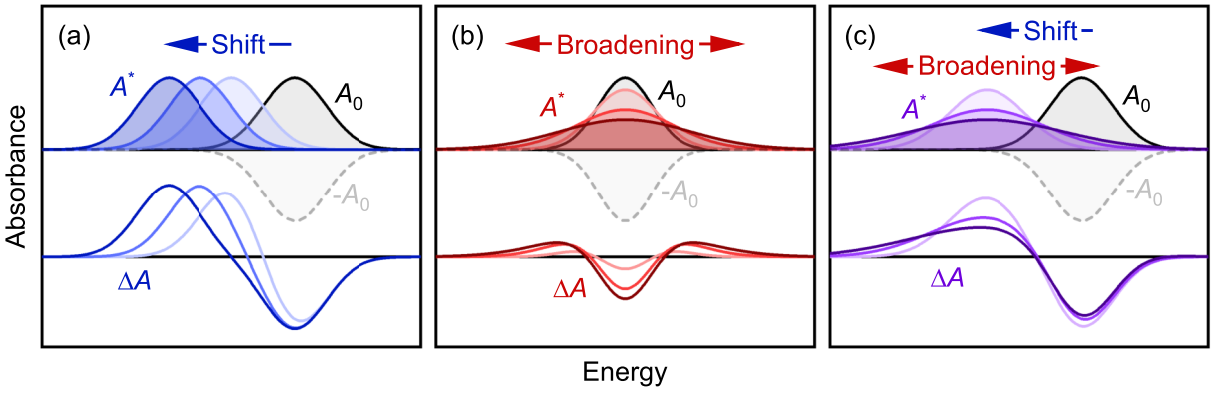

Figure 3.4: Generic signals for typical absorption band changes in TA spectroscopy. The upper curves represent the original absorbance A_0 and the altered peaks, subject to changes of different magnitude. The negative of the initial band is depicted as well according to equation (3.1) to illustrate the formation of the transient signals shown in the bottom. (a) Effect of a (red) shift. A peak pair results, where the negative one remains largely independent of the shift magnitude, while the positive one moves further to lower energies. (b) Broadening of the original absorption. In this case, a symmetric sequence of three features emerges, a negative one at the peak center, accompanied by a positive band at each side. (c) Constant (red) shift combined with increasing broadening. Again, the negative peak in the TA signal does not change significantly for different widths of the shifted A^*, whereas the positive counterpart clearly exhibits the broadening and its maximum slightly moves to lower energies on top.

4 Left out in the cold - Coupling between electronic and phononic system [P3]

The first key objective of this thesis is to unravel ultrafast processes in pristine TMDC flakes by means of TA spectroscopy, as sketched in the previous section 3.3. However, to be able to disentangle and extract different dynamics from the data, we focus on understanding the general formation of the signal to start with. Subsequently, we turn to distinguish the individual processes shaping the TA spectra over time, directing particular attention to the relaxation dynamics. This chapter represents several pivotal findings from publication [P3].

4.1 Formation of transient spectra by peak shift and broadening

Striving to identify the individual contributions to the transient signal, we focus on 1L-WS_2, where the different features occur relatively well separated[25–27]. The static absorption of the A exciton occurs slightly above 2.0 eV, the much weaker B band resides at 2.4 eV, see figure 4.1 (b). The C feature follows at even higher energies above 2.8 eV. In contrast to the previous two, this peak arises from band nesting and is not associated with the direct formation of excitons[94,98,157].

Figure 4.1 shows the continuous time evolution of the transient spectra in a 2D plot (a), whereas (b) illustrates their excitation fluence dependence at characteristic times, in other words probe delays. A pair of a negative peak at roughly 2.0 eV and a energetically lower positive one stands out. Given that the negative partner matches the wavelength of the A exciton absorption band in WS_2, this pair embodies the photoinduced red shift of this excitonic transition, as illustrated in section 3.3.2, figure 3.4. Ergo, we label the two peaks A^+ and A^-, respectively. A similar dual feature is lacking for the B exciton, supposedly owing to its drastically weaker amplitude[25,27]. Although such a shift to longer wavelengths is generally observed in TMDCs for excitonic and nonexcitonic peaks alike[74,76,158–171] [P1][P3][F1], the underlying physical mechanism is still subject to debates. The widespread approach of band gap renormalization (BGR)[172] assumes completely delocalized excited specimens - free carriers or excitons - with a spatially homogeneous density. Consequently, the resulting red shift would increase with fluence or in turn shrink during the recombination of the excited specimens. In [P1], however, we explicitly investigated the peak positions in the TA spectra of MoS_2 and demonstrated a constant displacement between the negative and positive excitonic bands during the whole recombination of the excited population. These findings question the BGR model and suggest a rather localized nature of the excited specimens. From the latter perspective, each of the single excitations contributes a small signal fraction to the spectrum, all of which are identical. Ergo, a higher density augments the transient amplitude but conserves the spectral position of the bands.

Naturally, the A^- peak maintains its shape and position, as it reflects the lacking original A band absorption in the parts of the crystal that contain an excitation. Nevertheless, we do observe changes in the width of A^+, both over time and with varying fluence. Initially, the hot excited specimens cause collisional broadening[158,161,166]. Accordingly, a higher excitation density enhances this effect. Over time, in contrast, a narrowing of the positive excitonic band takes place, pointing towards a cooling of the excited populations.

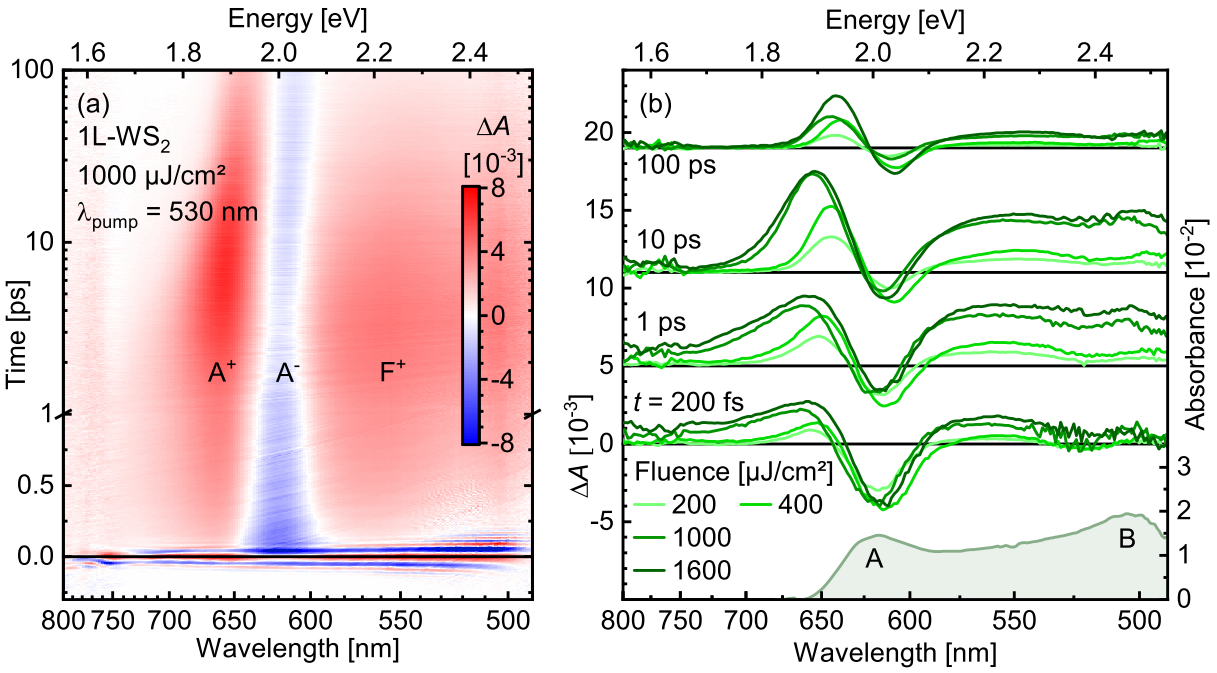

Figure 4.1: Formation and dynamics of the TA signal of 1L-WS_2 excited at 530 nm. (a) Time and wavelength-resolved 2D map of the absorbance change for a pump fluence of 1000 µJ cm^{-2}. (b) Excitation density-dependent TA spectra at characteristic probe delays and static absorbance. All TA curves share the same, original scaling but they are offset for clarity. In both depictions, a pair of a negative peak around 2.0 eV (A^-) and a red-shifted one A^+ characterizes the spectrum. Additionally, a broad, unstructured feature (F^+) occurs at higher energies. The static absorbance exhibits only the A exciton peak as a prominent feature, while B shows a rather weak signature. Adapted from [P3].

In addition to the excitonic peak pair $A^\pm$, a broad, unstructured feature spans the higher-energetic region, labeled F^+. Its spectrally constant amplitude cannot be linked to excitonic or other specific resonances and thus calls for a different explanation. Possibly, it may result from a modulation of the reflective background[25,26] of the material or from transitions into a diffuse variety of higher bands. Furthermore, this contribution exhibits a rather proportional growth with fluence. The excitonic signatures, on the other hand, clearly saturate at the fluences applied. Indeed, the Mott density, where the lattice is spatially filled with excitons, corresponds to a fluence of about 400 µJ cm^{-2} [10,161]. Any excessive excitons dissociate into free electrons and holes, capping the strength of the excitonic contributions. The free carrier density, in contrast, is not affected by this threshold, so that related signatures can grow further. Altogether, we conclude that - as suggested by its spectral shape and scaling of - the F^+ feature is related to free electrons and holes.

4.2 Thermal relaxation cascade

Now that we shed light on the mechanisms governing the formation of the TA spectra, we turn to the investigation of their time dependence. Starting from the 2D data $\Delta A(\lambda, t)$, we conduct a global fit analysis. As explained in section 3.3.2, such a procedure facilitates the disentanglement of the different processes, yielding the temporal scale plus the spectral signature of each single component. Here, we employ a model based on four exponential decays, each being described by a time constant τ_i and a amplitude spectrum $A_i(\lambda)$, the said DAS:

$$\Delta A(\lambda, t) = \sum_{i=1}^{4} A_i(\lambda) \cdot e^{-\frac{t}{\tau_i}} \tag{4.1}$$

The resulting DAS for each single decay and at different fluences can be found in figure 4.2 (a), while we illustrate the corresponding processes and intermediate states in figure 4.3. The DAS 1 contain virtually constant negative plateaus cut off roughly below 1.8 eV with only marginal modulations around the positions of the excitonic peaks. Instead of a decay, this rather described the emergence of the F^+ feature, which does not exist right from the beginning of the dynamics. In fact, the optical excitation mainly creates excitons above the band gap or in higher Rydberg states[11], see figure 4.3 (a). *Via* scattering within the electronic system, they relax to the band extrema on a subpicosecond time scale, with their excess energy transforming into a thermal distribution[160,170]. This yields elevated electronic temperatures, manifesting in a balance between bound and free carriers (figure 4.3 (b)), as has been demonstrated in studies using THz spectroscopy[173]. Ergo, we conclude that the free carriers manifest in the broad F^+. In this light, the lack of significant changes around the A^+ peak exclude a relevant heat transfer to the lattice on this time scale. Otherwise, the collisional broadening would be affected, causing a narrowing of the positive excitonic contribution.

Yet, a corresponding signature occurs in the DAS 2, consisting of a negative component around the position of A^+ accompanied by a small positive band on each side. This bears similarity with the broadening footprint discussed in figure 3.4 (b) in section 3.3.2. However, taking into account that in this case, we deal with the amplitude of a decaying signal, the DAS 2 describe the reduction of the broadening, that is in fact a narrowing. Apparently, the electronic temperature falls, within several picoseconds, hinting at an interaction with the lattice, *i.e.* phonons. This raises the question, why this does not cause a significant reduction of F^+, which after all hinges on the thermal balance between free carriers and excitons.

Such a phenomenon can be explained in the framework of a so-called hot-phonon effect[174–177]. According to this model, the electronic system couples more strongly to high-energetic phonons than to those with a low frequency. Consequently, the former quickly achieve a thermal equilibrium with the excited species. However, these phonons contribute only a limited fraction to the overall heat capacity of the lattice, thus sustaining a relatively high temperature, as indicated in figure 4.3 (c). Moreover, the dynamic balance between the high-frequency (hot) phonons and the electronic system implies reabsorption of the former by the latter, which contributes to keeping the electronic temperature high. Indeed, values of 1500 K have been proven to survive for at least multiple picoseconds[173], even at much lower fluences than applied here. In other words, a relevant fraction of the excess energy of the excited species above the band gap is preserved. In this light, the harvesting of this energy seems feasible, *e.g.* in terms of thermally activated charge transfer processes.

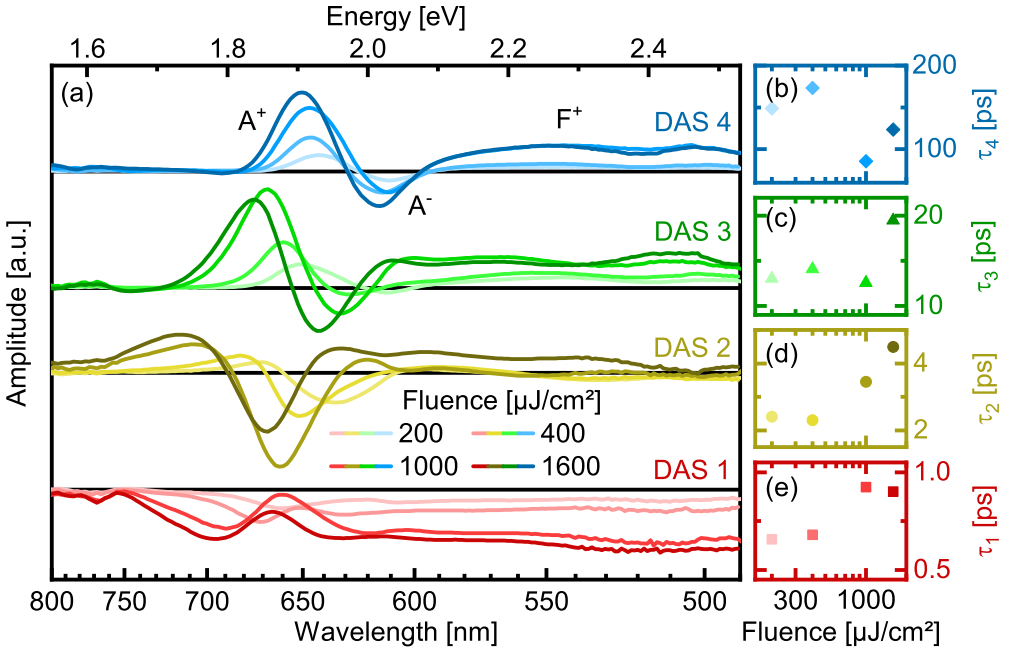

Figure 4.2: Four-exponential global analysis of transient dynamics in 1L-WS_2. (a) DAS corresponding to the four decays for different fluences. (b-e) Excitation density dependence of the time constants belong to each of the DAS. The three fastest processes decelerate with increasing fluence, whereas the slowest decay exhibits no systematic trend. The physical background of the four different signatures is illustrated in figure 4.3. Adapted from [P3].

In relation to the excitation density, one additionally notices that the features of the DAS 2 occur at longer wavelengths as the fluence values increase. Evidently, the center of the narrowing peak shifts to the red, which signifies a decline in the corresponding transition energy. We ascribe this to the pronounced thermal occupation of the discussed high-energy phonon modes, slightly displacing the mean position of the atomic nuclei, which in turn may shrink the band gap. As a direct consequence, the optical absorption band causes the A^+ signature to shift to the red.

Within the next step of the dynamics, this particular difference between the various fluences vanishes. The most striking feature of the DAS 3 is a peak pair around 1.9 eV, matching the current position of A^+. The decay of a positive amplitude at the low-energy side and of a negative one at shorter wavelengths in principle describes a displacement towards the blue spectral region, see section 3.3.2. In the present situation, this means the reversion of the red shift related to the high-frequency lattice vibrations, as discussed at the end of the previous paragraph. Apparently, the population of hot phonons diminishes, indicating further cooling. Therefore, we conclude a coupling to the remaining phononic modes, leading to a thermal equilibrium of the whole system, meaning the excited species and lattice.

On top of that and similar to the DAS 2, the signatures in the DAS 3 reside at lower energies for higher fluences, while they are largely independent of the excitation density for the DAS 4. This indicates that during this final thermalization, the third phase of the dynamics, the majority of the hot phonon occupation is annulled. As figure 4.3 (d) sketches, the new equilibrium temperature appears to lie significantly lower than before. Accordingly, this should affect the thermal balance between excitons and free carriers in favor of the former. Indeed, the carrier-related F^+ starts to decay as well, as reflected by the broad feature in the DAS 3 of figure 4.2 (a) that prevails from 2.0 eV upwards.

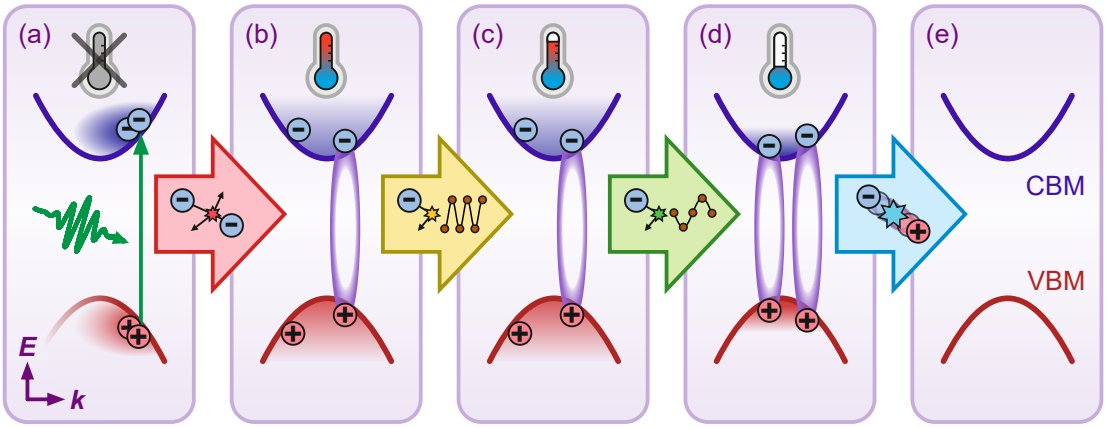

Figure 4.3: Thermalization cascade in 1L-TMDCs after optical excitation above the band gap. (a) Initially excited, nonthermal distribution beyond the band extrema. *Via* carrier-carrier scattering, it relaxes into (b), a high-temperature equilibrium between free carriers and excitons around the CBM and VBM, respectively. Next, coupling to high-energy phonons occurs, but implies only minor changes of the temperature and the equilibrium from (b) to (c). Subsequently, the remaining phonon species couple to the electronic system, cooling it down substantially and causing the bound electron-hole pairs to prevail in (d). Finally, the latter recombine, bringing the system back into the original ground state shown in (e). The color fillings of the bands illustrate the energetic distributions of the excited specimens at each stage. The horizontal arrows correspond to the processes associated with the DAS and time constants in figure 4.2.

In view of these two separate cooling steps, the phononic spectrum apparently cannot be treated as a single thermal bath but rather has to be subdivided into multiple populations. They couple differently to the electronic system and require some time to exchange heat between each other, allowing for transiently differing temperatures of both subsystems. Nevertheless, the excess energy above the band gap will ultimately dissipate between the excited species and the lattice.

After the thermal equilibration of the electronic and phononic system, the final step to take place is the recombination of the excited specimens. At the end of this process, the excited populations have decayed and the system has returned to the ground state, as depicted in figure 4.3 (e). While we will thoroughly treat these recombination dynamics in the next chapter 5, we may already draw some fundamental information from the spectral fingerprint. The DAS 4 in figure 4.2 (a) each essentially consist of a peak pair that resembles the actual TA signal at this point. According to section 3.3.2, figure 3.4, such a pair reflects a blue shift. In this case, however, it expresses that the red shift that originally gave rise to the basic TA spectrum is annulled. In other words, the transient signal simply decays.

In this light, it is noteworthy that the peak positions in the DAS 4 bear no prominent, systematic fluence dependence, in contrast to the previous two processes. On the one hand, this underpins the argumentation in section 4.1 pro a local nature of the excited specimens, as opposed to the delocalized picture of BGR. In the latter case, the photoinduced red shift of the original absorption would grow with rising excitation density, thus pushing A^+ further towards lower energies. On the other hand, the similar spectral shapes of all DAS 4 indicates that in the thermally equilibrated state, no significant difference in temperature occurs between the applied fluences. This means that the equilibration ends at about room temperature and leaves no substantial difference to the unexcited surroundings. Nevertheless, at the two highest excitation densities, the DAS 4

contain a broad, positive amplitude corresponding to the F^+ feature, which is related to free carriers. However, in this case, the dissociation of excitons does not result from an elevated electronic temperature but from the high number of excited specimens above the Mott density. In the course of the recombination, the exciton population will fall below this threshold and the free carriers will form bound pairs again. Ergo, F^+ decays, which is reflected by the DAS 4.

In addition to the amplitude spectra, figure 4.2 (b-e) also shows the corresponding decay time constants τ_i for various fluences. At higher values, we observe a slow-down of the dynamics' first three steps, namely the thermalization and cooling processes. Three different mechanisms can contribute to this deceleration at high excitation densities[175]. First, whenever large numbers of particles relax into certain states, they will amass a significant occupation in the course there. Consequently, for the following specimens, fewer free states are provided, lowering the transition rate into them. Second, excitons and free carriers cause Coulomb screening that may attenuate the electron-phonon coupling, which governs the cooling. Finally, the combination of the hot-phonon effect and the high fluences prolongs the second step of the dynamics. A high number of excited specimens coupling to the high-energy phonons create a large population of the latter. At a certain point, the creation and reabsorption of the phonons reach a balance. This represents a dynamic equilibrium, where effectively, no heat is transferred to the lattice system anymore, thus inhibiting cooling. The higher the initial excitation density, the sooner this point will be approached and the slower the cooling will proceed.

All in all, the TA signal of TMDCs results from a photoinduced red shift of the static absorption peaks. On top, this shifted band is subject to collisional broadening with rising fluence. Parallelly, free carriers stemming from dissociated excitons manifest as an unstructured positive feature at shorter wavelengths. With respect to the first research question of this thesis, we shed light on how electron-phonon coupling governs the equilibration dynamics of the excited species. The evolution at early times is characterized by thermal relaxation in multiple steps: Initially, the electronic system thermalizes within itself. Next, its cooling proceeds, starting with coupling to high-energy phonons, followed by the lower-energetic ones. Hence, significantly elevated electronic temperatures can be maintained for up to some 10 ps, preserving the excess energy after off-resonant excitation. This demonstrates that electron-phonon coupling is not just one single interaction but comprises a spectrum of such.

5 Through thick and thin - Recombination dynamics in bulk *versus* monolayer [P1]

As the previous chapter has illustrated, the recombination of the excited species represents the last step of the dynamics after optical excitation. At this stage, the electronic system and the lattice have essentially reached a thermal equilibrium, with temperatures in the rough order of magnitude of room temperature, see section 4.2. Therefore, charge carriers are bound in form of excitons in 1Ls, while they remain dissociated in bulk TMDCs, as discussed in section 2.1.1. As a consequence, the latter case requires two independent particles to meet in order to recombine, suggesting a superlinear relation between carrier density and their recombination rate[178,179]. Given bound excitons, on the other hand, one would expect a geminate process that is not influenced by the overall number of excitations. In the following, we investigate the impact of these two opposing natures of the excited specimens on the recombination dynamics based on publication [P1].

To that end, we compare time traces of 1L-MoS_2 at characteristic wavelengths for multiple pump fluences, in other words for different initial excited specimen densities (figure 5.1). The normalized curves for the bulk material in panel (a) demonstrate that after a few picoseconds of thermalization and cooling dynamics, the signal decay proceeds substantially faster, the higher the fluence. Quantitatively, the signal falls from its amplitude after thermal equilibration to half of that value within about 2 ns at the lowest *versus* 100 ps at the highest excitation density. This points towards multi-particle interactions governing the recombination dynamics, in agreement with aforementioned expectations.

At the same time, the decays seem to decelerate over time for high excitation densities in relation to lower ones, as the normalized traces for the two highest fluences intersect again around 2 ns. This suggests the involvement of additional species or states that are significantly consumed or occupied during the recombination of large numbers of charge carriers. As a matter of fact, crystal imperfections such as vacancies and antisites[90,180] are known to mediate the process, leading to the model of defect-assisted Auger recombination[20,74–78,181]. Here, a scattering process between two electrons leads to one of them being trapped at a defect site, while the other one takes up the excess energy. The latter will quickly relax back to the band minimum, whereas the trapped carrier can subsequently recombine with a hole from the valence band. While this last step appears to exceed the experimental time window in these measurements, we fit the temporal evolution of the TA signal according to the trapping process:

$$\frac{\mathrm{d}n_\mathrm{e}}{\mathrm{d}t} = -\frac{\mathrm{d}n_\mathrm{d}^*}{\mathrm{d}t} = -\kappa_\mathrm{A}\, n_\mathrm{e}^2(t)\,(n_{\mathrm{d},0} - n_\mathrm{d}^*(t)) \tag{5.1}$$

where n_e represents the free electron density and n_d^* is that of the occupied defects, as opposed to the total accessible ones $n_{\mathrm{d},0}$. κ_A describes the Auger rate constant. The initially excited electron density $n_0 = n_\mathrm{e}(t = 0)$ scales proportionally to the signal amplitude at the beginning and is the only individual parameter for each fitting curve. All the other ones are fitted together for all fluences, yielding single, unified values. Therefore, we use the initial densities as measures for the individual amplitudes in order to normalize the data and fit curves in figure 5.1 (a). They exhibit an excellent agreement for high fluences, whereas for lower values, the decay initially starts a bit faster than the model predicts. This might indicate the influence of an additional recombination mechanism that scales rather linear with the carrier density and thus plays a role only at low fluences.

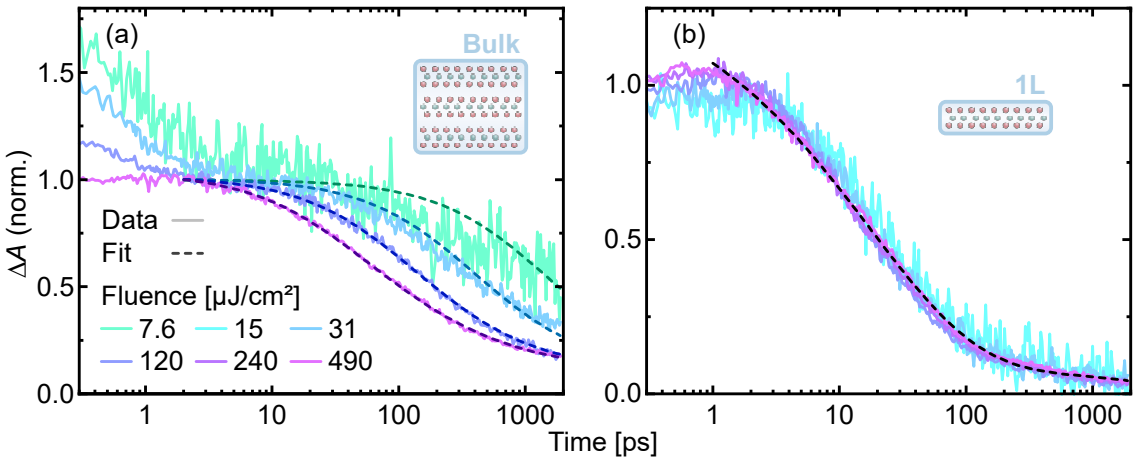

Figure 5.1: Recombination dynamics in MoS_2 in dependence on the flake thickness. The panels show normalized TA time traces (pale, solid lines) plus corresponding fits (dark, dashed lines) for a bulk (a) and monolayer (b) sample at various excitation fluences, respectively. (a) The signal decay generally accelerates for higher fluences. Still, at the highest excitation density, it slows down at longer times, even falling behind the next lower fluence. (b) For the 1L, in contrast, the curve shape is independent of the excitation density. Adapted from [P1].

Nevertheless, defect-assisted Auger recombination reproduces the prominent behavior at higher excitation densities. To conclude, this model covers the aforementioned key characteristics of the signal dynamics.

In the case of monolayer MoS_2, the TA decay takes place on shorter time scales than in the bulk, reaching half of the initial amplitude within circa 20 ps. Most strikingly, however, the normalized traces in figure 5.1 (b) bear almost identical shapes for all excitation densities, in stark contrast to the thick crystal. These two points hint at a geminate recombination of the bound electron-hole pairs. However, the low photoluminescence quantum yield in TMDC suggests a dominance of nonradiative *versus* radiative channels[24,47,48]. Indeed, defects are known to govern the recombination in monolayers as well[74–76,164]. Given that electron and hole are already bound to each other, the decay of excitons is essentially limited by their 2D diffusion towards the defect sites. This model results in a stretched exponential time evolution of the excited population[182,183]. Additionally, we incorporate an exponential lifetime τ_X of those excitons that never meet a defect. These considerations lead to the following fitting function:

$$n_X(t) = n_0 \left[e^{-B\sqrt{t}} + \alpha e^{-\frac{t}{\tau_X}} \right] \tag{5.2}$$

with the initial exciton density n_0 and the fraction α of excitons that do not recombine at a defect site. The rate coefficient $B = c_{2D}\sqrt{n_d D}$ comprises the dimension-dependent constant $c_{2D} = 8.525$[182], the defect density n_d, and the diffusion coefficient D. Again, the fit is performed for all fluences using the same parameter set, except for n_0, which reflects the amplitude at time zero. Like for the bulk data, we normalized data and fit in figure 5.1 (b) to this initial signal as obtained from the fit. Consequently, all fitted curves are identical in this representation and plotted as the black, dashed line. It bears a good agreement with the data, suggesting that the chosen model covers the major characteristics of the decay mechanism.

Unfortunately, the model described by equation (5.2) does not allow for a separate determination of the diffusion coefficient and the defect density, as they fuse to the single fitting parameter B. Yet, assuming diffusion coefficients in the rough order of magnitude of $1 \times 10^{-1}\,\mathrm{cm^2\,s^{-1}}$[120,166,184], we obtain areal defect densities of $1 \times 10^{10}\,\mathrm{cm^{-2}}$, slightly lower than previously reported values[74,90,163,164,185]. However, on the one hand, not all types of defects may contribute equally to the exciton recombination. On the other hand, both diffusion and defects[185] crucially depend on the crystal quality and the preparation procedure.

In summary, we tackled the second fundamental question on the layer-dependent recombination dynamics of the excited species, as raised in the introduction. By the comparison of samples with differences thicknesses, we reveal fundamental distinctions in the physics and dynamics of the recombination process. In bulk MoS_2, we find a defect-assisted, multi-particle Auger scattering, which accelerates with increasing fluence from nanoseconds to 100 ps. In the monolayer, in contrast, the decay proceeds faster, on a 20 ps timescale, owing to the geminate recombination of electron and hole within the exciton they form. To that end, this bound pair has to diffuse to a defect site, which eventually limits the excited state lifetime. Thus, in the light of optoelectronic devices, diffusion equally governs the intended function as well as trapping leading to losses. Consequently, a targeted optimization strategy has to lower the defect density or the required path lengths of excitons rather than focus on accelerating their diffusion itself.

6 Having a good vibe - Coherently excited phononic motion [P3]

In this chapter, we investigate a fundamentally different process taking part in the transient evolution of optically excited 1L-TMDCs. The previous two chapters focused on the path that leads the excited species back into the electronic ground state. Following the principle of monotonously increasing entropy, the consecutive steps of thermalization, cooling, and recombination redistribute the excitation energy irreversibly within the sample. This takes place on time scales from half a picosecond up to some nanoseconds. However, at shorter times, a nonmonotonous effect appears, resulting in oscillating transient signals. With sufficiently high time resolution, specific phonon modes of the TMDCs can be coherently excited and monitored. In the following, on the basis of publication [P3], we first extract the oscillatory part from the TA data. Afterwards, we investigate its dependence on the material, the wavelength and the excitation density.

6.1 Isolation of the oscillatory part of the transient dynamics

A profound analysis of the coherent phonons requires to separate their periodic signatures from the rather monotonous rest of the dynamics at first. Here, we demonstrate the corresponding procedure on the data for 1L-$MoSe_2$, where the oscillations emerge much more clearly from the data than for WS_2.

Generally, the basic TA signal follows the same scheme for all TMDCs, namely the photoinduced red shift of their absorption bands, as discussed in section 4.1. This holds for $MoSe_2$ as well, the differences merely lie in the number of peaks contributing and their exact wavelength, see figure 6.1 (a). Indeed, we observe the signatures of the shifted A, B and C bands, each manifesting in a negative signal at their original spectral position and a positive one at longer wavelengths. Solely A^+, the embodiment of the displaced A exciton absorption after excitation, falls out of the investigated spectral interval on its low-energy side. Beyond the peak shifts, the broad, unstructured F^+ feature occurs likewise. Yet, it overlaps with the numerous other contributions, especially C^+, veiling the exact spectral shape and dynamics. In principle, the TA signal exhibits the same pattern for different TMDCs.

However, what catches the eye in the $MoSe_2$ 2D data in contrast to WS_2 are temporal oscillations superposing the TA signal during the first few picoseconds. To isolate them from the other contributions, we fit and subtract all exponential, nonoscillatory dynamics, using a function similar to equation (4.1) in section 4.2. Beforehand, the data before 0.2 ps has been cut out with the intent to avoid any impact of the zero point artifact. Likewise, scans employing a logarithmic time axis, have been additionally limited to a short duration, with maximum probe delays of 3 ps. Beyond this boundary, the spacing of the time points reaches the order of magnitude of the oscillation period. Consequently, the logarithmic sampling does not capture the oscillatory nature properly anymore. Given this shorter time interval compared to τ_3 and τ_4 of the previous global fit, three instead of four exponential decays suffice. In return, the fit was performed for each wavelength individually to increase its accuracy.

The subtraction of the fit result from the original data yields the residue signal, as depicted in figure 6.1 (b). It underlines the aforementioned observations, showing clear oscillations throughout the whole spectrum that persist for multiple picoseconds. On top

of that, one recognizes a remarkably stable phase from 550 nm to 700 nm that begins to drift continuously when leaving this range. In particular, no sudden flips of the sign can be found while moving alongside the energy axis.

The final step in extracting the oscillatory characteristics from the signal comprises the separation of individual frequency components employing a fast Fourier transform (FFT). The obtained 2D map of the FFT amplitude in dependence of the wavelength and the frequency is given in figure 6.1 (c). It features a single dominant frequency band at approximately 7 THz. Such material responses need to be taken into account when aiming at THz electronics based on TMDCs. Otherwise, these oscillations may disturb the carefully engineered properties of such devices in the relevant spectral region, impairing their performance. From this perspective, this finding indicates the involvement of one particular resonance and thus lays the foundation for its identification, which will be tackled in the next section.

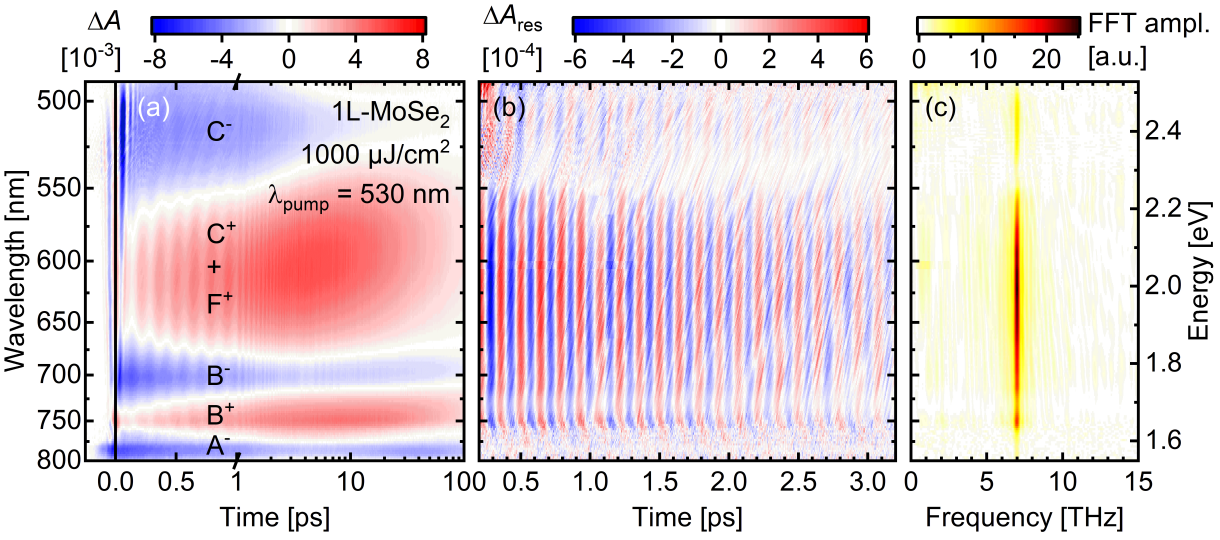

Figure 6.1: Isolating and characterizing coherent oscillations in the TA signal of 1L-$MoSe_2$. (a) 2D TA map showing shift signatures for all static absorption peaks. On top, oscillatory features occur within the first few picoseconds. (b) Residue data after fitting a three-exponential decay to the short-term time evolution of the TA spectra. The residual dynamics are dominated by temporal oscillations covering nearly the whole spectrum and enduring for multiple picoseconds. The excitation conditions were identical for (a) and (b), but (a) spans a longer time interval scanned with logarithmic spacing, while (b) represents a linear, more detailed scan. (c) 2D map of the Fourier transform amplitude of the data in (b). A single frequency band at 7 THz stretches over almost the entire measured spectral region. Adapted from [P3].

6.2 Interplay between coherent lattice dynamics, electronically excited states and optical properties

Based on the isolated oscillation data, further analyses can be conducted. Both the FFT frequency decomposition and suitable fits allow for the extraction of key parameters like frequency, lifetime and amplitude as well as their behavior under varying experimental conditions such as the excitation density. Throwing light on these characteristics facilitates the identification of the relevant physical processes causing and determining the periodic imprint on the transient dynamics.

6.2.1 Identification of involved Raman modes

In fact, previous studies reported similar temporal oscillations in various 1L-TMDCs and ascribed them to the coherent excitation of phonons corresponding to the A_1' Raman mode[69–72]. To verify this assignment, we compare the FFT curves of spectrally averaged time traces from different 1L-TMDCs to their Raman fingerprint in figure 6.2.

The clearest constellation occurs in 1L-$MoSe_2$, where the Raman signatures of the A_1' and E′ mode prevail in the spectrum and lie well distinguishably apart from each other[62,64,68]. The FFT peak, in turn, resides at 234 cm^{-1} and thus lies closely to and on the red side of the A_1' Raman band. This small spectral displacement between FFT and Raman exists for all materials and will be discussed in section 6.2.3.

For 1L-WSe_2, the A_1' and E′ modes occur at almost identical frequencies[62,63,65,67]. Moreover, in the Raman spectra, several others gather along with them in the spectral proximity of the single peak in the FFT spectrum. Accordingly, the ascription of the oscillation to a specific mode appears more complicated. To that end, Jeong *et al.*[69] utilized the different layer number dependence of the modes' frequencies. Going from monolayer to bulk flakes, they ascertained a decrease of the period found in the TA data which is in line with the stiffening of A_1' as opposed to the softening of E′. In our data, the FFT peak for WSe_2 again matches the slightly red-shifted A_1' mode, in agreement with the other materials and the literature.

Finally, we turn to 1L-WS_2, where the two characteristic lattice vibrations are again well separated[62,63,65,67]. In this case, and the dominant FFT band can be found marginally below the A_1' frequency of 12.5 THz. Therefore, we attribute the oscillations in this material to the out-of-plane Raman mode once more.

Evidently, the ultrashort pump pulses that are employed in the TA setup trigger a collective nuclear motion following the normal coordinates of the A_1' mode. As sketched in section 2.1.2, this simultaneous excitation of phonons could in principle proceed either *via* ISRS, which is a scattering mechanism, or due to DECP, which implies a relocation of the nuclear equilibrium positions in an electronically excited state[110,186]. Experimentally, these two can be distinguished based on the initial phase or displacement of the resulting oscillations. In ISRS, solely a transfer of momentum occurs, ergo the periodic motion starts at a finite velocity but at zero displacement. In DECP, on the contrary, energy and momentum of the photon are absorbed by the electronic system, therefore the lattice remains initially unchanged and still. However, owing to the altered equilibrium position, the nuclei indeed exhibit a maximum displacement from the perspective of this new balance. In our work, we extracted a maximum negative signal around time zero by applying fits, thus these findings support the DECP model [P3]. Concludingly, previous studies and this thesis agree on the displacive excitation of the A_1' mode of 1L-TMDCs upon absorbing photons.

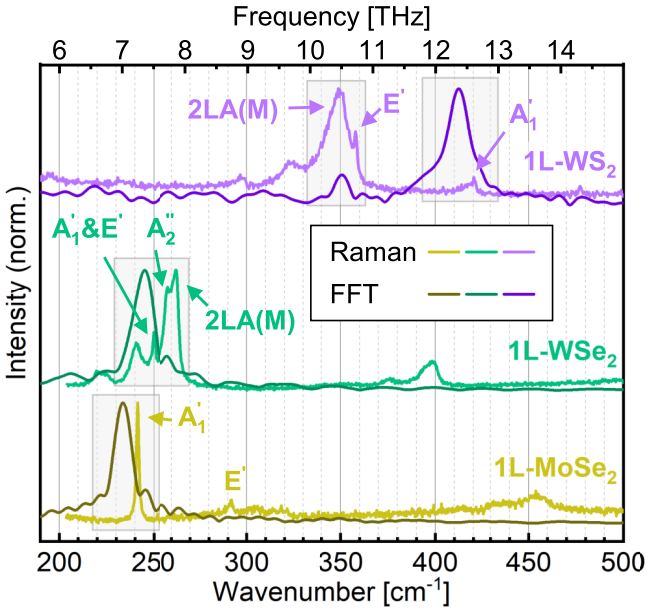

Figure 6.2: Assigning the frequency components to Raman modes for different TMDCs. FFT *versus* Raman spectra for the three materials, respectively. In each case, the main FFT frequency band lies close to the A_1' Raman mode, but at a slightly lower wavenumber. In WS_2, a second FFT peak occurs, matching the weakly red-shifted E′ vibration. The labeling of the Raman features corresponds to that in references[62,64,67]. The 2LA(M) peaks stem from the excitation of two longitudinal acoustic phonons at two M points with opposite wave vectors, as discussed in section 2.1.2. The nuclear motions corresponding to the two characteristic modes are illustrated in figure 2.2 (a,b). Adapted from [P3].

Yet, in contrast to the other TMDCs, the WS_2 FFT spectrum bears a second, weaker peak. Taking a red shift from Raman to FFT spectrum similar to the one for the A_1' mode into account, this smaller contribution accords to the E′ lattice vibration. To our best knowledge, a corresponding feature had not been observed in 1L-TMDCs up to this point. As a matter of fact, some studies even argued that the DECP can exclusively take place for symmetric modes like A_1'[70,186]. However, in the case of the present 1L-TMDCs, the crystal structure itself breaks the inversion symmetry (see section 2.1.1), abolishing this fundamental constraint. Our work proves that the excitation of the E′ lattice vibration occurs as well, albeit with a more subtle mark left on the TA signal. This expands the ambit of the DECP mechanism and makes 1L-TMDCs an ideal platform to study its nature, especially the dependence on the pump wavelength.

Summing up, comparing the frequency components of the TA residue to the Raman spectra confirms the dominant DECP of the A_1' mode for all three materials. On top, we find a second, previously unknown contribution with a much weaker amplitude and attribute it to the E′ mode.

6.2.2 Spectrally broad imprint of the coherent lattice vibrations onto the transient signal

Now that the physical background for the excitation of coherent phonons has been identified, we move from their cause on to their effect on the sample properties. As we probe the latter in terms of the transient change of the absorption, the key lies in analyzing the spectral TA amplitude associated with the oscillations.

To obtain this fingerprint for the A_1' mode, we integrate the 2D FFT amplitudes (*e.g.* figure 6.1 (c) for $MoSe_2$) over the width of the dominant frequency band. The resulting data is normalized and plotted in figure 6.3 (a) for all three TMDCs. What the different curves have in common is a generally broad distribution of the oscillation amplitude over almost the entire depicted spectrum. In addition, modulations occur for each material at individual wavelengths. This brings up the question whether the

peaks and dips may be in some way linked to the general transient features discussed in section 4.1. For a direct comparison, the bottom panel (b) of figure 6.3 shows the spectra at a probe delay of 1 ps. Indeed, all local minima of the oscillation amplitude coincide with zeros of the TA signal, although *vice versa*, not all TA zero-crossings are accompanied by such a dip. The local maxima of the oscillation strength, in turn, mostly occur at the spectral positions of extrema in the TA signal, albeit - again - not all of the latter manifest in a peaking oscillation amplitude. Nonetheless, there seems to exist a link between the major transient signatures and the spectral modulation of the signal strength that the coherent phonons imprint onto the TA. Yet, the principal nature of the oscillation amplitude still remains a broad distribution over a large portion of the investigated wavelength interval.

Previous studies have tried to find the physical mechanism of how the coherent lattice motion translates into a transient change of the material's absorption. Their approach consists of band structure simulations, in which the nuclei are displaced according to the normal coordinates of the A_1' mode[69–71]. These calculations yield a narrowing or widening of the band gap for nuclear motion in either direction, respectively. Consequently, the lattice vibration would mainly manifest in periodic shifts of the absorption bands, *i.e.* the (positive) transient peaks. This mechanism would lead to several striking characteristics of the oscillatory imprint on the TA signal. When - for instance - a positive peak shifts to lower energies, the signal increases on its red side while it decreases on the blue one (comparable to figure 3.4 (a)). Ergo, the oscillation would exhibit a different sign, that is an opposite phase, on either side of the (mean) peak position. Regarding the amplitudes, a shift of the band which is small compared to its width essentially follows the first derivative of the peak shape. That means a maximum signal change in the flanks, where the slope is the steepest. Around the peak center, in turn, the derivative is essentially zero, signifying a vanishing oscillatory component in the middle of the band. Taken together, this model predicts that each affected absorption band results in two maxima of the oscillation amplitude, occurring on each side of the underlying peak, distinguished by a phase flip in between. In fact, this sudden phase change has been observed in $MoTe_2$, where the calculations generally yield a good agreement with the data[71]. For MoS_2, on the other hand, there is a significant discrepancy between the predicted and measured oscillation amplitude spectrum[70].

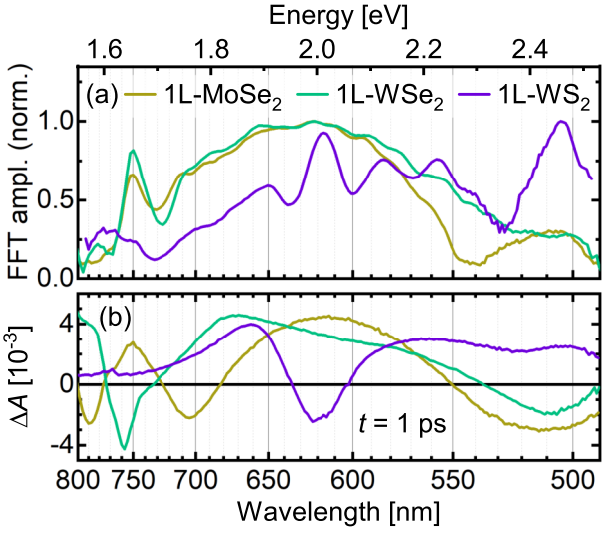

Figure 6.3: Integrated and normalized spectral amplitude of the A_1' oscillation FFT band (a) compared to the TA signal at a probe delay of 1 ps (b) for several 1L-TMDCs. The amplitude spectra generally exhibit a broad shape spanning almost the entire investigated wavelength regime, dropping at its rim. On top, around some of the excitonic TA peaks, the oscillation amplitude is modulated. Here, the minima match the zeros of the TA peak, while the maximum amplitude occurs at the extrema of the transient spectrum. Adapted from [P3].

A qualitative comparison of our experimental findings with these theoretical predictions highlights fundamental differences. The latter comprise multiple distinct peaks in the amplitude spectra of the periodic signal, whereas we observe a single contribution spanning the entire investigated wavelength region. Moreover, the calculated band shift would result in sign flips of the oscillatory signal between the two sides of each shifting feature. However, in our data, the phase stays constant throughout the major part of the spectral range, drifting only gradually towards its rim. Thus, our findings bear a stark contrast to the aforementioned theoretical approach. This demonstrates the need for a different model to describe the effects of coherent phonic motion on the optical absorption properties of 1L-TMDCs.

6.2.3 Softening of the A_1' mode with increasing excitation density

As we discussed in the preceding sections, the coherently excited lattice motion induces a broad spectral response of the material. The substantial excitation densities applied in the TA experiments raise the question, whether this reaction bears any nonlinearities. In classical Raman spectroscopy, for instance, the modes shift with higher laser power due to heating of the sample[187,188]. The ultrafast timescales accessible in TA spectroscopy, in contrast, allow for an investigation of this effect beyond thermal equilibrium. With this in mind, we fit the spectrally averaged oscillation time traces to monitor the progression of the key parameters under variation of the pump fluence.

While the oscillation amplitude grows largely proportionally to the excitation density, we do observe a nonlinear behavior concerning the frequency. The fitted values are plotted in figure 6.4. With a higher excitation density, the frequency gradually falls, the oscillation becomes slower. At high occupations of electronically excited states, constituted by antibonding orbitals, the total strength of the covalent bonds decreases. On the one hand, this manifests in the displacement of the equilibrium nuclear positions, which initially results in the DECP. On the other hand, a weaker bond is usually accompanied by a flattened potential, in other words a lower curvature, which expresses a reduced frequency of the harmonic oscillator derived from it. In contrast to this nonequilibrium electronic mechanism, we can exclude a purely thermal effect, as a relevant heating of substrate-supported flakes requires mean laser intensities in the order of $\mathrm{mW\,\mu m^{-2}}$ [187], while we apply $\mathrm{mW\,cm^{-2}}$. Admittedly, the peak power during the pulse lies much higher in TA spectroscopy, but at this stage of the dynamics, this energy has not relaxed into a thermal distribution yet, as demonstrated in chapter 4.2.

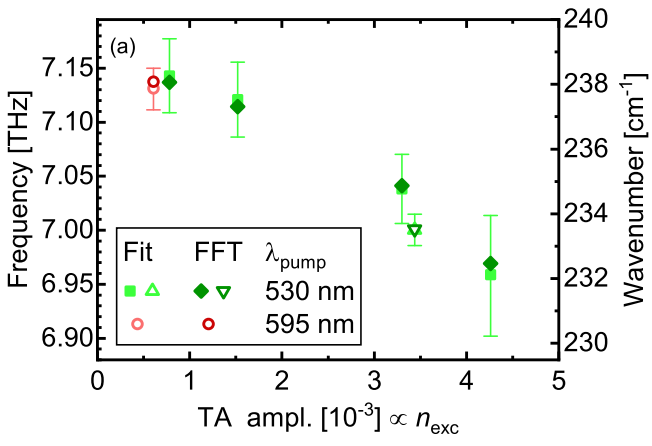

Figure 6.4: Mode softening at high excitation densities. The y-axis shows the oscillation frequency, as obtained from fitting and the FFT analysis. On the x-axis, in turn, the mean TA signal from 500 nm to 520 nm at 0.2 ps is represented, as a measure for the excitation density that is independent of the pump wavelength. Solid symbols stem from TA scans with a logarithmic time scale, whereas open ones correspond to an equidistant time axis with small steps. Adapted from [P3].

The slow-down of the oscillation at high excitation densities appears to be the major cause for the discrepancy in the frequencies found in the Raman spectra *versus* the FFT of the TA signal. In contrast to the high fluences of $1000\,\mu J\,cm^{-2}$ applied in the TA measurement featured in figure 6.2, the continuous wave nature of the Raman spectroscopy constitutes a vanishing excitation density. Taking this into account, the initially observed A_1' mode frequency shift in the Raman *versus* the FFT spectrum of $\approx 10\,cm^{-1}$ at the highest fluence shrinks to a few cm^{-1} at the lowest one.

The discussed dependence of the oscillation frequency on the excitation density allows for a manipulation of the materials response by choosing corresponding experimental parameters. With our work, we extend the portfolio of tunabilities, which already contained doping, strain, layer number[109], and temperature[63,66] as parameters by which to influence the Raman modes of 1L-TMDCs.

In this chapter, we answered research question three on coherent phononic motions by exciting and tracking them *via* TA spectroscopy with ultrahigh time resolution. The dominant contribution corresponds to the A_1' vibrational mode in all materials. However, in WS_2, exclusively, an additional peak appears matching the E' mode, which had not been observed in previous TA studies. Ergo, the mechanism for exciting coherent phonons appears more widely applicable than previously suggested. A_1', in turn, manifests as a broad spectral response, casting doubt on theoretical models that principally predict a periodic shift of transient peaks. These results indicate that the interaction between the coherent lattice motions and the electronic system is not yet fully understood. Anyway, they crucially matter for TMDC-based devices operating in the THz regime, since the lattice motions might interfere with the intended functionality. Furthermore, on the positive side, a higher excitation density red-shifts the A_1' mode, thus opening an opportunity to partially tune its frequency.

7 Till death do us part - Charge separation in hybrid structures [P2]

After the preceding in-depth investigations of pristine TMDCs, we now turn to the combined systems, meaning hybrid structures involving dye molecules. They facilitate interfacial charge transfer and thus form a promising basis for optoelectronic applications. Previous studies typically applied rather thick coatings in the nanometer regime[124,129,132–134,138,140]. Aside from that, the focus often lay on the impact of the molecular coverage on the TMDC-PL[123,140,189]. However, the perspective of the molecular side in case of monomeric films remains unknown. Therefore, we turn to investigate the dye fluorescence using µPL and FLIM to track down interfacial interactions, based on publication [P2].

Figure 7.1 comprises the spatially and spectrally resolved emission of a PO/1L-WSe_2 hybrid *versus* a PO/hBN reference sample. The micrographs in (a) and (d) give an overview of the flake topography, which allows to target specific regions for the spectroscopic investigation. Their resulting emission spectra are shown in (c). On hBN, PO exhibits the three-peak Frank-Condon progression that compares with the spectral fingerprint of a monomeric solution, see figure 2.3 in section 2.2. Solely the 0-0 fluorescence peak appears significantly weaker, which may be owing to its vicinity to the cut-off wavelength of the filter for the excitation light. On WSe_2, in contrast, this signature of PO vanishes, pointing towards quenching of the emission. In return, the PL of the 1L-WSe_2 arises at lower energies of 1.6 eV to 1.7 eV.

Integrating the 3D intensity data $I(x, y, \lambda)$ from the µPL scans over this spectral region yields the 2D map of the monolayer emission. This is depicted in (f) and reflects the topography of the 1L areas exclusively. A similar procedure can be performed to extract the signal from PO. However, in this case, we base it on FLIM measurements, as the single photon counting employed there provides a higher sensitivity. Besides, the explicit selection of the monomeric PO emission can be achieved by a bandpass filter from 500 nm to 550 nm. It transmits the 0-0 fluorescence of the dye exclusively and explicitly blocks contributions from agglomerated dye molecules or the 1L-TMDCs. The corresponding 2D maps are given in (b) and (e) for the hBN and WSe_2 flakes, respectively. In the former case, only minor differences between the PO fluorescence intensity on the substrate *versus* the flake can be observed. On the WSe_2 flakes, on the other hand, we detect barely any dye emission, again indicating a strong quenching.

Despite a substantial reduction of the emitted light, the conclusion of quenching requires a second criterion to be fulfilled[118]. Mathematically, we can describe this phenomenon by two competing decay channels, a radiative and a nonradiative one. Both are characterized by an individual rate constant $\kappa_{(\mathrm{n})\mathrm{rad}} = {}^{1}/_{\tau_{(\mathrm{n})\mathrm{rad}}}$, which represents the reciprocal time coefficient of each separate process. In the view of the overall dynamics, the two rates add up to a single effective one, whereas the molecules split up between the two paths according to the ratio of the rate constants. For the fluorescence, this means that its quantum yield

$$\Phi_{\mathrm{fl}} = \frac{\kappa_{\mathrm{rad}}}{(\kappa_{\mathrm{rad}} + \kappa_{\mathrm{nrad}})} \tag{7.1}$$

is reduced in the presence of a quenching channel. The higher the according nonradiative rate in relation to the radiative one, the more excited molecules follow the former path, while a declining part of the population still emits.

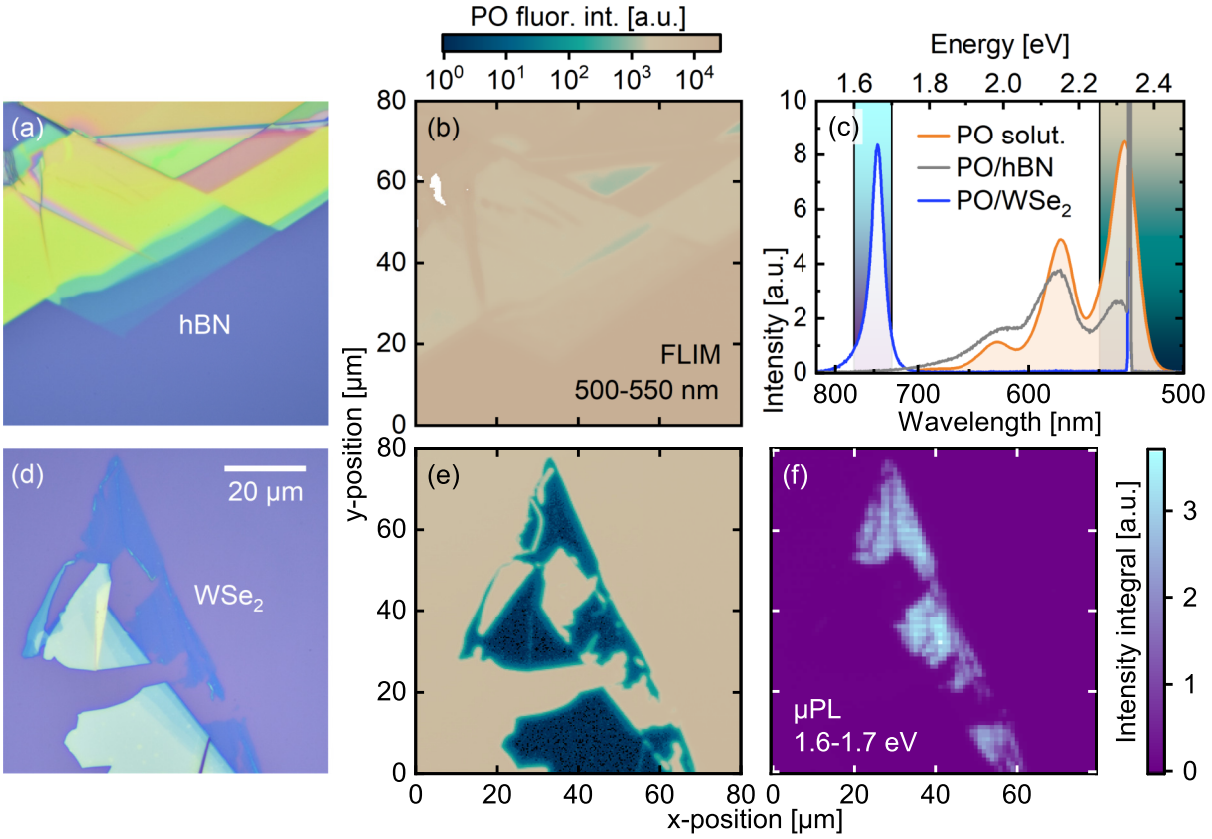

Figure 7.1: Emission maps and spectra of hybrid structures. (a,d) Microscope images of hBN and WSe_2 flakes, respectively. (b,e) FLIM intensity maps for the areas depicted in (a,d). They were acquired employing 440 nm pump pulses and using a bandpass filter from 500 nm to 550 nm in front of the detector to select only the 0-0 fluorescence of PO. While the logarithmic scaling barely shows any differences between flake and substrate in the case of hBN, the emission of the dye is drastically reduced on the WSe_2 flakes. (c) Emission spectra for the hybrid structures after excitation at 532 nm and a dilute PO solution in chloroform as a comparison, the latter scaled to roughly match the given intensities. For PO/hBN, the spectrum roughly resembles the monomer fluorescence. For PO/WSe_2, the dye emission vanishes, whereas the TMDC-PL emerges between 1.6 eV to 1.7 eV. The colored areas represent the spectral intervals represented in the 2D maps in (b,e) and (f), respectively. (f) PL intensity map for the 1L-WSe_2 emission, reflecting the topography of the monolayer region. Adapted from [P2].

In the experiment, the emergence of a nonradiative pathway manifests as the intensity drop that we observe for the PO on the TMDC flake as the first criterion for quenching. For the total excited state population, in turn, this leads to the following time dependence of the number of excited molecules $N(t)$:

$$\dot{N}(t) = -N(t) \cdot (\kappa_{\mathrm{rad}} + \kappa_{\mathrm{nrad}}) \tag{7.2}$$

$$\rightarrow N(t) = N_0 \cdot e^{-(\kappa_{\mathrm{rad}}+\kappa_{\mathrm{nrad}})\cdot t} =: N_0 \cdot e^{-\frac{t}{\tau_{\mathrm{eff}}}} \tag{7.3}$$

Owing to the summation of the two individual rates, the overall decay speeds up under the influence of an additional nonradiative channel. This shortening of the effective lifetime constitutes the second criterion for deriving quenching from spectroscopic measurements. As such, it complements the already discussed fluorescence intensity drop. In the case

of dominance of the nonradiative pathway ($\kappa_{\mathrm{nrad}} \gg \kappa_{\mathrm{rad}}$), meaning a strong quenching, as found in the presented data, the effective lifetime and the fluorescence QY can be expressed in a simplified manner:

$$\tau_{\mathrm{eff}} = \tau_{\mathrm{nrad}} \tag{7.4}$$

$$\Phi_{\mathrm{fl}} = \frac{\kappa_{\mathrm{rad}}}{\kappa_{\mathrm{nrad}}} = \frac{\tau_{\mathrm{nrad}}}{\tau_{\mathrm{rad}}} \tag{7.5}$$

By means of these equations, we can now tackle the question of quenching in a more quantitative fashion in terms of the observed yield Φ_{fl} and time constant τ_{eff}. To that end, we extracted the key information from the FLIM measurements, namely the fluorescence time trace and the intensities from the different flakes of interest. The ratio of the latter divided by the value on the surrounding substrate region serves as a rough measure for the QY. The PO on the silicon wafer surface can be used as a reference, since the insulating native SiO_2 layer on top prevents substantial influences on the PO molecules and their fluorescence. Furthermore, the normalization to the intensity on the substrate environment corrects variations in the dye coverage between different samples. The so-obtained relative molecular 0-0 fluorescence strength is depicted in figure 7.2 (a). It reveals a drastic difference between the TMDC and the hBN flakes. The latter score high values from 0.2 to almost 1. Despite this variance, they clearly protrude from all the TMDCs, which range around 10^{-3}. Here, WS_2 is the only exception with slightly stronger relative emission, although this additional light probably stems from residual PL of the 1L flake, which is partially transmitted through the bandpass filter. Apart from that, all TMDCs consistently show a PO intensity three orders of magnitude below the neighboring substrate areas, respectively, pointing to a massive quenching of the dye fluorescence.

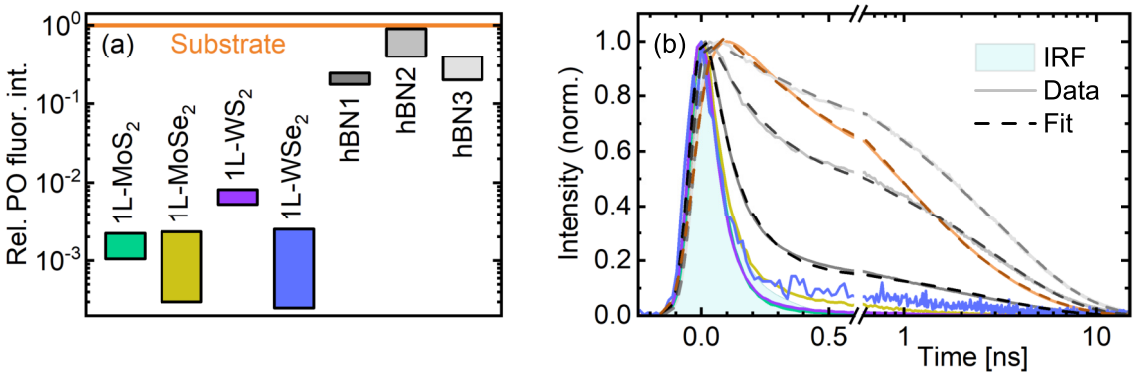

Figure 7.2: Quenching of the dye emission in hybrid structures. (a) Fluorescence intensity of PO on different flakes normalized to the value on the surrounding substrate (orange, horizontal line), respectively. On all TMDCs, the intensity drops by two to three orders of magnitude, whereas for the insulating hBN, the values range from 0.2 up to near-unity. (b) Time-resolved PO fluorescence on the same areas as in (a). While the signal on hBN and on the substrate mostly decays on a nanosecond time scale, the curves for the TMDCs essentially follow the instrument response. For all these measurements, a bandpass filter from 500 nm to 550 nm exclusively selected the 0-0 emission of the PO monomers for detection. In the case of the hBN3 sample, regions with strong agglomeration were excluded from the data, yielding a mostly monomeric behavior. Adapted from [P2].

At this point, we turn to the time traces for the identical flakes, shown in figure 7.2 (b), in order to verify whether this trend translates to the dynamics as well. In this context, the curves for all TMDC samples virtually trace the instrument response function IRF, albeit with a weak tail persisting for longer times. Hence, the experimental time resolution of about 100 ps inhibits a quantitative evaluation of the even more rapid underlying dynamics. Yet, on a qualitative level, we can conclude that the major fluorescence decay proceeds on even drastically shorter time scales. Ergo, from the perspective of their emission, the excited dye molecules are deactivated orders of magnitude faster than the nanosecond lifetime of PO monomers in solution[45,190]. Thus, the second criterion for strong quenching is also matched.

For hBN, in contrast, the traces differ significantly, yet sharing a common pattern of an initial, fast decay and a following slower one. Consequently, we fit the curves with biexponential functions, yielding the two according time constants $\tau_{1,2}$ and the ratio of the corresponding amplitudes A_2/A_1, which are listed in table 7.1. On hBN, the first process occurs within several 100 ps, while the long-term dynamics yield a time constant of about 3 ns, in line with the fluorescence lifetime of monomeric PO[45,190]. Regarding the fast component, we are able to assign this to agglomerates of the dye molecules. In the case of the hBN3 sample, the deposited coverage was chosen a little higher than in the standard procedure, therefore favoring the growth of local PO accumulations. These became large enough to appear in the FLIM map as bright dots with a drastically reduced fluorescence lifetime, owing to fast relaxation into excimer states[111,191]. The visual emergence of these agglomerates allows to exclude them from the analysis, leaving those areas of the flake with a relatively homogeneous and largely monomeric dye coating. All data shown for hBN3 is based solely on these regions. Here, the slower decay component dominates the temporal evolution, manifesting in a large amplitude ratio, confirming the prevalence of monomers in this case. To summarize, monomeric dye molecules on hBN flakes exhibit a fluorescence lifetime of about 3 ns, whereas the PO emission decays drastically faster on all 1L-TMDCs.

Taken together, these findings confirm the quenching in PO/TMDC hybrids that we already suspected from the 2D maps, now in both intensity and temporal domain. The effective fluorescence lifetime appears to lie well below the experimental resolution of 100 ps. Parallelly, the substantial intensity drop provides an estimate for the QY in the order of 10^{-3}, which demonstrates a quenching efficiency far beyond the values from previous studies on other dye/TMDC hybrids[130,132,138,192]. Applying the equations (7.4) and (7.5) from above, this quenching by three orders of magnitude translates into a nonradiative time constant of a few picoseconds. Ergo, the corresponding process exhibits an almost perfect efficiency, *i.e.* a near-unity QY.

Table 7.1: Fitted time constants and amplitude ratios for the PO fluorescence traces from figure 7.2 (b), based on a biexponential decay model. The substrate values indicate the parameter range obtained from analyzing multiple samples.

Underlying layer for PO	τ_1 [ns]	τ_2 [ns]	A_2/A_1
Substrate	0.5-1.0	2.2-3.2	0.6-1.3
hBN1	0.1	2.9	0.1
hBN2	0.2	3.1	1.0
hBN3	0.5	3.5	3.3

Yet, this estimate of the quenching is probably even too conservative due to the imperfections of the underlying substrate as well as of the dye film itself. On the one hand, the fluorescence time traces on the substrates also deviate from a purely monoexponential behavior and show an additional, faster decay component (figure 7.2 (b) and table 7.1), indicating some impact of quenching. This is presumably caused by unsaturated, so-called dangling bonds[193], excimer-forming agglomerates[194], or surface contaminants[195]. Consequently, the reference intensities for the normalization in figure 7.2 (a) are reduced compared to actually undisturbed PO molecules. Accounting for this, *i.e.* referencing with respect to truly pristine molecules would lead to even lower relative PO fluorescence intensity values for all flakes. On the other hand, agglomerations or surface contaminations - for instance by PDMS from the stamping process[149] - assumingly impair the contact between dye and flake, leaving a small fraction of the molecules unquenched. This would lead to the time traces for the PO/TMDC hybrids showing a weak tail, which we indeed observe in figure 7.2 (b). Eventually, this residual emission would manifest in a higher detected intensity in the flake regions, hence also reducing the observed quenching. Ergo, the derived value of about three orders of magnitude merely represents a lower limit. Likewise, the nonradiative time constant could lie below the few-picoseconds estimate. In fact, pump-probe-based techniques reported values ranging from several 100 fs down to 40 fs for the CT from molecular films towards TMDC layers[132–134,136,138,139].

However, purely emissive measurement techniques cannot distinguish between CT and ET, as explained in section 2.3. The latter would mean the transfer of the whole exciton from molecule to TMDC, ergo the dye fluorescence would be suppressed as well. Nevertheless, following the type II band alignment, one would still expect a subsequent electron transfer afterwards, which would result in the identical final state of separated charges. Still, this additional step could lower the total QY of charge separation.

In this chapter, we closed in on the final research question on the efficiency and time scale of a potential charge transfer in PO/TMDC hybrid structures. Emission measurements demonstrated a massive quenching of the dye fluorescence in the hybrids by three orders of magnitude, which manifests in both intensity and time evolution. These findings strongly hint at charge transfer, which embodies a prerequisite for the conversion of absorbed light into electrical currents in solar cells or photodetectors. We deduced an upper limit for corresponding time constant of a few picoseconds. This points to a near-unity charge separation yield in case of the excitation of the molecule, promising efficient devices from these material combinations.

8 Summary and outlook

This thesis dived into the transient dynamics that follow the optical excitation of blank TMDCs as well as their hybrids in combination with dye molecules. For the investigation of the pristine flakes, we applied TA spectroscopy to disentangle the different processes taking place from the initially excited state back into the ground state. In this framework, we focused on three major aspects, two of them being related to interactions of the electronic with the phononic system. Right at the beginning, the absorption of sufficiently short pump pulses create a coherent, periodic motion of the crystal. Afterwards, phonons likewise govern the redistribution of the excess energy from the initially excited electrons towards the nuclei, thermally equilibrating these two subsystems. Eventually, the recombination of the excited species constitutes the third point of the dynamics. Regarding the hybrid structures, we used emission techniques such as µPL and FLIM to monitor the behavior of the dye fluorescence as an indicator for interfacial interactions, in particular charge transfer.

At the start of the dynamics, we analyzed the coherent lattice vibrations in three 1L-TMDCs in terms of the periodic mark they leave on the TA signal. The comparison of the different materials yielded a consistent picture of a dominant contribution from the A_1' mode, confirming the results of previous studies. However, in the case of WS_2, we additionally observed a so far unknown feature stemming from the E' vibration. It emerges after excitation with green light, as opposed to longer wavelengths not triggering it. These findings demonstrate the spectral dependence of electron-phonon coupling, which mediates the initiation of the lattice motion. With reference to the underlying physical mechanism, the phase of the A_1' oscillation clearly suggests a displacive excitation. In the reverse direction, the coherent phonons influence the optical absorption properties of the material as well. We found a spectrally broad and phase-synchronous response in the TA oscillations, containing only minor modulations around the excitonic resonances. This bears a fundamental contrast to existing models, which predict a periodic growth and shrinkage of the band gaps, resulting in characteristic amplitude peak pairs with flipped phases. Ergo, our work reveals the shortcomings of the current theoretical concepts employed to derive the spectral fingerprint that the coherent lattice motion translates to. As a last point, we showed that the frequency of the A_1' mode falls when applying higher excitation densities. This behavior could be exploited as a tunability of the lattice's reaction to ultrashort laser pulses.

In parallel to the aforementioned coherent motion, the thermalization of the excited species takes place in 1L-TMDCs right after their creation. Here, we were capable of distinguishing between multiple individual steps. First, interelectronic collisions drive their thermalization around the band minima. In the resulting equilibrium, free charge carriers and bound excitons coexist due to high electronic temperatures. During the next stage, the thermal energy is redistributed towards the lattice, cooling the excited species. Again, the coupling between the electronic and phononic systems plays a crucial role in this process. In fact, we found not just one according signature in the dynamics but a spectrum of such interactions, where high-frequency phonons couple more strongly to the excited species than lower-energetic ones. Consequently, the equilibration initially includes solely the former subgroup. In the framework of the hot-phonon effect, their reabsorption leads to the persistence of elevated electronic temperatures and accordingly also of the exciton-carrier equilibrium over a few tens of picoseconds. This presents a window of opportunity to harvest the excess energy provided by excitation above the band gap in electronic devices by means of thermally activated processes. Afterwards, the coupling to the remaining phonon bath completes the cooling cascade and finally

yields a thermally equilibrated system, where excitons prevail as the principal excited species. From here, their recombination represents the last missing step back into the system's ground state.

In relation to this final process, we investigated its dynamics comparing a monolayer to a bulk flake of MoS_2, where either bound excitons or free carriers dominate the excited populations, respectively. This difference translates into a fast geminate recombination in the 2D layer, as opposed to a slower, density-dependent relative rate in the 3D crystal. Still, in both cases, defect sites mediate the processes by acting as traps for excited specimens, constituting a pivotal parameter to describe the electronic dynamics in TMDCs. From the perspective of device optimization with the aim of a long lifetime facilitating efficient charge separation and extractions, these findings advise the avoidance or engineering of defect states. For the bulk-based electronics, on top, the operation in a regime of low carrier densities appears favorable to avoid recombination losses.

The last part of this thesis dealt with the combination of TMDCs with dye molecules. For such hybrids, a proper energy alignment can result in interfacial charge separation after optical excitation, enabling an electronic current flow. Hence, these systems provide one possibility to create optoelectronic devices. In view of possible interactions at the interface, we observed a strong quenching of the fluorescence of PO monomers on various 1L-TMDCs as an indication for CT towards the flakes. This quenching manifests in a dye emission intensity reduction by three orders of magnitude and a drastic lifetime shortening, hinting at an efficient charge separation process. This proves that dye/TMDC hybrids indeed offer a promising material combination for optoelectronics.

However, future research should rather focus on completely flat molecules that arrange in an ordered fashion in full-coverage films. In this case, the density of states of both layers of the hybrid are rather balanced, facilitating a more pronounced impact on the properties of the TMDC flakes as well. For instance, the optical excitation of the molecular layer with a subsequent CT into the semiconductor could offer a method for transient doping. In this way, a photoswitchable tuning of the ratio between neutral and charged excitons (trions) seems possible. Likewise, the A_1' Raman mode frequency is expected to react to carrier injection. From this perspective, a higher pump fluence provides more carriers that are injected into the material, therefore extending the A_1' frequency dependence on the excited species' density discussed above.

To conclude, this thesis succeeded in unraveling the electronic and phononic dynamics in 1L-TMDCs and related hybrid structures. We disentangled the manifold facets of electron-phonon coupling imprinting their mark on the transient absorption signal on various time scales. Furthermore, we linked the differing nature of the excited species in the bulk material *versus* monolayers to fundamental changes in the corresponding recombination kinetics. Beyond pristine flakes, our investigations of dye/TMDC hybrids indicated efficient charge transfer, paving the way for optoelectronic applications.

Bibliography

1. Novoselov, K. S., Geim, A. K., Morozov, S. V., Jiang, D., Zhang, Y., Dubonos, S. V., Grigorieva, I. V. & Firsov, A. A. Electric Field Effect in Atomically Thin Carbon Films. *Science* **306,** 666–669. doi:10.1126/science.1102896 (Oct. 2004).
2. Novoselov, K. S., Jiang, D., Schedin, F., Booth, T. J., Khotkevich, V. V., Morozov, S. V. & Geim, A. K. Two-dimensional atomic crystals. *Proceedings of the National Academy of Sciences* **102,** 10451–10453. doi:10.1073/pnas.0502848102 (July 2005).
3. Novoselov, K. S., Mishchenko, A., Carvalho, A. & Castro Neto, A. H. 2D materials and van der Waals heterostructures. *Science* **353.** doi:10.1126/science.aac9439 (July 2016).
4. Wang, G., Chernikov, A., Glazov, M. M., Heinz, T. F., Marie, X., Amand, T. & Urbaszek, B. Colloquium : Excitons in atomically thin transition metal dichalcogenides. *Reviews of Modern Physics* **90,** 021001. doi:10.1103/revmodphys.90.021001 (Apr. 2018).
5. Glazov, M., Arora, A., Chaves, A. & Gobato, Y. G. Excitons in two-dimensional materials and heterostructures: Optical and magneto-optical properties. *MRS Bulletin* **49,** 899–913. doi:10.1557/s43577-024-00754-1 (Aug. 2024).
6. Mak, K. F. & Shan, J. Photonics and optoelectronics of 2D semiconductor transition metal dichalcogenides. *Nature Photonics* **10,** 216–226. doi:10.1038/nphoton.2015.282 (Mar. 2016).
7. Li, H., Jia, X., Zhang, Q. & Wang, X. Metallic Transition-Metal Dichalcogenide Nanocatalysts for Energy Conversion. *Chem* **4,** 1510–1537. doi:10.1016/j.chempr.2018.03.012 (July 2018).
8. Li, Z., Attanayake, N. H., Blackburn, J. L. & Miller, E. M. Carbon dioxide and nitrogen reduction reactions using 2D transition metal dichalcogenide (TMDC) and carbide/nitride (MXene) catalysts. *Energy & Environmental Science* **14,** 6242–6286. doi:10.1039/d1ee03211a (2021).
9. Zhao, L., Wang, B. & Wang, R. A Critical Review on New and Efficient 2D Materials for Catalysis. *Advanced Materials Interfaces* **9.** doi:10.1002/admi.202200771 (Sept. 2022).
10. Cheiwchanchamnangij, T. & Lambrecht, W. R. L. Quasiparticle band structure calculation of monolayer, bilayer, and bulk MoS_2. *Physical Review B* **85,** 205302. doi:10.1103/physrevb.85.205302 (May 2012).
11. Chernikov, A., Berkelbach, T. C., Hill, H. M., Rigosi, A., Li, Y., Aslan, O. B., Reichman, D. R., Hybertsen, M. S. & Heinz, T. F. Exciton Binding Energy and Nonhydrogenic Rydberg Series in Monolayer WS_2. *Phys. Rev. Lett.* **113.** doi:10.1103/physrevlett.113.076802 (Aug. 2014).
12. Zhang, C., Wang, H., Chan, W., Manolatou, C. & Rana, F. Absorption of light by excitons and trions in monolayers of metal dichalcogenide MoS_2: Experiments and theory. *Physical Review B* **89.** doi:10.1103/physrevb.89.205436 (May 2014).
13. Macfarlane, G., McLean, T., Quarrington, J. & Roberts, V. Exciton and phonon effects in the absorption spectra of germanium and silicon. *Journal of Physics and Chemistry of Solids* **8,** 388–392. doi:10.1016/0022-3697(59)90372-5 (Jan. 1959).

14. Bogardus, E. H. & Bebb, H. B. Bound-Exciton, Free-Exciton, Band-Acceptor, Donor-Acceptor, and Auger Recombination in GaAs. *Physical Review* **176,** 993–1002. doi:10.1103/physrev.176.993 (Dec. 1968).

15. Beal, A. R. & Liang, W. Y. Intercalation studies of some transition metal dichalcogenides. *Philosophical Magazine* **27,** 1397–1416. doi:10 . 1080 / 14786437308226895 (June 1973).

16. Scholes, G. D. & Rumbles, G. Excitons in nanoscale systems. *Nature Materials* **5,** 683–696. doi:10.1038/nmat1710 (Sept. 2006).

17. Fox, M. *Optical Properties of Solids* Second Edition (Oxford University Press, 2010).

18. Green, M. A. Improved value for the silicon free exciton binding energy. *AIP Advances* **3.** doi:10.1063/1.4828730 (Nov. 2013).

19. Cadiz, F., Robert, C., Courtade, E., Manca, M., Martinelli, L., Taniguchi, T., Watanabe, K., Amand, T., Rowe, A. C. H., Paget, D., Urbaszek, B. & Marie, X. Exciton diffusion in WSe_2 monolayers embedded in a van der Waals heterostructure. *Applied Physics Letters* **112.** doi:10.1063/1.5026478 (Apr. 2018).

20. Kulig, M., Zipfel, J., Nagler, P., Blanter, S., Schüller, C., Korn, T., Paradiso, N., Glazov, M. M. & Chernikov, A. Exciton Diffusion and Halo Effects in Monolayer Semiconductors. *Physical Review Letters* **120,** 207401. doi:10.1103/physrevlett.120.207401 (May 2018).

21. Uddin, S. Z., Kim, H., Lorenzon, M., Yeh, M., Lien, D.-H., Barnard, E. S., Htoon, H., Weber-Bargioni, A. & Javey, A. Neutral Exciton Diffusion in Monolayer MoS_2. *ACS Nano* **14,** 13433–13440. doi:10.1021/acsnano.0c05305 (Sept. 2020).

22. Lebègue, S. & Eriksson, O. Electronic Structure of Two-Dimensional Crystals from ab initio Theory. *Phys. Rev. B* **79.** doi:10.1103/physrevb.79.115409 (Mar. 2009).

23. Splendiani, A., Sun, L., Zhang, Y., Li, T., Kim, J., Chim, C.-Y., Galli, G. & Wang, F. Emerging Photoluminescence in Monolayer MoS_2. *Nano Letters* **10,** 1271–1275. doi:10.1021/nl903868w (Mar. 2010).

24. Mak, K. F., Lee, C., Hone, J., Shan, J. & Heinz, T. F. Atomically Thin MoS_2: A New Direct-Gap Semiconductor. *Physical Review Letters* **105,** 136805. doi:10.1103/physrevlett.105.136805 (Sept. 2010).

25. Li, Y., Chernikov, A., Zhang, X., Rigosi, A., Hill, H. M., van der Zande, A. M., Chenet, D. A., Shih, E.-M., Hone, J. & Heinz, T. F. Measurement of the optical dielectric function of monolayer transition-metal dichalcogenides: MoS_2, $MoSe_2$, WS_2, and WSe_2. *Physical Review B* **90,** 205422. doi:10.1103/physrevb.90.205422 (Nov. 2014).

26. Tang, W., Rassay, S. S. & Ravindra, N. M. Electronic & Optical properties of Transition-Metal Dichalcogenides. *Madridge Journal of Nanotechnology & Nanoscience* **2,** 58–64. doi:10.18689/mjnn-1000111 (July 2017).

27. Hsu, C., Frisenda, R., Schmidt, R., Arora, A., de Vasconcellos, S. M., Bratschitsch, R., van der Zant, H. S. J. & Castellanos-Gomez, A. Thickness-Dependent Refractive Index of 1L, 2L, and 3L MoS_2, $MoSe_2$, WS_2, and WSe_2. *Advanced Optical Materials* **7.** doi:10.1002/adom.201900239 (May 2019).

28. Withers, F., Del Pozo-Zamudio, O., Mishchenko, A., Rooney, A. P., Gholinia, A., Watanabe, K., Taniguchi, T., Haigh, S. J., Geim, A. K., Tartakovskii, A. I. & Novoselov, K. S. Light-emitting diodes by band-structure engineering in van der Waals heterostructures. *Nature Materials* **14,** 301–306. doi:10.1038/nmat4205 (Feb. 2015).

29. Lopez-Sanchez, O., Lembke, D., Kayci, M., Radenovic, A. & Kis, A. Ultrasensitive photodetectors based on monolayer MoS_2. *Nature Nanotechnology* **8,** 497–501. doi:10.1038/nnano.2013.100 (June 2013).

30. Massicotte, M., Schmidt, P., Vialla, F., Schädler, K. G., Reserbat-Plantey, A., Watanabe, K., Taniguchi, T., Tielrooij, K. J. & Koppens, F. H. L. Picosecond photoresponse in van der Waals heterostructures. *Nature Nanotechnology* **11,** 42–46. doi:10.1038/nnano.2015.227 (Oct. 2015).

31. Nassiri Nazif, K., Daus, A., Hong, J., Lee, N., Vaziri, S., Kumar, A., Nitta, F., Chen, M. E., Kananian, S., Islam, R., Kim, K.-H., Park, J.-H., Poon, A. S. Y., Brongersma, M. L., Pop, E. & Saraswat, K. C. High-specific-power flexible transition metal dichalcogenide solar cells. *Nature Communications* **12.** doi:10.1038/s41467-021-27195-7 (Dec. 2021).

32. Rono, N., Ahia, C. C. & Meyer, E. L. Recent advances in transition metal dichalcogenides-based materials for fourth-generation perovskite solar cell devices. *AIP Advances* **14.** doi:10.1063/5.0211610 (July 2024).

33. Jin, C., Ma, E. Y., Karni, O., Regan, E. C., Wang, F. & Heinz, T. F. Ultrafast dynamics in van der Waals heterostructures. *Nature Nanotechnology* **13,** 994–1003. doi:10.1038/s41565-018-0298-5 (Nov. 2018).

34. Jiang, Y., Chen, S., Zheng, W., Zheng, B. & Pan, A. Interlayer exciton formation, relaxation, and transport in TMD van der Waals heterostructures. *Light: Science & Applications* **10.** doi:10.1038/s41377-021-00500-1 (Apr. 2021).

35. Tang, J., Zheng, Y., Jiang, K., You, Q., Yin, Z., Xie, Z., Li, H., Han, C., Zhang, X. & Shi, Y. Interlayer exciton dynamics of transition metal dichalcogenide heterostructures under electric fields. *Nano Research* **17,** 4555–4572. doi:10.1007/s12274-023-6325-3 (Dec. 2023).

36. Kunstmann, J., Mooshammer, F., Nagler, P., Chaves, A., Stein, F., Paradiso, N., Plechinger, G., Strunk, C., Schüller, C., Seifert, G., Reichman, D. R. & Korn, T. Momentum-space indirect interlayer excitons in transition-metal dichalcogenide van der Waals heterostructures. *Nature Physics* **14,** 801–805. doi:10.1038/s41567-018-0123-y (Apr. 2018).

37. Ubrig, N., Ponomarev, E., Zultak, J., Domaretskiy, D., Zólyomi, V., Terry, D., Howarth, J., Gutiérrez-Lezama, I., Zhukov, A., Kudrynskyi, Z. R., Kovalyuk, Z. D., Patané, A., Taniguchi, T., Watanabe, K., Gorbachev, R. V., Fal'ko, V. I. & Morpurgo, A. F. Design of van der Waals interfaces for broad-spectrum optoelectronics. *Nature Materials* **19,** 299–304. doi:10.1038/s41563-019-0601-3 (Feb. 2020).

38. Hong, X., Kim, J., Shi, S.-F., Zhang, Y., Jin, C., Sun, Y., Tongay, S., Wu, J., Zhang, Y. & Wang, F. Ultrafast charge transfer in atomically thin MoS_2/WS_2 heterostructures. *Nature Nanotechnology* **9,** 682–686. doi:10.1038/nnano.2014.167 (Aug. 2014).

39. Ceballos, F., Bellus, M. Z., Chiu, H.-Y. & Zhao, H. Ultrafast Charge Separation and Indirect Exciton Formation in a MoS2–MoSe2 van der Waals Heterostructure. *ACS Nano* **8,** 12717–12724. doi:10.1021/nn505736z (Nov. 2014).

40. Chen, H., Wen, X., Zhang, J., Wu, T., Gong, Y., Zhang, X., Yuan, J., Yi, C., Lou, J., Ajayan, P. M., Zhuang, W., Zhang, G. & Zheng, J. Ultrafast formation of interlayer hot excitons in atomically thin MoS2/WS2 heterostructures. *Nature Communications* **7.** doi:10.1038/ncomms12512 (Aug. 2016).

41. Zhu, H., Wang, J., Gong, Z., Kim, Y. D., Hone, J. & Zhu, X.-Y. Interfacial Charge Transfer Circumventing Momentum Mismatch at Two-Dimensional van der Waals Heterojunctions. *Nano Letters* **17,** 3591–3598. doi:10.1021/acs.nanolett.7b00748 (May 2017).

42. Ceballos, F., Ju, M.-G., Lane, S. D., Zeng, X. C. & Zhao, H. Highly Efficient and Anomalous Charge Transfer in van der Waals Trilayer Semiconductors. *Nano Letters* **17,** 1623–1628. doi:10.1021/acs.nanolett.6b04815 (Feb. 2017).

43. Böttcher, H. Specific optical and electrical properties of Vacuum-Deposited Thin Films of Dyes. *Journal für Praktische Chemie/Chemiker-Zeitung* **334,** 14–24. doi:10.1002/prac.19923340104 (1992).

44. Chowdhury, T., Mujid, F., Naqvi, Z., Ray, A., Liang, C., Muller, D. A., Guisinger, N. P. & Park, J. Spectra-Orthogonal Optical Anisotropy in Wafer-Scale Molecular Crystal Monolayers. *Nano Letters* **25,** 5852–5859. doi:10.1021/acs.nanolett.5c00731 (Mar. 2025).

45. Würthner, F. Perylene bisimide dyes as versatile building blocks for functional supramolecular architectures. *Chem. Commun.* **14,** 1564–1579. doi:10.1039/b401630k (2004).

46. Würthner, F., Saha-Möller, C. R., Fimmel, B., Ogi, S., Leowanawat, P. & Schmidt, D. Perylene Bisimide Dye Assemblies as Archetype Functional Supramolecular Materials. *Chemical Reviews* **116,** 962–1052. doi:10.1021/acs.chemrev.5b00188 (Aug. 2015).

47. Jin, C., Kim, J., Wu, K., Chen, B., Barnard, E. S., Suh, J., Shi, Z., Drapcho, S. G., Wu, J., Schuck, P. J., Tongay, S. & Wang, F. On Optical Dipole Moment and Radiative Recombination Lifetime of Excitons in WSe_2. *Advanced Functional Materials* **27.** doi:10.1002/adfm.201601741 (Sept. 2016).

48. Roy, S., Sharbirin, A. S., Lee, Y., Kim, W. B., Kim, T. S., Cho, K., Kang, K., Jung, H. S. & Kim, J. Measurement of Quantum Yields of Monolayer TMDs Using Dye-Dispersed PMMA Thin Films. *Nanomaterials* **10,** 1032. doi:10.3390/nano10061032 (May 2020).

49. Zou, S.-J., Shen, Y., Xie, F.-M., Chen, J.-D., Li, Y.-Q. & Tang, J.-X. Recent advances in organic light-emitting diodes: toward smart lighting and displays. *Materials Chemistry Frontiers* **4,** 788–820. doi:10.1039/c9qm00716d (2020).

50. Nayak, D. & Choudhary, R. B. A survey of the structure, fabrication, and characterization of advanced organic light emitting diodes. *Microelectronics Reliability* **144,** 114959. doi:10.1016/j.microrel.2023.114959 (May 2023).

51. Solak, E. K. & Irmak, E. Advances in organic photovoltaic cells: a comprehensive review of materials, technologies, and performance. *RSC Advances* **13,** 12244–12269. doi:10.1039/d3ra01454a (2023).

52. Yi, J., Zhang, G., Yu, H. & Yan, H. Advantages, challenges and molecular design of different material types used in organic solar cells. *Nature Reviews Materials* **9,** 46–62. doi:10.1038/s41578-023-00618-1 (Dec. 2023).

53. He, K., Kumar, N., Zhao, L., Wang, Z., Mak, K. F., Zhao, H. & Shan, J. Tightly Bound Excitons in Monolayer WSe_2. *Physical Review Letters* **113.** doi:10.1103/physrevlett.113.026803 (July 2014).

54. Wang, G., Palleau, E., Amand, T., Tongay, S., Marie, X. & Urbaszek, B. Polarization and time-resolved photoluminescence spectroscopy of excitons in $MoSe_2$ monolayers. *Applied Physics Letters* **106,** 112101. doi:10.1063/1.4916089 (Mar. 2015).

55. Liu, G., Wang, Y., Xu, Z., Zeng, Z., Huang, L., Ge, C. & Wang, X. Out-of-plane polarization induces a picosecond photoresponse in rhombohedral stacked bilayer WSe_2. *Beilstein Journal of Nanotechnology* **15,** 1362–1368. doi:10.3762/bjnano.15.109 (Nov. 2024).

56. Chen, S., Fan, F., Miao, Y., He, X., Zhang, K. & Chang, S. Ultrasensitive terahertz modulation by silicon-grown MoS_2 nanosheets. *Nanoscale* **8,** 4713–4719. doi:10.1039/c5nr08101g (2016).

57. Zheng, W., Fan, F., Chen, M., Chen, S. & Chang, S.-J. Optically pumped terahertz wave modulation in MoS_2-Si heterostructure metasurface. *AIP Advances* **6.** doi:10.1063/1.4958878 (July 2016).

58. Gopalan, P. & Sensale-Rodriguez, B. 2D Materials for Terahertz Modulation. *Advanced Optical Materials* **8.** doi:10.1002/adom.201900550 (Aug. 2019).

59. Hu, L., Wei, D. & Huang, X. Second harmonic generation property of monolayer TMDCs and its potential application in producing terahertz radiation. *The Journal of Chemical Physics* **147.** doi:10.1063/1.5000561 (Dec. 2017).

60. Xie, Y., Liang, F., Chi, S., Wang, D., Zhong, K., Yu, H., Zhang, H., Chen, Y. & Wang, J. Defect Engineering of MoS_2 for Room-Temperature Terahertz Photodetection. *ACS Applied Materials & Interfaces* **12,** 7351–7357. doi:10.1021/acsami.9b21671 (Jan. 2020).

61. Shi, Z., Zhang, H., Khan, K., Cao, R., Zhang, Y., Ma, C., Tareen, A. K., Jiang, Y., Jin, M. & Zhang, H. Two-dimensional materials toward terahertz optoelectronic device applications. *Journal of Photochemistry and Photobiology C: Photochemistry Reviews* **51,** 100473. doi:10.1016/j.jphotochemrev.2021.100473 (June 2022).

62. Chen, S.-Y., Zheng, C., Fuhrer, M. S. & Yan, J. Helicity-Resolved Raman Scattering of MoS_2, $MoSe_2$, WS_2, and WSe_2 Atomic Layers. *Nano Letters* **15,** 2526–2532. doi:10.1021/acs.nanolett.5b00092 (Mar. 2015).

63. Zhang, X., Qiao, X.-F., Shi, W., Wu, J.-B., Jiang, D.-S. & Tan, P.-H. Phonon and Raman scattering of two-dimensional transition metal dichalcogenides from monolayer, multilayer to bulk material. *Chemical Society Reviews* **44,** 2757–2785. doi:10.1039/c4cs00282b (2015).

64. Nam, D., Lee, J.-U. & Cheong, H. Excitation energy dependent Raman spectrum of $MoSe_2$. *Scientific Reports* **5.** doi:10.1038/srep17113 (Nov. 2015).

65. Del Corro, E., Botello-Méndez, A., Gillet, Y., Elias, A. L., Terrones, H., Feng, S., Fantini, C., Rhodes, D., Pradhan, N., Balicas, L., Gonze, X., Charlier, J.-C., Terrones, M. & Pimenta, M. A. Atypical Exciton–Phonon Interactions in WS_2 and WSe_2 Monolayers Revealed by Resonance Raman Spectroscopy. *Nano Letters* **16,** 2363–2368. doi:10.1021/acs.nanolett.5b05096 (Mar. 2016).

66. Huang, X., Gao, Y., Yang, T., Ren, W., Cheng, H.-M. & Lai, T. Quantitative Analysis of Temperature Dependence of Raman shift of monolayer WS_2. *Scientific Reports* **6.** doi:10.1038/srep32236 (Aug. 2016).

67. Shi, W., Lin, M.-L., Tan, Q.-H., Qiao, X.-F., Zhang, J. & Tan, P.-H. Raman and photoluminescence spectra of two-dimensional nanocrystallites of monolayer WS_2 and WSe_2. *2D Materials* **3,** 025016. doi:10.1088/2053-1583/3/2/025016 (Apr. 2016).

68. Soubelet, P., Bruchhausen, A. E., Fainstein, A., Nogajewski, K. & Faugeras, C. Resonance effects in the Raman scattering of monolayer and few-layer $MoSe_2$. *Physical Review B* **93,** 155407. doi:10.1103/physrevb.93.155407 (Apr. 2016).

69. Jeong, T. Y., Jin, B. M., Rhim, S. H., Debbichi, L., Park, J., Jang, Y. D., Lee, H. R., Chae, D.-H., Lee, D., Kim, Y.-H., Jung, S. & Yee, K. J. Coherent Lattice Vibrations in Mono- and Few-Layer WSe_2. *ACS Nano* **10,** 5560–5566. doi:10.1021/acsnano.6b02253 (Apr. 2016).

70. Trovatello, C., Miranda, H. P. C., Molina-Sánchez, A., Borrego-Varillas, R., Manzoni, C., Moretti, L., Ganzer, L., Maiuri, M., Wang, J., Dumcenco, D., Kis, A., Wirtz, L., Marini, A., Soavi, G., Ferrari, A. C., Cerullo, G., Sangalli, D. & Conte, S. D. Strongly Coupled Coherent Phonons in Single-Layer MoS_2. *ACS Nano* **14,** 5700–5710. doi:10.1021/acsnano.0c00309 (Apr. 2020).

71. Sayers, C. J., Genco, A., Trovatello, C., Conte, S. D., Khaustov, V. O., Cervantes-Villanueva, J., Sangalli, D., Molina-Sanchez, A., Coletti, C., Gadermaier, C. & Cerullo, G. Strong Coupling of Coherent Phonons to Excitons in Semiconducting Monolayer $MoTe_2$. *Nano Letters* **23,** 9235–9242. doi:10.1021/acs.nanolett.3c01936 (Sept. 2023).

72. Zou, J., Zhu, R., Wang, J., Meng, H., Wang, Z., Chen, H. & Weng, Y.-X. Coherent Phonon-Mediated Many-Body Interaction in Monolayer WSe_2. *The Journal of Physical Chemistry Letters* **14,** 4657–4665. doi:10.1021/acs.jpclett.3c00870 (May 2023).

73. Lu, J., Liu, H., Tok, E. S. & Sow, C.-H. Interactions between lasers and two-dimensional transition metal dichalcogenides. *Chemical Society Reviews* **45,** 2494–2515. doi:10.1039/c5cs00553a (2016).

74. Wang, H., Zhang, C. & Rana, F. Ultrafast Dynamics of Defect-Assisted Electron–Hole Recombination in Monolayer MoS_2. *Nano Lett.* **15,** 339–345. doi:10.1021/nl503636c (Dec. 2014).

75. Wang, H., Strait, J. H., Zhang, C., Chan, W., Manolatou, C., Tiwari, S. & Rana, F. Fast exciton annihilation by capture of electrons or holes by defects via Auger scattering in monolayer metal dichalcogenides. *Physical Review B* **91.** doi:10.1103/physrevb.91.165411 (Apr. 2015).

76. Wang, H., Zhang, C. & Rana, F. Surface Recombination Limited Lifetimes of Photoexcited Carriers in Few-Layer Transition Metal Dichalcogenide MoS_2. *Nano Lett.* **15,** 8204–8210. doi:10.1021/acs.nanolett.5b03708 (Nov. 2015).

77. Li, Y., Shi, J., Chen, H., Wang, R., Mi, Y., Zhang, C., Du, W., Zhang, S., Liu, Z., Zhang, Q., Qiu, X., Xu, H., Liu, W., Liu, Y. & Liu, X. The Auger Process in Multilayer WSe_2 Crystals. *Nanoscale* **10,** 17585–17592. doi:10.1039/c8nr02567c (2018).

78. Li, Y., Shi, J., Mi, Y., Sui, X., Xu, H. & Liu, X. Ultrafast carrier dynamics in two-dimensional transition metal dichalcogenides. *Journal of Materials Chemistry C* **7,** 4304–4319. doi:10.1039/c8tc06343e (2019).

79. Yu, Z., Ong, Z.-Y., Li, S., Xu, J.-B., Zhang, G., Zhang, Y.-W., Shi, Y. & Wang, X. Analyzing the Carrier Mobility in Transition-Metal Dichalcogenide MoS_2 Field-Effect Transistors. *Advanced Functional Materials* **27.** doi:10.1002/adfm.201604093 (Jan. 2017).

80. Rosati, R., Brem, S., Perea-Causín, R., Schmidt, R., Niehues, I., Michaelis de Vasconcellos, S., Bratschitsch, R. & Malic, E. Strain-dependent exciton diffusion in transition metal dichalcogenides. *2D Materials* **8,** 015030. doi:10.1088/2053-1583/abbd51 (Dec. 2020).

81. Rasmussen, F. A. & Thygesen, K. S. Computational 2D Materials Database: Electronic Structure of Transition-Metal Dichalcogenides and Oxides. *The Journal of Physical Chemistry C* **119,** 13169–13183. doi:10.1021/acs.jpcc.5b02950 (June 2015).

82. Wilson, J. & Yoffe, A. The transition metal dichalcogenides discussion and interpretation of the observed optical, electrical and structural properties. *Advances in Physics* **18,** 193–335. doi:10.1080/00018736900101307 (May 1969).

83. Lee, Y.-C., Chang, S.-W., Chen, S.-H., Chen, S.-L. & Chen, H.-L. Optical Inspection of 2D Materials: From Mechanical Exfoliation to Wafer-Scale Growth and Beyond. *Advanced Science* **9.** doi:10.1002/advs.202102128 (Oct. 2021).

84. Saliba, M., Atanas, J. P., Howayek, T. M. & Habchi, R. Molybdenum disulfide, exfoliation methods and applications to photocatalysis: a review. *Nanoscale Advances* **5,** 6787–6803. doi:10.1039/d3na00741c (2023).

85. Bonaccorso, F., Lombardo, A., Hasan, T., Sun, Z., Colombo, L. & Ferrari, A. C. Production and processing of graphene and 2D crystals. *Materials Today* **15,** 564–589. doi:10.1016/s1369-7021(13)70014-2 (Dec. 2012).

86. Raza, A., Hassan, J. Z., Ikram, M., Ali, S., Farooq, U., Khan, Q. & Maqbool, M. Advances in Liquid-Phase and Intercalation Exfoliations of Transition Metal Dichalcogenides to Produce 2D Framework. *Advanced Materials Interfaces* **8.** doi:10.1002/admi.202002205 (June 2021).

87. Cai, Z., Liu, B., Zou, X. & Cheng, H.-M. Chemical Vapor Deposition Growth and Applications of Two-Dimensional Materials and Their Heterostructures. *Chemical Reviews* **118,** 6091–6133. doi:10.1021/acs.chemrev.7b00536 (Jan. 2018).

88. Shree, S., George, A., Lehnert, T., Neumann, C., Benelajla, M., Robert, C., Marie, X., Watanabe, K., Taniguchi, T., Kaiser, U., Urbaszek, B. & Turchanin, A. High optical quality of MoS_2 monolayers grown by chemical vapor deposition. *2D Materials* **7,** 015011. doi:10.1088/2053-1583/ab4f1f (Nov. 2019).

89. Wang, J., Li, T., Wang, Q., Wang, W., Shi, R., Wang, N., Amini, A. & Cheng, C. Controlled growth of atomically thin transition metal dichalcogenides via chemical vapor deposition method. *Materials Today Advances* **8,** 100098. doi:10.1016/j.mtadv.2020.100098 (Dec. 2020).

90. Jeong, H. Y., Lee, S. Y., Ly, T. H., Han, G. H., Kim, H., Nam, H., Jiong, Z., Shin, B. G., Yun, S. J., Kim, J., Kim, U. J., Hwang, S. & Lee, Y. H. Visualizing Point Defects in Transition-Metal Dichalcogenides Using Optical Microscopy. *ACS Nano* **10,** 770–777. doi:10.1021/acsnano.5b05854 (Jan. 2016).

91. Molina-Sánchez, A., Sangalli, D., Hummer, K., Marini, A. & Wirtz, L. Effect of spin-orbit interaction on the optical spectra of single-layer, double-layer, and bulk MoS_2. *Physical Review B* **88.** doi:10.1103/physrevb.88.045412 (July 2013).

92. Coehoorn, R., Haas, C., Dijkstra, J., Flipse, C. J. F., de Groot, R. A. & Wold, A. Electronic structure of $MoSe_2$, MoS_2, and WSe_2. I. Band-structure calculations and photoelectron spectroscopy. *Physical Review B* **35,** 6195–6202. doi:10.1103/physrevb.35.6195 (Apr. 1987).

93. Qiu, D. Y., da Jornada, F. H. & Louie, S. G. Optical Spectrum of MoS_2: Many-Body Effects and Diversity of Exciton States. *Phys. Rev. Lett.* **111.** doi:10.1103/physrevlett.111.216805 (Nov. 2013).

94. Gillen, R. & Maultzsch, J. Light-Matter Interactions in Two-Dimensional Transition Metal Dichalcogenides: Dominant Excitonic Transitions in Mono- and Few-Layer MoX_2 and Band Nesting. *IEEE J. Sel. Top. Quantum Electron.* **23,** 219–230. doi:10.1109/JSTQE.2016.2604359 (Jan. 2017).

95. Xiao, D., Liu, G.-B., Feng, W., Xu, X. & Yao, W. Coupled Spin and Valley Physics in Monolayers of MoS_2 and Other Group-VI Dichalcogenides. *Physical Review Letters* **108,** 196802. doi:10.1103/PhysRevLett.108.196802 (May 2012).

96. Ramasubramaniam, A. Large excitonic effects in monolayers of molybdenum and tungsten dichalcogenides. *Physical Review B* **86.** doi:10.1103/physrevb.86.115409 (Sept. 2012).

97. Kormányos, A., Burkard, G., Gmitra, M., Fabian, J., Zólyomi, V., Drummond, N. D. & Fal'ko, V. Corrigendum: k.p theory for two-dimensional transition metal dichalcogenide semiconductors (2015 2D Mater. 2 022001). en. *2D Materials* **2,** 049501. doi:10.1088/2053-1583/2/4/049501 (Nov. 2015).

98. Hein, P., Stange, A., Hanff, K., Yang, L. X., Rohde, G., Rossnagel, K. & Bauer, M. Momentum-resolved hot electron dynamics at the 2H-MoS_2 surface. *Physical Review B* **94,** 205406. doi:10.1103/physrevb.94.205406 (Nov. 2016).

99. Li, T. & Galli, G. Electronic Properties of MoS_2 Nanoparticles. *The Journal of Physical Chemistry C* **111,** 16192–16196. doi:10.1021/jp075424v (Oct. 2007).

100. Zhu, Z. Y., Cheng, Y. C. & Schwingenschlögl, U. Giant spin-orbit-induced spin splitting in two-dimensional transition-metal dichalcogenide semiconductors. *Physical Review B* **84.** doi:10.1103/physrevb.84.153402 (Oct. 2011).

101. Beal, A. R., Knights, J. C. & Liang, W. Y. Transmission spectra of some transition metal dichalcogenides. II. Group VI A: trigonal prismatic coordination. *Journal of Physics C: Solid State Physics* **5,** 3540–3551. doi:10.1088/0022-3719/5/24/016 (Dec. 1972).

102. Bordas, J. in *Optical and Electrical Properties* 145–229 (Springer Netherlands, 1976). doi:10.1007/978-94-010-1478-6_2.

103. Komsa, H.-P. & Krasheninnikov, A. V. Effects of confinement and environment on the electronic structure and exciton binding energy of MoS_2 from first principles. *Physical Review B* **86.** doi:10.1103/physrevb.86.241201 (Dec. 2012).

104. Zhu, B., Chen, X. & Cui, X. Exciton Binding Energy of Monolayer WS_2. *Scientific Reports* **5.** doi:10.1038/srep09218 (Mar. 2015).

105. Berkelbach, T. C., Hybertsen, M. S. & Reichman, D. R. Theory of neutral and charged excitons in monolayer transition metal dichalcogenides. *Physical Review B* **88.** doi:10.1103/physrevb.88.045318 (July 2013).

106. Molina-Sánchez, A. & Wirtz, L. Phonons in single-layer and few-layer MoS_2 and WS_2. *Physical Review B* **84,** 155413. doi:10.1103/physrevb.84.155413 (Oct. 2011).

107. Zhao, W., Ghorannevis, Z., Amara, K. K., Pang, J. R., Toh, M., Zhang, X., Kloc, C., Tan, P. H. & Eda, G. Lattice dynamics in mono- and few-layer sheets of WS_2 and WSe_2. *Nanoscale* **5,** 9677. doi:10.1039/c3nr03052k (2013).

108. Dhakal, K. P., Duong, D. L., Lee, J., Nam, H., Kim, M., Kan, M., Lee, Y. H. & Kim, J. Confocal Absorption Spectral Imaging of MoS_2: Optical Transitions Depending on the Atomic Thickness of Intrinsic and Chemically Doped MoS_2. *Nanoscale* **6,** 13028–13035. doi:10.1039/c4nr03703k (Sept. 2014).

109. Iqbal, M. W., Shahzad, K., Akbar, R. & Hussain, G. A review on Raman finger prints of doping and strain effect in TMDCs. *Microelectronic Engineering* **219,** 111152. doi:10.1016/j.mee.2019.111152 (Jan. 2020).

110. Ishioka, K. & Misochko, O. V. in *Progress in Ultrafast Intense Laser Science* 23–46 (Springer Berlin Heidelberg, Oct. 2009). doi:10.1007/978-3-642-03825-9_2.

111. Kang, S., Choi, W., Ahn, J., Kim, T., Oh, J. H. & Kim, D. Impact of Packing Geometry on Excimer Characteristics and Mobility in Perylene Bisimide Polycrystalline Films. *ACS Applied Materials & Interfaces* **16,** 18134–18143. doi:10.1021/acsami.3c19140 (Mar. 2024).

112. Kinderman, R., Slooff, L. H., Burgers, A. R., Bakker, N. J., Büchtemann, A., Danz, R. & van Roosmalen, J. A. M. I-V Performance and Stability Study of Dyes for Luminescent Plate Concentrators. *Journal of Solar Energy Engineering* **129,** 277–282. doi:10.1115/1.2737469 (Apr. 2006).

113. Benjamin, W. E., Veit, D. R., Perkins, M. J., Bain, E., Scharnhorst, K., McDowall, S., Patrick, D. L. & Gilbertson, J. D. Sterically Engineered Perylene Dyes for High Efficiency Oriented Fluorophore Luminescent Solar Concentrators. *Chemistry of Materials* **26,** 1291–1293. doi:10.1021/cm403286v (Jan. 2014).

114. Huang, C., Barlow, S. & Marder, S. R. Perylene-3,4,9,10-tetracarboxylic Acid Diimides: Synthesis, Physical Properties, and Use in Organic Electronics. *The Journal of Organic Chemistry* **76,** 2386–2407. doi:10.1021/jo2001963 (Mar. 2011).

115. Ludwig, C., Gompf, B., Petersen, J., Strohmaier, R. & Eisenmenger, W. STM investigations of PTCDA and PTCDI on graphite and MoS_2. A systematic study of epitaxy and STM image contrast. *Zeitschrift für Physik B Condensed Matter* **93,** 365–373. doi:10.1007/bf01312708 (Sept. 1994).

116. Umbach, E., Glöckler, K. & Sokolowski, M. Surface "architecture" with large organic molecules: interface order and epitaxy. *Surface Science* **402–404,** 20–31. doi:10.1016/s0039-6028(98)00014-4 (May 1998).

117. Hooks, D. E., Fritz, T. & Ward, M. D. Epitaxy and Molecular Organization on Solid Substrates. *Advanced Materials* **13,** 227–241. doi:10.1002/1521-4095(200102)13:4<227::aid-adma227>3.0.co;2-p (Feb. 2001).

118. Lakowicz, J. R. *Principles of Fluorescence Spectroscopy* 3rd. doi:10.1007/978-0-387-46312-4 (Springer US, 2006).

119. Franck, J. & Dymond, E. G. Elementary processes of photochemical reactions. *Transactions of the Faraday Society* **21,** 536. doi:10.1039/tf9262100536 (1926).

120. Condon, E. U. Nuclear Motions Associated with Electron Transitions in Diatomic Molecules. *Physical Review* **32,** 858–872. doi:10.1103/physrev.32.858 (Dec. 1928).

121. Koch, N. Opportunities for energy level tuning at inorganic/organic semiconductor interfaces. *Applied Physics Letters* **119.** doi:10.1063/5.0074963 (Dec. 2021).

122. Ramanan, C., Smeigh, A. L., Anthony, J. E., Marks, T. J. & Wasielewski, M. R. Competition between Singlet Fission and Charge Separation in Solution-Processed Blend Films of 6,13-Bis(triisopropylsilylethynyl)pentacene with Sterically-Encumbered Perylene-3,4:9,10-bis(dicarboximide)s. *Journal of the American Chemical Society* **134,** 386–397. doi:10.1021/ja2080482 (Dec. 2011).

123. Choi, J., Zhang, H. & Choi, J. H. Modulating Optoelectronic Properties of Two-Dimensional Transition Metal Dichalcogenide Semiconductors by Photoinduced Charge Transfer. *ACS Nano* **10,** 1671–1680. doi:10.1021/acsnano.5b07457 (Jan. 2016).

124. Homan, S. B., Sangwan, V. K., Balla, I., Bergeron, H., Weiss, E. A. & Hersam, M. C. Ultrafast Exciton Dissociation and Long-Lived Charge Separation in a Photovoltaic Pentacene–MoS_2 van der Waals Heterojunction. *Nano Letters* **17,** 164–169. doi:10.1021/acs.nanolett.6b03704 (Dec. 2016).

125. Cao, Z., Harb, M., Lardhi, S. & Cavallo, L. Impact of Interfacial Defects on the Properties of Monolayer Transition Metal Dichalcogenide Lateral Heterojunctions. *The Journal of Physical Chemistry Letters* **8,** 1664–1669. doi:10.1021/acs.jpclett.7b00518 (Mar. 2017).

126. Kang, J., Tongay, S., Zhou, J., Li, J. & Wu, J. Band offsets and heterostructures of two-dimensional semiconductors. *Applied Physics Letters* **102,** 012111. doi:10.1063/1.4774090 (Jan. 2013).

127. Gong, C., Zhang, H., Wang, W., Colombo, L., Wallace, R. M. & Cho, K. Band alignment of two-dimensional transition metal dichalcogenides: Application in tunnel field effect transistors. *Applied Physics Letters* **103,** 053513. doi:10.1063/1.4817409 (July 2013).

128. Iberi, V., Liang, L., Ievlev, A. V., Stanford, M. G., Lin, M.-W., Li, X., Mahjouri-Samani, M., Jesse, S., Sumpter, B. G., Kalinin, S. V., Joy, D. C., Xiao, K., Belianinov, A. & Ovchinnikova, O. S. Nanoforging Single Layer $MoSe_2$ Through Defect Engineering with Focused Helium Ion Beams. *Scientific Reports* **6,** 30481. doi:10.1038/srep30481 (Aug. 2016).

129. Zhu, T., Yuan, L., Zhao, Y., Zhou, M., Wan, Y., Mei, J. & Huang, L. Highly mobile charge-transfer excitons in two-dimensional WS_2/tetracene heterostructures. *Science Advances* **4,** eaao3104. doi:10.1126/sciadv.aao3104 (Jan. 2018).

130. Liu, X., Gu, J., Ding, K., Fan, D., Hu, X., Tseng, Y.-W., Lee, Y.-H., Menon, V. & Forrest, S. R. Photoresponse of an Organic Semiconductor/Two-Dimensional Transition Metal Dichalcogenide Heterojunction. *Nano Letters* **17,** 3176–3181. doi:10.1021/acs.nanolett.7b00695 (Apr. 2017).

131. Wickramaratne, D., Weston, L. & de Walle, C. G. V. Monolayer to Bulk Properties of Hexagonal Boron Nitride. *The Journal of Physical Chemistry C* **122,** 25524–25529. doi:10.1021/acs.jpcc.8b09087 (Oct. 2018).

132. Kafle, T. R., Kattel, B., Lane, S. D., Wang, T., Zhao, H. & Chan, W.-L. Charge Transfer Exciton and Spin Flipping at Organic–Transition-Metal Dichalcogenide Interfaces. *ACS Nano* **11,** 10184–10192. doi:10.1021/acsnano.7b04751 (Oct. 2017).

133. Zhong, C., Sangwan, V. K., Wang, C., Bergeron, H., Hersam, M. C. & Weiss, E. A. Mechanisms of Ultrafast Charge Separation in a PTB7/Monolayer MoS_2 van der Waals Heterojunction. *The Journal of Physical Chemistry Letters* **9,** 2484–2491. doi:10.1021/acs.jpclett.8b00628 (Apr. 2018).

134. Padgaonkar, S., Amsterdam, S. H., Bergeron, H., Su, K., Marks, T. J., Hersam, M. C. & Weiss, E. A. Molecular-Orientation-Dependent Interfacial Charge Transfer in Phthalocyanine/MoS_2 Mixed-Dimensional Heterojunctions. *The Journal of Physical Chemistry C* **123,** 13337–13343. doi:10.1021/acs.jpcc.9b04063 (May 2019).

135. Ye, L., Liu, Y., Zhou, Q., Tao, W., Li, Y., Wang, Z. & Zhu, H. Ultrafast Singlet Energy Transfer before Fission in a Tetracene/WSe_2 Type II Hybrid Heterostructure. *The Journal of Physical Chemistry Letters* **12,** 8440–8446. doi:10.1021/acs.jpclett.1c02540 (Aug. 2021).

136. Schwinn, M. C., Rather, S. R., Lee, C., Bland, M. P., Song, T. W., Sangwan, V. K., Hersam, M. C. & Chen, L. X. Charge transfer dynamics and interlayer exciton formation in MoS_2/VOPc mixed dimensional heterojunction. *The Journal of Chemical Physics* **157.** doi:10.1063/5.0107791 (Nov. 2022).

137. Markeev, P. A., Najafidehaghani, E., Samu, G. F., Sarosi, K., Kalkan, S. B., Gan, Z., George, A., Reisner, V., Mogyorosi, K., Chikan, V., Nickel, B., Turchanin, A. & de Jong, M. P. Exciton Dynamics in MoS_2-Pentacene and WSe_2-Pentacene Heterojunctions. *ACS Nano* **16,** 16668–16676. doi:10.1021/acsnano.2c06144 (Sept. 2022).

138. Kafle, T. R., Kattel, B., Yao, P., Zereshki, P., Zhao, H. & Chan, W.-L. Effect of the Interfacial Energy Landscape on Photoinduced Charge Generation at the ZnPc/MoS_2 Interface. *Journal of the American Chemical Society* **141,** 11328–11336. doi:10.1021/jacs.9b05893 (June 2019).

139. Wang, Z., Sun, C., Xu, X., Liu, Y., Chen, Z., Yang, Y. M. & Zhu, H. Long-Range Hot Charge Transfer Exciton Dissociation in an Organic/2D Semiconductor Hybrid Excitonic Heterostructure. *Journal of the American Chemical Society* **145,** 11227–11235. doi:10.1021/jacs.3c01192 (May 2023).

140. Kong, Y., Obaidulla, S. M., Habib, M. R., Wang, Z., Wang, R., Khan, Y., Zhu, H., Xu, M. & Yang, D. Interlayer exciton emission in a MoS_2/VOPc inorganic/organic van der Waals heterostructure. *Materials Horizons* **9,** 1253–1263. doi:10.1039/d1mh01622a (2022).

141. Thompson, J. J. P., Lumsargis, V., Feierabend, M., Zhao, Q., Wang, K., Dou, L., Huang, L. & Malic, E. Interlayer exciton landscape in WS_2/tetracene heterostructures. *Nanoscale* **15,** 1730–1738. doi:10.1039/d2nr02055f (2023).

142. Dziobek-Garrett, R. & Kempa, T. J. Excitons at the interface of 2D TMDs and molecular semiconductors. *The Journal of Chemical Physics* **160.** doi:10.1063/5.0206417 (May 2024).

143. Förster, T. Zwischenmolekulare Energiewanderung und Fluoreszenz. *Annalen der Physik* **437,** 55–75. doi:10.1002/andp.19484370105 (Jan. 1948).

144. Thompson, J. J. P., Gerhard, M., Witte, G. & Malic, E. Optical signatures of Förster-induced energy transfer in organic/TMD heterostructures. *npj 2D Materials and Applications* **7.** doi:10.1038/s41699-023-00430-z (Sept. 2023).

145. Benameur, M. M., Radisavljevic, B., Héron, J. S., Sahoo, S., Berger, H. & Kis, A. Visibility of dichalcogenide nanolayers. *Nanotechnology* **22,** 125706. doi:10.1088/0957-4484/22/12/125706 (Feb. 2011).

146. Puebla, S., Li, H., Zhang, H. & Castellanos-Gomez, A. Apparent Colors of 2D Materials. *Advanced Photonics Research* **3,** 2100221. doi:10.1002/adpr.202100221 (Jan. 2022).

147. Castellanos-Gomez, A., Buscema, M., Molenaar, R., Singh, V., Janssen, L., van der Zant, H. S. J. & Steele, G. A. Deterministic transfer of two-dimensional materials by all-dry viscoelastic stamping. *2D Materials* **1,** 011002. doi:10.1088/2053-1583/1/1/011002 (Apr. 2014).

148. Frisenda, R., Navarro-Moratalla, E., Gant, P., Lara, D. P. D., Jarillo-Herrero, P., Gorbachev, R. V. & Castellanos-Gomez, A. Recent Progress in the Assembly of Nanodevices and van-der-Waals Heterostructures by Deterministic Placement of 2D Materials. *Chem. Soc. Rev.* **47,** 53–68. doi:10.1039/c7cs00556c (2018).

149. Tilmann, R., Bartlam, C., Hartwig, O., Tywoniuk, B., Dominik, N., Cullen, C. P., Peters, L., Stimpel-Lindner, T., McEvoy, N. & Duesberg, G. S. Identification of Ubiquitously Present Polymeric Adlayers on 2D Transition Metal Dichalcogenides. *ACS Nano* **17,** 10617–10627. doi:10.1021/acsnano.3c01649 (May 2023).

150. Seybold, G. & Wagenblast, G. New perylene and violanthrone dyestuffs for fluorescent collectors. *Dyes and Pigments* **11,** 303–317. doi:10.1016/0143-7208(89)85048-x (1989).

151. Megerle, U., Pugliesi, I., Schriever, C., Sailer, C. F. & Riedle, E. Sub-50 fs broadband absorption spectroscopy with tunable excitation: putting the analysis of ultrafast molecular dynamics on solid ground. *Applied Physics B* **96,** 215–231. doi:10.1007/s00340-009-3610-0 (June 2009).

152. Päpcke, A., Friedrich, A. & Lochbrunner, S. Revealing the initial steps in homogeneous photocatalysis by time-resolved spectroscopy. *Journal of Physics: Condensed Matter* **32,** 153001. doi:10.1088/1361-648x/ab5ed1 (Jan. 2020).

153. Riedle, E., Beutter, M., Lochbrunner, S., Piel, J., Schenkl, S., Spörlein, S. & Zinth, W. Generation of 10 to 50 fs tunable through all of the visible and the NIR. *Applied Physics B* **71,** 457–465. doi:10.1007/s003400000351 (Sept. 2000).

154. Manzoni, C. & Cerullo, G. Design criteria for ultrafast optical parametric amplifiers. *Journal of Optics* **18,** 103501. doi:10.1088/2040-8978/18/10/103501 (Aug. 2016).

155. Boyd, R. W. *Nonlinear Optics* (Academic Press, 1992).

156. Knorr, F. J. & Harris, J. M. Resolution of multicomponent fluorescence spectra by an emission wavelength-decay time data matrix. *Analytical Chemistry* **53,** 272–276. doi:10.1021/ac00225a033 (Feb. 1981).

157. Kozawa, D., Kumar, R., Carvalho, A., Kumar Amara, K., Zhao, W., Wang, S., Toh, M., Ribeiro, R. M., Castro Neto, A. H., Matsuda, K. & Eda, G. Photocarrier relaxation pathway in two-dimensional semiconducting transition metal dichalcogenides. *Nature Communications* **5.** doi:10.1038/ncomms5543 (July 2014).

158. Sim, S., Park, J., Song, J.-G., In, C., Lee, Y.-S., Kim, H. & Choi, H. Exciton dynamics in atomically thin MoS_2: Interexcitonic interaction and broadening kinetics. *Physical Review B* **88,** 075434. doi:10.1103/physrevb.88.075434 (Aug. 2013).

159. He, J., He, D., Wang, Y., Cui, Q., Ceballos, F. & Zhao, H. Spatiotemporal dynamics of excitons in monolayer and bulk WS_2. *Nanoscale* **7,** 9526–9531. doi:10.1039/c5nr00188a (2015).

160. Borzda, T., Gadermaier, C., Vujicic, N., Topolovsek, P., Borovsak, M., Mertelj, T., Viola, D., Manzoni, C., Pogna, E. A. A., Brida, D., Antognazza, M. R., Scotognella, F., Lanzani, G., Cerullo, G. & Mihailovic, D. Charge Photogeneration in Few-Layer MoS_2. *Advanced Functional Materials* **25,** 3351–3358. doi:10.1002/adfm.201500709 (Apr. 2015).

161. Chernikov, A., Ruppert, C., Hill, H. M., Rigosi, A. F. & Heinz, T. F. Population inversion and giant bandgap renormalization in atomically thin WS_2 layers. *Nature Photonics* **9,** 466–470. doi:10.1038/nphoton.2015.104 (June 2015).

162. Vega-Mayoral, V., Vella, D., Borzda, T., Prijatelj, M., Tempra, I., Pogna, E. A. A., Conte, S. D., Topolovsek, P., Vujicic, N., Cerullo, G., Mihailovic, D. & Gadermaier, C. Exciton and charge carrier dynamics in few-layer WS_2. *Nanoscale* **8,** 5428–5434. doi:10.1039/c5nr08384b (2016).

163. Vega-Mayoral, V., Borzda, T., Vella, D., Prijatelj, M., Pogna, E. A. A., Backes, C., Coleman, J. N., Cerullo, G., Mihailovic, D. & Gadermaier, C. Charge trapping and coalescence dynamics in few layer MoS_2. *2D Materials* **5,** 015011. doi:10.1088/2053-1583/aa8d42 (Oct. 2017).

164. Cunningham, P. D., McCreary, K. M., Hanbicki, A. T., Currie, M., Jonker, B. T. & Hayden, L. M. Charge Trapping and Exciton Dynamics in Large-Area CVD Grown MoS_2. *The Journal of Physical Chemistry C* **120,** 5819–5826. doi:10.1021/acs.jpcc.6b00647 (Mar. 2016).

165. Pogna, E. A. A., Marsili, M., De Fazio, D., Dal Conte, S., Manzoni, C., Sangalli, D., Yoon, D., Lombardo, A., Ferrari, A. C., Marini, A., Cerullo, G. & Prezzi, D. Photo-Induced Bandgap Renormalization Governs the Ultrafast Response of Single-Layer MoS_2. *ACS Nano* **10,** 1182–1188. doi:10.1021/acsnano.5b06488 (Jan. 2016).

166. Shi, H., Yan, R., Bertolazzi, S., Brivio, J., Gao, B., Kis, A., Jena, D., Xing, H. G. & Huang, L. Exciton Dynamics in Suspended Monolayer and Few-Layer MoS_2 2D Crystals. *ACS Nano* **7,** 1072–1080. doi:10.1021/nn303973r (Jan. 2013).

167. Kumar, N., He, J., He, D., Wang, Y. & Zhao, H. Charge Carrier Dynamics in Bulk MoS_2 Crystal Studied by Transient Absorption Microscopy. *J. Appl. Phys.* **113,** 1–6. doi:10.1063/1.4799110 (2013).

168. Kumar, N., Cui, Q., Ceballos, F., He, D., Wang, Y. & Zhao, H. Exciton-exciton annhilation in $MoSe_2$ monolayers. *Physical Review B* **89,** 1–6. doi:10.1103/PhysRevB.89.125427 (Mar. 2014).

169. Kumar, N., Cui, Q., Ceballos, F., He, D., Wang, Y. & Zhao, H. Exciton Diffusion in Monolayer and Bulk $MoSe_2$. *Nanoscale* **6,** 4915–4919. doi:10.1039/c3nr06863c (2014).

170. Nie, Z., Long, R., Sun, L., Huang, C., Zhang, J., Xiong, Q., Hewak, D. W., Shen, Z., Prezhdo, O. & Loh, Z. Ultrafast Carrier Thermalization and Cooling Dynamics in Few-Layer MoS_2. *ACS Nano* **8,** 10931. doi:10.1021/nn504760x (Oct. 2014).

171. Cui, Q., Ceballos, F., Kumar, N. & Zhao, H. Transient Absorption Microscopy of Monolayer and Bulk WSe_2. *ACS Nano* **8,** 2970–2976. doi:10.1021/nn500277y (Feb. 2014).

172. Steinhoff, A., Rösner, M., Jahnke, F., Wehling, T. O. & Gies, C. Influence of Excited Carriers on the Optical and Electronic Properties of MoS_2. *Nano Letters* **14,** 3743–3748. doi:10.1021/nl500595u (June 2014).

173. Steinleitner, P., Merkl, P., Nagler, P., Mornhinweg, J., Schüller, C., Korn, T., Chernikov, A. & Huber, R. Direct Observation of Ultrafast Exciton Formation in a Monolayer of WSe_2. *Nano Letters* **17,** 1455–1460. doi:10.1021/acs.nanolett.6b04422 (Feb. 2017).

174. Pötz, W. & Kocevar, P. Electronic power transfer in pulsed laser excitation of polar semiconductors. *Physical Review B* **28,** 7040–7047. doi:10.1103/physrevb.28.7040 (Dec. 1983).

175. Chi, Z., Chen, H., Zhao, Q. & Weng, Y.-X. Observation of the hot-phonon effect in monolayer MoS_2. *Nanotechnology* **31,** 235712. doi:10.1088/1361-6528/ab79ad (Mar. 2020).

176. Wang, W., Sui, N., Chi, X., Kang, Z., Zhou, Q., Li, L., Zhang, H., Gao, J. & Wang, Y. Investigation of Hot Carrier Cooling Dynamics in Monolayer MoS_2. *The Journal of Physical Chemistry Letters* **12,** 861–868. doi:10.1021/acs.jpclett.0c03110 (Jan. 2021).

177. Wei, X., Wang, Z., Wang, Z., Lu, Y., Ji, Q. & Liu, W. Unveiling Spatiotemporal Diffusion of Hot Carriers Influenced by Spatial Nonuniform Hot Phonon Bottleneck Effect in Monolayer MoS_2. *Nano Letters* **24,** 9269–9275. doi:10.1021/acs.nanolett.4c02059 (July 2024).

178. Li, S. S. *Semiconductor Physical Electronics* 2nd. Chapter 6.3 & 6.4. doi:10.1007/0-387-37766-2 (Springer New York, 2006).

179. Malý, P., Lüttig, J., Rose, P. A., Turkin, A., Lambert, C., Krich, J. J. & Brixner, T. Separating single- from multi-particle dynamics in nonlinear spectroscopy. *Nature* **616,** 280–287. doi:10.1038/s41586-023-05846-7 (Mar. 2023).

180. Zhou, W., Zou, X., Najmaei, S., Liu, Z., Shi, Y., Kong, J., Lou, J., Ajayan, P. M., Yakobson, B. I. & Idrobo, J.-C. Intrinsic Structural Defects in Monolayer Molybdenum Disulfide. *Nano Letters* **13,** 2615–2622. doi:10.1021/nl4007479 (May 2013).

181. Strait, J. H., Nene, P. & Rana, F. High intrinsic mobility and ultrafast carrier dynamics in multilayer metal-dichalcogenide MoS_2. *Physical Review B* **90,** 245402. doi:10.1103/physrevb.90.245402 (Dec. 2014).

182. Grassberger, P. & Procaccia, I. The Long Time Properties of Diffusion in a Medium with Static Traps. *J. Chem. Phys.* **77,** 6281–6284. doi:10.1063/1.443832 (Dec. 1982).

183. Kayser, R. F. & Hubbard, J. B. Diffusion in a Medium with a Random Distribution of Static Traps. *Phys. Rev. Lett.* **51,** 79–82. doi:10.1103/physrevlett.51.79 (July 1983).

184. Radisavljevic, B., Radenovic, A., Brivio, J., Giacometti, V. & Kis, A. Single-Layer MoS_2 Transistors. *Nat. Nanotechnol.* **6,** 147–150. doi:10.1038/NNANO.2010.279 (Jan. 2011).

185. Hong, J., Hu, Z., Probert, M., Li, K., Lv, D., Yang, X., Gu, L., Mao, N., Feng, Q., Xie, L., Zhang, J., Wu, D., Zhang, Z., Jin, C., Ji, W., Zhang, X., Yuan, J. & Zhang, Z. Exploring Atomic Defects in Molybdenum Disulphide Monolayers. *Nat. Commun.* **6.** doi:10.1038/ncomms7293 (Feb. 2015).

186. Zeiger, H. J., Vidal, J., Cheng, T. K., Ippen, E. P., Dresselhaus, G. & Dresselhaus, M. S. Theory for displacive excitation of coherent phonons. *Physical Review B* **45,** 768–778. doi:10.1103/physrevb.45.768 (Jan. 1992).

187. Taghinejad, H., Taghinejad, M., Tarasov, A., Tsai, M.-Y., Hosseinnia, A. H., Moradinejad, H., Campbell, P. M., Eftekhar, A. A., Vogel, E. M. & Adibi, A. Resonant Light-Induced Heating in Hybrid Cavity-Coupled 2D Transition-Metal Dichalcogenides. *ACS Photonics* **3,** 700–707. doi:10.1021/acsphotonics.6b00085 (Apr. 2016).

188. Yu, Y., Minhaj, T., Huang, L., Yu, Y. & Cao, L. In-Plane and Interfacial Thermal Conduction of Two-Dimensional Transition-Metal Dichalcogenides. *Physical Review Applied* **13,** 034059. doi:10.1103/physrevapplied.13.034059 (Mar. 2020).

189. Mouri, S., Miyauchi, Y. & Matsuda, K. Tunable Photoluminescence of Monolayer MoS_2 via Chemical Doping. *Nano Letters* **13,** 5944–5948. doi:10.1021/nl403036h (Nov. 2013).

190. Ford, W. E. & Kamat, P. V. Photochemistry of 3,4,9,10-perylenetetracarboxylic dianhydride dyes. 3. Singlet and triplet excited-state properties of the bis(2,5-di-tert-butylphenyl)imide derivative. *The Journal of Physical Chemistry* **91,** 6373–6380. doi:10.1021/j100309a012 (Dec. 1987).

191. Bialas, A. L. & Spano, F. C. A Holstein–Peierls Approach to Excimer Spectra: The Evolution from Vibronically Structured to Unstructured Emission. *The Journal of Physical Chemistry C* **126,** 4067–4081. doi:10.1021/acs.jpcc.1c10255 (Feb. 2022).

192. Sideri, I. K., Jang, Y., Garcés-Garcés, J., Sastre-Santos, Á., Canton-Vitoria, R., Kitaura, R., Fernández-Lázaro, F., D'Souza, F. & Tagmatarchis, N. Unveiling the Photoinduced Electron-Donating Character of MoS_2 in Covalently Linked Hybrids Featuring Perylenediimide. *Angewandte Chemie International Edition* **60,** 9120–9126. doi:10.1002/anie.202016249 (Mar. 2021).

193. Sakurai, T. & Sugano, T. Theory of continuously distributed trap states at Si-SiO_2 interfaces. *Journal of Applied Physics* **52,** 2889–2896. doi:10.1063/1.329023 (Apr. 1981).

194. Musser, A. J., Rajendran, S. K., Georgiou, K., Gai, L., Grant, R. T., Shen, Z., Cavazzini, M., Ruseckas, A., Turnbull, G. A., Samuel, I. D. W., Clark, J. & Lidzey, D. G. Intermolecular states in organic dye dispersions: excimers vs. aggregates. *Journal of Materials Chemistry C* **5,** 8380–8389. doi:10.1039/c7tc02655b (2017).

195. Renn, L., Walter, L. S., Watanabe, K., Taniguchi, T. & Weitz, R. T. All About the Interface: Do Residual Contaminants at A High-Quality h-BN Monolayer Perylene Diimide Interface Cause Charge Trapping? *Advanced Materials Interfaces* **9,** 2101701. doi:10.1002/admi.202101701 (Jan. 2022).

List of publications including declaration of own contributions

Within the thematic and temporal framework of this thesis

[P1] **Fluence-dependent dynamics of localized excited species in monolayer versus bulk MoS_2**

Tim Völzer, Franziska Fennel, Tobias Korn, and Stefan Lochbrunner
Physical Review B 2021, **103**, 045423
https://doi.org/10.1103/PhysRevB.103.045423

As the first author, I conceptualized the project, prepared the samples and conducted virtually all experiments as well as analyses. Furthermore, I wrote the manuscript and implemented all necessary changes during the review process, under the supervision of the other authors.

[P2] **Strong quenching of dye fluorescence in monomeric perylene orange/TMDC hybrid structures**

Tim Völzer, Alina Schubert, Erik von der Oelsnitz, Julian Schröer, Ingo Barke, Rico Schwartz, Kenji Watanabe, Takashi Taniguchi, Sylvia Speller, Tobias Korn, and Stefan Lochbrunner
Nanoscale Advances 2023, **5**, 3348
https://doi.org/10.1039/D3NA00276D

As the first author, I conceptualized the project, conducted the majority of the experimental work and of the writing of the manuscript, respectively, except the parts related to the AFM measurements. In detail, I tested and established the dye deposition techniques together with A. Schubert and E. von der Oelsnitz. I performed the optical measurements at room temperature with the help of A. Schubert and those at low temperatures in collaboration with J. Schröer. Furthermore, I conducted all related analyses. On top, I prepared the manuscript including all review and publication iterations.

[P3] **Having a good vibe: Strong coupling to the electronic system creates incoherent and coherent phonons in 1L-TMDCs**

Tim Völzer, Marvin Krupp, Julian Schröer, Annika Bergmann-Iwe, Tobias Korn, and Stefan Lochbrunner
2D Mater. 2025, **12**, 035012
https://doi.org/10.1088/2053-1583/addf5a

I conceptualized the project as well as wrote and edited the manuscript throughout the whole review process under the supervision of S. Lochbrunner and T. Korn. I performed the transient absorption and Raman experiments together with M. Krupp and J. Schröer, respectively. Moreover, I conducted all data processing and evaluation.

Further publications

[F1] **Recombination dynamics of optically excited charge carriers in bulk MoS_2**

Tim Völzer, Matthias Lütgens, Franziska Fennel, and Stefan Lochbrunner
Journal of Physics B: Atomic, Molecular and Optical Physics 2017, **50**, 194003
https://doi.org/10.1088/1361-6455/aa89df

This contribution was based on my bachelor thesis and does not fall under the framework of this dissertation.

As the first author, I prepared the samples and performed the analysis. I conducted the experiments with the help of M. Lütgens. Furthermore, I wrote the manuscript under the supervision of the other authors, up to the point of submission, however, I was not involved during the review process.

[F2] **Chercher de l'eau: The switching mechanism of the rotary switch ethyl-2-(2-(quinolin-8-yl)hydrazono)-2-(pyridin-2-yl)acetate**

Vera Deneva, Nikolay G. Vassilev, Silvia Hristova, Dancho Yordanov, Yoshihiro Hayashi, Susumu Kawauchi, Franziska Fennel, Tim Völzer, Stefan Lochbrunner, Liudmil Antonov
Computational Materials Science 2020, **177**, 109570
https://doi.org/10.1016/j.commatsci.2020.109570

In this work, I performed the transient absorption measurements under the supervision of F. Fennel and S. Lochbrunner. Together with F. Fennel, I analyzed the corresponding data.

[F3] **Photoisomerization of a phosphorus-based biradicaloid: Ultrafast dynamics through a conical intersection**

Tim Völzer, H. Beer, A. Schulz, S. Lochbrunner, J. Bresien
Physical Chemistry Chemical Physics 2021, **23**, 7434-7441
https://doi.org/10.1039/D1CP00428J

This publication represents a shared first authorship between H. Beer and me. My contribution spans the conduct and the evaluation of the transient absorption spectroscopy as well as writing the according part of the manuscript under the supervision of S. Lochbrunner, A. Schulz and J. Bresien.

[F4] **Benzothiazol picolin/isonicotinamides molecular switches: Expectations and reality**

Anton Georgiev, Vera Deneva, Dancho Yordanov, Tim Völzer, Steffen Wolter, Franziska Fennel, Stefan Lochbrunner, Liudmil Antonov
Journal of Molecular Liquids 2022, **356**, 118968
https://doi.org/10.1016/j.molliq.2022.118968

In this work, I performed the transient absorption measurements in collaboration with S. Wolter and F. Fennel.

[F5] **Ultrathin Defective Nanosheet Subunit $ZnIn_2S_4$ Hollow Nanoflowers for Efficient Photocatalytic Hydrogen Evolution**

Shuoping Ding, Igor Medic, Norbert Steinfeldt, Tianao Dong, Tim Völzer, Simon Haida, Jabor Rabeah, Juncheng Hu, Jennifer Strunk
Small Structures 2023, **4**(10), 2300091
https://doi.org/10.1002/sstr.202300091

For this publication, I conducted the fluorescence lifetime imaging microscopy.

Conference papers

[C1] **Ultrafast Charge Carrier Dynamics in Bulk MoS_2 Following Optical Excitation**

Tim Völzer, Matthias Lütgens, Franziska Fennel, and Stefan Lochbrunner
Proceedings of the International Conference on Ultrafast Phenomena, 2016
http://dx.doi.org/10.1364/UP.2016.UTh4A.35

This contribution was based on my bachelor thesis and does not fall under the framework of this dissertation.

The work belongs to [F1], therefore my contribution is identical.

[C2] **Characteristics of Spectral Properties and Morphological Aspects in Thiacarbocyanine J-aggregates**

Polina Pisklova, Iryna Ropakova, Svetlana Yefimova, Yen-Ting Chen, Tim Völzer, Stefan Lochbrunner, and Oleksandr Sorokin
Proceedings of the International Conference on Nanomaterials: Application & Properties (NAP), 2024
https://doi.org/10.1109/NAP62956.2024.10739690

For this publication, I performed the fluorescence lifetime imaging microscopy.

Conference contributions

Talks

1. **Ultrafast carrier dynamics in bulk MoS_2 studied by transient absorption spectroscopy**
   Spring Meeting of the German Physical Society (Condensed Matter Section), 2016, Regensburg, Germany
   Tim Völzer, Matthias Lütgens, Franziska Fennel, and Stefan Lochbrunner
   This contribution was based on my bachelor thesis and does not fall under the framework of this dissertation.

2. **Fluence-dependent dynamics of localised excited species in monolayer versus bulk MoS_2**
   8th International Symposium on Optics & its applications, 2021, Rostock, Germany
   Tim Völzer, Franziska Fennel, Tobias Korn, and Stefan Lochbrunner

3. **Strong Fluorescence Quenching in Hybrid Structures**
   Graduate School Workshop, 2022, Malente, Germany
   Tim Völzer

4. **Strong Quenching of Dye Fluorescence in Perylene Orange/TMDC Hybrid Structures**
   Meeting of the German Physical Society (Condensed Matter Section), 2022, Regensburg, Germany
   Tim Völzer, Alina Schubert, Erik von der Oelsnitz, Rico Schwartz, Ingo Barke, Sylvia Speller, Tobias Korn, and Stefan Lochbrunner

5. **Strong Quenching of Dye Fluorescence in Perylene Orange/TMDC Hybrid Structures**
   Retreat of the Collaborative Research Center LiMatI, 2022, Gut Ulrichshusen, Germany
   Tim Völzer, Alina Schubert, Erik von der Oelsnitz, Rico Schwartz, Ingo Barke, Sylvia Speller, Tobias Korn, and Stefan Lochbrunner

6. **Towards measuring charge transfer in hybrid structures of sub-monolayer dye films on 2D materials**
   Spring Meeting of the German Physical Society (Condensed Matter Section), 2024, Berlin, Germany
   Tim Völzer, Julian Schröer, Erik von der Oelsnitz, Tobias Korn, and Stefan Lochbrunner

Poster presentations

1. **Ultrafast Carrier Dynamics in Bulk MoS_2 Following Optical Excitation**
   International Conference on Ultrafast Phenomena, 2016, Santa Fe, New Mexico, USA
   Tim Völzer, Matthias Lütgens, Franziska Fennel, and Stefan Lochbrunner
   This contribution was based on my bachelor thesis and does not fall under the framework of this dissertation.

2. **2D versus 3D Decay Dynamics in Transition Metal Dichalcogenides**
   Dynamics Days Europe, 2019, Rostock, Germany
   Tim Völzer, Franziska Fennel, and Stefan Lochbrunner

3. **2D versus 3D Decay Dynamics in Transition Metal Dichalcogenides**
   55th Symposium on Theoretical Chemistry, 2019, Rostock, Germany
   Tim Völzer, Franziska Fennel, and Stefan Lochbrunner

4. **Strong Quenching of Dye Fluorescence in Perylene Orange/TMDC Hybrid Structures**
   Flatlands Beyond Graphene, 2022, Teguise, Lanzarote, Spain
   Tim Völzer, Alina Schubert, Erik von der Oelsnitz, Rico Schwartz, Ingo Barke, Kenji Watanabe, Takashi Taniguchi, Sylvia Speller, Tobias Korn, and Stefan Lochbrunner

5. **Photoinduced charge injection into single layer WSe_2 via deposited dye molecules?**
   Spring Meeting of the German Physical Society (Condensed Matter Section), 2023, Dresden, Germany
   Tim Völzer, Alina Schubert, Julian Schröer, Rico Schwartz, Tobias Korn, and Stefan Lochbrunner

6. **From coherent phonons to 2D material/dye molecule hybrids: A glimpse into the vast world of TMDCs**
   1st International Conference on Light-Matter-Interactions at Interfaces, 2024, Rostock, Germany
   Tim Völzer, Marvin Krupp, Erik von der Oelsnitz, Julian Schröer, Alina Schubert, Rico Schwartz, Tobias Korn, Stefan Lochbrunner

7. **From coherent phonons to 2D material/dye molecule hybrids: A glimpse into the vast world of TMDCs**
   6th International Conference on Intelligent Materials InMAT, 2025, Rostock, Germany
   Tim Völzer, Marvin Krupp, Erik von der Oelsnitz, Julian Schröer, Alina Schubert, Rico Schwartz, Tobias Korn, Stefan Lochbrunner

Publications in the thematic and temporal context of this thesis

[P1]

Fluence-dependent dynamics of localized excited species in monolayer versus bulk MoS_2

Tim Völzer, Franziska Fennel, Tobias Korn, and Stefan Lochbrunner

Physical Review B 2021, **103**, 045423

https://doi.org/10.1103/PhysRevB.103.045423

PHYSICAL REVIEW B **103**, 045423 (2021)

Fluence-dependent dynamics of localized excited species in monolayer versus bulk MoS_2

Tim Völzer, Franziska Fennel, Tobias Korn, and Stefan Lochbrunner*
Institute of Physics and Department "Life, Light & Matter," University of Rostock, 18059 Rostock, Germany

(Received 11 March 2020; accepted 4 January 2021; published 20 January 2021)

Transition-metal dichalcogenides are characterized by a layered lattice structure, facilitating the fabrication of two-dimensional crystals. Concerning their electronic properties, these monolayers differ fundamentally from the bulk material, exhibiting direct band gaps and significantly higher exciton binding energies. Hence, to shed light on how the crystal thickness influences the relevant excited states and in particular their dynamics, we performed time-resolved optical pump-probe spectroscopy on monolayer and bulk samples of molybdenum disulfide (MoS_2) for a broad range of excitation fluences. The observed transient spectra result from photoinduced shifts in the band structure. Here, we find evidence for a localized nature of the excited species as opposed to the common model of band-gap renormalization. At high excitation densities, strong collisional broadening of the shifted absorption occurs. Within the first picosecond after excitation, the free carriers thermalize, while in the monolayer, additionally, electrons and holes pair to form excitons. On longer time scales up to several nanoseconds, the excited populations decay. In the bulk sample, the corresponding signal reduction could be described in terms of a defect-assisted Auger recombination of electrons and holes. For monolayer MoS_2, in contrast, two-dimensional diffusion leads to recombination of the excitons at defect sites.

DOI: 10.1103/PhysRevB.103.045423

I. INTRODUCTION

Transition-metal dichalcogenides (TMDCs) have emerged as two-dimensional (2D) materials, as their layered structure with weak van der Waals interlayer forces facilitates the fabrication of atomically thin crystals. Here, the limiting case of a triatomic monolayer (1L) differs decisively from the bulk, exhibiting drastically enhanced exciton binding energies and a direct band gap [1–4], i.e., resulting in a pronounced rise of the photoluminescence (PL) [5,6].

Apart from these fundamental issues, these thin films have raised particular interest in view of various applications [7]. Generally, as a consequence of the strong light-matter interactions in TMDCs, they are predestined for optoelectronics such as light-emitting diodes [8] and phototransistors [9]. In the field of photodetectors, developments towards high responsivities [10] and ultrafast response times [11] have been pursued. In the latter case, short carrier diffusion pathways in atomically thin layers allow for a fast charge separation after exciton dissociation. Yet, these processes compete with loss mechanisms, such as trapping and recombination, lowering the quantum efficiency of the devices [10].

Furthermore, especially in molybdenum and tungsten disulfides (MoS_2 and WS_2, respectively), the energy of the conduction-band (CB) minimum matches the redox potential of the hydrogen evolution reaction (HER) in the process of water splitting [12]. Hence, these materials constitute promising HER photo- [13–15] and electrocatalysts [16,17]. Here, the crystal edges have been identified as the catalytically active sites [12], thus making thin and small flakes preferable catalytic systems, owing to their high specific surfaces or active center densities. On the downside, this location of the sites causes the (quantum) efficiency of the catalytic reaction to depend critically on an undisturbed, low-loss transport of excitation energy or excited species through the material to the edges [14,15,18], similar to the situation in (opto)electronics.

All in all, this demonstrates the importance of excited species dynamics for applying TMDCs in the aforementioned technologies. Considering the impact of thickness on their electronic properties, we expect distinct behaviors for the 1L and the bulk. Common approaches for investigating the excited species' ultrafast dynamics are transient absorption or reflectance spectroscopy, which have been performed by various groups on mono- and few-layer [19–26] as well as on bulk [20,27–29] flakes of different TMDCs. The obtained signals or spectra bear striking similarities in most studies; however, their evaluations and interpretations concerning the physical origin of the signatures strongly differ. Here, various excitonic effects [19,23,27] and band filling [20,28] were considered, although the model of band-gap renormalization (BGR) [19,21,24] has gained broader acceptance lately. Likewise, various processes governing the dynamics and decay of the signals are discussed, yet there are fundamental differences between these studies regarding sample quality and thickness, excitation fluence regime, and probe wavelength. In our view, systematic variation of the excitation density should allow for a better characterization of the excited species and resolve some of the contradicting interpretations. With this goal in mind, we studied the light-induced dynamics in 1L and bulk MoS_2 in dependence on the excitation fluence and developed a physical model resulting in a consistent interpretation of the time-resolved dynamics.

In this work, we present all optical pump-probe [30] measurements of 1L and bulk MoS_2, exciting with a wavelength of 400 nm and probing the whole visible range with a white light continuum. In particular, the dynamics are analyzed with respect to their dependence on the excitation fluence, providing

*stefan.lochbrunner@uni-rostock.de

insights into the nature of the excited species. Thus, we can trace and separate decay mechanisms that behave nonlinearly with respect to the excitation density or nonexponentially with time. Careful analysis of the transient spectra is performed by globally fitting the transient spectra to discriminate different signatures, such as shifts, broadenings, and decays, to associate the spectral features to the underlying mechanisms. In the course of this, we find subtle contradictions to the common BGR model, especially to the predicted peak shift with increasing density of the excited species. Hence, we propose a picture of localized species, which cause spatially limited distortions of the lattice and the respective energy bands.

II. RESULTS AND DISCUSSION

A. Preparation and identification of monolayer MoS_2 flakes

We fabricated atomically thin films on a polydimethylsiloxane (PDMS) substrate, following the advanced exfoliation approach developed by Castellanos-Gomez *et al.* [31,32]. We scanned for and selected promising flakes via optical microscopy. A monolayer area was identified based on its transmission contrast [33–35] and PL [5,6]. As a bulk sample for comparison, we selected a crystal of several tens of nanometers of vertical extent. The details of the sample preparation and thickness determination for both samples are given in Secs. I and II of the Supplemental Material (SM) [36], respectively.

The absorption spectra in the visible range of the monolayer and bulk samples feature the same three prominent peaks(see Fig. 1). The lower energetic peaks A and B at about 650 and 600 nm, respectively, correspond to excitonic transitions located at the *K* point [37,38], while the energetically broader and higher contribution C near 450 nm can be assigned to band nesting in different regions of the Brillouin zone, especially in the environment of the Γ point [38–40]. For the A and C peaks, we note a blueshift from bulk to monolayer, as has previously been observed for dry as well as liquid-phase exfoliated flakes [24,37].

B. Transient band shifts induced by localized excited species

We now turn to the transient absorption spectra $\Delta A(\lambda, t)$, which were obtained by pump-probe spectroscopy with a time resolution of 100 fs. Details of the experimental setup are presented in the SM, Sec. III [36]. All measurements were performed under ambient conditions. Despite the difference in the C transition energies between monolayer and bulk MoS_2, the high excess energy of the 400-nm pump pulses with respect to this absorption band suggests the excitation of free charge carriers in several parts of the Brillouin zone in both cases.

When comparing the transient spectra of bulk and monolayer MoS_2, as shown in Figs. 1(a) and 1(b), respectively, one finds strikingly similar patterns in both cases: Negative ΔA peaks (A^- and B^-) at the positions of the original static absorption bands A and B are accompanied by redshifted positive features (A^+ and B^+) [24,40], suggesting a photoinduced shift of the absorption to lower energies. Accordingly, each pair of positive and negative peaks resembles a single process, namely, the shift of the original, static absorption peak. These

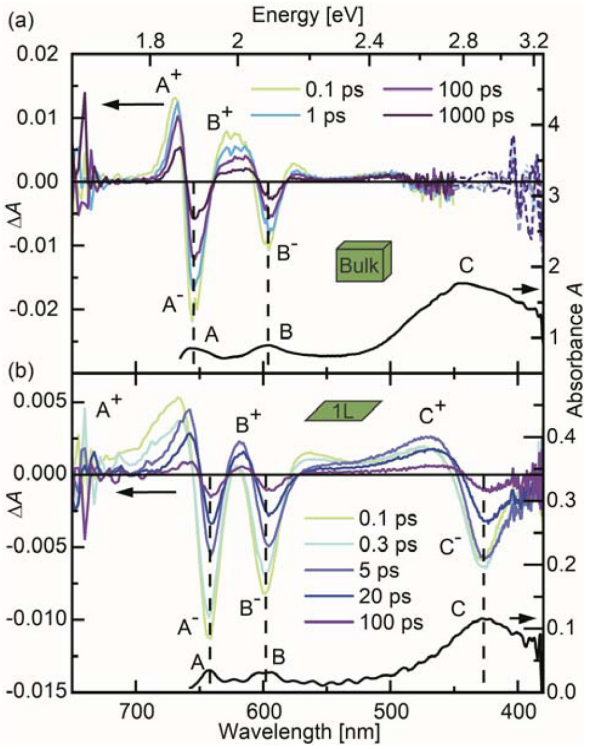

FIG. 1. (a) Bulk and (b) monolayer static absorption (black lines) and transient spectra (colored lines) for an excitation fluence of 31 μJ/cm^2 at various probe delays. The negative transient peaks match the static absorption peaks, as indicated by the dashed vertical lines. Each of these transient signatures is accompanied by a corresponding redshifted, positive feature. For the monolayer, these peaks appear broader than in the bulk case and an additional peak pair arises around the wavelength of the C absorption. The dashed curves in (a) indicate a region of high noise and are therefore smoothed.

observations are consistent with the results of our previous work [29], where we excited a bulk sample at 665 nm. Consequently, the shift is caused by the excited species irrespective of their exact location in the band structure.

With reference to the underlying mechanism for this shift in the bulk, we already discussed a variety of possible explanations in that earlier study. Here, we expand this discussion to the single layer. Considering the similarity of the bulk and monolayer spectra, despite the enormous difference in exciton binding energy, excitonic effects such as trion or biexciton formation seem highly improbable as the origin of the shift. The intensely discussed approach of band-gap renormalization [19–21,24,41], on the contrary, provides the benefit of being equally applicable to crystals of every thickness. Pogna *et al.* obtained transient spectra in 1L MoS_2 similar to ours and explained them mostly with BGR [22]. In this picture, the different charge distribution of the excited species compared to the ground state affects the band structure and shifts the band levels and likewise the absorption peaks. However, as the carriers are regarded as completely delocalized over the whole crystal, the magnitude of the redshift directly depends on the excited carrier density [42].

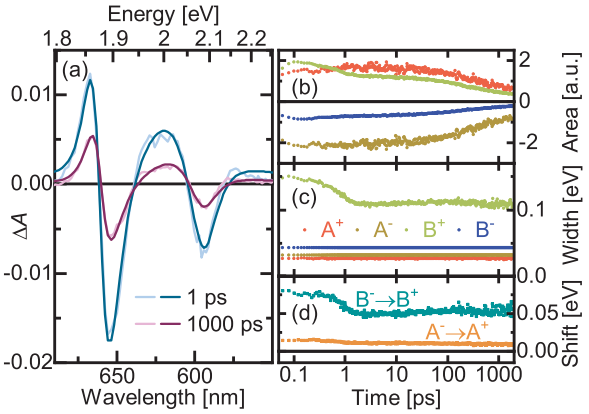

FIG. 2. Lorentzian peak fitting of the $A^{\pm}$ and $B^{\pm}$ features in the transient spectra for the bulk sample excited with a fluence of 31 $\mu J/cm^2$. (a) Measured and fitted transient absorption spectra at different probe delays. Bright lines represent the data and dark lines stand for the fits, showing a good agreement between the two. (b) Temporal evolution of the areas of the four Lorentz peaks. All curves clearly decrease in amplitude. (c) Time-resolved peak widths. The B^- width decreases within the first few picoseconds, while all other features exhibit constant values. (d) Peak shift magnitude from negative to positive contribution for the A and B pair over time. The shift is reduced during the first few picoseconds and does not change afterwards.

To probe the applicability of this model to our data, we fitted the transient spectra by a sum of four Lorentzian profiles in the range of the $A^{\pm}$ and $B^{\pm}$ peaks to distinguish between a shift of the positive peaks' positions and a mere reduction of the peak areas, as the excited species density decreases over time. As the negative features originate from the static absorption, we fixed their center energy and width to reduce the number of free parameters. The respective values were extracted from the static absorption spectra, as depicted in Fig. 1. The resulting fits, which match the data well, as well as the time evolution of the obtained parameter are presented in Fig. 2. The extracted parameters demonstrate that the long-term decay of the signal corresponds to merely a reduction of the peak area, whereas the shift, i.e., the center position difference between negative and positive peaks, remains constant. Fittings performed for higher excitation fluences and for the monolayer, as well as results obtained by using another line-shape function, can be found in Sec. IV of the SM [36]. Despite a higher noise and interfering additional spectral signatures, they reproduce the tendency that the dynamics are determined by the evolution of the peak area rather than that of the shift. These findings contradict the model of BGR resulting from delocalized excited species. Since our data mainly describe a shrinkage of the transient peaks with decaying excited populations instead of shifts, we propose a rather localized nature of the excited species. In this case, the locally altered charge distribution interacts with the band structure, leading to a new equilibrated electronic structure with a shifted absorption. Here, a higher number of excited species only causes a larger fraction of the crystal volume to be affected by the shift in absorption, but it does not change the spectral magnitude of the shift. A possible explanation for the localization could be the formation of polarons. These quasiparticles are commonly understood as carriers inducing deformation of the lattice and the charge distribution in their vicinity and traveling together with the potential dip that is caused by their own presence [43]. This interpretation would explain the local nature of the excited species, as Holstein polarons typically extend over about one unit cell. Furthermore, this picture intrinsically contains energy shifts in terms of the potential dip, accounting for the signatures in the transient spectra. Polarons have already been observed in surface-doped 1L MoS_2, causing energy shifts of several tens of meV [44]. Likewise, theoretical studies predict similar mechanisms and shifts for excitonic polarons in monolayer TMDCs [45]. Thus, this concept can be generally applied to free carriers as well as excitons independent of the crystal thickness.

In spite of their similarities, the spectra of the two samples differ from each other in two aspects: First, in the 1L MoS_2, we clearly observe an additional pair of a positive and negative peak, denoted as C^+ and C^-, corresponding to the C absorption band, while comparable signatures barely stand out from the noise in the bulk spectra. This can be explained by the larger width of the static C absorption peak in the thick crystal compared to the monolayer, making it less sensitive to shifts. As a second point, we note that the positive transient signals in the thinner sample appear significantly broader than their bulk counterparts. This enlarged width can be interpreted in terms of a collisional broadening as a consequence of Coulomb scattering of the excited species [19,23,28]. In the bulk, the Coulomb potential is screened more effectively [1,41] and the successive absorption of pump fluence during propagation through the sample leads to a lower average excited carrier density, resulting in a less pronounced broadening than in the monolayer. In the latter, however, the positive peaks A^+ and B^+ strongly overlap and partially cancel out with the negative signals A^- and B^-, causing the B^+ contribution to seemingly almost vanish.

The temporal evolution of the transient spectra for both samples is split into two major regimes on the (sub)picosecond and subnanosecond time scale. In the bulk, the fast dynamics manifest as a slight decrease of the transient amplitude and an apparent blueshift of the peak maximum at A^+. As the fit results in Fig. 2 prove, this is caused by a partial reduction of the photoinduced redshift and by narrowing of the positive peaks.

Generally, these fast processes are associated with the thermalization of excited carriers [24,27,29]. On a closer look, however, one has to distinguish between two separate effects. First, the carriers excited to high-lying regions of the CB rapidly relax into their respective band minimum or maximum by carrier-carrier scattering [46], as reported by time- and angle-resolved photoelectron spectroscopy (trARPES) [39,47]. Since this process takes place within 50–100 fs, we are not able to resolve it in our measurements. After this relaxation into the band extremum, the carriers follow a thermal distribution with an extremely high temperature, corresponding to their excess energy. From there on, carrier-phonon interaction dissipates this energy as heat to the crystal lattice. We attribute the picosecond-time-scale dynamics to

this process. As the excited species and the lattice equilibrate, the former cool down, reducing collisional broadening and therefore narrowing the positive peaks [see Fig. 2(c)]. Additionally, the reduced shift that occurs on this time span in Fig. 2(d) shows that cooled excited carriers disturb the local charge distribution and in turn alter the band structure less strongly than hot ones.

In the monolayer, a closer look especially at the A^+ peak in Fig. 1(b) reveals a further distinction of the thermalization component. First, on a time scale of several hundred femtoseconds, a signal reduction occurs, somewhat faster than, yet comparable to, the cooling times observed in the bulk. We interpret this as a proceeding localization of the excited carriers. In a local picture, a hot carrier will be characterized by a spatially smeared-out charge distribution that barely adapts to the local potential. Upon losing their excess energy, however, the particles will accumulate in local energy minima. This localization leads to a reduced affected crystal volume and, thus, a lower transient signal amplitude results as observed. Afterwards, within several picoseconds, we register a notable decrease of the collisional broadening, as the positive peaks narrow and rise in amplitude (see SM, Fig, S6 [36]). We interpret this as an evidence for exciton formation from thermalized carriers, as a consequence of the high exciton binding energy in the monolayer [48]. In the initial electron-hole plasma, the carriers move independently, each surrounded by their (dielectrically screened) Coulomb potential, despite an overall charge neutrality. When electron and hole form a bound pair, though, their charges compensate, reducing their Coulomb-scattering cross sections. Simultaneously, the excited particle density halves; hence, collisional broadening weakens and the positive transient peaks narrow.

As the second part of the dynamics, we observe the decay of the spectra on a subnanosecond time scale. Here, the recombination of electrons and holes (respectively, excitons) takes place. Irrespective of the sample thickness, the signal at all characteristic peaks decays at the same rate (see Sec. V of the SM [36]) and the spectral shape remains constant. This provides another evidence that the (thermalized) excited species density merely influences the amplitude of the transient peaks, while their positions do not change. In other words, with fewer excited species present, the photoinduced redshift of the static absorption affects a smaller fraction of the crystal volume, yet the absorption is shifted by the same amount of energy. Consequently, we can take the transient signal amplitude as a measure for the excited species density. A comprehensive analysis of their recombination mechanisms is presented in Sec. II D.

C. Density-dependent peak broadening and saturable absorption

To gain insight into the detailed nature of the decay dynamics, we vary the pump fluence searching for indications of nonlinear multiparticle processes. With an increase of the pump fluence, the transient spectra of both bulk and monolayer MoS_2 experience a sublinear amplitude growth as well as a further broadening of the positive peaks, as can be noted in Fig. 3. The latter results from the higher density of excited species, delivering more potential scattering partners, ergo stronger collisional broadening.

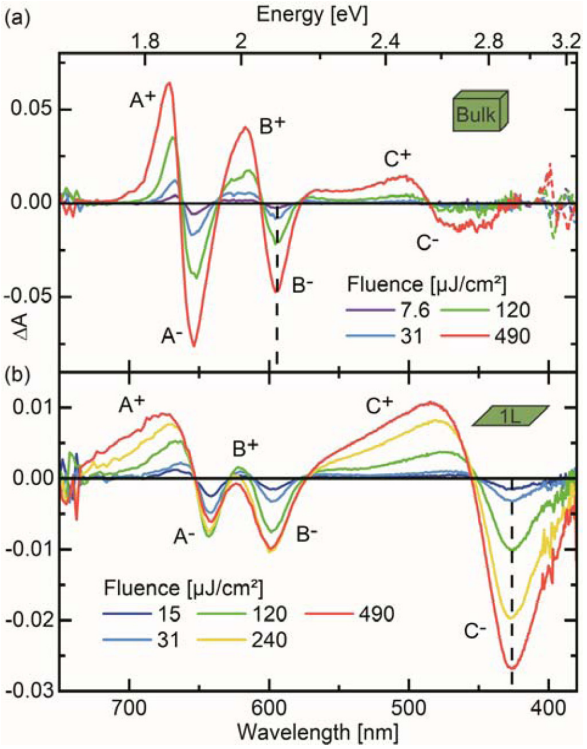

FIG. 3. (a) Bulk and (b) monolayer transient spectra at a probe delay of 1 ps for different pump fluences. The dashed lines mark the wavelengths considered for the analysis of the signal dynamics in the following sections. (a) The spectral shape remains essentially constant, with the amplitude increasing with fluence. The dashed curves indicate a region of high noise and are therefore smoothed. (b) The positive contributions broaden, and some stagnate or shrink, distorting the shape at high intensities.

In the bulk, one notices this effect most clearly for the A^+ peak [Fig. 3(a)]. Moreover, the peak heights increase sublinearly with pump fluence, indicating a saturated absorption behavior [29,49]. Yet, all four contributions related to the A and B peaks exhibit equal decay curves even at the highest fluence (see SM, Fig. S7(b) [36]), suggesting the signals to directly represent the excited carrier density. In accordance with previous studies [29], we chose the B^- peak at 596 nm for a detailed analysis of the bulk decay dynamics. The results of the fittings, in contrast, are not suitable for this purpose, since they should only be regarded qualitatively, as discussed in detail in Sec. IV of the SM [36].

In the monolayer, however, due to the weakened screening, collisional broadening is significantly more prominent, as can be seen in Fig. 3(b). Here, the $A^\pm$ and $B^\pm$ features overlap so strongly that the spectral shape is drastically distorted and the relation between excitation density and transient signal deviates significantly from a linear or even monotonic behavior in the corresponding wavelength region. As the peak fitting procedure yielded no results in case of high fluences(see Sec. IV of the SM [36]), we also cannot analyze peak areas as a measure for the exciton density. Therefore, we chose the C^- peak at 427 nm for a detailed investigation of the decay dynamics.

As the excitons induce a shift of the complete absorption, they cause the C^- contribution despite being located around the band minima. Here, the signal amplitude grows linearly with pump fluence, suggesting that it directly represents the exciton density. The sole exception from this behavior is observed for the highest intensity. Here, however, a saturation of the absorption similar to the bulk might come into play. In addition to this, the exciton density of up to 2×10^{14} cm^{-2} for the highest excitation fluence approaches the range of the Mott density in the order of 10^{14} cm^{-2}, as follows from an exciton Bohr radius of roughly 1 nm [1,4,19,38]. In this regime, the lattice is (spatially) saturated with excitons, causing a stagnation of the transient signal strength. In the extreme case of drastically higher excited species densities compared to our work, Chernikov *et al.* even observed an almost complete bleaching of the (shifted) absorption after excitation of WS_2 monolayers [19].

D. Auger recombination and diffusion-limited exciton trapping

To shed light on the underlying mechanisms for the excited species recombination in monolayer and bulk, we compare time traces at characteristic wavelengths for various pump fluences. Following their linear density dependence, as discussed in the previous section, we selected time traces of the B^- feature at 596 nm for the bulk and of the C^- peak at 427 nm for the monolayer sample. In Fig. 4, we compare the traces normalized to their value after the initial thermalization to find indications for multiparticle processes.

For the bulk material, we find a distinct acceleration of the signal decay with growing fluence, pointing to a quadratic dependence of the rate on the carrier density, as for the recombination of an electron from the conduction band with a hole from the valence band (VB). On top of that, we observe a counterintuitive phenomenon at the long-term tails of the high-fluence traces: For a quadratic recombination rate, a curve normalized to its starting value will decay faster the higher the initial signal or population. Nevertheless, the decay for the highest excitation density [red curve in Fig. 4(a)] falls behind the one for the next-lower fluence [green curve in Fig. 4(a)] for a time delay larger than 1000 ps. This may be explained by the involvement of a third species that catalyzes the recombination. If a significant fraction of this species is occupied when large numbers of carriers recombine, the signal decay will be slowed down. Such a behavior may be caused by defects, which mediate the recombination yet become inactive when occupied. The characteristics of these dynamics can be described by the model of defect-assisted Auger recombination [25,26,29,40,49,50]. Correspondingly, we fitted the time traces in terms of the following differential equation, describing the trapping of a free electron at a defect site via Auger scattering with another CB electron:

$$\frac{dn_e}{dt} = -\frac{dn_d^*}{dt} = -k_A n_e^2 (n_{d,0} - n_d^*(t)),$$
$$n_d^*(0) = 0, \; n_e(0) = n_0, \qquad (1)$$

with $n_e(t)$ and $n_d^*(t)$ being the time-dependent volume densities of free electrons and occupied defects, respectively, k_A the Auger rate constant, as well as $n_{d,0}$ and n_0 the overall available defect density and the initially excited electron density,

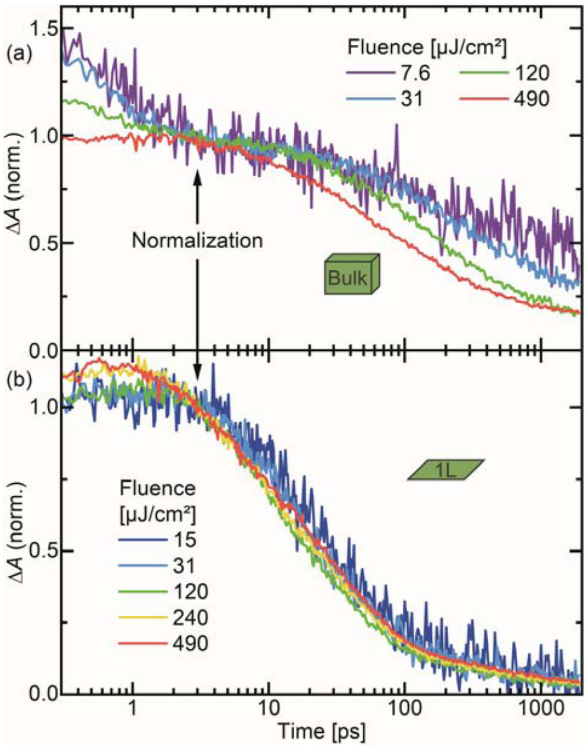

FIG. 4. Normalized time traces for various pump fluences at characteristic peak wavelengths, as indicated in Fig. 3, for (a) bulk at 596 nm and (b) monolayer at 427 nm. The arrows mark the time points used for the normalization. (a) Generally, the decay proceeds faster with increasing fluence. Yet, the green and red lines intersect at longer times. (b) The curves exhibit almost identical shape, independent of the applied pump fluence.

respectively. The second step of the Auger model, namely, the recombination of a trapped electron and a VB hole, turned out to exceed the experimental time range and was not fitted. Nevertheless, we accounted for amplitude contributions of holes or occupied defects. The measured and fitted curves are displayed in Fig. 5(a), showing an excellent agreement and yielding a trapping rate of $k_A \approx 10^{-30}$ cm^6 s^{-1}, and an overall defect density of $n_{d,0} \approx 10^{20}$ cm^{-3}. Additionally, we found a weak signature of holes and defects associated with $n_d^*(t)$, making up roughly 10% of the total amplitude. These extracted parameters bear a strong resemblance to those obtained for bulk MoS_2 excited at 665 nm [29], confirming that the recombination does not depend significantly on the excitation wavelength.

For the monolayer, in contrast to the bulk, the normalized time traces in Fig. 4(b) show virtually identical shapes, exhibiting hardly any fluence dependence. This behavior indicates a decay rate depending linearly on the exciton density and allows to exclude excitation density-dependent decay mechanisms like exciton-exciton annihilation for the monolayer. Yet, defects are still expected to play an important role as traps in the recombination [25], especially since they are particularly located at the crystal surface [26]. As a decisive difference to the mobile, free carriers in the bulk, we suppose

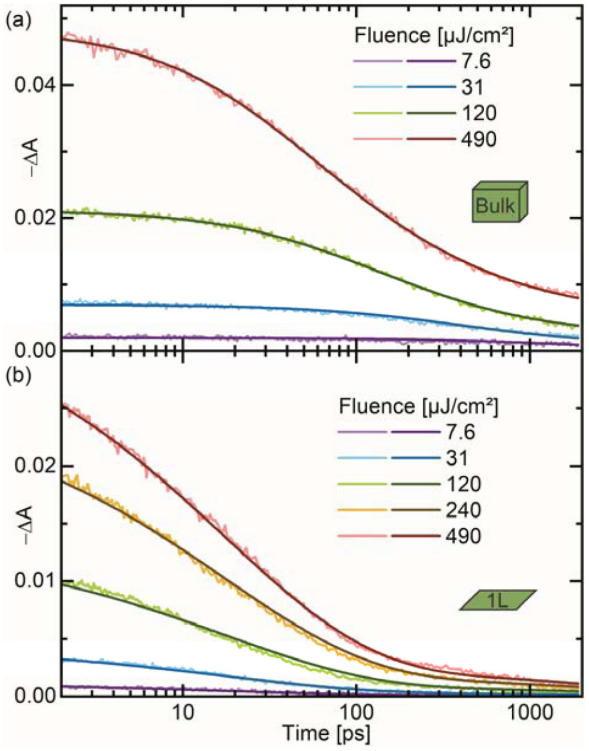

FIG. 5. Fitted decay dynamics for (a) bulk and (b) monolayer. Pale colors indicate the experimental data at the wavelengths indicated in Fig. 3, while dark shaded lines represent the fit. Both diagrams demonstrate a good agreement between the measurement and the fit.

the excitons in 1L MoS_2 exhibit a much lower mobility, owing to their bound nature. Consequently, we propose a trapping of excitons at defect sites, with a temporal evolution governed by the diffusion of the excitons towards the spatially fixed, randomly distributed traps [51]. The time dependence of such a diffusion-limited decay in d dimensions has been solved in theoretical studies, yielding a stretched exponential decay of the diffusive particle density $n(t)$ [52,53]:

$$n(t) \propto \exp(-Bt^{\frac{d}{d+2}}),$$
$$B = cn_t^{\frac{2}{d+2}} D^{\frac{d}{d+2}}, \tag{2}$$

with the diffusion coefficient D and the static trap density n_t. The numeric constant c depends on the dimensionality of the system, taking a value of $c = 8.525$ in a two-dimensional crystal [52].

An intuitive approach to understanding the origin of the stretched exponential is provided by the random spatial distribution of the defects. In regions with a high local trap density, the mean exciton diffusion pathway is short, resulting in a fast decay, while, on the other hand, larger crystal volumes free from defects exist, where excitons diffuse for a long time before meeting a trap site [52]. Consequently, the latter case will dominate the dynamics in the long term, successively prolonging the effective exciton lifetime as the decay proceeds.

Data fitting based on Eq. (2) indicated a good agreement of the diffusion model with the experiment during the first 100 ps. On a longer term, however, the fit approaches the baseline much faster than the data, suggesting the existence of a further species or contribution with a lifetime beyond the experimentally accessible time window of 1.9 ns. To describe this slow dynamics, we approximate this signature with a simple exponential decay with a lifetime τ_X. Moreover, we assume the contribution of this long-living component to scale linearly by a factor α with the amplitude A_0 of the excitonic contribution, i.e., with the exciton density, in accordance with the congruence of the time traces at different pump fluences. In summary, we obtain the following functional form for the transient signal:

$$\Delta A(t) = A_0\left[\exp(-Bt^{\frac{1}{2}}) + \alpha \exp\left(-\frac{t}{\tau_X}\right)\right],$$
$$B = c(n_t D)^{\frac{1}{2}}. \tag{3}$$

To test the potential influence of trap occupation, we additionally included the deactivation of traps during their occupation by subtracting the trapped excitons from the otherwise constant trap density n_t in Eq. (3). However, this fit resulted in a diverging n_t, which leaves the conclusion that the number of occupied defects remains negligible compared to the overall defects throughout the whole decay. Considering that the exciton densities of up to roughly 10^{14} cm^{-2} significantly exceed the reported defect densities in the range of 2×10^{10} to 3.5×10^{13} cm^{-2} for monolayer MoS_2 [21,24,25,54,55], a constant number of available or active traps only appears possible if occupied ones are rapidly depopulated again, i.e., if the trapped excitons recombine. Alternatively, the defects might function as traps irrespective of their occupation. Either way, even after catalyzing the recombination of an exciton, the defect can almost instantly function as a trap again; ergo the available or active defect density can be effectively treated as a constant.

The experimental data and the fit, as obtained from Eq. (3), match well for the monolayer flake, as shown in Fig. 5(b). We extracted a trapping rate constant of $B = 2.4 \times 10^5$ $s^{-\frac{1}{2}}$, which reflects the exciton diffusion coefficient and the trap density. Unfortunately, we are not aware of accurate measurements of exciton diffusion in mechanically exfoliated 1L MoS_2. Therefore, we estimate the exciton diffusion coefficient on the one hand to lie below the value of 3×10^{-1} cm^2 s^{-1} in WS_2 [50], where excitons are characterized by a lower effective mass than in MoS_2. On the other hand, due to higher effective carrier masses, the free carrier diffusion coefficient of 2.5×10^{-2} cm^2 s^{-1} for mono- and few-layer exfoliated MoS_2, as obtained from electrical mobility measurements on MoS_2 transistors [28,56], may be regarded as a lower limit for the excitonic value. From the range provided by these values, we estimate a trap areal density of about $n_t \approx 10^{10}$ cm^{-2}. This defect concentration lies slightly below the regime of reported values [21,24,25,54,55]. However, both diffusion and defects critically depend on experimental parameters such as the material, the sample thickness, and the preparation procedure.

Regarding the diffusion coefficient, studies on exciton and carrier diffusion in various monolayer and bulk TMDCs yielded a wide range of values. Many followed the approach

of monitoring the Gaussian width of the transient signal's spatial profile [20,27,57]. This method entails a potential major drawback, though, especially when merely a narrow wavelength regime is probed. Fluence-dependent spectral broadening effects as well as nonlinear recombination rates intrinsically cause a distortion of the initially excited Gaussian profile, drastically increasing the apparent diffusion coefficients with growing exciton density [50].

For the comparison of defect densities, similar problems arise. Generally, the amount of defects strongly varies with crystal quality and preparation method [54]. Moreover, the involvement as trapping states in the carrier or exciton dynamics may be limited to certain types of defects, representing merely a small fraction of their total number [24]. The energetic levels introduced by a defect may promote exciton recombination in particular for a certain kind of antisite or vacancy that accounts for only 1% of the overall defects [54]. This may cause the discrepancy between the trap concentration found in this work and the defect densities reported in other studies. Naturally, the multiplicity of parameters complicates the direct comparison of the obtained defect densities. Yet, the good agreement between fit and experimental data proves that the number of available defects does not change throughout the decay.

Besides the exciton diffusion, the fit additionally yields a small contribution of the exponential component around $\alpha = 7\%$ of the exciton amplitude A_0. The corresponding exponential lifetime of $\tau_X = 3.7$ ns should be regarded as no more than an indication for the rough time scale of this part of the dynamics, as the value already exceeds the observed temporal regime.

In principle, this long-living component may be attributed to trapped excitons, remaining free carriers that have not bound to form excitons, or thermal effects. In the former two cases, though, we would expect some variations of the temporal evolution of the signal with increasing pump fluence, caused by a limited availability of defects or a quadratic recombination rate equation, analogous to the bulk sample. As we do not observe this kind of fluence dependence, we exclude trapped excitons and remaining free carriers as the source of the long-term component. The latter option of thermal effects, in contrast, can indeed provide an explanation for the long-living signal. Laser irradiance is able to cause significant heating in MoS_2 monolayers, with the temperature increase depending roughly linearly on the applied excitation fluence [34]. With rising temperature, the absorption peaks are redshifted and broadened [58], causing transient signals similar to the observed ones. Finally, the heat dissipation to the substrate could happen on time scales comparable to the extracted exponential lifetime [34,59]. A detailed discussion of the impact and time regime of heating and cooling is presented in Sec. VI of the SM [36].

In total, our developed interpretation of the transient spectral signatures and their dynamics consistently describes measurements of other groups as well. Considering the work of Pogna *et al.* [22] and Vega-Mayoral *et al.* [24], their transient spectra of MoS_2 excited at 400 nm are consistent with an absorption redshift induced by localized species. On a picosecond time scale, the increased absorption peaks narrow, as explained by the thermalization of excited carriers. Afterwards, the spectra decay while retaining their shape, in agreement with our analysis of the recombination dynamics.

III. CONCLUSIONS

In this work, we conducted a comparative investigation of the transient dynamics in bulk versus monolayer MoS_2. We found the transient spectra to result from a redshift of the absorption bands based on local energy shifts in the environment of rather localized excited species. On top of that, the shifted absorption bands experience density-dependent collisional broadening due to Coulomb scattering of excited particles, especially in the monolayer.

Regarding the dynamics of the system, first, a thermalization of the excited carriers takes place on a subpicosecond time scale. In the monolayer, in addition, electrons and holes pair to form excitons in the course of this process. Second, the decay of the transient signal proceeds due to recombination processes. Here, the systematic variation of the excitation fluence allowed for the distinction between single- and multiparticle processes. In bulk MoS_2, we found a defect-assisted Auger recombination of electrons and holes, resulting in a decay rate depending superlinearly on the carrier densities. In the monolayer, on the contrary, we observed a diffusion-limited trapping of the excitons, with a linear influence of the exciton density in the rate equation.

All in all, we are able to resolve contradictions of the BGR model by introducing a localized nature of the excited species. Comparing bulk and monolayer MoS_2, we demonstrated the decisive impact of the different electronic properties, i.e., the band gap and the exciton binding energy, on the excited species dynamics. Notwithstanding, defects play an important role as trap states in the decay in thin as well as in thick flakes.

ACKNOWLEDGMENTS

The work was financially supported by the DFG via the Priority Program SPP 2102, "Light-controlled reactivity of metal complexes" (LO 714/11-1). T.V. thanks the University of Rostock for support via their Ph. D. Scholarship Program. T.K. gratefully acknowledges funding by the DFG via Grant No. KO 3612/4-1.

[1] T. Cheiwchanchamnangij and W. R. L. Lambrecht, Phys. Rev. B **85**, 205302 (2012).

[2] A. Chernikov, T. C. Berkelbach, H. M. Hill, A. Rigosi, Y. Li, O. B. Aslan, D. R. Reichman, M. S. Hybertsen, and T. F. Heinz, Phys. Rev. Lett. **113**, 076802 (2014).

[3] S. Lebègue and O. Eriksson, Phys. Rev. B **79**, 115409 (2009).

[4] D. Y. Qiu, F. H. da Jornada, and S. G. Louie, Phys. Rev. Lett. **111**, 216805 (2013).

[5] K. F. Mak, C. Lee, J. Hone, J. Shan, and T. F. Heinz, Phys. Rev. Lett. **105**, 136805 (2010).

[6] A. Splendiani, L. Sun, Y. Zhang, T. Li, J. Kim, C.-Y. Chim, G. Galli, and F. Wang, Nano Lett. **10**, 1271 (2010).
[7] K. F. Mak and J. Shan, Nat. Photonics **10**, 216 (2016).
[8] F. Withers, O. D. Pozo-Zamudio, A. Mishchenko, A. P. Rooney, A. Gholinia, K. Watanabe, T. Taniguchi, S. J. Haigh, A. K. Geim, A. I. Tartakovskii, and K. S. Novoselov, Nat. Mater. **14**, 301 (2015).
[9] H. S. Lee, S.-W. Min, Y.-G. Chang, M. K. Park, T. Nam, H. Kim, J. H. Kim, S. Ryu, and S. Im, Nano Lett. **12**, 3695 (2012).
[10] O. Lopez-Sanchez, D. Lembke, M. Kayci, A. Radenovic, and A. Kis, Nat. Nanotechnol. **8**, 497 (2013).
[11] M. Massicotte, P. Schmidt, F. Vialla, K. G. Schädler, A. Reserbat-Plantey, K. Watanabe, T. Taniguchi, K. J. Tielrooij, and F. H. L. Koppens, Nat. Nanotechnol. **11**, 42 (2015).
[12] A. Kudo and Y. Miseki, Chem. Soc. Rev. **38**, 253 (2009).
[13] D. Merki and X. Hu, Energy Environ. Sci. **4**, 3878 (2011).
[14] J. Ran, J. Zhang, J. Yu, M. Jaroniec, and S. Z. Qiao, Chem. Soc. Rev. **43**, 7787 (2014).
[15] Y. Zhu, Q. Ling, Y. Liu, H. Wang, and Y. Zhu, Phys. Chem. Chem. Phys. **17**, 933 (2015).
[16] T. Corrales-Sánchez, J. Ampurdanés, and A. Urakawa, Int. J. Hydrogen Energy **39**, 20837 (2014).
[17] M. Sarno and E. Ponticorvo, Int. J. Hydrogen Energy **44**, 4398 (2019).
[18] Y. Yu, S.-Y. Huang, Y. Li, S. N. Steinmann, W. Yang, and L. Cao, Nano Lett. **14**, 553 (2014).
[19] A. Chernikov, C. Ruppert, H. M. Hill, A. F. Rigosi, and T. F. Heinz, Nat. Photonics **9**, 466 (2015).
[20] Q. Cui, F. Ceballos, N. Kumar, and H. Zhao, ACS Nano **8**, 2970 (2014).
[21] P. D. Cunningham, K. M. McCreary, A. T. Hanbicki, M. Currie, B. T. Jonker, and L. M. Hayden, J. Phys. Chem. C **120**, 5819 (2016).
[22] E. A. A. Pogna, M. Marsili, D. De Fazio, S. Dal Conte, C. Manzoni, D. Sangalli, D. Yoon, A. Lombardo, A. C. Ferrari, A. Marini, G. Cerullo, and D. Prezzi, ACS Nano **10**, 1182 (2016).
[23] S. Sim, J. Park, J.-G. Song, C. In, Y.-S. Lee, H. Kim, and H. Choi, Phys. Rev. B **88**, 075434 (2013).
[24] V. Vega-Mayoral, T. Borzda, D. Vella, M. Prijatelj, E. A. A. Pogna, C. Backes, J. N. Coleman, G. Cerullo, D. Mihailovic, and C. Gadermaier, 2D Mater. **5**, 015011 (2017).
[25] H. Wang, C. Zhang, and F. Rana, Nano Lett. **15**, 339 (2014).
[26] H. Wang, C. Zhang, and F. Rana, Nano Lett. **15**, 8204 (2015).
[27] N. Kumar, J. He, D. He, Y. Wang, and H. Zhao, J. Appl. Phys. **113**, 133702 (2013).
[28] H. Shi, R. Yan, S. Bertolazzi, J. Brivio, B. Gao, A. Kis, D. Jena, H. G. Xing, and L. Huang, ACS Nano **7**, 1072 (2013).
[29] T. Völzer, M. Lütgens, F. Fennel, and S. Lochbrunner, J. Phys. B: At. Mol. Opt. Phys. **50**, 194003 (2017).
[30] U. Megerle, I. Pugliesi, C. Schriever, C. F. Sailer, and E. Riedle, Appl. Phys. B **96**, 215 (2009).
[31] A. Castellanos-Gomez, M. Buscema, R. Molenaar, V. Singh, L. Janssen, H. S. J. van der Zant, and G. A. Steele, 2D Mater. **1**, 011002 (2014).
[32] R. Frisenda, E. Navarro-Moratalla, P. Gant, D. P. D. Lara, P. Jarillo-Herrero, R. V. Gorbachev, and A. Castellanos-Gomez, Chem. Soc. Rev. **47**, 53 (2018).
[33] C. Hsu, R. Frisenda, R. Schmidt, A. Arora, S. M. Vasconcellos, R. Bratschitsch, H. S. J. van der Zant, and A. Castellanos-Gomez, Adv. Opt. Mater. **7**, 1900239 (2019).
[34] G. Plechinger, A. Castellanos-Gomez, M. Buscema, H. S. J. van der Zant, G. A. Steele, A. Kuc, T. Heine, C. Schüller, and T. Korn, 2D Mater. **2**, 015006 (2015).
[35] N. S. Taghavi, P. Gant, P. Huang, L. Niehues, R. Schmidt, S. M. de Vasconcellos, R. Bratschitsch, M. Garcá-Hernández, R. Frisenda, and A. Castellanos-Gomez, Nano Res. **12**, 1691 (2019).
[36] See Supplemental Material at http://link.aps.org/supplemental/10.1103/PhysRevB.103.045423 for sample preparation and characterization, details on the pump-probe setup, peak fitting, and a discussion of thermal effects on the transient spectra.
[37] K. P. Dhakal, D. L. Duong, J. Lee, H. Nam, M. Kim, M. Kan, Y. H. Lee, and J. Kim, Nanoscale **6**, 13028 (2014).
[38] R. Gillen and J. Maultzsch, IEEE J. Sel. Top. Quantum Electron. **23**, 219 (2017).
[39] P. Hein, A. Stange, K. Hanff, L. X. Yang, G. Rohde, K. Rossnagel, and M. Bauer, Phys. Rev. B **94**, 205406 (2016).
[40] Y. Li, J. Shi, Y. Mi, X. Sui, H. Xu, and X. Liu, J. Mater. Chem. C **7**, 4304 (2019).
[41] M. M. Ugeda, A. J. Bradley, S.-F. Shi, F. H. da Jornada, Y. Zhang, D. Y. Qiu, W. Ruan, S.-K. Mo, Z. Hussain, Z.-X. Shen, F. Wang, S. G. Louie, and M. F. Crommie, Nat. Mater. **13**, 1091 (2014).
[42] A. Steinhoff, M. Rösner, F. Jahnke, T. O. Wehling, and C. Gies, Nano Lett. **14**, 3743 (2014).
[43] T. Holstein, Ann. Phys. **8**, 325 (1959).
[44] M. Kang, S. W. Jung, W. J. Shin, Y. Sohn, S. H. Ryu, T. K. Kim, M. Hoesch, and K. S. Kim, Nat. Mater. **17**, 676 (2018).
[45] A. Thilagam, Physica B Condens. Matter **464**, 44 (2015).
[46] Z. Nie, R. Long, L. Sun, C. Huang, J. Zhang, Q. Xiong, D. W. Hewak, Z. Shen, O. Prezhdo, and Z. Loh, ACS Nano **8**, 10931 (2014).
[47] R. Wallauer, J. Reimann, N. Armbrust, J. Güdde, and U. Höfer, Appl. Phys. Lett. **109**, 162102 (2016).
[48] P. Steinleitner, P. Merkl, P. Nagler, J. Mornhinweg, C. Schüller, T. Korn, A. Chernikov, and R. Huber, Nano Lett. **17**, 1455 (2017).
[49] Y. Li, J. Shi, H. Chen, R. Wang, Y. Mi, C. Zhang, W. Du, S. Zhang, Z. Liu, Q. Zhang, X. Qiu, H. Xu, W. Liu, Y. Liu, and X. Liu, Nanoscale **10**, 17585 (2018).
[50] M. Kulig, J. Zipfel, P. Nagler, S. Blanter, C. Schüller, T. Korn, N. Paradiso, M. M. Glazov, and A. Chernikov, Phys. Rev. Lett. **120**, 207401 (2018).
[51] A. Singh, G. Moody, K. Tran, M. E. Scott, V. Overbeck, G. Berghäuser, J. Schaibley, E. J. Seifert, D. Pleskot, N. M. Gabor, J. Yan, D. G. Mandrus, M. Richter, E. Malic, X. Xu, and X. Li, Phys. Rev. B **93**, 041401(R) (2016).
[52] P. Grassberger and I. Procaccia, J. Chem. Phys. **77**, 6281 (1982).
[53] R. F. Kayser and J. B. Hubbard, Phys. Rev. Lett. **51**, 79 (1983).
[54] J. Hong, Z. Hu, M. Probert, K. Li, D. Lv, X. Yang, L. Gu, N. Mao, Q. Feng, L. Xie, J. Zhang, D. Wu, Z. Zhang, C. Jin, W. Ji, X. Zhang, J. Yuan, and Z. Zhang, Nat. Commun. **6**, 6293 (2015).
[55] H. Y. Jeong, S. Y. Lee, T. H. Ly, G. H. Han, H. Kim, H. Nam, Z. Jiong, B. G. Shin, S. J. Yun, J. Kim, U. J. Kim, S. Hwang, and Y. H. Lee, ACS Nano **10**, 770 (2016).
[56] B. Radisavljevic, A. Radenovic, J. Brivio, V. Giacometti, and A. Kis, Nat. Nanotechnol. **6**, 147 (2011).

[57] N. Kumar, Q. Cui, F. Ceballos, D. He, Y. Wang, and H. Zhao, Nanoscale **6**, 4915 (2014).

[58] E. Yalon, O. B. Aslan, K. K. H. Smithe, C. J. McClellan, S. V. Suryavanshi, F. Xiong, A. Sood, C. M Neumann, X. Xu, K. E. Goodson, T. F. Heinz, and E. Pop, ACS Appl. Mater. Interfaces **9**, 43013 (2017).

[59] S. V. Suryavanshi, A. J. Gabourie, A. B. Farimani, and E. Pop, J. Appl. Phys. **126**, 055107 (2019).

Supplementary Information

Fluence-dependent Dynamics of Localized Excited Species in Monolayer versus Bulk MoS_2

Tim Völzer, Franziska Fennel, Tobias Korn, and Stefan Lochbrunner

Content:

I. Preparation and microscopy of suitable samples

We prepared atomically thin films of molybdenum disulfide (MoS_2), using the exfoliation technique introduced by Castellanos-Gomez *et al.*[1] Using a customary adhesive tape, we separated sub-millimeter films from a thick crystal of MoS_2 (SPI Suppliers). A further, successive reduction of the flakes' thickness is achieved by repeated transfer to and between pieces of a tape with lower adhesive force (SPV 224PR-M, Nitto Denko Corporation). Finally, the flakes are transferred to an optically transparent polymethylsiloxane (PDMS) film (PF-30-X4 6.5 mil, Gel-Pak), suitable for spectroscopy.

Figure S 1 comprises the transmission micrographs of several flakes of MoS_2, showing different colors depending on their thickness. The green shade of the area in a) indicates a bulk-like crystal of several 10 nm vertical extent.[2] For the pale crystal in b), we suppose a much smaller thickness in the few-layer regime.

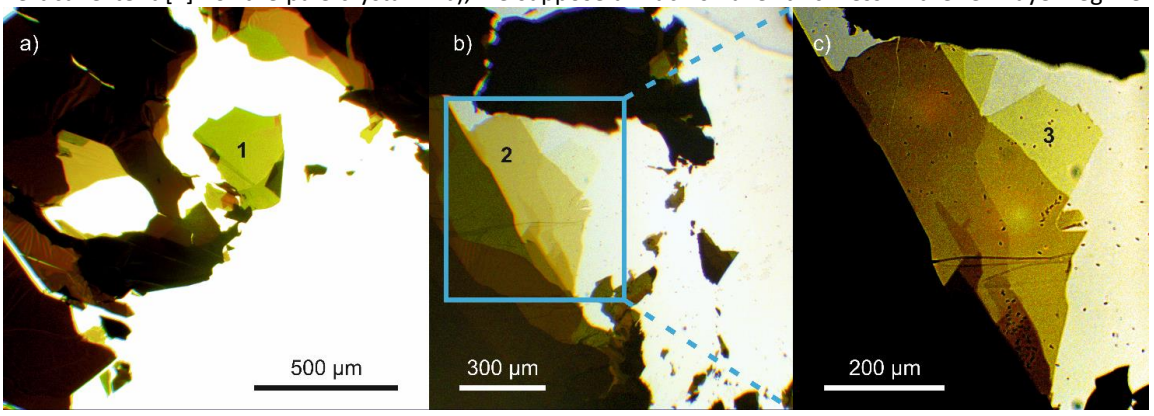

Figure S 1: Micrographs of MoS_2 flakes with different thicknesses. (a) Green bulk crystal area (1) (b) Pale few-layer sample (2) with terrace-like adjacent flakes. The blue frame marks the area depicted in (c). (c) Contrast-enhanced image of the few-layer, revealing adjoining, even thinner monolayer regions (3).

When enhancing the contrast of this picture (see part c)), we find an even thinner region that turned out to consist of a single TMDC layer, as presented in the following section.

II. Thickness determination

To obtain the thickness of the thinnest flake, we applied a simple optical approach, using the blue color channel of microscopic images to determine the blue light transmission of the MoS_2 film (**Figure S 2** (a) and (b)). We obtained a transmission of roughly 90 % relative to the surrounding areas of bare substrate, which indeed corresponds to a monolayer of MoS_2.[3-5] Additionally, we took photoluminescence (PL) images of the respective area with a fluorescence lifetime imaging microscope (MicroTime 200, PicoQuant), as depicted in **Figure S 2** (c). Due to the uniquely strong luminescence of the monolayer compared to thicker crystals,[6,7] the 1L-flake stands out clearly against the dark bulk and few-layer domains in its vicinity. Furthermore, we identify a weakly glowing bilayer region in the top left of the PL images, which represents an intermediate situation, in accordance with the well-known PL behavior of these materials.

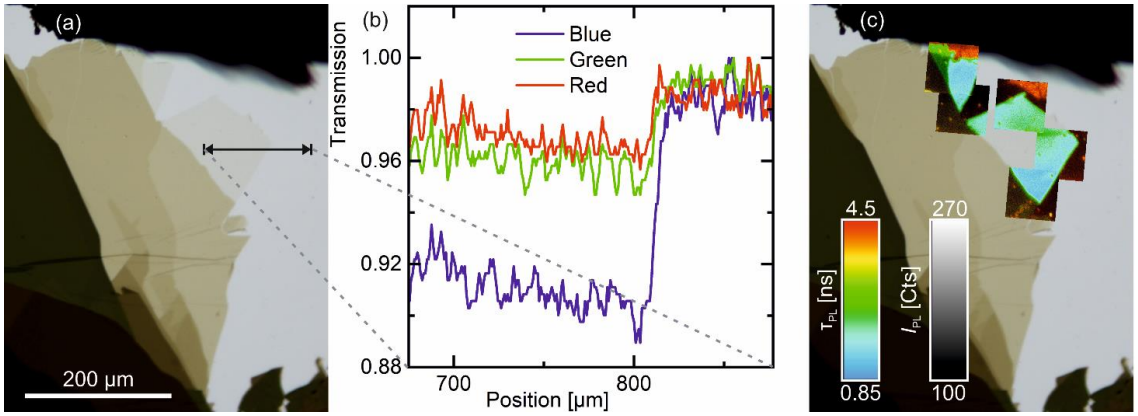

Figure S 2: Identification of monolayer flake: (a) White balanced micrograph of the area of interest: The double arrow marks the pixels evaluated in (b). (b) Color channel-separated intensity transmission along the axis indicated in (a): The sudden fall around pixel 925 corresponds to the crystal edge and amounts to roughly 0.1 for the blue channel. (c) Micrograph of the flake overlayed with PL images: Brightness corresponds to PL intensity, while the color indicates the averaged lifetime. The 1L-flake clearly contrasts to its substrate and few-layer environment. Next to a second monolayer top left from the first one, we observe a weakly luminescent region, thus characterizing it as a bilayer.

For the bulk, in contrast, an optical determination of the thickness appears difficult, as no measurable PL occurs and the absorption mixes with scattering and reflective losses. On top of that, due to thickness-dependent band structure changes, even the pure absorption of bulk and monolayer is not directly scalable. Hence, we constrain the analysis to a rough estimate of the crystal thickness. An upper limit can be deduced from interference patterns in a wavelength range beyond the absorption regime,[2] which occur most prominently for samples with a height of 100-200 nm. From the absence of these signatures for the investigated flake, we can conclude a thickness of less than 40 nm. As a lower limit, amplitude and width of the C-peak for the bulk compared to the monolayer suggest a thickness for the former of more than 10 nm.

III. Pump-probe setup with probe referencing

The applied pump-probe setup mostly follows the standard approach to this technique,[8] featuring excitation at 400 nm and probing over the whole visible range. To that end, fundamental pulses of 300 µJ energy with a center wavelength of 800 nm and a pulse length of 50 fs, originating from a Ti:sapphire amplifier (Spitfire PRO, Spectra Physics) operating at a repetition rate of 1 kHz, are split up into two beams. The first one is frequency-doubled in a beta barium borate crystal to obtain 400 nm pump pulses. The remaining fundamental light is blocked by a filter and the pump power is tuned using a combination of

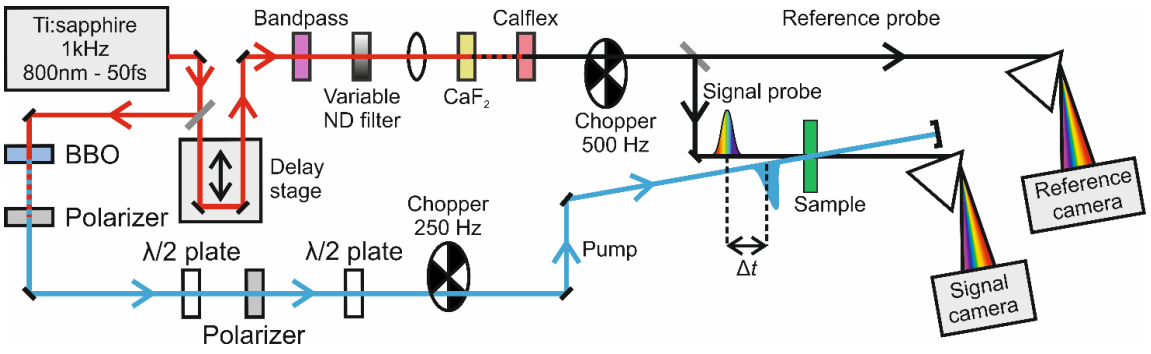

Figure S 3: Setup for optical pump-probe spectroscopy: Red, blue, and black lines represent the beam paths for the 800 nm fundamental, the 400 nm second harmonic and the white light. Dichromatically dashed lines show the simultaneous presence of two different spectral components. Focusing mirrors are omitted for simplicity.

polarizers and half-wave plates, yielding pulses with horizontal polarization and energies from 1 to 64 nJ. The second part of the near-infrared light is delayed via a motorized linear delay stage and focused into a calcium fluoride crystal, where self-focusing and self-phase modulation result in supercontinuum generation. Here, again, the fundamental light around 800 nm is filtered out.

At this point, modifications to the standard setup come into play. In the probe and the pump beam, two choppers instead of one run at one half and one quarter of the laser repetition rate, respectively, creating a four-pulse sequence. This allows for a real-time monitoring of the excitation stray light. Behind the chopper, the probe is split again: One fraction of the white light is detected as a reference to keep track of spectral intensity fluctuations of the supercontinuum. The remaining fraction is focused onto the sample, together with the pump. Here, the $1/e^2$-diameters of pump and probe spot at the sample position amount to 170 µm and 65 µm, respectively. Behind the sample, the transmitted probe light is dispersed by a fused silica prism and detected spectrally resolved by an array detector. The resulting signal spectra are related to the simultaneously acquired reference spectra to eradicate fluctuations of the probe light, before being processed to yield the transient spectra in terms of the pump-induced change in absorbance.

IV. Fitting of A- and B-peaks in the transient spectra

As discussed in the main body, section II. B., we globally fitted the transient spectra in the spectral region of the A- and B-peaks to distinguish between a broadening, a shift and a shrinkage of the positive peaks, as the excited species recombine. This leads to the distinction between the BGR model, where the peak areas should remain constant and their positions shift in dependence of the excited particle density, and the local model, where the number density of the excited species only influences the peak area, while the spectral magnitude of the shift is left unchanged.

As we are not aware of any analytical line shape function that accurately describes the A- and B-absorption bands in bulk and 1L-MoS_2, we implemented both Lorentzian $L(E)$ and Gaussian $G(E)$ profiles to simultaneously test the influence of changes in the peak shape. We used the following functions:

$$L(E) = \frac{A_L \cdot w_L}{(E - E_0)^2 + {w_L}^2}$$

$$G(E) = a_G \cdot e^{-\frac{2(E-E_0)^2}{{w_G}^2}}$$

With the energy value of the peak position E_0, the Lorentzian and Gaussian widths w_L and w_G, respectively, as well as the Lorentz peak area A_L and the Gaussian amplitude a_G. As a measure for the Gaussian peak area, we multiplied width and amplitude to obtain $A_G = a_G \cdot w_G$. Fitting four separate peaks, we obtain a total of twelve free parameters. However, as the TA spectra originate from the photoinduced shift of absorption

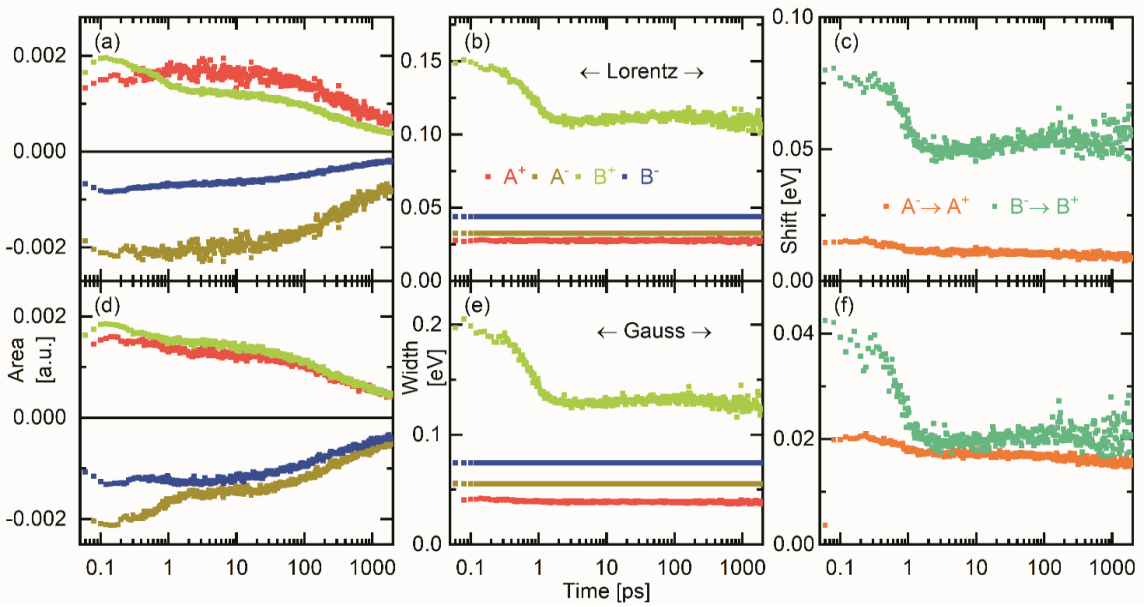

Figure S 4: Lorentzian (Top row) and Gaussian (Bottom row) peak fitting of the transient spectra for the bulk sample excited at a fluence of 31 $\mu J/cm^2$. (a,d) Fitted peak area for the $A^{\pm}$- and $B^{\pm}$-contributions over time. All curves distinctly decay over time with similar shapes for each pair of a positive and a negative peak. Yet, the exact temporal evolution differs between the peak pairs as well as between the two implemented line shapes. (b,e) Fitted peak width for the $A^{\pm}$- and $B^{\pm}$-contributions over time. The negative peaks remain constant by definition. The A^+-feature exhibits no dynamics as well, while the B^+-width falls within the first few ps and levels afterwards. Again, the exact values vary between the two peak functions. (c,f) Shift in position from negative to positive peak of each pair. A reduction of the shifts takes place around 1 ps after which they remain unchanged for the rest of the investigated time span. Still, the results for Lorentzian and Gaussian profiles differ quantitatively.

bands, the negative peaks merely describe the lacking original static absorption. Consequently, we manually extracted the center positions and full widths at half maximum of the static absorption peaks from **Figure 1**, yielding the following parameter values.

Bulk	**Monolayer**
$E_{0,A^-} = 1.880$ eV	$E_{0,A^-} = 1.926$ eV
$w_{L,A^-} = 32.5$ meV	$w_{L,A^-} = 18.8$ meV
$w_{G,A^-} = 55.2$ meV	$w_{G,A^-} = 31.9$ meV
$E_{0,B^-} = 2.084$ eV	$E_{0,B^-} = 2.072$ eV
$w_{L,B^-} = 43.7$ meV	$w_{L,B^-} = 36.0$ meV
$w_{G,B^-} = 74.3$ meV	$w_{G,B^-} = 61.1$ meV

With this reduction to eight free parameters, we obtain more stable fits and clearer results.

The parameters extracted from the bulk spectra for a low excitation fluence are depicted in **Figure S 4**. When comparing the temporal evolution of the peak area and the shift, *i.e.* the position difference between negative and positive peak of a pair, both of which can in principle cause a signal reduction, we clearly find that the long-term decay is determined by the shrinkage of the peak areas. The shift, on the contrary, does not change throughout the decay, except for a decrease in the time regime around 1 ps that occurs most prominently for the B-pair. Simultaneously, the B^+-feature narrows significantly. Due to the similar time scale, we associate these processes to the cooling of the excited carriers. Hot carriers cause a stronger collisional

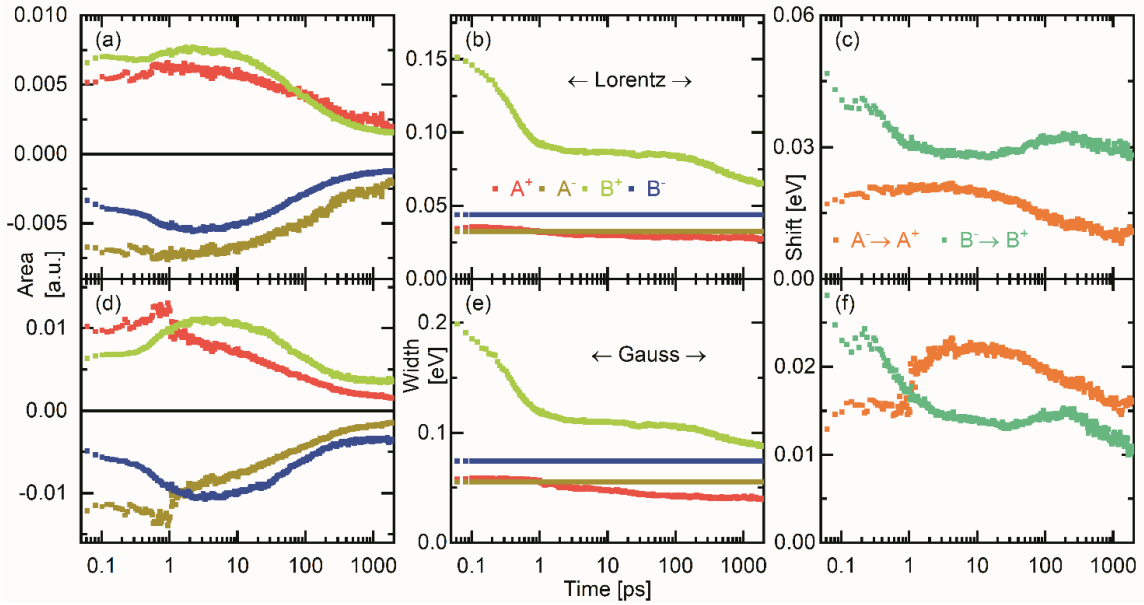

Figure S 6: Lorentzian (Top row) and Gaussian (Bottom row) peak fitting on transient spectra for the bulk sample excited at a fluence of 490 $\mu J/cm^2$. (a,d) Fitted peak area for the $A^{\pm}$- and $B^{\pm}$-contributions over time. All curves distinctly decay over time with similar shapes for each pair of a positive and a negative peak. Yet, the exact temporal evolution differs between the peak pairs as well as between the two implemented line shapes. (b,e) Fitted peak width for the $A^{\pm}$- and $B^{\pm}$-contributions over time. The negative peaks remain constant by definition. The A^+-feature narrows slightly, predominantly during the first few ps, while the B^+-width falls drastically within this time span, then levels and slowly decreases afterwards. Again, the exact values vary between the two peak functions. (c,f) Shift in position from negative to positive peak of each pair. A notable change of the shifts takes place within the first few picoseconds after which only weak dynamics follow for the rest of the investigated time span. Still, the results for Lorentzian and Gaussian profiles differ quantitatively.

broadening and, following from their high energy, may influence the local charge distribution and band levels more heavily than cooled ones.

The comparison of the results obtained from Lorentzian versus Gaussian peak fitting yields a good qualitative agreement between both line shapes. All aforementioned points equally apply in both cases. Nevertheless, absolute values of the shifts differ, as do the exact time traces of the peak areas. The latter even differ when

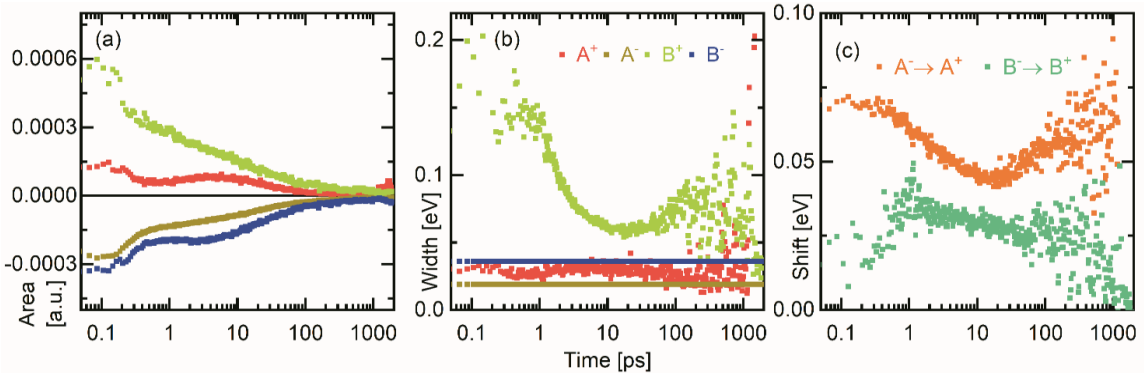

Figure S 5: Lorentzian peak fitting on transient spectra for the monolayer sample excited at a fluence of 31 $\mu J/cm^2$. (a) Fitted peak area for the $A^{\pm}$- and $B^{\pm}$-contributions over time. All curves decay almost to zero over time with a significant shrinkage during the first picosecond. Yet, the exact temporal evolution differs between the various peaks. (b) Fitted peak width for the $A^{\pm}$- and $B^{\pm}$-contributions over time. The negative peaks remain constant by definition. The A^+-feature exhibits no dynamics as well, while the B^+-width falls drastically within several picoseconds, then levels and spreads heavily, as the signal fades into the noise. (c) Shift in position from negative to positive peak of each pair. Despite the nearly vanishing transient signal between a few and a hundred picoseconds, the shifts do not approach zero but only fall slightly before being outweighed by the dramatically increasing noise.

comparing the A- and B-pair. We conclude that our fits result in reproducible qualitative results, while exact numbers or the precise temporal evolution depend crucially on the actual line shape of those peaks, which we do not know. Hence, a quantitative analysis of the peak areas cannot be conducted. Still, the constant width and peak shift at times beyond a few ps demonstrate that the amplitude accurately represents the true signal strength.

At higher excitation fluences, as shown in **Figure S 6**, the same tendency as for weak excitation is found, despite the findings being less clear. The decay of the peak area continues to dominate the signal dynamics, although the spectral shift experiences an - albeit weaker - reduction as well. We suppose this results from the fact that we do not know the exact line shape. The broader the peaks become with higher excitation density, the more sensitive the parameters react to slight inaccuracies of the input line shape function.

In the monolayer, already at low fluences, this effect interferes even stronger, especially at short times, where changes in the broadening determine the dynamics. On the long-term, however, the signal strength has decayed so far that the noise of the parameters dramatically increases, see **Figure S 5**. Nevertheless, we observe that while the peak areas drop to almost zero within a few 100 ps, the shift does not, which again confirms a rather localized picture of the excited species. Note that the thermal effects discussed in section VI. would result in a shifted absorption as well, but with the shift not the peak area decaying, as the sample cools down over time, analog to the BGR model. Hence, our results point to the presence of localized carriers

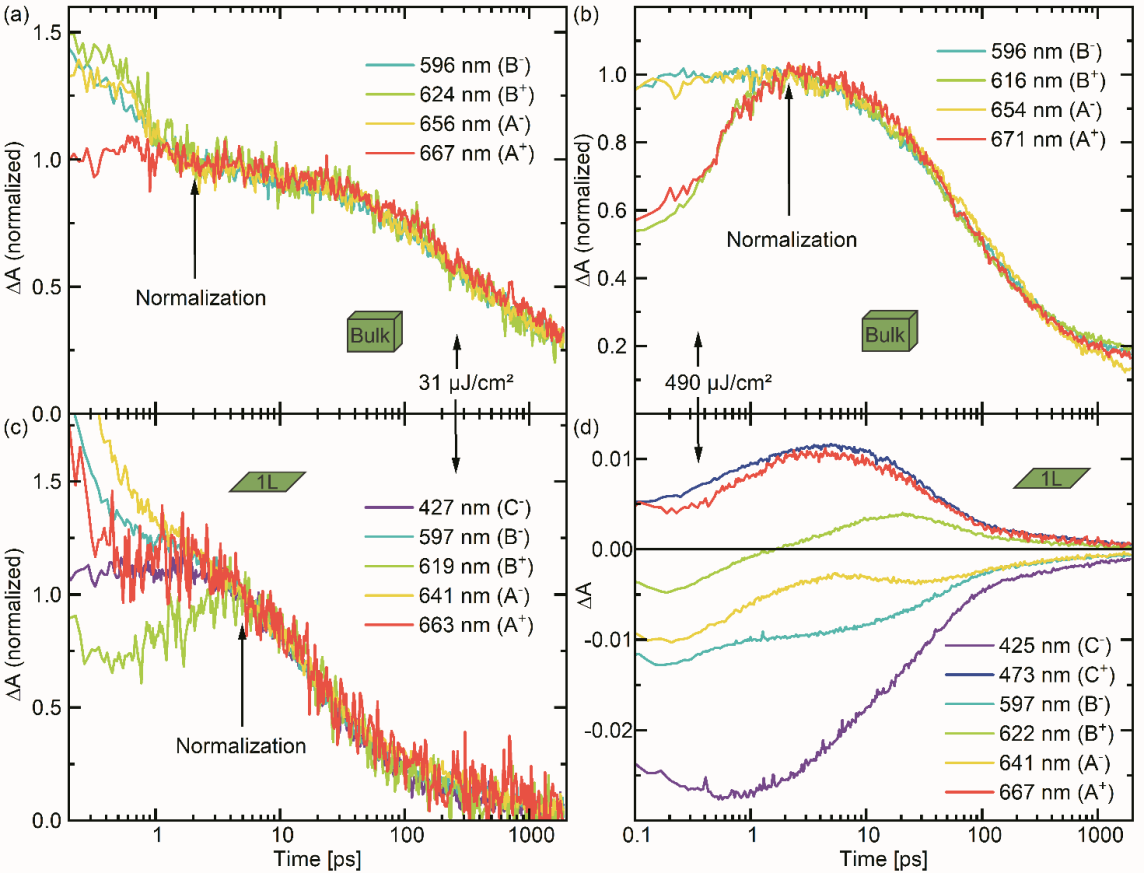

Figure S 7: Decay dynamics at different characteristic wavelengths for excitation fluences of $31\ \mu J/cm^2$ (left) and $490\ \mu J/cm^2$ (right) in the bulk (top) and monolayer (bottom). (a)-(c) Normalized time traces: The respective time point used for the normalization is marked by an arrow. In (a) and (b), from that point on, the curves are virtually identical. In (c), the shapes of the curves likewise exhibit a striking similarity. (d) Original time traces: The traces are obviously dissimilar, ergo we refrain from a normalization in this case.

or excitons, respectively. For higher fluences in the monolayer, the fits became instable due to the enormous broadening and the superposition of the B-peaks with the low-energy tail of the C^+-feature, such that we were not able to extract any meaningful parameters from those data.

V. Signal decay at different wavelengths

Comparing the dynamics at different points of the spectrum may provide information about potential different origins of the various peaks. For the bulk sample, after the initial thermalization, the decay of the $A^{\pm}$- and $B^{\pm}$-peaks proceeds identically, in the case of low as well as high fluences, as **Figure S 7** (a) and (b) show. Thus, the dynamics of the whole spectrum appears to be directly related to the population of the excited species, namely the excited carrier density. For the monolayer (**Figure S 7** (c) and (d)), variations between the curves at different probe wavelengths occur already at low intensities. At high values, finally, the dynamics are completely dissimilar. Here, the ever-changing broadening and overlap of the different peaks creates nonlinear dependences of the signal on the exciton density. Nevertheless, we expect the exciton density to be the dominant driving force for all these effects. To evaluate the dynamics of the latter, we focus on the C^--peak, since it is rather isolated and sufficiently broad to experience merely a weak influence of further broadening and overlap effects.

VI. Thermal contributions to the transient signal

With respect to the long-term contribution to the transient signal, we discussed heating effects in section II. D. Indeed, an increased temperature results in a red-shift and broadening of the static absorption peaks.[9] In the transient spectra, this would yield an alternating sequence of positive and negative peaks, similar to the major signal contribution, as discussed in section II. D. In order to check this, we globally fitted the whole spectral evolution for the highest excitation fluence in terms of equation (3). However, as suggested by the fundamentally different time traces in **Figure S 7** (d), broadening adds further dynamics that cannot be described by the two discussed components. Nevertheless, to separate short- and long-term contributions, we assign the time constants for stretched and simple exponential decay the values obtained from the monochromatic fit from section II. D. and compute the corresponding amplitude spectra, as displayed in **Figure S 8** (blue: diffusion-driven contribution, red: thermal contribution). The resulting fitted time traces

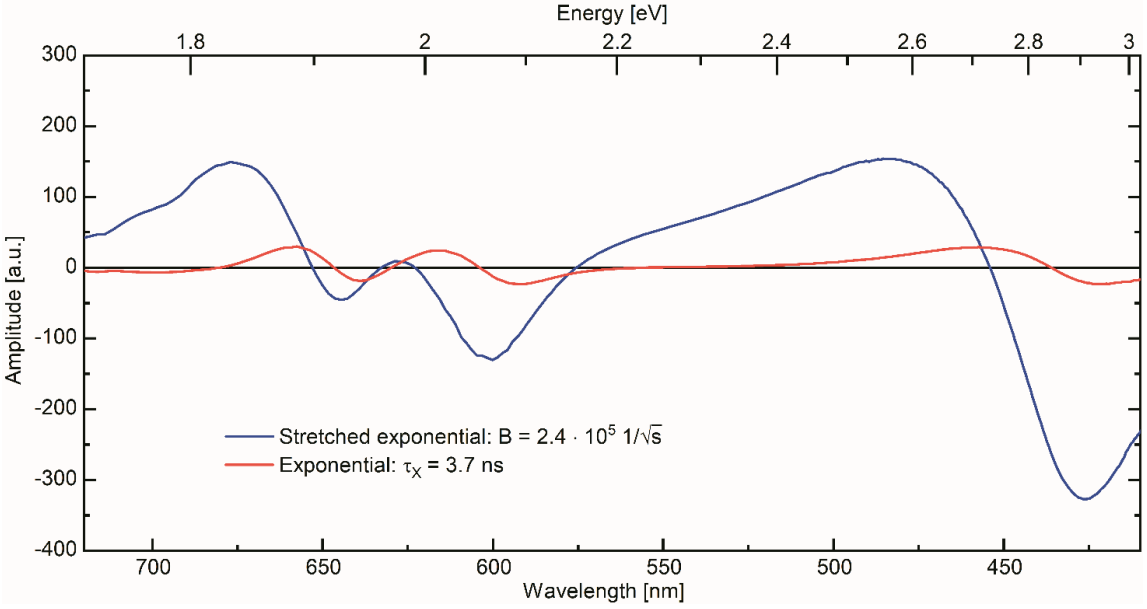

Figure S 8: Fitted amplitude spectra of the diffusive (blue line) and exponential part (red line) of the signal decay for an excitation fluence of $490\ \mu J/cm^2$. The two spectra show a similar scheme of alternating peaks, with a notable relative shift of most features.

resemble the characteristic features of the temporal evolution of the experimental spectra. Yet, in the range of and especially between the $A^{\pm}$- and $B^{\pm}$-peaks, where spectral broadening strongly influences the transient signal, the fit strongly deviates from the data, since neither of the two decay components can account for the strong broadening effects. Nevertheless, we obtain qualitative results for the spectral signatures of the two decays. In fact, the amplitude spectrum corresponding to the long-living component at a fluence of $490\ \mu J/cm^2$ consists of the discussed alternating features, as depicted in **Figure S 8** (red line). Given that at 427 nm, peak broadening and superposition effects should be weak and the exponential amplitude is small compared to the overall signal, we expect a more or less linear influence of a temperature change on the transient signal in this wavelength region. Likewise, a linear rise in temperature with increasing fluence appears reasonable in a moderate heating range.[3] All in all, a potential thermal contribution to the signal would be approximately proportional to the incoming excitation fluence, as we observed in section II. C. and D.

In the following, we discuss whether the observed amplitude and time scale are compatible with a thermal effect. To generate a considerable transient amplitude, the sample has to experience a notable rise in temperature due to the pump pulse and a thermal relaxation on the nanosecond time scale. Indeed, laser irradiance can cause significant heating, as demonstrated in a continuous wave (cw) experiment with a pump wavelength of 532 nm.[3] Here, a MoS_2 monolayer on a PDMS substrate was heated by 54 K above ambient conditions when irradiated with an intensity $I_{\mathrm{rad}} = 2 \cdot 10^9 \frac{\mathrm{W}}{\mathrm{m}^2}$. Considering an absorption coefficient of roughly 0.1 at this wavelength, this corresponds to an absorbed intensity of $I_{\mathrm{heat}} = 2 \cdot 10^8 \frac{\mathrm{W}}{\mathrm{m}^2}$. In the thermal equilibrium, the heat intensity has to be fully compensated by cooling. Since black body radiation merely accounts for a negligible emission in the order of some $10^2 \frac{\mathrm{W}}{\mathrm{m}^2}$ at these conditions, the sample temperature is determined entirely by the heat diffusion to the environment. Equating the absorbed intensity I_{heat} with the heat flow $\dot{q} = U \cdot \Delta T$ out of the sample yields a thermal conductance of $U = 4 \cdot 10^6 \frac{\mathrm{W}}{\mathrm{m}^2 \cdot \mathrm{K}}$ from the 1L-MoS_2 to the PDMS substrate (and air environment) in the case of a quasi-static equilibrium.

In our experiments, in contrast, a rather dynamical situation is encountered. While the pump pulse itself primarily excites electrons and does not alter the crystal temperature, the excitation energy still dissipates into heat during the thermalization, exciton formation as well as trapping and recombination, all of which are essentially finished after about 100 ps. Hereby, enormous intensities may occur, compared to the cw case, with even the time-averaged heat fluxes ranging from below $10^9 \frac{\mathrm{W}}{\mathrm{m}^2}$ for the lowest fluence up to several $10^{10} \frac{\mathrm{W}}{\mathrm{m}^2}$ for the strongest excitation. Still, this does not automatically lead to correspondingly high temperatures for the following reasons: First, the sample itself takes some time to heat up. Second, as even the adjacent part of the PDMS substrate starts at room temperature, the initially high temperature gradient mediates a drastically faster heat diffusion than in the equilibrium case. Thereby, extreme temperatures causing thermal damaging of the sample are avoided. Accordingly, no sample damage was observed in the experiments, even at the highest excitation levels. After the dissipation of the excitation energy is completed, the temporal evolution of the crystal temperature is determined by the heat flow from sample to environment. If the thermal conductance U as well as the specific heat capacity c and density ρ of the monolayer are approximately constant, an exponential decay of the time-dependent temperature difference $\Delta T(t)$ between sample and ambient environment follows:

$$\Delta T(t) \cdot U = \dot{q} = -\Delta \dot{T}(t) \cdot c_{\mathrm{MoS_2}} \cdot \rho_{\mathrm{MoS_2}} \cdot d_{\mathrm{1L}}$$

$$\rightarrow \Delta T(t) = e^{-\beta \cdot t}; \quad \beta = \frac{U}{c_{\mathrm{MoS_2}} \cdot \rho_{\mathrm{MoS_2}} \cdot d_{\mathrm{1L}}}$$

With the heat capacity $c_{MoS_2} = 380 \frac{J}{kg \cdot K}$ for monolayer MoS_2,[10] the bulk density $\rho_{MoS_2} = 5060 \frac{kg}{m^3}$ and the height for one monolayer in the bulk crystal $d_{1L} = 6.15$ Å, the product of the latter two yielding the area mass density of one monolayer.

For the above mentioned thermal conductance $U = 4 \cdot 10^6 \frac{W}{m^2 \cdot K}$ from the cw experiment, a time constant of $\tau = \frac{1}{\beta} \approx 300$ ps is calculated, whereas for instantaneously heated 1L-MoS_2 on SiO_2, even shorter lifetimes around 100 ps have been simulated.[10] In contrast to the latter, the heating proceeds over a certain time span in this work, allowing the temperature profile to flatten and broaden, which successively slows down the temperature fall. While in the former, quasi-stationary cw case, this effect is balanced by the constant heating of the monolayer, our experiments are lacking such a compensation. For that reason, the cooling process is further prolonged over time. On the one hand, this may close the gap between the 300 ps time constant discussed above and the decay time of 3.7 ns, as obtained from the monochromatic fit in section II. D. On the other hand, it demonstrates the complexity of the cooling dynamics, which are at most roughly estimated by an exponential function. A precise model would have to include a detailed simulation of the heat diffusion process.

Concluding, our considerations provide evidence for temperature effects as the origin of the long-living transient component. The corresponding signatures match the thermal shift and broadening of the static spectrum. Moreover, we showed that the pump light can cause significant sample heating, while the cooling time constant is expected to be in rough agreement with the fitted parameters.

VII. References

[1] A. Castellanos-Gomez, M. Buscema, R. Molenaar, V. Singh, L. Janssen, H. S. J. van der Zant, and G. A. Steele, *2D Mater.* **1**, 011002 (2014).

[2] T. Völzer, M. Lütgens, F. Fennel, and S. Lochbrunner, *J. Phys. B: At., Mol. Opt. Phys.* **50**, 194003 (2017).

[3] G. Plechinger, A. Castellanos-Gomez, M. Buscema, H. S. J. van der Zant, G. A. Steele, A. Kuc, T. Heine, C. Schüller, and T. Korn, *2D Mater.* **2**, 015006 (2015).

[4] C. Hsu, R. Frisenda, R. Schmidt, A. Arora, S. M. Vasconcellos, R. Bratschitsch, H. S. J. van der Zant, and A. Castellanos-Gomez, *Adv. Opt. Mater.*, 1900239 (2019).

[5] N. S. Taghavi, P. Gant, P. Huang, I. Niehues, R. Schmidt, S. M. de Vasconcellos, R. Bratschitsch, M. Garcá-Hernández, R. Frisenda, and A. Castellanos-Gomez, A. *Nano Res.* **12**, 1691–1695 (2019).

[6] A. Splendiani, L. Sun, Y. Zhang, T. Li, J. Kim, C.-Y. Chim, G. Galli, and F. Wang, *Nano Lett.* **10**, 1271–1275 (2010).

[7] K.F. Mak, C. Lee, J. Hone, J. Shan, and T. F. Heinz, T. F. *Phys. Rev. Lett.* **105**, 136805 (2010).

[8] U. Megerle, I. Pugliesi, C. Schriever, C. F. Sailer, and E. Riedle, *Appl. Phys. B* **96**, 215–231 (2009).

[9] E. Yalon, O. B. Aslan, K. K. H. Smithe, C. J. McClellan, S. V. Suryavanshi, F. Xiong, A. Sood, C. M. Neumann, X. Xu, K. E. Goodson, T. F. Heinz, and E. Pop, *ACS Appl. Mater. Interfaces* **9**, 43013–43020 (2017).

[10] S. V. Suryavanshi, A. J. Gabourie, A. B. Farimani, and E. Pop, *J. Appl. Phys.* **126**, 055107 (2019).

[P2]

Strong quenching of dye fluorescence in monomeric perylene orange/TMDC hybrid structures

Tim Völzer, Alina Schubert, Erik von der Oelsnitz, Julian Schröer, Ingo Barke, Rico Schwartz, Kenji Watanabe, Takashi Taniguchi, Sylvia Speller, Tobias Korn, and Stefan Lochbrunner

Nanoscale Advances 2023, **5**, 3348

https://doi.org/10.1039/D3NA00276D

Reprinted from *Nanoscale Advances* 2023, **5**, 3348.

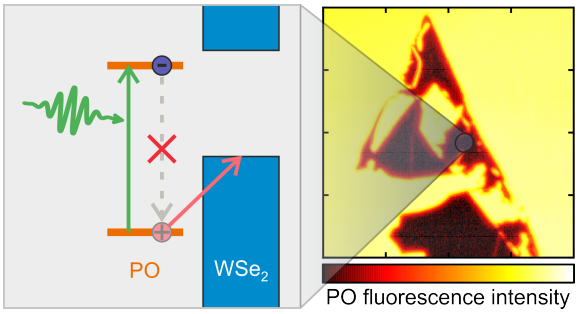

Nanoscale Advances

ROYAL SOCIETY OF CHEMISTRY

PAPER

View Article Online
View Journal | View Issue

Cite this: *Nanoscale Adv.*, 2023, **5**, 3348

Strong quenching of dye fluorescence in monomeric perylene orange/TMDC hybrid structures†

Tim Völzer, [ab] Alina Schubert, [ab] Erik von der Oelsnitz,[ab] Julian Schröer, [ab] Ingo Barke,[ab] Rico Schwartz,[a] Kenji Watanabe, [c] Takashi Taniguchi,[d] Sylvia Speller,[ab] Tobias Korn [ab] and Stefan Lochbrunner *[ab]

Hybrid structures with an interface between two different materials with properly aligned energy levels facilitate photo-induced charge separation to be exploited in optoelectronic applications. Particularly, the combination of 2D transition metal dichalcogenides (TMDCs) and dye molecules offers strong light–matter interaction, tailorable band level alignments, and high fluorescence quantum yields. In this work, we aim at the charge or energy transfer-related quenching of the fluorescence of the dye perylene orange (PO) when isolated molecules are brought onto monolayer TMDCs *via* thermal vapor deposition. Here, micro-photoluminescence spectroscopy revealed a strong intensity drop of the PO fluorescence. For the TMDC emission, in contrast, we observed a relative growth of the trion *versus* exciton contribution. In addition, fluorescence imaging lifetime microscopy quantified the intensity quenching to a factor of about 10^3 and demonstrated a drastic lifetime reduction from 3 ns to values much shorter than the 100 ps width of the instrument response function. From the ratio of the intensity quenching that is attributed to hole or energy transfer from dye to semiconductor, we deduce a time constant of several picoseconds at most, pointing to an efficient charge separation suitable for optoelectronic devices.

Received 25th April 2023
Accepted 22nd May 2023

DOI: 10.1039/d3na00276d

rsc.li/nanoscale-advances

1. Introduction

In the past decade, transition metal dichalcogenides (TMDCs) have emerged as 2D semiconductors. The key features of these materials are the transition from indirect to direct semiconductors, which is accompanied by the emergence of their photoluminescence,[1,2] as well as a drastic rise of the exciton binding energy when thinned down from bulk to a monolayer (1L).[3] This shifts the recombination dynamics from the regime of Auger scattering of free carriers to being governed by the diffusion of excitons.[4,5] In combination with the strong light–matter interaction, these monolayer properties promise potential applications in photonics and optoelectronics ranging from LEDs to photodetectors.[6] In the latter case, charge separation and transfer following optical excitation can be facilitated by the fabrication of heterostructures, where 1L-TMDCs are combined with one another,[7,8] other 2D semiconductors,[9] graphene,[10] or hybrid structures with 0D objects such as small molecules or quantum dots, 1D nanostructures, as well as 3D bulk materials.[11,12] As an already established research field, TMDC heterostructures represent the first choice among the above named. Here, ultrafast charge transfer times of 50 fs and less have been found.[13,14] Yet, these heterostructures remain limited regarding their performance and costs.[11]

Beyond such heterostructures, the combination of 2D semiconductors with dye molecules brings several benefits on its own, which touch different aspects of the systems. First, on the fundamental side, hybrid structures allow the combination of two contrary regimes of exciton mobility, namely the discrete Förster transfer between essentially 0D molecules[15,16] as opposed to the continuous exciton diffusion in the 2D TMDCs.[4,5] Second, from a preparational point of view, many methods for molecule deposition on surfaces can be scaled, offering the opportunity of preparing large-area hybrid structures, starting from full-coverage chemical vapor deposition (CVD-)grown monolayers.[17,18] Third, the band levels of molecules such as perylene diimides (PDIs) can easily be tailored by exchanging their organic substituents,[19] while their optical spectra exhibit characteristic shapes that significantly change

[a]*Institute of Physics, University of Rostock, Albert-Einstein-Str. 23, 18059 Rostock, Germany. E-mail: stefan.lochbrunner@uni-rostock.de*

[b]*Department "Life, Light and Matter", University of Rostock, Albert-Einstein-Str. 25, 18059 Rostock, Germany*

[c]*Research Center for Electronic and Optical Materials, National Institute for Materials Science, 1-1 Namiki, Tsukuba 305-0044, Japan*

[d]*Research Center for Materials Nanoarchitectonics, National Institute for Materials Science, 1-1 Namiki, Tsukuba 305-0044, Japan*

† Electronic supplementary information (ESI) available: Parametrization of preparation techniques, photodegradation of dye molecules, AFM scans, PL results at 10 K, additional FLIM results for the hBN, MoS_2, $MoSe_2$, and WS_2 samples and without the use of the band pass filter. See DOI: https://doi.org/10.1039/d3na00276d

View Article Online
Paper Nanoscale Advances

upon aggregation[20] or charge transfer.[21] Finally, in view of spectroscopic investigations, the near-unity fluorescence quantum yield of these dyes ensures strong signals,[19] in contrast to typical values below 1% for pristine 1L-TMDCs.[1,22]

Several studies on hybrid molecule/1L-TMDC structures have been conducted with their focus lying on changes of the photoluminescence from the TMDC monolayer.[23–26] To that end, comparably thick dye layers of several 10 nm have been deposited. In this case, the molecules function as an essentially infinite charge trap, *i.e.* draining excited electrons or holes from the absorbing TMDC layer on a timescale of picoseconds.[27–30]

In the inverse situation, where molecular layers (of several nm thickness) on a 2D material are excited, the charge transfer takes place towards the TMDC and proceeds significantly faster, with reported upper limits for the time constants of a few 100 fs down to 40 fs. The charge transfer is typically followed by thermal relaxation of the hot charge carriers or interlayer excitons, even spin flips and the formation of triplet excitons may occur.[29–32]

While these studies mostly focus on nanometer films of electron-donating metal phtalocyanine molecules[30–33] on MoS_2, investigations with purely organic dyes such as the electron-accepting PDIs were conducted in wet media.[21,34] In this work, however, we create hybrid structures by vapor depositing monomeric dye molecules of the PDI *N*,*N*′-bis(2,6-diisopropylphenyl)-3,4,9,10-perylenetetracarboxylic diimide, commonly referred to as perylene orange (PO). In contrast to previous studies, we chose a molecular coverage well below a monolayer, creating essentially 0D regimes as opposed to 2D continuous or even 3D bulk-like dye films. As the inorganic counterpart in the hybrid structures and deposition target, we prepared mechanically exfoliated monolayer flakes of the four most common TMDCs (MX_2 with M = Mo, W and X = S, Se) as well as multilayer hexagonal boron nitride (hBN) as a reference. Fig. 1 shows their relevant energy levels, that is the valence band (VB) maximum and conduction band (CB) minimum for the 2D materials and the highest occupied and lowest unoccupied molecular orbital (HOMO and LUMO, respectively) of the dye. When a photon is absorbed by the PO (TMDC), an electron from the HOMO (VB) will be raised to the LUMO (CB), leaving a hole in the HOMO (VB) with whom it forms an exciton. As the hBN band gap completely comprises the relevant energy levels of PO, neither charge nor energy transfer is expected from the dye into the hBN. For each of the PO/TMDC hybrids, in contrast, both processes are possible, offering a rapid nonradiative decay channel. Consequently, we expect the fluorescence lifetime to shorten drastically and the intensity to decrease strongly, as the molecular exciton will less likely recombine radiatively. Thus, we investigate the hybrids *via* spectrally, spatially and temporally resolved emission spectroscopy.

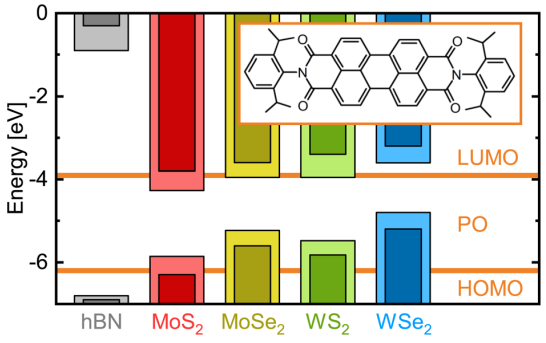

Fig. 1 Electronic energy levels of various 2D materials *versus* perylene orange. The vacuum level is set to zero. The horizontal lines show the HOMO and LUMO energies of the isolated dye molecule, whose molecular structure is depicted in the inset.[35] Pale and dark bars indicate the value range for VBM and CBM energies extracted from various publications reporting on density functional theory calculations (hBN;[36] MoS_2;[23,27,37–39] $MoSe_2$;[23,38–40] WS_2;[28,37–39,41] WSe_2 (ref. 23, 38 and 39)). In these calculations, excitonic effects were not considered. While the hBN band levels lie far from the molecular orbitals, for each TMDC, at least one of the band extrema falls into the HOMO–LUMO-gap of PO.

2. Experimental

Hybrid structures were prepared by thermal vapor deposition (TVD) of monomer PO films onto mechanically exfoliated 2D flakes transferred to Si/SiO_2 wafers.[42] PO powder (Exciton, Exalite 578) is heated to temperatures from 430 K to 450 K and evaporated in vacuum ($\leq 1 \times 10^{-2}$ mbar) in order for the molecules to condense onto the target substrate kept at about room temperature. The total process duration amounted to 40 min, including roughly 15 min of heating up the powder reservoir from room to the evaporation temperature. The specific evaporation temperature was adjusted to the target coverage by coating glass slides as references in advance. Here, we aimed at a coverage of about 2.4×10^{-2} nm^{-2}, corresponding to roughly $\frac{1}{30}$ of a monolayer and ensuring the monomeric behavior of the deposited molecules (see ESI, Sections 1.1 and 1.2†). As an alternative coating technique, stamping was also tested in Section 1.3 of the ESI.† This offers a low-threshold method similar to the deterministic transfer of 2D materials. However, it yields more inhomogeneous molecular films.

For micro-photoluminescence (μ-PL) spectroscopy, a 532 nm (RLTMGL-532-100-3, Roithner) or 633 nm (OBIS 633LXSF, Coherent) continuous wave laser is focused onto the sample. The emitted radiation is collected by a microscope objective, filtered from the scattered excitation light using a long-pass plus a spatial filter with a 50 μm pinhole, and analyzed by a grating spectrometer (Acton 2300i). In our experiments, the excitation power was about 4.5 μW for the green and 9 μW for the red laser, with a focus diameter of about 1.0 μm to 1.5 μm. The sample was scanned beneath the fixed optical beam path to obtain a 2D raster of the relevant area, with one spectrum acquired at each position within 1 s. To prevent photooxidation of the dye molecules,[43] the samples were kept in vacuum during the experiment. An investigation of photodegradation under ambient conditions is presented in the ESI, Section 2.† If not mentioned otherwise, all measurements were conducted at room temperature and employing the green laser. The cooling

View Article Online
Nanoscale Advances Paper

for low-temperature scans was provided by liquid nitrogen for 80 K and by liquid helium for 10 K.

Fluorescence lifetime imaging microscopy (FLIM) measurements were performed using the MicroTime 200 system by PicoQuant. In these experiments, the sample is excited by 442 nm pulses with an energy of 0.3 pJ at a repetition rate of 40 MHz (equivalent to 12.5 μW), focused down to a diameter of 0.9 μm. The emitted light is detected *via* time-correlated single photon counting, yielding a high sensitivity as well as a time resolution of about 100 ps. Analogously to the μ-PL spectroscopy, the sample area is scanned to obtain a 2D map, with a dwell time of 50 ms per pixel. This short exposure time is crucial to minimize the photodegradation of the dye in those measurements, as they have to be conducted under ambient conditions. Another difference of this setup compared to the μ-PL spectroscopy lies in the lack of spectral resolution. Consequently, we are not able to separate the PO fluorescence from the contributions of the monolayer photoluminescence (see ESI, Section 4.2†). To solve this problem, we placed a 50 nm band pass filter with a central wavelength of 525 nm in the probe beam right in front of the detector, in addition to the standard filters for blocking the excitation light. We tested the filter performance using 1L-WS_2, which – among the four investigated TMDCs – has the strongest PL (in that particular setup) that is also the closest to the filter transmission range. Here, we demonstrated an intensity suppression of the PL by a factor of about 10^4. As a positive side-effect, the selected spectral range roughly matches the 0–0-peak of the dye fluorescence. When comparing this to the spectra of any agglomerated molecular species (see ESI, Sections 1 and 3†), we find that those contributions are essentially excluded from the signal. Accordingly, the measurements with the band pass filter are mostly sensitive to the monomer PO. The instrument response function (IRF) was determined as the detected time trace of the back-reflected excitation light. It was measured using a blank wafer sample and omitting both filters. Here, we extracted an IRF duration of about 150 ps (FWHM) with an asymmetry in terms of a prolonged tail at positive times.

3. Spectral emission landscape of hybrid structures

To characterize the deposited molecular films and their interaction with the substrate or the underlying flakes, we conducted optical experiments on TVD-fabricated 1L-TMDC/PO and hBN/PO hybrid structures. First, μ-PL spectroscopy was performed to elaborate any spectral changes that would indicate a coupling between the 2D material and the dye molecules or even within the molecular layer.

Fig. 2(a) and (d) show two investigated hybrid structures of PO on hBN and WSe_2, respectively, with the resulting μ-PL spectra being depicted in (c) for PO on the wafer substrate, on hBN, and on 1L-WSe_2. Despite the use of a long-pass filter, a sharp peak from the excitation light remains around 2.33 eV. Although the long-pass filter weakens the 0–0 band of the molecular fluorescence band, PO contributes the characteristic multi-peak Franck–Condon structure of its emission.[19] This indicates dye monomers as the dominant species (Spectral signatures of other species are discussed in the ESI, Sections 1.1 and 3†). Additionally, the monolayer WSe_2 flake features a strong, sharp, and distinct photoluminescence peak at around 1.65 eV. This allows a spectral separation of the two emission bands, facilitating a separate mapping of the integrated dye fluorescence (1.8 eV to 2.325 eV) and 1L-PL intensity (1.6 eV to 1.7 eV), as depicted in Fig. 2(b), (e) and (f), respectively. The so-obtained integrated intensity maps reproduce the crystal topography, as can be seen comparing Fig. 2(a) and (d) with Fig. 2(b) and (e). When regarding the spectral range of the semiconductor PL (Fig. 2(f)), the monolayer regions clearly stand out of their dark surroundings, as expected by the strong luminescence enhancement due to the transition from direct to indirect band gaps in TMDC monolayers compared to thicker flakes.[1,2] The dye fluorescence, on the other hand, appears weaker on the hBN flakes compared to the wafer substrate and vanishes almost completely in the PO/WSe_2 hybrid, as evident in the PL spectra as well. For an ideal PO/hBN hybrid structure, we would not expect any modulation or reduction of the fluorescence intensity, given the band level alignment. In reality, the moderate intensity drop on the hBN can be caused by adsorbed species acting as charge traps.[44] Alternatively, it could be that during TVD, evaporated molecules less likely deposit on hBN compared to the SiO_2 surface of the wafer, resulting in a lower PO coverage and correspondingly lower signal. Nevertheless, sufficiently many PO molecules reside on top of the flake, since the dye fluorescence is clearly detected from the hBN area. Due to the similarity of the hBN and TMDC surfaces, we assume a similar molecule coverage on the WSe_2 flake. We conclude that in this case, the PO emission is unambiguously quenched as a consequence of charge or energy transfer into the TMDC.

With the suppression of the dye fluorescence below the experimental sensitivity, we turn to investigate the WSe_2 PL counterpart in more detail to track changes introduced by the deposited molecules. Under this scope, low-temperature measurements offer the distinction of different emission features like neutral excitons and charged ones, *i.e.* trions,[45] whose balance reacts to changes in doping or defect availability.[46] PL spectra acquired at liquid nitrogen temperature show a clear separation of the exciton (X^0) and negative trion (X^-, identified *via* measurements at 10 K, see ESI Section 4.1†) emission bands (Fig. 3). Upon deposition of PO, the latter grows relatively to the former. On first sight, this appears as a sign for charge transfer.[33] In our case, however, this interpretation would contradict the band alignment of PO and 1L-WSe_2, as depicted in Fig. 1, since electrons would have to migrate energetically uphill towards the WSe_2 CB or holes downhill into the PO HOMO. In other words, the observed change in the trion emission is of opposite sign as the charge transfer expected from the band levels. Furthermore, the spectral shape is independent of the excitation wavelength and thus unaffected by whether the molecules are excited or not. Ergo, the major effect originates already from the presence of molecules in their electronic ground state. A possible explanation for the enhanced trion PL could arise from changes in the nonradiative recombination

View Article Online
Paper Nanoscale Advances

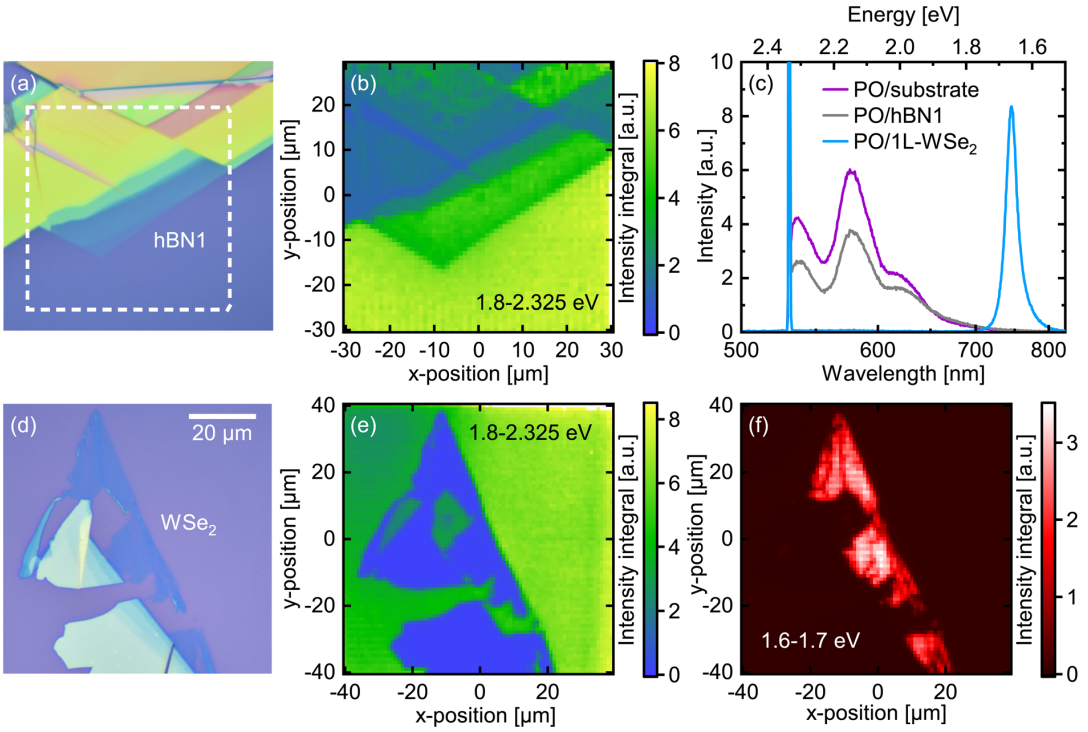

Fig. 2 µ-PL spectroscopy after excitation of TVD-coated hBN and WSe_2 at 532 nm. (a and d) Micrographs of the sample flakes and their environment. The dashed square in (a) marks the area depicted in (b), while (d)–(f) show identical regions. (b and e) Integrated PO fluorescence intensity maps. The intensity appears slightly lower on the thin hBN and almost zero on the WSe_2 flake compared to the surrounding substrate. (c) PL spectra of PO on different 2D crystals *vs.* substrate reference. The sharp peak at 2.33 eV is assigned to stray light from the excitation, the three-peak structure matches the PO emission, and the single low-energy contribution corresponds to the monolayer WSe_2 PL. (f) Integrated 1L-WSe_2 PL intensity map. The monolayer part stands out brightly from the surrounding thicker crystals and the substrate.

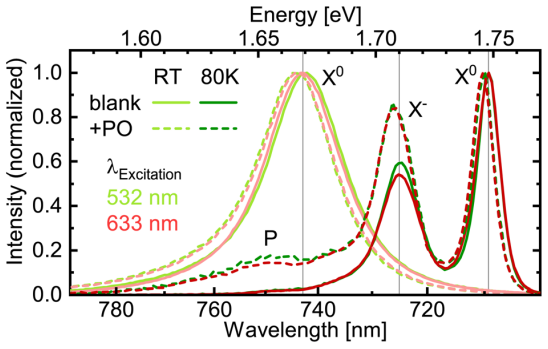

Fig. 3 Normalized PL spectra of blank WSe_2 (solid lines) and PO/WSe_2 hybrid structure (dashed lines) at room temperature and 80 K (bright and dark colors, respectively) after excitation at 532 nm (green) and 633 nm (red). The latter are pairwise essentially identical. At low temperature, the 1L-PL blue-shifts and splits up spectrally into exciton (X^0) and negative trion (X^-) emission. Upon deposition of the dye molecules, the trion contribution grows relative to the excitonic one. Additionally, a weak signal appears at 750 nm (marked as P).

channels in 1L-WSe_2. Deposited molecules could screen defects, thereby reducing the rate for trapping at those sites[24,47] that takes place within several 10 ps at room temperature.[4] This would largely benefit the trionic emission that occurs on similar time scales while the comparatively short-living excitons remain relatively unaffected.[48,49] Consequently, the peak ratio might evolve in favor of the negative trions without an actual change of the doping. In principle, this effect could even conceal a minor charge transfer in the (expected) opposite direction. As an alternative explanation, the deposition of PO molecules could eliminate other adsorbates that initially suppressed the formation of or the emission from negative trions. Either way, the dye molecules apparently do not drain enough electrons from or – if excited – inject enough holes into the 1L-WSe_2 to significantly alter the charge balance there. This appears reasonable, given the low dye coverage of 2.4×10^{12} cm^{-2}, *i.e.* one molecule per roughly 40 nm^2 (see ESI, Section 1.2†) compared to the areal size of the 1L-WSe_2 unit cell of 0.1 nm^2 ($\equiv 10^{15}$ cm^{-2}).[39] Hence, in this coverage regime, molecular functionalization does not affect the doping level of 2D semiconductors significantly. Indeed, studies that observed a pronounced charge transfer-related change of the exciton–trion balance employed much thicker molecular layers of several nm.[33] In addition to the excitonic and trionic peak, we observe a weak emission band (P) around 750 nm that emerges in the hybrid structure at low temperatures. While a detailed investigation of this feature exceeds the scope of this work, several possible physical origins are conceivable. First, the

View Article Online
Nanoscale Advances Paper

emission could stem from the triplet state T_1 of PO. For perylene derivatives, these states usually lie energetically low, frequently down to half of the singlet S_1 energy.[50] However, this phosphorescence would be expected to exhibit a spectral width comparable to the fluorescence peaks, which does not hold for the P contribution.[51] Second, excitons and trions could combine to form (charged) biexcitons (see ESI Section 4.1†) or bind to defects, creating localized, yet luminescent excitons.[52,53] This process could be enabled by the deposited dye molecules either *via* the modified Fermi level or the screening of defects. Finally, the emission peak could be a sign of interlayer exciton formation, where the electron resides in the PO layer and the hole in the WSe_2.[28,54,55]

Summing up the μ-PL measurements, we found a strong indication for fluorescence intensity quenching as well as a relatively enhanced trion PL when combining PO with WSe_2 in a hybrid structure. Yet, we cannot distinguish unambiguously between charge and energy transfer as the dominant contribution to the fluorescence quenching. Nevertheless, as charge transfer is generally observed in type II band alignments,[27–33] we favor this interpretation. Even if energy transfer would outcompete hole transfer from the molecular into the semiconductor layer, a consecutive back-transfer of electrons is expected in PO/WSe_2 hybrids, resulting in charge separation after all.[30] Regardless of the specific mechanism responsible for the quenching, any fast nonradiative decay channel does not only reduce the fluorescence intensity but shortens its lifetime as well. Aiming at the quantification of this phenomenon, we turn to temporally resolved measurements.

4. Rapid fluorescence quenching in TMDC hybrids

To be capable of time-resolved detection of even the weak fluorescence from various PO/TMDC hybrids, we performed FLIM on these samples, achieving a higher sensitivity than in the μ-PL spectroscopy and tracking the temporal evolution of the emission signal. For the analysis, spatial and temporal information were regarded separately. First, we take a look at the time-integrated FLIM data for each pixel. Here, in analogy to the μ-PL, the integration yields 2D intensity maps of the scanned sample areas, as illustrated in Fig. 4(a) and (b) for the hBN and WSe_2 flakes shown in Fig. 2(a) and (d), respectively. For hBN, the flake topography is resembled by the intensity of the PO fluorescence varying between different regions of the crystal. Yet, no systematic dependence on the thickness is found and the variation of the overall intensity within the hBN area as well as *versus* the substrate reaches one order of magnitude at most. The PO-coated WSe_2 flakes, in contrast, exhibit an enormous discrepancy compared to the environment, with the intensities dropping by three orders of magnitude. To properly quantify this effect, we determined both the minimum and maximum absolute intensity values for the substrate area and the thinnest flake regions for two different hBN samples as well as for the four 1L-TMDCs. We calculated the minimum relative fluorescence intensity as the ratio of the minimum value on the flake divided by the maximum on the substrate and *vice versa* for the maximum relative intensity. This way, the comparison with the substrate should eliminate differences in dye molecule coverage between the samples. The resulting relative intensity ranges are presented in Fig. 4(c), while the original data for the remaining flakes in terms of 2D maps may be looked up in the ESI, Fig. S9.†

Regarding the relative intensities, we clearly observe a systematic difference between the TMDC monolayers and the hBN references. Surprisingly, the hBN1 and hBN2 samples – albeit prepared in an identical manner – yield clearly different values. However, experiments on a third sample with a slightly higher coverage (hBN3) demonstrated that the fluorescence signal is affected by the formation of PO agglomerates on the hBN surface (see ESI, Section 4.2†). Such agglomerates may form due to diffusion of the molecules on the surface, which

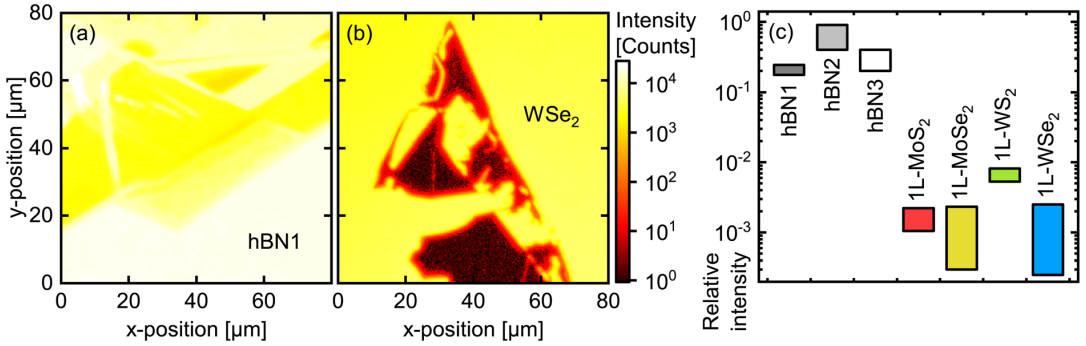

Fig. 4 (a and b) Intensity maps of TVD-coated hBN1 and WSe_2, respectively, as obtained by time-integrating the FLIM data. The depicted areas match the micrographs from Fig. 2(a) and (d), with the crystal topography being clearly reproduced in the FLIM map. The intensity drop from substrate to flake is drastically stronger on WSe_2 than on hBN. (c) FLIM intensity on different 2D flakes relative to their respective substrate environment. The bars cover the uncertainty interval of each value. While the three hBN samples range between 0.2 and near-unity, the 1L-TMDCs exhibit relative intensities in the order of 10^{-3}. As discussed in the ESI, Section 4.2,† the hBN3 sample represents a lower bound for the relative intensity of PO on hBN. Note that the value for WS_2 is overestimated, as there is still some amount of 1L-PL transmitted through the band pass filter (see ESI, Sections 4.3 and 4.4†).

View Article Online
Paper Nanoscale Advances

has been monitored by AFM scans (see ESI, Section 3†). As a result, small differences in PO coverage together with varying surface characteristics of the hBN1 and hBN2 flakes can lead to strong distinctions between those samples regarding agglomerate formation and correspondingly differing fluorescence intensities. To exclude this effect, the white bar for hBN3 in Fig. 4(c) represents a largely agglomerate-free region, *i.e.* with a homogeneous, almost pure monomer coating. Considering that the agglomerates form by draining molecules from their environment, this homogeneous area is probably characterized by a lower molecule coverage than the flake in total as well as the surrounding substrate. Consequently, the hBN3 value can be regarded as a lower bound for the relative intensity of the fluorescence of monomer PO on hBN, leaving a range from about 0.3 to unity. The PO/TMDC hybrids, in contrast, reach values of about 10^{-3}, close to the noise level. Merely PO/1L-WS_2 scores 1%. However, in this case, the monolayer PL is strong enough to still contribute some photon counts despite the usage of the band pass filter. Taking this into account, we conclude a fluorescence intensity reduction by a factor of roughly 10^3 on the TMDC monolayers compared to the hBN. This stands out from other hybrid structures with thicker molecular layers where the fluorescence intensity on the 1L-TMDC *vs.* substrate differ by a factor of ten at most.[21,31,32,41] In our case, the planar shape of the molecule probably leads to a face-down orientation on the TMDC monolayers, which in turn promotes efficient charge transfer. Another reason for the drastic effect in our case supposedly lies in the monomeric coating, while in films of several nanometer thickness, excitons have to diffuse towards the interface before charge transfer can take place. This leaves more time for radiative recombination and therefore increases the residual fluorescence intensity. Although these findings strongly point to the occurrence of some quenching mechanism, a final conclusion still requires information on the time evolution of the fluorescence. In order to analyze the emission decay dynamics, we extracted the time-resolved intensity by integrating the FLIM data over the respective regions of interest, namely the substrate, the thinnest hBN areas, and the TMDC monolayers. The obtained normalized time traces are depicted in Fig. 5 as bright, solid lines. For the substrate and the hBN flakes, we observe a fast signal reduction on the sub-nanosecond scale followed by a long-term contribution decaying over several ns. The time traces of the PO/TMDC hybrids, on the contrary, essentially follow the course of the IRF, indicating a decay time constant well below the experimental time resolution.

For a detailed analysis, we fitted the time traces by two exponentials, yielding a good agreement with the data, as can be seen from the dark, dashed lines in Fig. 5. In this process, the signal rise was modeled by an error function. The resulting parameters are summarized in Table 1. For the shorter exponential time constant τ_1 on hBN, we obtain values of a few 100 ps, varying between the different samples and regions. The longer time constant τ_2, in contrast, consistently yields about 3 ns. We assign this to the monomer PO molecules, as it is comparable to the fluorescence lifetime of almost 4 ns in solutions of similar monomers.[56,57] The origin of the shorter lifetime can again be elucidated with the help of the hBN3 sample. Here, we were able to separate regions dominated by agglomerates from areas largely governed by homogeneously deposited monomer PO (see ESI Section 4.2†). While for the former regions, the fast decay accounts for most of the amplitude and the slow component almost vanishes, an opposite behavior is observed in the latter. Thus, we conclude that τ_1 can be assigned to energy transfer from excited PO monomers into agglomerate-associated multi-particle states, *e.g.* excimers, which do not emit in the spectral range of the bandpass filter.[20] Furthermore, when comparing the fit parameters for the different hBN flakes and regions, we find

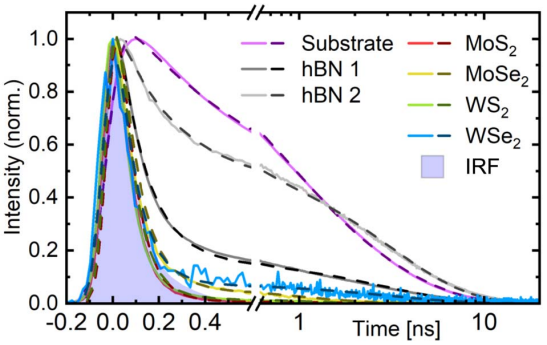

Fig. 5 Normalized fluorescence decay of PO films on different materials. The curves result from integrating the FLIM data over the respective areas of interest. Solid lines represent the data, dashed lines show the fits, which are in good agreement with the data, and the filled area marks the instrument response function. The TMDC curves essentially follow the IRF – despite a small long-living component – while the curves for substrate and hBN show a much slower decrease or at least a long-term tail.

Table 1 Time constants and amplitude ratios from biexponential time trace fitting. All underlying fluorescence time traces were measured employing the 500–550 nm band pass filter. Here, τ_1 for the PO/TMDC hybrids is very close to the time constants for the IRF, indicating that the underlying dynamics could not be separated from the instrument response. The SiO_2 entries represent a summary of the values for the coated wafer environment of all hBN and TMDC samples. The time traces for hBN3 are depicted in the ESI, Fig. S8(b)

Substrate for PO layer	τ_1 [ns]	τ_2 [ns]	$\frac{A_2}{A_1}$
SiO_2	0.5–1.0	2.2–3.2	0.60–1.3
IRF	0.065	0.14	0.53
hBN1	0.12	2.9	0.13
hBN2	0.22	3.1	0.97
hBN3 (homogeneous)	0.46	3.5	3.3
hBN3 (agglomerates)	0.10	2.2	0.045
1L-MoS_2	0.073	1.4	0.0056
1L-$MoSe_2$	0.087	0.92	0.048
1L-WS_2	0.071	0.92	0.015
1L-WSe_2	0.085	3.1	0.050

View Article Online
Nanoscale Advances Paper

that τ_1 takes smaller values, the higher the amplitude of the fast decay compared to the slow one. This could point to a mechanism where the presence of more or bigger agglomerates actually speeds up the decay, *e.g.* in a diffusion-mediated exciton trapping model. Alternatively, this behavior may result as a fitting artifact from the superposition with the asymmetric IRF. Indeed, the latter can also be fitted biexponentially with $\tau_1 = 65$ ps and $\tau_2 = 140$ ps.

The PO/TMDC hybrids, as already expected from the measured time traces, essentially follow the IRF, manifesting in the values of τ_1 from 70 ps to 90 ps. Note that these only indicate the resolution limit as determined by the IRF. They are not to be confused with the actual time constants of the underlying physical processes, which lie well below the time resolution of this setup. In addition to the fast decay, the fits reveal different, yet in any case weak long-term contributions to the time traces. Following the interpretation of charge or energy transfer-induced quenching, this tail could stem from imperfect contact between the dye and the TMDC layer, leaving some PO molecules only weakly or even unquenched. They would emit residual long-living fluorescence, thereby leading to an overestimation of the relative intensity on the PO/TMDC hybrid structures in Fig. 4(c) as well.

With this information and taking into account the intensity ratios discussed above, we can estimate the time constant of the nonradiative decay. For hBN, the relative intensity takes values of 0.3–1, although in the case of the hBN2 sample with a prevailing monomer contribution in the decay, it approaches unity. In contrast, the TMDCs achieve values of about 10^{-3}. Assuming a comparable PO coverage due to the similar surface, we obtain a quenching factor of nearly 10^3. As this also resembles the ratio of the nonradiative *vs.* the radiative time constant of 3 ns, we end up with a charge or energy transfer time from dye to semiconductor of several picoseconds. Yet, we have to consider that even the hBN2 area shows agglomerate features in the time trace. This results in a lower fluorescence than for a perfect monomer coating and thus an underestimation of the quenching in the PO/TMDC hybrids. The same holds for the possibly imperfect contact of the molecules on the respective 2D material that – in the case of the TMDCs – would inhibit charge or energy transfer for a fraction of the molecules and thus reduce the observed quenching. All taken together, this is in agreement with charge transfer time constants of 40 up to several 100 fs for metal phtalocyanine/TMDC hybrid systems.[29–32]

5. Conclusion

In this study, we investigated PO/1L-TMDC hybrid structures with a molecular sub-monolayer by means of μ-PL spectroscopy and FLIM to gather evidence for charge or energy transfer after optical excitation. We observe a drastic reduction of the dye fluorescence intensity on all TMDCs, as opposed to the PO/hBN references. Simultaneously, the lifetime of the emission signal is strongly reduced from about 3 ns to values well below the FLIM time resolution. This verifies the occurrence of a strong quenching mechanism induced by the TMDC monolayers. *Vice versa*, the deposition of PO molecules enhances the trion emission of WSe_2 at low temperatures. This cannot be accounted for by charge transfer, so it may result from the PO screening defects of the monolayer. Based on the quenching ratio and the radiative lifetime of the unquenched dye monomers, we deduced an upper limit for the corresponding hole or energy transfer time constant in the order of several picoseconds. These results are in line with previous research on charge transfer in metal phtalocyanines and pave the way for its exploitation in optoelectronic devices.

Author contributions

T. V., S. L., T. K., I. B., and S. S. conceptualized and planned the project as well as contributed to writing the manuscript. T. V., A. S. and E. O. tested and established the coating techniques. K. W. and T. T. provided the hBN bulk crystals. R. S. set up the μ-PL spectroscopy. T. V. and A. S. performed the preparation and optical characterization of the hybrid structures at room temperature. T. V. and J. S. executed the low-temperature experiments. I. B. conducted the AFM measurements. S. L., T. K., and S. S. supervised the project.

Conflicts of interest

There are no conflicts to declare.

Acknowledgements

This work was funded by the Deutsche Forschungsgemeinschaft (DFG, German Research Foundation) – SFB 1477 "Light–Matter Interactions at Interfaces", project number 441234705. T. V. expresses his gratitude to the University of Rostock for its financial support *via* the PhD Scholarship Program. T. K. gratefully acknowledges funding by the DFG *via* grant no. KO 3612/7-1, project number 467549803. K. W. and T. T. acknowledge support from the JSPS KAKENHI (grant numbers 20H00354 and 23H02052). We thank Regina Lange for assisting the AFM measurements.

References

1 K. F. Mak, C. Lee, J. Hone, J. Shan and T. F. Heinz, *Phys. Rev. Lett.*, 2010, **105**, 136805.
2 A. Splendiani, L. Sun, Y. Zhang, T. Li, J. Kim, C.-Y. Chim, G. Galli and F. Wang, *Nano Lett.*, 2010, **10**, 1271–1275.
3 T. Cheiwchanchamnangij and W. R. L. Lambrecht, *Phys. Rev. B: Condens. Matter Mater. Phys.*, 2012, **85**, 205302.
4 T. Völzer, F. Fennel, T. Korn and S. Lochbrunner, *Phys. Rev. B*, 2021, **103**, 045423.
5 M. Kulig, J. Zipfel, P. Nagler, S. Blanter, C. Schüller, T. Korn, N. Paradiso, M. M. Glazov and A. Chernikov, *Phys. Rev. Lett.*, 2018, **120**, 207401.
6 K. F. Mak and J. Shan, *Nat. Photonics*, 2016, **10**, 216–226.
7 M. M. Furchi, A. Pospischil, F. Libisch, J. Burgdörfer and T. Mueller, *Nano Lett.*, 2014, **14**, 4785–4791.

8 D. Somvanshi and S. Jit, *2D Nanoscale Heterostructured Materials*, Elsevier, 2020, pp. 125–149.
9 N. Ubrig, E. Ponomarev, J. Zultak, D. Domaretskiy, V. Zólyomi, D. Terry, J. Howarth, I. Gutiérrez-Lezama, A. Zhukov, Z. R. Kudrynskyi, Z. D. Kovalyuk, A. Patané, T. Taniguchi, K. Watanabe, R. V. Gorbachev, V. I. Fal'ko and A. F. Morpurgo, *Nat. Mater.*, 2020, **19**, 299–304.
10 M. Massicotte, P. Schmidt, F. Vialla, K. G. Schädler, A. Reserbat-Plantey, K. Watanabe, T. Taniguchi, K. J. Tielrooij and F. H. L. Koppens, *Nat. Nanotechnol.*, 2015, **11**, 42–46.
11 D. Jariwala, T. J. Marks and M. C. Hersam, *Nat. Mater.*, 2016, **16**, 170–181.
12 S. Padgaonkar, J. N. Olding, L. J. Lauhon, M. C. Hersam and E. A. Weiss, *Acc. Chem. Res.*, 2020, **53**, 763–772.
13 X. Hong, J. Kim, S.-F. Shi, Y. Zhang, C. Jin, Y. Sun, S. Tongay, J. Wu, Y. Zhang and F. Wang, *Nat. Nanotechnol.*, 2014, **9**, 682–686.
14 C. Jin, E. Y. Ma, O. Karni, E. C. Regan, F. Wang and T. F. Heinz, *Nat. Nanotechnol.*, 2018, **13**, 994–1003.
15 F. Fennel and S. Lochbrunner, *Phys. Rev. B: Condens. Matter Mater. Phys.*, 2012, **85**, 094203.
16 T. Förster, *Ann. Phys.*, 1948, **437**, 55–75.
17 Z. Cai, B. Liu, X. Zou and H.-M. Cheng, *Chem. Rev.*, 2018, **118**, 6091–6133.
18 S. Shree, A. George, T. Lehnert, C. Neumann, M. Benelajla, C. Robert, X. Marie, K. Watanabe, T. Taniguchi, U. Kaiser, B. Urbaszek and A. Turchanin, *2D Mater.*, 2019, **7**, 015011.
19 F. Würthner, C. R. Saha-Möller, B. Fimmel, S. Ogi, P. Leowanawat and D. Schmidt, *Chem. Rev.*, 2015, **116**, 962–1052.
20 A. L. Bialas and F. C. Spano, *J. Phys. Chem. C*, 2022, **126**, 4067–4081.
21 I. K. Sideri, Y. Jang, J. Garcés-Garcés, Á. Sastre-Santos, R. Canton-Vitoria, R. Kitaura, F. Fernández-Lázaro, F. D'Souza and N. Tagmatarchis, *Angew. Chem., Int. Ed.*, 2021, **60**, 9120–9126.
22 S. Roy, A. S. Sharbirin, Y. Lee, W. B. Kim, T. S. Kim, K. Cho, K. Kang, H. S. Jung and J. Kim, *Nanomaterials*, 2020, **10**, 1032.
23 J. Choi, H. Zhang and J. H. Choi, *ACS Nano*, 2016, **10**, 1671–1680.
24 H. Nan, Z. Wang, W. Wang, Z. Liang, Y. Lu, Q. Chen, D. He, P. Tan, F. Miao, X. Wang, J. Wang and Z. Ni, *ACS Nano*, 2014, **8**, 5738–5745.
25 S. Mouri, Y. Miyauchi and K. Matsuda, *Nano Lett.*, 2013, **13**, 5944–5948.
26 S. Park, T. Schultz, X. Xu, B. Wegner, A. Aljarb, A. Han, L.-J. Li, V. C. Tung, P. Amsalem and N. Koch, *Commun. Phys.*, 2019, **2**, 109.
27 S. B. Homan, V. K. Sangwan, I. Balla, H. Bergeron, E. A. Weiss and M. C. Hersam, *Nano Lett.*, 2016, **17**, 164–169.
28 T. Zhu, L. Yuan, Y. Zhao, M. Zhou, Y. Wan, J. Mei and L. Huang, *Sci. Adv.*, 2018, **4**, eaao3104.
29 C. Zhong, V. K. Sangwan, C. Wang, H. Bergeron, M. C. Hersam and E. A. Weiss, *J. Phys. Chem. Lett.*, 2018, **9**, 2484–2491.
30 S. Padgaonkar, S. H. Amsterdam, H. Bergeron, K. Su, T. J. Marks, M. C. Hersam and E. A. Weiss, *J. Phys. Chem. C*, 2019, **123**, 13337–13343.
31 T. R. Kafle, B. Kattel, S. D. Lane, T. Wang, H. Zhao and W.-L. Chan, *ACS Nano*, 2017, **11**, 10184–10192.
32 T. R. Kafle, B. Kattel, P. Yao, P. Zereshki, H. Zhao and W.-L. Chan, *J. Am. Chem. Soc.*, 2019, **141**, 11328–11336.
33 Y. Kong, S. M. Obaidulla, M. R. Habib, Z. Wang, R. Wang, Y. Khan, H. Zhu, M. Xu and D. Yang, *Mater. Horiz.*, 2022, **9**, 1253–1263.
34 T. Scharl, G. Binder, X. Chen, T. Yokosawa, A. Cadranel, K. C. Knirsch, E. Spiecker, A. Hirsch and D. M. Guldi, *J. Am. Chem. Soc.*, 2022, **144**, 5834–5840.
35 C. Ramanan, A. L. Smeigh, J. E. Anthony, T. J. Marks and M. R. Wasielewski, *J. Am. Chem. Soc.*, 2011, **134**, 386–397.
36 D. Wickramaratne, L. Weston and C. G. V. de Walle, *J. Phys. Chem. C*, 2018, **122**, 25524–25529.
37 Z. Cao, M. Harb, S. Lardhi and L. Cavallo, *J. Phys. Chem. Lett.*, 2017, **8**, 1664–1669.
38 J. Kang, S. Tongay, J. Zhou, J. Li and J. Wu, *Appl. Phys. Lett.*, 2013, **102**, 012111.
39 C. Gong, H. Zhang, W. Wang, L. Colombo, R. M. Wallace and K. Cho, *Appl. Phys. Lett.*, 2013, **103**, 053513.
40 V. Iberi, L. Liang, A. V. Ievlev, M. G. Stanford, M.-W. Lin, X. Li, M. Mahjouri-Samani, S. Jesse, B. G. Sumpter, S. V. Kalinin, D. C. Joy, K. Xiao, A. Belianinov and O. S. Ovchinnikova, *Sci. Rep.*, 2016, **6**, 30481.
41 X. Liu, J. Gu, K. Ding, D. Fan, X. Hu, Y.-W. Tseng, Y.-H. Lee, V. Menon and S. R. Forrest, *Nano Lett.*, 2017, **17**, 3176–3181.
42 A. Castellanos-Gomez, M. Buscema, R. Molenaar, V. Singh, L. Janssen, H. S. J. van der Zant and G. A. Steele, *2D Mater.*, 2014, **1**, 011002.
43 J. Lub, P. A. van Hal, R. Smits, L. Malassenet, J. Pikkemaat and R. A. Hikmet, *J. Lumin.*, 2019, **207**, 585–588.
44 L. Renn, L. S. Walter, K. Watanabe, T. Taniguchi and R. T. Weitz, *Adv. Mater. Interfaces*, 2022, **9**, 2101701.
45 K. F. Mak, K. He, C. Lee, G. H. Lee, J. Hone, T. F. Heinz and J. Shan, *Nat. Mater.*, 2012, **12**, 207–211.
46 J. Jadczak, M. Glazov, J. Kutrowska-Girzycka, J. J. Schindler, J. Debus, C.-H. Ho, K. Watanabe, T. Taniguchi, M. Bayer and L. Bryja, *ACS Nano*, 2021, **15**, 19165–19174.
47 D. Kiriya and D.-H. Lien, *Nano Express*, 2022, **3**, 034002.
48 G. Wang, E. Palleau, T. Amand, S. Tongay, X. Marie and B. Urbaszek, *Appl. Phys. Lett.*, 2015, **106**, 112101.
49 P. Nagler, M. V. Ballottin, A. A. Mitioglu, M. V. Durnev, T. Taniguchi, K. Watanabe, A. Chernikov, C. Schüller, M. M. Glazov, P. C. Christianen and T. Korn, *Phys. Rev. Lett.*, 2018, **121**, 057402.
50 F. S. Conrad-Burton, T. Liu, F. Geyer, R. Costantini, A. P. Schlaus, M. S. Spencer, J. Wang, R. H. Sánchez, B. Zhang, Q. Xu, M. L. Steigerwald, S. Xiao, H. Li, C. P. Nuckolls and X. Zhu, *J. Am. Chem. Soc.*, 2019, **141**, 13143–13147.
51 Z. Yu, Y. Wu, Q. Peng, C. Sun, J. Chen, J. Yao and H. Fu, *Chem.–Eur. J.*, 2016, **22**, 4717–4722.
52 T. Godde, D. Schmidt, J. Schmutzler, M. Aßmann, J. Debus, F. Withers, E. M. Alexeev, O. D. Pozo-Zamudio, O. V. Skrypka,

K. S. Novoselov, M. Bayer and A. I. Tartakovskii, *Phys. Rev. B*, 2016, **94**, 165301.
53 Z. Li, T. Wang, Z. Lu, C. Jin, Y. Chen, Y. Meng, Z. Lian, T. Taniguchi, K. Watanabe, S. Zhang, D. Smirnov and S.-F. Shi, *Nat. Commun.*, 2018, **9**, 3719.
54 J. J. P. Thompson, V. Lumsargis, M. Feierabend, Q. Zhao, K. Wang, L. Dou, L. Huang and E. Malic, *Nanoscale*, 2023, **15**, 1730–1738.
55 L. Zhang, F. Zhou, X. Zhang, S. Yang, B. Wen, H. Yan, T. Yildirim, X. Song, Q. Yang, M. Tian, N. Wan, H. Song, J. Pei, S. Qin, J. Zhu, S. Wageh, O. A. Al-Hartomy, A. G. Al-Sehemi, H. Shen, Y. Liu and H. Zhang, *Adv. Mater.*, 2022, 2206212.
56 F. Würthner, *Chem. Commun.*, 2004, 1564–1579.
57 W. E. Ford and P. V. Kamat, *J. Phys. Chem.*, 1987, **91**, 6373–6380.

Electronic Supplementary Material (ESI) for Nanoscale Advances.

Strong Quenching of Dye Fluorescence in Monomeric Perylene Orange/TMDC Hybrid Structures

Supporting Information

Tim Völzer[a,b], Alina Schubert[a,b], Erik von der Oelsnitz[a,b], Julian Schröer[a,b], Ingo Barke[a,b], Rico Schwartz[a], Kenji Watanabe[c], Takashi Taniguchi[d], Sylvia Speller[a,b], Tobias Korn[a,b], and Stefan Lochbrunner[a,b,*]

a) Institute of Physics, University of Rostock, Albert-Einstein-Str. 23, 18059 Rostock, Germany

b) Department "Life, Light and Matter", University of Rostock, Albert-Einstein-Str. 25, 18059 Rostock, Germany

c) Research Center for Electronic and Optical Materials, National Institute for Materials Science, 1-1 Namiki, Tsukuba 305-0044, Japan

d) Research Center for Materials Nanoarchitectonics, National Institute for Materials Science, 1-1 Namiki, Tsukuba 305-0044, Japan

*stefan.lochbrunner@uni-rostock.de

Contents

1 Coating techniques for the preparation of hybrid structures

1.1 Thermal vapor deposition at different temperatures

In the experimental section of the main body of the manuscript, we presented the optimal, standard procedure to create hybrid structures via thermal vapor deposition (TVD). Nevertheless, going beyond this optimum can provide insight in the limits of this preparation technique and how to recognize them. The most relevant parameter for TVD lies in the temperature, determining the evaporation rate of the coating substance as well as the kinetic energy of the molecules hitting the target. Therefore, we varied this parameter to investigate its influence on the absorption and emission spectra of the resulting perylene orange (PO) layer as well as to find the optimum value for monomer coating. Here, we remark that the optimum evaporation temperature may vary by several 10 K depending on the exact amount and distribution of the dye powder in the reservoir, plus the thermal contact at the different interfaces of the setup.

In different coating procedures, the temperature of the PO powder was tuned from 440 to 470 K. Each sample was coated for 40 min including the heating up. As they were performed consecutively in one series, the heating block with the dye powder never started at room temperature but was still warm from the previous run. The resulting absorption and emission spectra are depicted in Figure S1. For the absorption, we observe a prominent multi-peak structure resulting from the Frank-Condon progression, that remains essentially constant in shape for all regarded evaporation temperatures. Merely the amplitude rises with increasing temperature, as more molecules are evaporated in the same time span. The emission spectra also exhibit the monomer-related multi-peak structure at low evaporation temperature that indicates the presence of monomer PO. At higher evaporation temperatures, the first thing to change is the fluorescence intensity rising. Afterwards, the 0-0 peak shrinks, while the broad emission band at the long-wavelength tail of the spectrum emerges. This contribution is likely caused by the formation of aggregates[1] or nanocrystals[2,3] that support excimer emission. While the absorption is still governed by single molecules, the energy is then transferred to the lower-lying excimer state that eventually emits[4,5], typically with a broad red-shifted fluorescence band[6]. Upon raising the evaporation temperature even further up to roughly 470 K, three separate peaks form anew, although their weighting differs from the monomer situation. Here, the 0-2-peak seems strongest, which may possibly indicate the presence of further aggregate

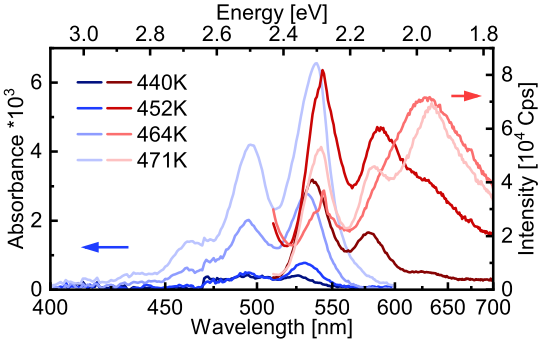

Figure S1: Absorption and emission spectra of TVD PO films in dependence of the evaporation temperature. In contrast to the absorption simply growing with increasing temperature and maintaining its multi-peak structure, as more molecules evaporate, the behavior of the emission involves a higher degree of complexity. First, the signal rises, roughly keeping its shape. From 452 to 464 K, the already discussed broad emission band emerges, parallel to the 0-0-peak shrinking. A further temperature increase, however, leads to a recovery of the multi-peak structure, albeit with a higher weighting of the low-energy signatures.

states, accessible due to the higher kinetic energy of the evaporated molecules.[6]

1.2 Estimation of dye coverage

Based on the absorption strength of the optimal monomer film, as discussed in section 1.1, we are able to calculate the molecular coverage after TVD with standard parameters. We take an absorbance value of $A = 0.5{\cdot}10^{-3}$ for the 0-0-peak of the optimal monomer coating (see Figure S1) and an extinction coefficient for PO of $\varepsilon = 8.5 \times 10^4\,\mathrm{M^{-1}\,cm^{-1}} = 8.5 \times 10^7\,\mathrm{cm^2\,mol^{-1}}$ measured in chloroform solution[7]. Lambert-Beer's law constitutes the relation between the absorbance and the areal molecular density ϱ as follows:

$$A = \varepsilon_{\mathrm{eff}} \cdot c \cdot l = \varepsilon_{\mathrm{eff}} \cdot \varrho \tag{1}$$

with the concentration c and the path length l through the medium. $\varepsilon_{\mathrm{eff}}$ denotes the effective extinction coefficient. It differs from the one in solution, as we assume a flat orientation of the molecules on the surface (x- and y-direction). For PO, the transition dipole moment $\vec{M}$ lies parallel to the longer symmetry axis, i.e. in-plane[8]. Consequently, the mean orientation of $\vec{M}$ and the electric field $\vec{E}$ is advantageous compared to a random distribution. This results in a higher absorbance, scaling with $A \propto |\vec{M} \cdot \vec{E}|^2$. To quantify this effect, we calculate the normalized mean squared projection q of $\vec{M}$ onto $\vec{E}$, with the latter being fixed parallel to the x-axis - for perpendicular incidence, i.e. z-direction light beam and with no loss of generality. In the following, we use spherical coordinates, yielding $\frac{|\vec{M}\cdot\vec{E}|}{|\vec{M}|\cdot|\vec{E}|} = \cos\varphi \cdot \sin\theta$.
For a random orientation as in solution, we obtain:

$$q_{\mathrm{random}} = \frac{\int_0^{2\pi}\int_0^{\pi}(\cos^2\varphi \cdot \sin^2\theta)\sin\theta\,d\theta\,d\varphi}{\int_0^{2\pi}\int_0^{\pi}\sin\theta\,d\theta\,d\varphi} = \frac{1}{3} \tag{2}$$

stating an attenuation of the absorption by a factor of three in random orientation versus perfect parallel alignment of transition dipole moment and electric field. Analogously, in-plane orientation of the molecules (i.e. $\theta = \frac{\pi}{2}$) results in

$$q_{\mathrm{in-plane}} = \frac{\int_0^{2\pi}\cos^2\varphi\,d\varphi}{\int_0^{2\pi}d\varphi} = \frac{1}{2} \tag{3}$$

In terms of extinction coefficients, this constitutes the relation:

$$\frac{\varepsilon_{\mathrm{eff}}}{\varepsilon} = \frac{q_{\mathrm{in-plane}}}{q_{\mathrm{random}}} = \frac{3}{2} \tag{4}$$

Hence, the face-down orientation of the molecules on the surface manifests in a 1.5-fold higher absorption per molecule compared to the value measured in solution.
Returning to Lambert-Beer's law (Equation (1)), this yields a areal molecule density of roughly

$$\varrho = \frac{2A}{3\,\varepsilon} \approx 2.4 \times 10^{-2}\,\mathrm{nm^{-2}} \equiv 2.4 \times 10^{12}\,\mathrm{cm^{-2}} \tag{5}$$

corresponding to an area of about $42\,\mathrm{nm^2}$ per molecule, i.e. roughly $\frac{1}{30}$ of a perfect dye monolayer, and a mean molecular distance of 6.5 nm compared to a molecule size of $0.7\,\mathrm{nm} \times 2\,\mathrm{nm}$. These values clearly confirm the monomer nature of the PO coating.

1.3 Inhomogeneities and quenching on stamp-coated 1L-TMDCs

As an alternative viable method for the deposition of molecules onto a target substrate, we tested stamping. Initially, the viscoelastic polydimethylsiloxane (PDMS) stamp is spin-coated

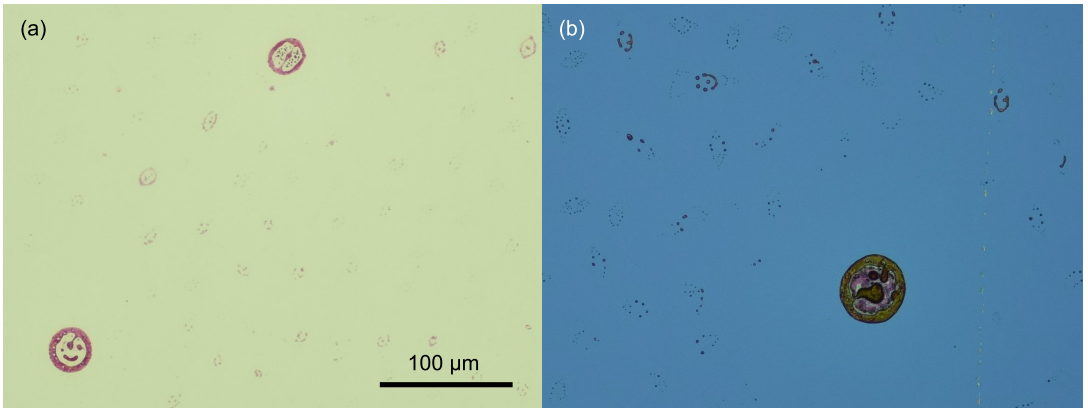

Figure S2: Stamp-coating of perylene orange. (a) Micrograph of a spin-coated PDMS stamp. The dye agglomerates on several spots to form clearly visible structures with a size of up to 50 µm as well as a variety of smaller spots. In between these accumulation centers, preferably in the vicinity of large structures, areas without visible inhomogeneities exist. (b) Microscope image of a stamp-coated Si/SiO_2 wafer. Here, the same structures as on the PDMS occur, suggesting a high transfer yield. Aiming a agglomerate-free region at the target flake during the stamping facilitates monomer coating.

with a 900 µM solution of PO in chloroform. Afterwards, the dye is transferred to the target by stamping, similar to the deterministic transfer of 2D flakes[9]. However, as the PDMS has a rather rough surface and the solution is quite concentrated, many spots of agglomerated PO form during the spin-coating, which will also transfer to the target substrate, see Figure S2. To avoid stamping such an agglomerate onto the flake of interest, one has to aim between those spots, where the molecule coverage is typically homogeneous. This can be monitored by an optical microscope commonly implemented in such stamping setups. Nevertheless, some

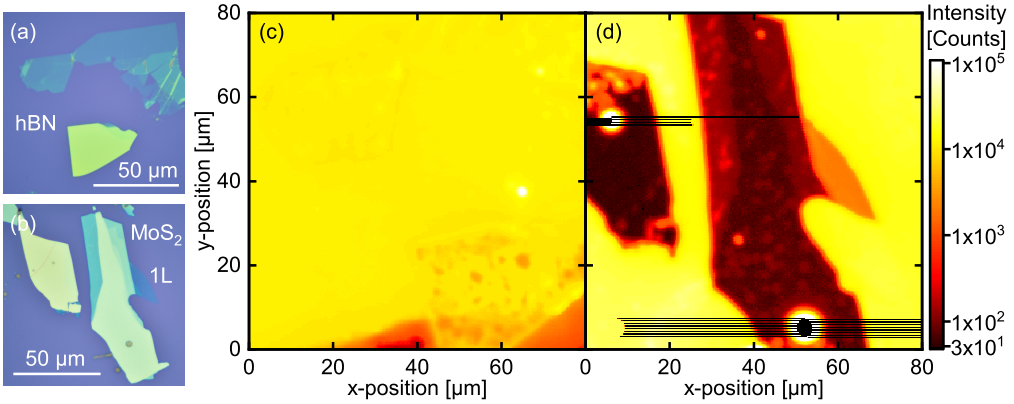

Figure S3: FLIM measurements of 2D crystals stamped with PO. No additional band pass filter was used in these experiments (a, b) Micrographs of hBN and MoS_2 flakes on wafer substrates, respectively. (c) FLIM intensity map of the hBN crystals depicted in (a). The intensity is homogeneous over the vast majority of the area. The only exceptions are two bright spots on the right and in the top right corner as well as the dark bottom right one, where the contact between PDMS and substrate ended. (d) FLIM intensity map of the MoS_2 crystals depicted in (b). While the intensity exhibits a constant level on the substrate, it drastically falls on the TMDC flakes. Exceptions occur with the two prominent bright spots on the flakes, which probably result from dye agglomerates. Here, the high emission intensities trigger a safety shutter in front of the FLIM detector for several seconds, blocking the incoming light and leading to the dark horizontal lines.

small (sub-)micron agglomerates may be barely visible, yet exhibiting much higher fluorescence signals than the monomer-coated environment, as the results from fluorescence lifetime imaging microscopy (FLIM) in Figure S3 (d) show. This leaves a small risk of accidentally putting a small agglomerate onto the flake of interest, creating an inhomogeneous coating.
Apart from these preparational shortcomings, the stamping method is able to reproduce the findings regarding the quenching observed on samples coated by thermal vapor deposition (TVD). Figure S3 presents the fluorescence lifetime imaging microscopy (FLIM) intensity maps for stamp-coated hBN and MoS_2 flakes. Analogously to the TVD samples, the hBN regions exhibit an intensity level similar to the wafer surroundings, while the MoS_2 crystals show a strong contrast, with the fluorescence dropping by up to three orders of magnitude compared to their environment. Note that no additional band pass filter was used in these measurements. Consequently, we observe extraordinarily bright spots that match the dye agglomerates, for instance when comparing Figure S3 (b) and (d). On top of that, the monolayer MoS_2 photoluminescence causes the respective area to stand out from the other flake regions, as it also happens in section 4.4. Thus, a quantitative analysis of the quenching as well as the time-resolved signal does not appear reasonable at this point. Nevertheless, the occurrence of strong quenching becomes evident in this case as well, supporting the findings from the main body, section "Rapid fluorescence quenching in TMDC hybrids".

2 Photodegradation of PO at ambient conditions

Since PO is prone to photooxidation[10], all measurements were performed either in vacuum or by applying only short illumination times to avoid degradation of the molecule film. To quantify the severity of this issue, we performed degradation measurements in the microscopic emission spectroscopy setup, in this case under ambient conditions. Omitting the cryostat with its glass window in the laser beam, we obtained a slightly smaller focal diameter of roughly 1 µm. On top of that, we doubled the excitation power to 10 µW at 532 nm. In sum, we applied an about four-fold intensity compared to the measurements under vacuum that were discussed in the main

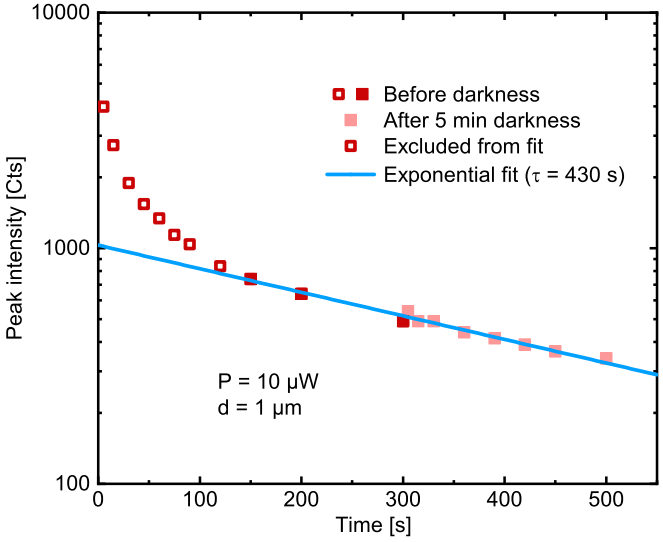

Figure S4: Photodegradation of PO on wafer substrate under ambient conditions. Following a non-monoexponential decay within the first 2 min, the intensity decreases exponentially, as indicated by the fit. During the 5 min of darkness, no substantial recovery of the signal is observed, suggesting a non-reversible degradation of the dye molecules.

body. We chose a spot on the wafer substrate, far from any flakes and monitored the emitted intensity of the 0-0-peak over time. The resulting signal evolution is presented in Figure S4. First, we observed a drastic signal decay by a factor of five within the first two minutes, which does not follow a simple exponential behavior. Afterwards, the curve evolves into a monoexponential signal reduction. After 5 min, we blocked the laser beam for the same duration, to check whether any recovery mechanism is present. However, no substantial increase of the signal was observed after 5 min of darkness, suggesting that the degradation is permanent. The exponential decay, on the other hand, continues at the same rate. A corresponding fit yielded a time constant of about 400 s. All in all, these findings demonstrate the importance of avoiding photooxidation during the measurements, as especially freshly prepared dye films lose a significant amount of intensity within a short time.

3 AFM measurements

Now that we established suitable preparation approaches, with the macroscopic optical spectra pointing to monomer characteristics of the deposited molecules, we strive for a structural characterization of the samples by atomic force microscopy (AFM). This ought to reveal or exclude the formation of larger supramolecular structures as well as to determine the flake and film thickness and homogeneity, even though molecular resolution lies beyond the scope of this work. AFM measurements were conducted in ambient (Park XE-100) using silicon cantilevers (SSS-NCHR, Nanosensors) and dynamic mode. Excitation frequencies slightly larger than the fundamental eigenfrequency and constant-amplitude set points between 65 % and 80 % of the free amplitude were chosen. Data analysis was done using Gwyddion[11] and Igor Pro (Wavemetrics, Inc.). For background correction, a linewise linear function as well as a 2D plane were subtracted. We chose a few-layer WSe_2 and hBN flake, exfoliated and transferred to a Si/SiO_2 wafer, respectively. They were annealed at 550 K and 4×10^{-4} mbar for 20 h, to desorb water and other physisorbed species, and obtain a largely clean surface for the AFM measurements. We investigated the blank samples before and after TVD coating and again five months afterwards. Note that in contrast to the standard procedure, we kept the samples in the evacuated TVD chamber at 3×10^{-5} mbar and room temperature over the weekend (2.7 days) before starting the actual coating process by heating up the dye reservoir. This ought to maintain a relatively clean sample surface, yet it might have an influence on the vapor deposition, as the lower pressure may cause a higher evaporation rate of the dye powder and the transport regime from reservoir to sample probably changed from diffusive to ballistic. On top of that, the desorption of other adsorbates may influence the mobilty of the PO molecules on the respective substrates. As a complement to the AFM measurements, we performed FLIM and micro-photoluminescence (µ-PL) spectroscopy on the same flakes to obtain correlative data.

The AFM analyses show clear differences in the sample topographies, induced by the dye molecule deposition, see Figure S5 (a), (b), (d) and (e). As the highest structures, we observe 3D molecular agglomerates that form exclusively on the substrate and not on the crystal flakes. They measure about 200 nm in diameter and 40 nm in height, exhibit an oblate shape and also appear in FLIM scans without the band pass filter as resolution-limited bright dots, as shown in Figure S5 (c). If converted into a homogeneous coating, these agglomerates correspond to a coverage of about 1 Å in height, i.e. about one third of a perfect monolayer of in-plane oriented flat PO molecules. In between the dots, however, a homogeneous residual fluorescence intensity is detected, pointing to a uniform molecule coverage aside from the 3D aggregates, compatible with a Stranski-Krastanov growth mode[12].

In a zone of $3 - 5$ µm around the flakes, however, no agglomerates are present and the areal fluorescence intensity is significantly reduced, suggesting a depletion of molecules, which are drawn towards the flakes. This assumption is confirmed by the change of the flake edge height due to PO coating, visible in the AFM line profiles in Figure S5 (f). While the thinnest regions

of the blank hBN and WSe_2 size to $h = 7$ and 4 nm in edge height, i.e. about twenty[13] and six[14–16] layers, they rise by about $\Delta h = 1.5$ nm (15 – 25 %) and 4 nm (90 – 100 %) upon molecule deposition, respectively. These values lie well beyond the calculated average molecule coverage on the remote substrate regions. Although the growth of the step height is accompanied by the emergence of PO fluorescence in the hBN flake area drastically exceeding the intensity on the substrate, no indications of larger structures of PO molecules on the crystal surface were found. Thus, we conclude a migration of the molecules below the flake.

Generally, when molecular species are deposited on surfaces with weak interaction, such as van-der-Waals crystals, their diffusion is high. Nevertheless, for the most part, after minutes to hours, molecular assemblies are formed. This can proceed via 2D surface "gas" over a liquid phase towards crystalline aggregates, on graphite[17] or graphene[18] surfaces. Only occasionally, persistence of the 2D gas of monomers or dimers or the liquid phase is observed. Examples are benzene on Cu(111) at 77 K[19], fluorinated copper phthalocyanine on Si(111)/Tl-(1×1)[20] and 2,5-dihydroxybenzoic acid (DHBA) molecules on calcite[21]. In our case, the PL spectrum of the PO in the hBN region features only a small contribution of monomer PO and is instead dominated by a broad low-energy band that occurs exclusively in this sample (Figure S6 (b)), yet baring similarities to the emission of thicker PO coatings (for comparison, see SI sections 1.1 and 1.3). This suggests the presence of the dye molecules in some aggregated form with a broad

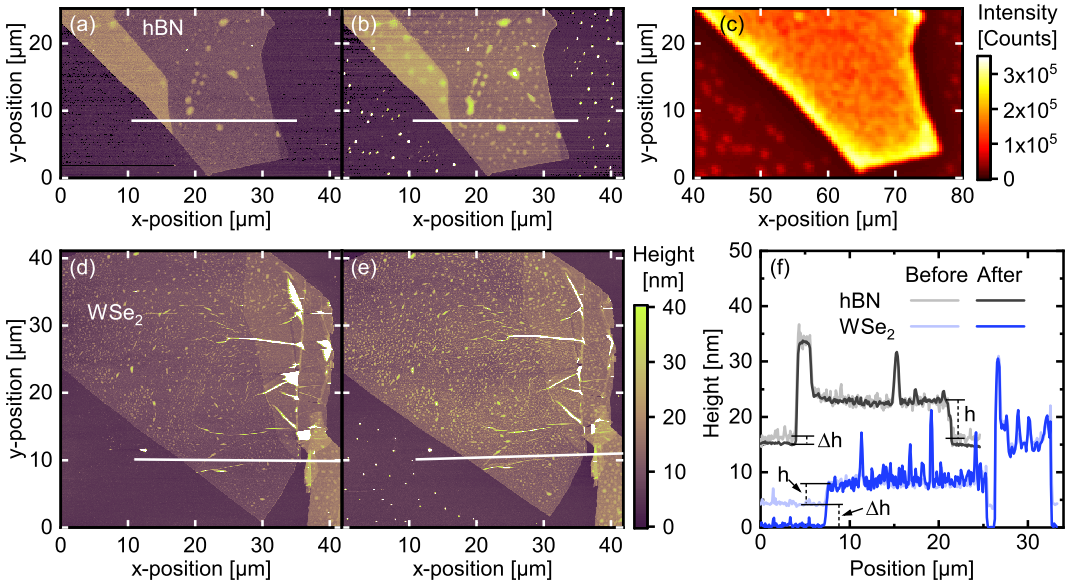

Figure S5: Topography of hybrid structures. Dynamic mode AFM height maps of hBN (a, b) and WSe_2 (d, e) before (a, d) and after (b, e) molecule deposition, respectively. Upon TVD, oblate dye agglomerates appear on the substrate surface, with a diameter of about 200 nm and an average height of 40 nm. In a halo of several µm around the flake, however, these dots are missing. On the crystals, especially on the hBN, in contrast, already present blobs grow and new ones form. The white lines mark the positions, at which the line height profiles in (f) were taken. (c) FLIM intensity map of the area depicted in (a) and (b). On the substrate, the agglomerates show as bright spots, with a homogeneous intensity in between. The halo around the flake is characterized by a reduced fluorescence signal, while the flake area already stands out and its rim exhibits an even brighter emission. Other than that, no intensity variations occur in the crystal area that would match any of the AFM topography patterns. (f) Height profiles taken along the lines marked in (a, b, d, e), each averaged over a width of two pixels. hBN curves are offset for clarity. Note that the profiles after molecule deposition are shifted relatively to match the flake surface before the coating, respectively, demonstrating that the height increase is constant over the whole crystal area.

emission band, which is further red-shifted by the dielectric environment in that encapsulated situation[22].

If not residing at the surface, the two fundamental options for the molecules are either the deposition between the substrate and the hBN, lifting up the flake, or the intercalation between the individual crystal layers, ergo stretching the material in out-of-plane direction[23,24]. However, as the height increase during PO deposition is essentially independent of the original flake thickness and so is the FLIM intensity, we favor the first explanation. Nevertheless, minor contributions from intercalation cannot be excluded.

On top of that, inverse to the situation on the substrate, the fluorescence intensity on the hBN flake rises in the vicinity of the crystal edge and levels within about 5 µm into the interior. This provides another indication for the migration of the dye molecules from the exposed substrate to the cleft between wafer and flake. The lateral size of the dark depletion and bright accumulation zones represents the average diffusion length of the PO molecules. For the WSe_2 flake, in contrast, the strong fluorescence quenching, which is explicitly investigated in the following section, inhibits a comparison between FLIM intensities and AFM topographies.

PO is a relatively large aromatic molecule, such that in view of the literature[17,18], molecular assembly is expected at room temperature. Similar molecules normally do form crystals[2,25], while literature on PO assembly structure on graphite or similar surfaces is lacking, to our best knowledge. In our study, however, aggregates form exclusively on the Si/SiO_2 surface, but not on top of the hBN and WSe_2 flakes. As mentioned above, most of the molecules have migrated underneath the flakes. Yet, on the flake, we still observe signatures of mobile species and AFM error images sometimes indicate persistent amplitude instabilities. An option for explanation is a very dilute, residual 2D molecule gas, which essentially aggregated after months. The density of molecules on the flake is extremely low, and a large amount might have been captured by the tip and shaft, dynamically changing the tip-sample configuration.

All in all, these measurements demonstrate the strong relation between the configuration of the deposited molecules and the corresponding emission spectra. Any deviation from the monomeric character seems to result in definite spectral changes, distorting the multi-peak structure. Thus, we regard the Franck-Condon progression as a clear indicator for the presence of monomer dye molecules.

With respect to the agglomerates on the wafer substrate, both the AFM measurements and the FLIM intensity maps (without the band pass filter) show dots emerging after the PO deposition. The overlay of these two images (see Figure S6 (a)) demonstrates the matching of the agglomerates' positions, proving their identity. While the AFM topographies yielded a width of about 200 nm for these structures, the spatial resolution of nearly 1 µm determines their size in the FLIM maps. In measurements employing the band pass filter from 500 to 550 nm, however, no traces of these spots are found, suggesting their emission to be red-shifted relative to the 0-0-band of the monomer fluorescence or to be generally weaker due to their small area compared to the homogeneous monomer background. In the hBN area, where the FLIM intensity is drastically enhanced compared to the substrate, the µ-PL spectrum is dominated by a broad contribution, peaking around 650 nm. Although its shape bears striking similarities with the supposed excimer band of thicker coatings (see section 1), it exhibits a further red-shift compared to the latter. We assign this energetic shift to the complete encapsulation of the PO, leading to a different dielectric environment. When molecules are placed in contact with insulating layers, their gap between the highest occupied and lowest unoccupied molecular orbital (HOMO-LUMO gap, as measured by tunneling spectroscopy) can substantially shrink further than solely upon aggregation. For instance, individual pentacene placed on hBN/Rh(111) exhibits only 68 % of the original gap energy[22]. This gap reduction may originate from transient ionic states, i.e. positive- and negative-ion resonances assuming a Coulomb model and a dielectric hBN spacer with $\varepsilon_r = 4$. Alternatively, it could be explained qua vibration, if in the aggregate, higher vibrational states are present that get frustrated in the flake.

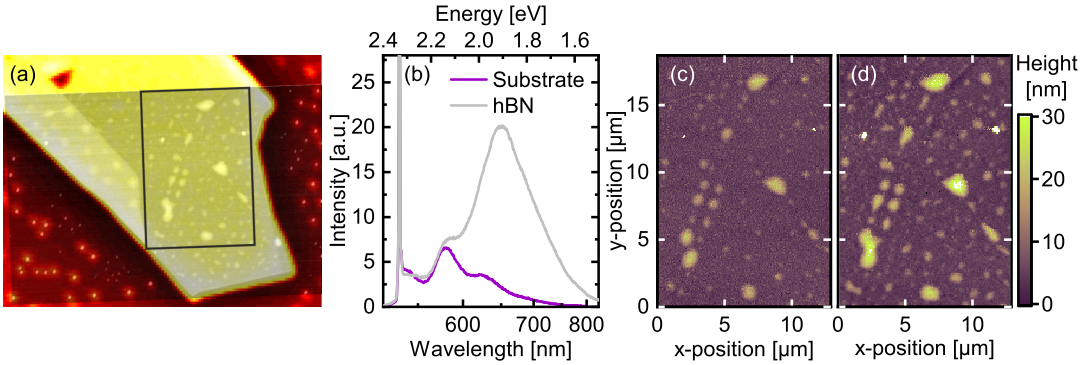

Figure S6: (a) Overlay of AFM topography (gray scale) and FLIM intensity map (fire color scale, logarithmic) of TVD-coated hBN flake, as already presented separately in Figure 3 (b) and (c). The positions of the "dots" on the substrate coincide for both images. The black rectangle marks the area depicted in (c) and (d). (b) µ-PL spectra of the different sample regions. While on the substrate, the spectrum remains similar to the monomer, it is dominated by a broad, low-energy contribution in the hBN region. This contribution is even red-shifted with respect to the excimer bands discussed in section 1.1. (c, d) AFM topography of the area marked in (a) before (c) and after (d) molecule deposition. The initially present blobs grow in height and area, some merge and even new ones are created.

On the 2D material flakes, we observe a growth in height at the crystal edges that – in case of the hBN – is accompanied by an enhanced fluorescence from the flake area with an even brighter region at the flake rim. We conclude the migration of molecules from the top and surrounding of the flakes into the cleft between flake and substrate. In other studies, however, height increases have been observed upon 200 s of irradiating WSe_2 flakes with a laser intensity of 5.1 mW at 532 nm focused through a 100x objective[16]. Here, the proposed explanation was photo-assisted formation of WO_3. In our case, in contrast, the FLIM was conducted after the first AFM measurements and excitation powers of only 12.5 µW were applied using a 20x objective. Hence, we exclude a photo-assisted oxidation as the cause for the growth of the flake heights.
In addition to the height increase at the flake edges, we observe blobs on the blank crystals that enlarge and in part even fuse, as depicted in Figure S6 (c) and (d). Since they are lacking phase contrast, we conclude that the respective material resides below the surface. Consequently, as the flake is locally elevated, they form a cavern that has to be supported by some material functioning as a pillar. Although we expect an accumulation of material, especially when the blobs grow during the PO deposition, no signs of an pronounced PO coverage is observed in the FLIM intensity maps of these regions. Ergo, we characterize these features as traps for adsorbed gases or other molecules, accumulating in the initially present blobs and thus contributing to their growth. This might have happened even before the dye molecule deposition during the evacuation of the TVD chamber.

4 Optical characterization

4.1 Multi-particle excitations at low temperatures

The charge of the trions observed in low-temperature measurements crucially determines the discussion about possible charge transfer and its direction in the PO/WSe_2 hybrid presented in the main body, Figure 3. To further investigate and distinguish the emission contributions, we performed µ-PL spectroscopy at 10 K. The resulting spectrum is shown in Figure S7.

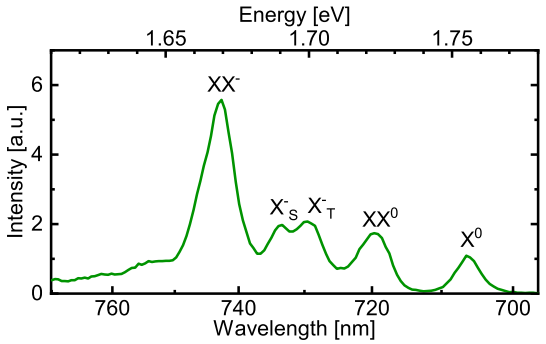

Figure S7: PL spectrum of PO/WSe_2 hybrid structure at 10 K. Several distinct peaks occur red-shifted from the neutral exciton emission (X^0). The double feature at around 1.7 eV is a characteristic of negative trions, while the remaining features are attributed to (charged) biexcitons.[26]

Following the trend of the measurements at room temperature and 80 K in Figure 3 of the main body, the WSe_2 emission is split up into multiple peaks, with the excitonic one as the energetically highest. Here, the occurrence of a double feature is a clear sign for negative trions, which subdivide into a singlet and triplet band. In contrast, the interpretation as well as the positions and relative distances of the remaining peaks vary in literature and supposedly depend strongly on the sample quality.[26–29]
From these results, we conclude that the WSe_2 flake is n-doped. Consequently, the additional PL peak at 80 K can be assigned to negative trions as well (see Figure 3 of the main body).

4.2 Agglomerate formation and dynamics on hBN3

To elucidate whether agglomeration effects play a role in the signal intensity and dynamics of the hBN1 and 2 samples, we TVD-coated the hBN3 sample with a higher molecular coverage, provoking the formation of dye agglomerates. Figure S8 (a) shows the corresponding FLIM intensity map, with bright spots on the hBN indicating the formation of agglomerates. Interestingly, this takes place only on the flake, while the intensity is equally distributed on the wafer substrate, as opposed to what was observed in the AFM measurements (chapter 3). We suppose the difference to originate from the long evacuation time in the preparation of the AFM samples. Without this, only the flat and inert hBN surface offers a mobility high enough for the molecules to meet each other to form larger structures, in contrast to the rough SiO_2 with its dangling bonds. however, when other adsorbates are largely removed before molecule deposition, the mobility is generally higher, allowing for agglomerate formation on the wafer. For the hBN, the dye mobility under this conditions is so high, that the molecules are able to migrate below the flake, as discussed before in section 3.
In the case of the hBN3 sample, we analyzed the temporal evolution of the fluorescence separately for the dots as well as the homogeneous background on the flake. The resulting time traces are depicted in Figure S8 (b), the parameters extracted from biexponential fitting are listed in the main body, Table 1. Here, the homogeneous part of the PO/hBN3 hybrid is dominated by the $\approx$ 3 ns decay associated with unquenched monomer PO. The fluorescence from the bright

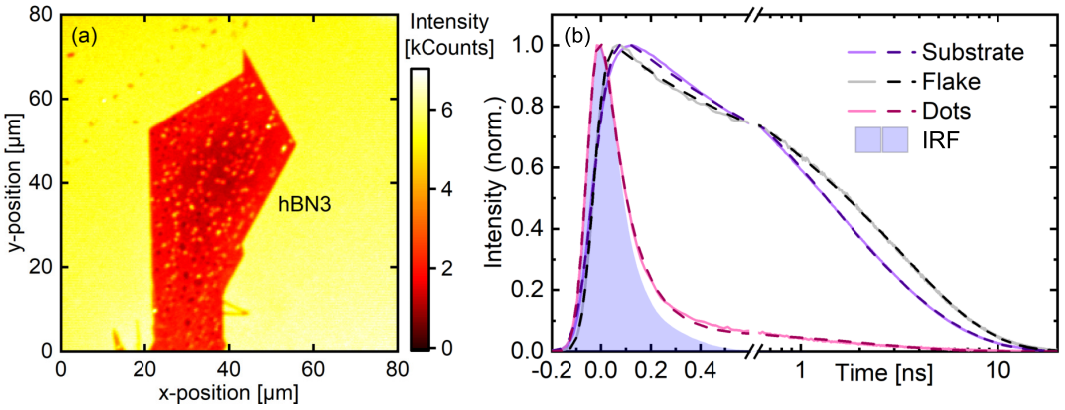

Figure S8: FLIM measurements of PO/hBN3. (a) Intensity map of PO-coated hBN3 flake and its surroundings. While the signal is homogeneous on the wafer, bright dots stand out from the flake area. In between these spots, the intensity grows only gradually from the inner region towards the rim. (b) Time traces from the different areas from (a). While for the substrate and the homogeneous part of the flake, the signal is long-living, it rapidly decreases at a similar speed as the IRF on the dots. Experimental data is depicted as pale and solid, fits as dark and dashed lines.

spots, however, essentially falls with the shape of the IRF, leaving merely a minor long-term contribution to the signal. We conclude that in the vicinity of the agglomerates, the excitons created upon pump absorption get quickly trapped in lower-lying excimer states, that emit light further in the red[6], which is barely transmitted by the bandpass filter (see section 1). The slow component of the decay may originate from the blue tail of this broad excimer emission or from monomer PO that resides too far from the relatively small agglomerates to get quenched by them but still resides and emits in the relatively large probe spot.

Given the variety in the size or brightness of the dots, we presume the existence of smaller agglomerates even on our standard samples. Note that due to their inherent quenching mechanism, this accumulation of dye will not result in an increase in fluorescence intensity until there is such a high number of molecules that their residual emission in the spectral range from 500 to 550 nm exceeds the monomer fluorescence of the surrounding homogeneous PO coating. Ergo, agglomerate formation will manifest in the time traces to start with. This explains the biexponential character of the monomer PO fluorescence decay on all hBN flakes. Additionally, these findings provide an approach to account for the different behavior of the hBN1 and hBN2 samples. The varying fluorescence intensity and contribution of the fast decay probably originate from slightly fluctuating molecule coverage in combination with different surface qualities of the two flakes, resulting in the formation of more or less agglomerates.

4.3 FLIM data of remaining flakes

In this part, we present the intensity maps for the remaining samples, whose relative intensities were analyzed in the main body, in the section "Rapid fluorescence quenching in TMDC hybrids". They were acquired with the same parameters, including the use of the band pass filter. The FLIM maps as well as the corresponding micrographs are depicted in Figure S9. Like for the hBN1 and WSe_2 flakes, we observe only a weak contrast between the insulating hBN flakes and their surroundings, while on the TMDC crystals, the fluorescence intensity of the PO is drastically reduced by up to three orders of magnitude. This demonstrates the quenching of the dye emission due to the charge or energy transfer from the excited molecules towards the underlying TMDC. Note that for the 1L-WS_2 flake, there is still some remaining signal from the monolayer photoluminescence transmitted by the filter.

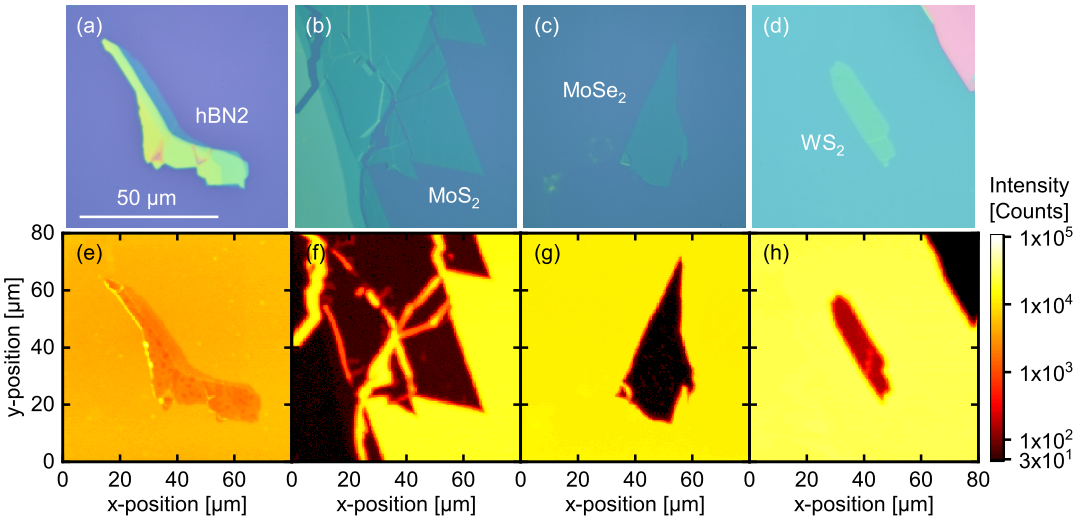

Figure S9: FLIM measurements of remaining hybrid structures. (a-d) Micrographs of hBN and 1L-TMDC flakes. (e-h) FLIM intensity maps of the regions depicted in (a-d). While for the hBN sample, the intensity difference between substrate and flake is comparably small, it exceeds two orders of magnitude in case of all the TMDCs. The intensity values from these measurements were used to calculate the quenching as shown in Figure 4 of the main body, while the corresponding time traces appear in Figure 5.

4.4 FLIM measurements without band pass filter

As mentioned in the main body, the advantages of the band pass filter are the exclusion of the 1L-TMDC photoluminescence as well as of the PO excimers or other agglomeration species. Here, we present an exemplary measurement on the WS_2 flake without the filter, see Figure S10 (a) and (b). Unlike in the filtered case, the TMDC flake stands out with a much higher intensity here, as the 1L photoluminescence is even stronger than the dye emission. Consequently, the detected intensity ratio does not relate to the quenching of the fluorescence anymore. This can also be

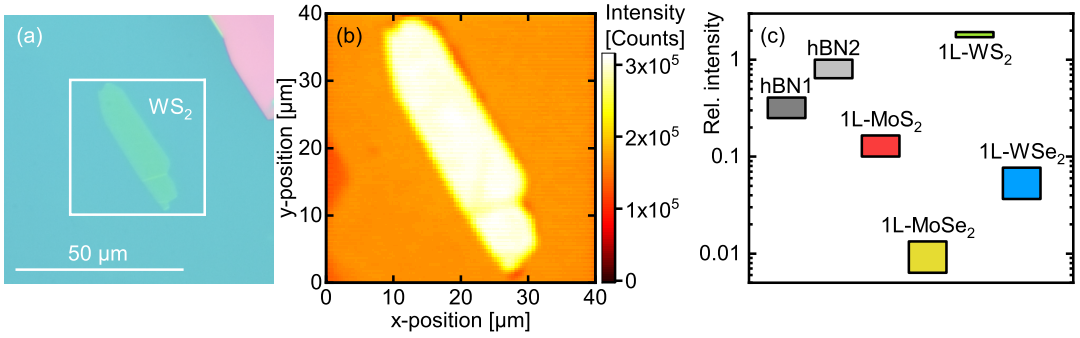

Figure S10: FLIM measurements without band pass filter. (a) Micrograph of the investigated WS_2 flake. The white square marks the area shown in (b). The flake is identical to Figure S9 (d). (b) FLIM intensity map of the area depicted in (a). In contrast to the measurements using a band pass filter, the flake clearly stands out brighter than its environment. (c) FLIM intensities on the different 2D material flakes relative to the respective substrate surroundings. Unlike for the filtered measurements, the intensities for the various TMDCs significantly differ from each other, with the 1L-WS_2 even exceeding the signal strength on the hBN flakes as well as the substrate. Generally, the relative intensities are higher than for the measurements using the filter.

deduced from Figure S10 (c), where the relative intensities of various flakes are compared. The TMDC intensities follow the same pattern as in the FLIM characterization before the molecule deposition, suggesting that those signals mostly originate from the flakes' photoluminescence. Ergo, the analysis of time traces would not yield any further information, as it would only show the decay of the TMDC-PL caused by exciton recombination, on a timescale of some 10 ps or even below[30–32], which hardly reaches the time resolution of these measurements.

4.5 Polarization-dependence of the fluorescence

Despite its function as a reference, we additionally used the hBN1 sample for polarization-dependent measurements, to trace any orientation preferences of the molecules relative to the hexagonally structured hBN surface. To that end, we kept the linear polarization of the excitation light fixed and rotated the wafer for consecutive scans. We then compared the intensity ratio between the (unordered) wafer substrate and that on the hBN between the different orientations. Statistical uncertainties arise from focus readjustments before each scan as well as the laser power fluctuations. Eventually, as demonstrated in Figure S11 (b), no systematic behavior was found, especially none with the expected periodicity of 60°. Au contraire, the ratio rather fell with the number of scans performed (Figure S11 (a)), pointing to a successive degradation of the molecules that proceeds faster on the hBN than on the wafer. Interestingly, the sharpest drop occurred during the 24-hour break between scan seven and eight, in which the sample was exposed to no laser light.

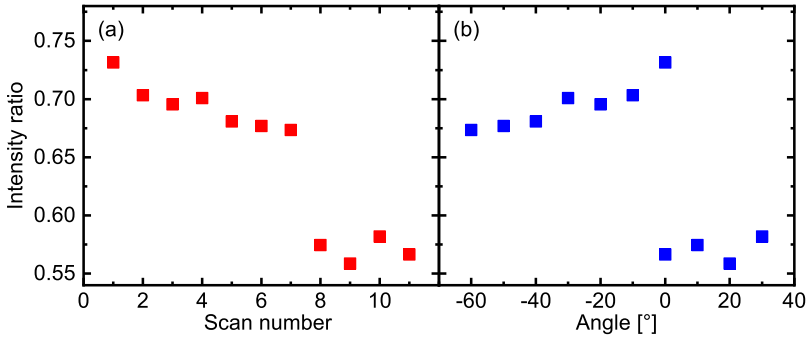

Figure S11: Investigation of polarization dependence of dye emission on the hBN1 flake in terms of the FLIM intensity ratio between flake and wafer plotted over (a) the temporal scan order and (b) the angle of the sample's in-plane orientation. (a) The intensity falls over time. Note that the change from scan seven to scan eight corresponds to a time span of one day, in which the measurements were interrupted. (b) No systematic dependence on the orientation angle ist observed. Especially the two measurements at 0° show that the changes over time dominate versus any potential polarization behavior.

References

[1] R. F. Fink, J. Seibt, V. Engel, M. Renz, M. Kaupp, S. Lochbrunner, H.-M. Zhao, J. Pfister, F. Würthner and B. Engels, *Journal of the American Chemical Society*, 2008, **130**, 12858–12859.

[2] D. Schmidt, M. Stolte, J. Süß, A. Liess, V. Stepanenko and F. Würthner, *Angewandte Chemie International Edition*, 2019, **58**, 13385–13389.

[3] Y. Shen, Z. Zhang, H. Liu, Y. Yan, S. Zhang, B. Yang and Y. Ma, *The Journal of Physical Chemistry C*, 2019, **123**, 13047–13056.

[4] R. D. Pensack, R. J. Ashmore, A. L. Paoletta and G. D. Scholes, *The Journal of Physical Chemistry C*, 2018, **122**, 21004–21017.

[5] Y. J. Bae, D. Shimizu, J. D. Schultz, G. Kang, J. Zhou, G. C. Schatz, A. Osuka and M. R. Wasielewski, *The Journal of Physical Chemistry A*, 2020, **124**, 8478–8487.

[6] A. L. Bialas and F. C. Spano, *The Journal of Physical Chemistry C*, 2022, **126**, 4067–4081.

[7] G. Seybold and G. Wagenblast, *Dyes and Pigments*, 1989, **11**, 303–317.

[8] F. Würthner, *Chem. Commun.*, 2004, 1564–1579.

[9] A. Castellanos-Gomez, M. Buscema, R. Molenaar, V. Singh, L. Janssen, H. S. J. van der Zant and G. A. Steele, *2D Materials*, 2014, **1**, 011002.

[10] J. Lub, P. A. van Hal, R. Smits, L. Malassenet, J. Pikkemaat and R. A. Hikmet, *Journal of Luminescence*, 2019, **207**, 585–588.

[11] D. Nečas and P. Klapetek, *Open Physics*, 2012, **10**, year.

[12] H. Lüth, *Solid Surfaces, Interfaces and Thin Films*, Springer Berlin Heidelberg, 2010, pp. 67–131.

[13] D. Wickramaratne, L. Weston and C. G. V. de Walle, *The Journal of Physical Chemistry C*, 2018, **122**, 25524–25529.

[14] J. Wilson and A. Yoffe, *Advances in Physics*, 1969, **18**, 193–335.

[15] M. M. Benameur, B. Radisavljevic, J. S. Héron, S. Sahoo, H. Berger and A. Kis, *Nanotechnology*, 2011, **22**, 125706.

[16] H. Li, G. Lu, Y. Wang, Z. Yin, C. Cong, Q. He, L. Wang, F. Ding, T. Yu and H. Zhang, *Small*, 2012, **9**, 1974–1981.

[17] D. den Boer, M. J. J. Coenen, J. A. A. W. Elemans and S. Speller, *Encyclopedia of nanoscience and nanotechnology*, American Scientific Publishers, Stevenson Ranch, Calif, 2nd edn, 2011, vol. 22.

[18] J. M. MacLeod and F. Rosei, *Small*, 2013, **10**, 1038–1049.

[19] S. J. Stranick, M. M. Kamna and P. S. Weiss, *Science*, 1994, **266**, 99–102.

[20] P. Matvija, F. Rozbořil, P. Sobotík, I. Ošt'ádal and P. Kocán, *The Journal of Physical Chemistry Letters*, 2017, **8**, 4268–4272.

[21] C. Paris, A. Floris, S. Aeschlimann, J. Neff, F. Kling, A. Kühnle and L. Kantorovich, *Communications Chemistry*, 2018, **1**, year.

[22] S. Koslowski, D. Rosenblatt, A. Kabakchiev, K. Kuhnke, K. Kern and U. Schlickum, *Beilstein Journal of Nanotechnology*, 2017, **8**, 1388–1395.

[23] Z. Wang, R. Li, C. Su and K. P. Loh, *SmartMat*, 2020, **1**, year.

[24] Q. Cao, F. Grote, M. Huβmann and S. Eigler, *Nanoscale Advances*, 2021, **3**, 963–982.

[25] F. Zhang, Y. Ma, Y. Chi, H. Yu, Y. Li, T. Jiang, X. Wei and J. Shi, *Scientific Reports*, 2018, **8**, year.

[26] J. Jadczak, M. Glazov, J. Kutrowska-Girzycka, J. J. Schindler, J. Debus, C.-H. Ho, K. Watanabe, T. Taniguchi, M. Bayer and L. Bryja, *ACS Nano*, 2021, **15**, 19165–19174.

[27] E. Courtade, M. Semina, M. Manca, M. M. Glazov, C. Robert, F. Cadiz, G. Wang, T. Taniguchi, K. Watanabe, M. Pierre, W. Escoffier, E. L. Ivchenko, P. Renucci, X. Marie, T. Amand and B. Urbaszek, *Physical Review B*, 2017, **96**, 085302.

[28] E. Liu, J. van Baren, C.-T. Liang, T. Taniguchi, K. Watanabe, N. M. Gabor, Y.-C. Chang and C. H. Lui, *Physical Review Letters*, 2020, **124**, 196802.

[29] M. Yang, L. Ren, C. Robert, D. V. Tuan, L. Lombez, B. Urbaszek, X. Marie and H. Dery, *Physical Review B*, 2022, **105**, 085302.

[30] D. Lagarde, L. Bouet, X. Marie, C. R. Zhu, B. L. Liu, T. Amand, P. H. Tan and B. Urbaszek, *Physical Review Letters*, 2014, **112**, 047401.

[31] E. A. A. Pogna, M. Marsili, D. D. Fazio, S. D. Conte, C. Manzoni, D. Sangalli, D. Yoon, A. Lombardo, A. C. Ferrari, A. Marini, G. Cerullo and D. Prezzi, *ACS Nano*, 2016, **10**, 1182–1188.

[32] T. Völzer, F. Fennel, T. Korn and S. Lochbrunner, *Physical Review B*, 2021, **103**, 045423.

[P3]

Having a good vibe: Strong coupling to the electronic system creates incoherent and coherent phonons in 1L-TMDCs

Tim Völzer, Marvin Krupp, Julian Schröer, Annika Bergmann-Iwe, Tobias Korn, and Stefan Lochbrunner

2D Mater. 2025, **12**, 035012

https://doi.org/10.1088/2053-1583/addf5a

Reprinted from *2D Mater.* 2025, **12**, 035012.

In the initially submitted version of this thesis, the corresponding revised and submitted manuscript was included. After the latter being accepted by the journal, it was replaced by the final publication in this updated version.

IOP Publishing 2D Mater. 12 (2025) 035012 https://doi.org/10.1088/2053-1583/addf5a

2D Materials

PAPER

Having a good vibe: strong coupling to the electronic system creates incoherent and coherent phonons in 1L-TMDCs

T Völzer[1,2], M Krupp[1,2], J Schröer[1,2], A Bergmann-Iwe[1,2], T Korn[1,2] and S Lochbrunner[1,2,*]

[1] Institute of Physics, University of Rostock, Albert-Einstein-Str. 23, 18059 Rostock, Germany
[2] Department 'Life, Light & Matter', University of Rostock,Albert-Einstein-Str. 25, 18059 Rostock, Germany
* Author to whom any correspondence should be addressed.

E-mail: stefan.lochbrunner@uni-rostock.de

Keywords: coherent phonons, transition metal dichalcogenides, transient absorption spectroscopy, electronic dynamics, Raman modes

Supplementary material for this article is available online

OPEN ACCESS

RECEIVED
20 November 2024

REVISED
17 February 2025

ACCEPTED FOR PUBLICATION
2 June 2025

PUBLISHED
12 June 2025

Abstract

The electronic dynamics in monolayer transition metal dichalcogenides (1L-TMDCs) following optical excitation crucially determine all their optoelectronic applications. The basic processes can be divided into energy redistribution leading to a thermal equilibrium of the electronic and the phononic system, and the recombination of the excited species. Furthermore, the displacive excitation of coherent phonons assigned to the A_1' Raman mode has been demonstrated employing sufficiently short pump pulses. In this study, we shed light on the ultrafast dynamics of three different 1L-TMDCs using transient absorption spectroscopy. We reveal a cascade-like cooling of the excited electronic states, owing to their differing coupling strengths to high- versus low-energy phonons. In addition, the coherently excited lattice vibrations imprint a strong oscillatory contribution onto the signal. We extract a dominating, spectrally broad signature of the A_1' mode, whose shape challenges existing models. On top of that, we identify a second frequency band matching the E' Raman peak in 1L-WS_2. Finally, measurements at high pump fluences demonstrate a phonon bottleneck for the cooling cascade. Simultaneously, the dominant A_1' mode softens, providing a new degree of tunability for these coherent lattice vibrations. Overall, our findings demonstrate the strong couplings between the electronic and phononic (sub)systems in 1L-TMDCs.

1. Introduction:

Over the past 15 years, transition metal dichalcogenides (TMDCs) have risen as versatile 2D materials [1, 2]. Their atomically thin monolayers (1L) drew particular interest of the scientific community, owing to their direct band gaps and extraordinarily high exciton binding energies [3–5]. These properties essentially constitute a new kind of material, highly suitable for (opto)electronic applications [6, 7]. Indeed, a plethora of devices have been fabricated, ranging from light-emitting diodes [8] and photodetectors [9, 10], up to solar cells [7, 11]. Common to these applications is their critical dependence on decent exciton mobilities and lifetimes. In this light, the ultrafast dynamics of 1L-TMDCs have been extensively studied by different, complementing methods. Time- and angle-resolved photoelectron spectroscopy is able to localize electronic populations and identify their relaxation pathways in the Brillouin zone [12]. It showed ultrafast scattering of non-resonantly excited electrons towards the conduction band minimum. THz pump-probe spectroscopy, in contrast, facilitates the distinction between bound and free carriers [13]. According to that work, exciton and hot carrier populations coexist in equilibrium for several picoseconds due to persisting high electronic temperatures. Here, the different coupling of high- vs. low-frequency phonons to the carriers and excitons governs the thermal equilibration of the electrons with the lattice. Furthermore, optical transient absorption (TA) spectroscopy provides a tool for thorough analyses of excitation density-dependent femtosecond to nanosecond dynamics as well as the spectral fingerprints of excited species [14–19]. In this technique, the high

IOP Publishing 2D Mater. 12 (2025) 035012 T Völzer et al

electronic temperatures manifest in the form of significant peak broadening [15, 19, 20]. On top, these studies have found the signal decay to be determined by the diffusion of excitons and defect-associated trap states that catalyze their recombination [14, 17–20].

In the past years, the advancing time resolution of TA experiments has facilitated the investigation of coherent phonons, i.e. lattice vibrations coherently excited by an ultrashort pump pulse [21]. The theoretical concept as well as different underlying mechanisms have been proposed decades ago, differentiating between displacive excitation of coherent phonons (DECP) and impulsive stimulated Raman scattering (ISRS) [22, 23]. Likewise, such signatures with frequencies of up to a few THz are well-known in metals and semiconductors [22] as well as topological insulators [24]; even layered materials [25, 26] and TMDCs [27]. However, they have only recently been observed in the transient signals of the most common 1L-TMDCs [28–30]. Their oscillations have remained hidden, due to their high frequencies that require both the pump and the probe process to take place within less than half of the vibrational period. In these materials, the coherent excitation of one particular vibrational mode has been demonstrated, namely the symmetric out-of-plane displacement of the chalcogen atoms in the monolayer, denoted as $A_1^{'}$. The second typical mode $E^{'}$ describes the opposing in-plane motions of chalcogen and transition metal atoms. These two vibrations play an important role in the characterization of atomically thin TMDC flakes via Raman spectroscopy, as they are sensitive to the layer number, doping and strain [31], as well as temperature [32, 33]. Yet, only the displacive excitation of $A_1^{'}$ has been described in TA experiments, owing to its high symmetry [22, 29].

The spectral signatures of the aforementioned mode have been theoretically approached by band structure calculations for an accordingly distorted crystal lattice. This yields a good agreement with the data for $MoTe_2$ [34], while exhibiting a clear discrepancy in the case of MoS_2 [29]. On top of that, the band structure is predicted to change under atom displacements along the $E^{'}$ mode as well, albeit having a smaller impact than for $A_1^{'}$ [28].

In this work, we investigated the dynamics of three different 1L-TMDCs (WS_2, WSe_2, and $MoSe_2$) using TA spectroscopy with a high time resolution. We focus on the coupling between the electronic and phononic system. This interaction causes the excitation of coherent phonons via absorption of optical pulses as well as phonon-mediated thermalization and cooling. For the latter, we find a stepwise process successively involving different phonon species, which manifests in the reduction of collisional peak broadening. The oscillatory dynamics are mostly attributed to the $A_1^{'}$ mode for all materials. However, in contrast to previous studies, we provide evidence for the involvement of the $E^{'}$ mode as well. All in all, our study demonstrates the strong coupling between the electronic and phononic system of 1L-TMDCs and sheds light on how this coupling depends on the excited states and the modes at play.

2. Methods

1L-TMDC flakes were mechanically exfoliated from thick WS_2, WSe_2, and $MoSe_2$ crystals (HQ graphene). Subsequently, they were deterministically transferred [35] to glass cover slips with thicknesses of about 100 μm to 150 μm.

The TA setup mainly follows the typical scheme [36, 37] plus incorporating several optimizations regarding sensitivity and time resolution. The supplementary material (SM) contains a schematic of the experimental layout in figure S1 and a more detailed description of its functionality in section 1. The setup was fed by the fundamental pulses of a Ti:Sa amplifier (Spitfire PRO, Spectra Physics), around a center wavelength of 800 nm and with pulse lengths of $\approx$ 50 fs at a repetition rate of 1 kHz. The pump pulses for excitation were generated in a noncollinear optical parametric amplifier (NOPA) [38], tuned to a center wavelength of 530 or 595 nm with a bandwidth of 35 and 50 nm, respectively. They were compressed using chirped mirrors, yielding pulse lengths below 20 fs in both cases. The probe pulses, originating from a broadband NOPA [39], cover a wavelength range from 500 nm to 800 nm but remain uncompressed and chirped. All in all, this yields a time resolution of up to 45 fs, see SM, figure S2. The two beams were focused onto the sample. We achieved spot sizes in terms of e^{-2}-diameters of less than 15 μm for the probe, using an off-axis parabolic mirror, and 110 μm for the 530 nm pump (280 μm for 595 nm). The spectrally resolved detection of the probe light was implemented using fused silica prisms for dispersion and a two-camera setup, splitting the beam using a wedge plate. Here, the weaker, reflected part passes the sample as described above and its spectral intensity is detected by the first camera. The second camera collects and monitors the transmitted part of the probe, i.e. a reference beam, allowing for a correction of intensity fluctuations. The pump and both probe beams were simultaneously chopped at one half and one quarter of the laser repetition rate, respectively. Thereby, we create a four-shot pattern, facilitating real-time tracking of dark current and scattered light. These terms refer to the camera signals without illumination and with only the excitation light being present, respectively, in addition to the probe intensity with and without preceding pump pulse used in standard TA setups. Finally, the ratio of the latter two leads to the absorption change induced by the excitation of the sample.

Raman spectroscopy was performed as a continuous wave experiment, using a 532 nm diode-pumped solid state laser for WS_2 and a 633 nm diode laser

IOP Publishing 2D Mater. 12 (2025) 035012 T Völzer et al

for the selenides. The excitation light was focused onto the sample by a 100x objective, with a spot size of about 1 μm. The sample itself was mounted onto an xy-stage to move the area of interest into the focus. The emitted light was captured with the same objective in a backscattering geometry. On its way to the detection, it passes through a longpass filter to block backreflected excitation light. Finally, the beam is guided into a grating spectrometer, where the spectral intensity is measured by a charge-coupled device (CCD) sensor, thermoelectrically cooled to −70 °C.

3. Photoinduced peak shift and broadening dynamics

To unravel the ultrafast dynamics in 1L-TMDCs, we performed TA spectroscopy. We excited the samples at 530 nm and probed from 500 nm to 800 nm for logarithmically spaced probe delays up to 100 ps. At this point, we focus on WS_2, as it yields relatively clear and well-separated spectral contributions (see figure 1). Around 2 eV, a pair of a positive (A^+) and a negative (A^-) peak characterizes the spectra. Since the reduced absorbance A^- matches the position and width of the A exciton absorption band [40, 41], these signatures are generally attributed to a photoinduced red-shift of the excitonic A band. The same effect occurs for all major absorption bands in $MoSe_2$ and WSe_2 as well, see SM, figures S3 and S4, respectively. Such a shift in TMDCs may be caused by either band gap renormalization induced by delocalized excited species [16, 17, 42–44], or localized excitations deforming the energetic landscape in a limited volume, i.e. polarons [19, 45, 46]. In the framework of such shift mechanisms, the A^- peak represents the original, static absorption that is now lacking. Consequently, it remains constant in position and shape and varies only in intensity, as time proceeds or the excitation fluence changes. A^+, on the other hand, which embodies the shifted absorption of the excitonic band after excitation, is subject to significant broadening. The peak width increases with fluence and decreases over time, hence seeming to be somehow related to the excited species. Indeed, this behavior has been reported as the result of collisional broadening [14, 15, 19, 43]. Moreover, the high fluences exceeding the Mott density ($\approx 1 \times 10^{14}\,\mathrm{cm}^{-2}$ [5, 43], $\simeq 400\,\mu\mathrm{J\,cm}^{-2}$) may result in fast exciton dissociation, thus broadening the excitonic absorption signature A^+ even further. Both aforementioned effects constitute a nonlinear response of the material. In addition to the $A^\pm$ peak pair, the high-energy side of the spectrum exhibits a broad, almost spectrally constant feature F^+ without any correlation to the excitonic transitions. These three major signatures differ from each other with respect to their fluence dependence. On the one hand, A^- saturates already at comparably weak excitation and A^+ broadens continuously, proving nonlinear behavior at high excitation densities. On the other hand, F^+ grows quite proportionally with rising fluence, suggesting a still rather linear absorption of the pump pulses (see figure S5 for a detailed analysis).

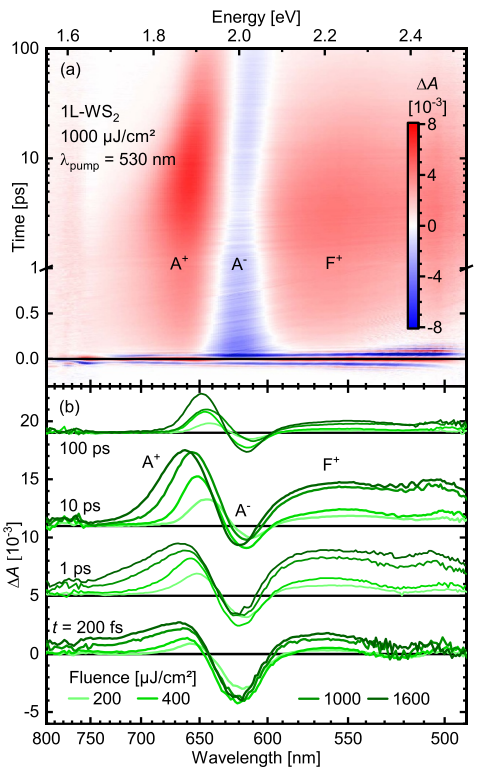

Figure 1. Spectral shape and evolution of TA signal of 1L-WS_2. (a) Spectrally and time-resolved 2D map of the change in absorbance ΔA for 1L-WS_2 excited at 530 nm with a fluence of 1000 μJ cm^{-2}. (b) Excitation fluence-dependent TA spectra at characteristic times. The curves are shifted for clarity but share the identical, original scaling. Generally, the signal is characterized by a pair of a negative peak A^- around 2.0 eV and a red-shifted positive one A^+ as well as a broad, roughly constant feature F^+ at higher energies.

Generally, these findings hold for 1L-WSe_2 and 1L-$MoSe_2$ as well (see figure 3 and SM, figures S3 and S4). The major limitation is that these two materials exhibit multiple excitonic transitions in the studied wavelength range. Thus, the stronger overlap of the corresponding TA signatures impedes the clear separation of the spectral components and complicates the dynamics.

To further characterize the nature of the broad F^+ contribution as well as to shed light on the dynamical processes at play in this system, we globally fitted the 2D TA data using four exponential decays (plus an oscillatory component, see section 4). The exact fitting function and a comparison between data and fit are given in the SM, section 2.3 and figure S6. There, we notice that the interval of ±100 up to ±200 fs around time zero is dominated by the coherent artifact. It contains the optical nonlinearities

IOP Publishing 2D Mater. 12 (2025) 035012 T Völzer et al

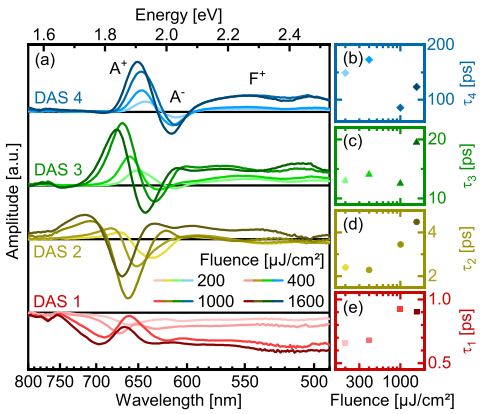

Figure 2. Global fitting analysis of 1L-WS_2 TA data, based on four exponential decays. (a) Amplitude spectra corresponding to the four decays for various fluences. (b)–(e) Fluence dependence of time constants corresponding to the DAS. While the three fastest decays show a deceleration with increasing fluence, no systematic behavior is revealed for the slowest process.

that alter the spectrum when pump and probe overlap temporally and depends largely on the intensities [47]. Consequently, it is determined by the pulse lengths. To avoid corruption of the fit due to this artifact, we cut the data before 0.2 ps in advance. This multiexponential fit generally describes the data reasonably well, although a number of factors impede an exact agreement with the data: First, the long-term dynamics exceed the investigated time span of 100 ps. Second, the signal decay in TMDCs is known to be largely governed by more complex recombination and trapping mechanisms such as exciton diffusion and Auger scattering [18, 19]. Finally, peak broadening or narrowing (as well as shifts) will intrinsically produce non-exponential time traces, regardless of their underlying temporal evolution. As a result, the fitted curves slightly deviate from the data, especially at later times and at the flank of the A^+ peak. Still, despite its limited accuracy in this case, the global analysis provides a powerful tool to separate the different occurring processes, extract their spectral signatures, and reveal fluence-related trends in their time constants.

The resulting decay-associated amplitude spectra (DAS) and time constants τ_i for the four exponentials are depicted in figure 2 for different excitation fluences. With regard to the fastest process, a broadband negative feature with a cut-off below approximately 1.7 eV to 1.8 eV constitutes the DAS 1. As there is no such signal that could decay, this component rather describes the retarded growth of the F^+ signature. Evidently, F^+ spans the spectral range of the excitonic $A^\pm$ bands as well. Consequently, its emergence manifests as an apparent shrinkage of A^- and rise of A^+, even though the DAS 1 exhibit only minor modulations in that spectral range, i.e. only minor dynamics of the excitonic peaks occur at short times. In particular, we observe no change of the A^+ peak shape. Via collisional broadening, its width is linked to the excess energy of the excited species - excitons as well as electrons and holes in the conduction and valence band, respectively. With this in mind, the DAS 1 show no sign of substantial heat exchange with the lattice. Consequently, we assume an energy redistribution within the electronic system. As a matter of fact, such a broadband increase of the TA (or decrease of the transient transmission) within the first picosecond like for the DAS 1 or with rising fluence can be found in the data of numerous previous works [15, 16, 20, 43, 44, 48]. It has been attributed to the formation of charge carriers as opposed to the initially excited excitons [44, 48]. Indeed, THz experiments have observed that free carriers and excitons form an equilibrium on similar, subpicosecond time scales [13]. The electronic system relaxes into a thermal balance between free and bound charge carriers located in the vicinity of the band extrema. Due to the high electronic temperature, the distribution between these two species might be almost even. This equilibrium may even be shifted further towards free carriers, taking the high excitation densities in the range of the Mott density into account [43]. It appears that this equilibrated electronic population causes an unstructured, additional absorption above the optical band gap.

The DAS 2 embody fluence-dependent narrowing dynamics of the positive excitonic peak A^+. The spectra are constituted by a strong dip roughly at the A^+ position framed by two weak positive features. For the given broad shape of the peak, this means a growing amplitude at the peak center and a simultaneously shrinking one at the flanks. Consequently, the shape narrows, as already observed in figure 1. In the framework of collisional broadening, the spectral width of the absorption bands is determined by both the density as well as the temperature of the excited species [49]. Since the former does not change significantly on these short time scales [16, 18, 19, 50], the narrowing indicates a cooling of the excited species, reducing their collision rate. Interestingly, despite the cooling, the thermal equilibrium between excitons and free charge carriers is not substantially effected. Apparently, the electronic temperature still remains relatively high. This phenomenon can be explained by a hot-phonon effect [51–54]: As per this model, high-energy phonons couple more strongly to the electronic system than low-energy ones, therefore the former two rapidly reach a thermal equilibrium. However, these high-energetic lattice vibrations make up just a fraction of the phononic spectrum and - correspondingly - of its heat capacity. Ergo, the electronic temperature yet lies way above that of the remaining lattice. On top of that, the hot phonons

IOP Publishing 2D Mater. 12 (2025) 035012 T Völzer et al

may be reabsorbed by the electronic system, creating a dynamic equilibrium that preserves the elevated temperatures. As a matter of fact, values of about 1500 K persisting for more than 5 ps have been reported in 1L-WSe_2 already for fluences one order of magnitude below the ones employed in this work [13]. In addition to the narrowing dynamics, the contributions in the DAS 2 indicate that the A^+ peak is further red-shifted at higher fluences. We suppose that this originates from the band gap shrinkage associated with the elevated temperature of the high-energetic phonon subsystem. This occupation of vibrational modes may slightly displace the mean positions of the atoms, thus modifying the energy of the optical transitions.

As a third step in the temporal evolution of the TA signal, we observe the reduction of the fluence-dependent red-shift of the A^+ peak within tens of picoseconds. The DAS 3 for the higher fluences exhibit a positive feature at the low-energy side and a negative one at the high-energy side of A^+, translating to a blue-shift. As we interpreted the initial red-shift of A^+ at high excitation densities in terms of an elevated (phononic) temperature, the DAS 3 corresponds to a further cooling of the electronic system and the hot phononic subsystem. Now, the low-energy phonons come into play, yielding a thermal equilibrium of both the whole lattice and the excited species. Hence, the balance between carriers and excitons tips in favor of the latter, thus simultaneously reducing the broadband F^+ contribution, which was associated with free carriers. For the lowest fluence, in contrast to the higher ones, the peaks in the DAS 3 happen to match the positions of the excitonic features $A^\pm$ instead of marking the red and blue tail of A^+. Ergo, the amplitude of the TA signal is reduced, indicating that recombination of excitons also plays some role on this time scale. In fact, recombination in monolayer TMDCs is known to proceed nonexponentially over tens up to hundreds of picoseconds, being governed by diffusion and trapping [18, 19]. Consequently, the spectral amplitude related to the final signal decay will be split up between the two slowest exponential components in our fit.

Indeed, recombination and the corresponding signal decay are what characterizes the final stage of the dynamics. The shape of the DAS 4, unlike in the two preceding steps, is largely independent of fluence, indicating a thermally rather equilibrated system. Furthermore, this underlines that the broadening and shift dynamics embodied by the DAS 2–3 do not result from the mere excited populations themselves but from the heat exchange with the lattice. If solely the density of the excited species were responsible for those effects, the differences in spectral shape between different fluences would persist until the end of the recombination. However, the shape of the DAS 4 is nearly identical for all excitation densities. Moreover, their two bands at about 1.9 eV and 2.0 eV match the $A^\pm$ contributions to the TA spectra, hence describing a mere decay of the remaining signal.

All of the discussed signatures occur in the other investigated TMDCs in a similar manner, as we show in the SM, figures S7 and S8. Here, unfortunately, multiple excitonic bands lie in the visible range. Their overlapping clouds the peak narrowing as well as shifts and thus poses a major restriction on the disentanglement of the dynamics.

Finally, we discuss the trends in the time constants of the four discussed processes, as different fluences were applied, see figure 2(b)–(e). For τ_1 to τ_3, we find a clear increase, ergo a deceleration of the dynamics with rising excitation density. This means that the thermalization and cooling - the energy redistribution steps - are slowed down at higher fluences. Chi *et al* [52] explained this phenomenon adducing three fundamental, nonlinear mechanisms. First, while a large population of excited species thermalizes, the target states will continuously build up a relevant occupation. For the remaining, still unthermalized particles, this results in less free states to relax into, constituting a bottleneck and thus slowing down the process. Second, excited populations induce Coulomb screening that might weaken the electron-phonon coupling. A final point results from the hot-phonon effect under the impression of the high fluences employed [52–54]. In this scenario, the cooling of the electronic system is accompanied by the creation of a substantial population of hot phonons, as discussed above. Consequently, electron-phonon coupling will not only result in creation of phonons anymore but will also include their reabsorption as well. This, in turn, represents a heat transfer back into the electronic system, hence slowing down its cooling and keeping the temperatures at a high level. The higher the excitation density, the more balanced the dynamic equilibrium between phonon creation and reabsorption will be, thus prolonging the cooling process. τ_4, in contrast, exhibits no systematic fluence dependence. Here, major fluctuations arise from the inaccuracy of the fit, owing to the limited investigated time interval and the nonexponential nature of the recombination. On top of that, the (normalized) signal evolution has been proven independent of the fluence [19]. However, the saturation of the excitonic peaks at high fluences near or above the Mott density could cause an apparent deceleration of the decay. In this regime, the signal amplitude barely changes with increasing fluence. Ergo, it does not change either as the excited species recombine, until their density falls below the saturation threshold. As a result, the observed decay occurs in a delayed or slowed-down fashion. Nevertheless, we can conclude that the values for τ_3 and τ_4, which contain the signal decline, are in line with the typical recombination timescales reported for 1L-TMDCs [16, 18, 19, 44, 48].

IOP Publishing 2D Mater. 12 (2025) 035012 T Völzer et al

All in all, the dynamics in 1L-WS_2 is characterized by three major steps: First, the excited species thermalize into a balance of carriers and excitons. Second, a cascade-like cooling of the electronic system takes place, initially by coupling to high-energy phonons and successively involving the lower-energetic ones. Lastly, the cooled species recombine.

4. Oscillatory signatures of Raman modes

Generally speaking, all three investigated TMDCs share the basic characteristics of the transient signals discussed above (see also SM, section 2.1). In a similar manner as for 1L-WS_2, the 2D map for 1L-$MoSe_2$ in figure 3(a) incorporates pairs of a short-wavelength negative and a long-wavelength positive peak each. They result from the discussed photoinduced red-shift of the original, static absorption bands. Here, the higher number of band transitions in the respective wavelength region manifests in numerous TA contributions. The low-energy side of the spectrum is characterized by the transient signatures A^- and $B^{\pm}$ attributed to the excitonic A and B direct band gap transitions, which are typical for TMDCs [40, 41]. The presumed A^+ peak already resides outside of the investigated spectral region. On the high-energy side, we find the footprint of the C transition that arises from band nesting [12, 19]. Again, the sequence of positive C^+ and negative C^- indicates a photoinduced absorption red-shift. Finally, the broad F^+ feature occurs, dominating especially the center of the spectrum and superposing C^+. Up to this point, the spectral signatures of both materials follow the same pattern.

Yet, there is a new feature to discover in 1L-$MoSe_2$ compared to 1L-WS_2. A closer look at the TA map reveals an oscillatory contribution in the early temporal evolution, which could not be seen as easily in 1L-WS_2. These periodical signatures are of fundamentally different nature than the electronic dynamics discussed up to this point, which all proceed monotonously. To capture the oscillations in detail, we repeated the TA measurement employing a shorter time axis ending already at 4 ps to 5 ps but in turn using fine, equidistant spacing of the time points. To isolate the oscillations, we again fitted the 2D data with three exponential decays. Unlike in section 3, the time trace for each wavelength pixel was analyzed separately to increase the fit accuracy. Subsequently, the fit result is subtracted from the data to obtain a residue that contains solely the oscillating part of the dynamics (see figure 3(b)). Indeed, we find a periodic pattern of negative and positive absorption changes lasting for several picoseconds. Interestingly, this pattern spans almost the entire spectral region, albeit with varying amplitude. Furthermore, the phase of this oscillation appears remarkably constant in the middle of the spectrum and changes only gradually towards the rim. To isolate and separate the frequency components present in the oscillatory residue of the TA data, we perform a fast Fourier transform (FFT) analysis. Comparing the frequencies found in the resulting spectra to known resonances of the material allows for the identification of the underlying physical processes. Indeed, the FFT analysis confirms a single peak at around 7 THz, shown in figure 3(c). This points towards a single characteristic vibrational mode being at play.

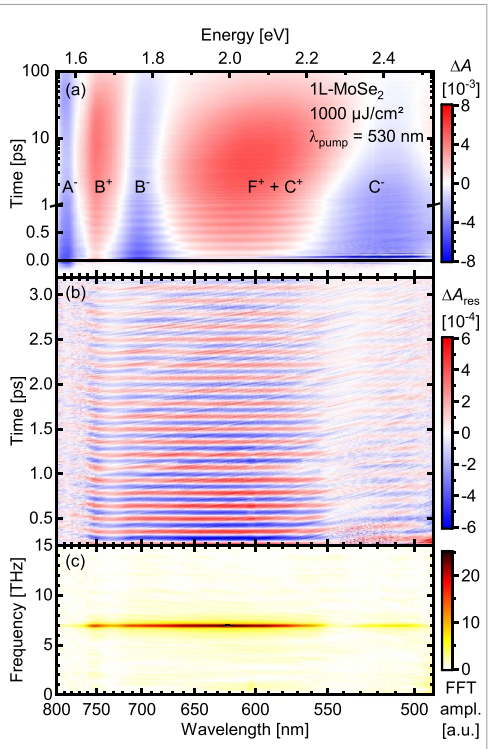

Figure 3. Oscillations in 1L-$MoSe_2$ TA data. (a) 2D TA signal for 1L-$MoSe_2$. (b) 2D Residue of a three-exponential fit onto the short-term TA signal. The plot clearly shows temporal oscillations that are in phase over a large spectral region and persist for several picoseconds. Note that the measurements for (a) and (b) were conducted under identical conditions except for the time axis. The former employed logarithmically spaced time points up to 100 ps while the latter used small, equidistant steps and ends at ≈ 4.2 ps. (c) 2D FFT amplitude map of the data shown in (b). The striking feature is a frequency band at around 7 THz that spans most of the investigated wavelength range.

In fact, previous studies on different TMDCs have attributed temporal oscillations of similar frequencies as belonging to the A_1' Raman mode [28–30, 34]. To confirm this assignment, we performed Raman spectroscopy on the same samples that were investigated in TA measurements beforehand. These spectra should include all optically active modes that could be excited by the pump pulse [57]. Figure 4 compares the Raman spectra (bright lines) to the FFT signal (dark lines) of spectrally averaged time traces (see SM, section 3.3 for details) for each of the three materials. In the case of 1L-$MoSe_2$, the clear separation between the Raman modes [55, 58, 59] facilitates

IOP Publishing 2D Mater. 12 (2025) 035012 T Völzer et al

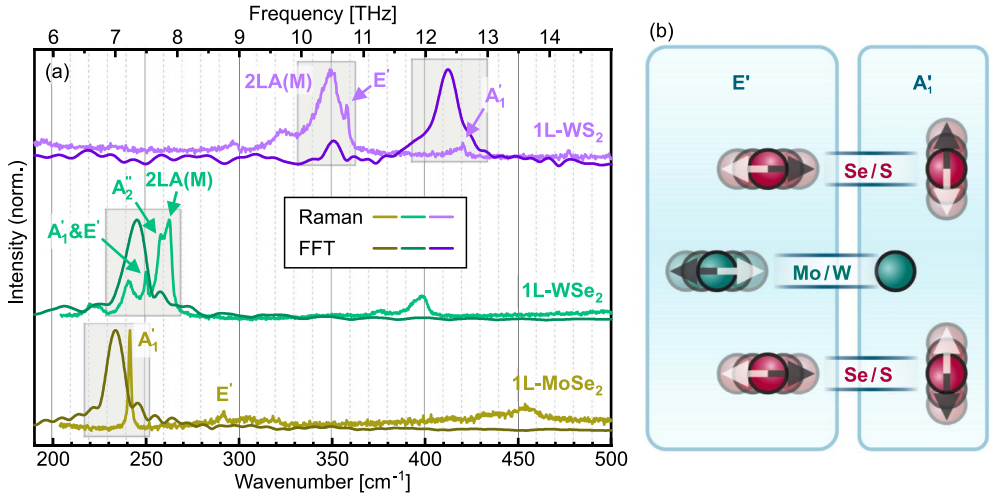

Figure 4. (a) Assigning the FFT bands to corresponding Raman modes of each TMDC. For all three materials, the major peak of the FFT spectrum resides slightly red-shifted from the corresponding Raman peak of the A_1' mode. In 1L-WS_2, we find an additional FFT signature, whose frequency of 10.5 THz lies slightly lower than the E' Raman mode. Peak labeling follows [55, 56]. (b) Real-space illustrations of the two discussed vibrations.

an unambiguous attribution of the FFT peak to the A_1' mode. Yet, we note that there is a slight frequency mismatch between the two, with the maximum of the FFT curve occurring at lower values, i.e. red-shifted. This frequency shift will be discussed later. For 1L-WSe_2, diverse Raman peaks gather in the vicinity of the FFT band around 250 cm^{-1}. Especially the A_1' and E' modes may even lie indistinguishably close to each other [32, 55, 56, 60]. To test which of the two the TA oscillation belongs to, Jeong *et al* [28] exploited the dependence of the vibrational mode on the number of layers. They found that the FFT band follows the frequency increase of A_1' from monolayer towards bulk WSe_2 whereas E' becomes softer. Thus, the frequency found in the TA signal corresponds to the slightly red-shifted A_1' Raman peak. In 1L-WS_2, in turn, the two major modes are well-separated again. The dominant FFT band lies a few cm^{-1} below the faint A_1' Raman signature at about 12.5 THz. Surprisingly, we find another peak in the Fourier spectrum, which is also confirmed by a characteristic phase feature at the same position (see SM, figure S14). This second frequency band occurs consistently for excitation at 530 nm but disappears when pumping at 595 nm, as shown in the SM, figure S11(f). Its wavenumber matches the (again slightly red-shifted) E' mode. This finding draws particular interest, as such a component neither occurs in the other two TMDCs nor in previous studies.

To possibly explain the emergence of this E', we first have to dive into the induction mechanism of the oscillations in general. Here, two possibilities exist, namely ISRS and DECP [22, 23]. In the former model, pump photons will scatter at the lattice, transferring energy onto the nuclei and thus starting their motion from the equilibrium position. Hence, the oscillatory signal will start at zero displacement. For DECP in contrast, the excitation of excitons or free carriers will alter the covalent bonding between the atoms, therefore shifting the equilibrium configuration. As the inert nuclei cannot adapt as quickly, they still reside at their original coordinates. Subsequently, they will begin to oscillate, starting at the maximum displacement with respect to their new equilibrium position. In agreement with the earlier studies, we find a maximum of the temporally oscillating TA signal at time zero (see SM, figure S15), thus concluding a DECP.

In this light, the coherent excitation of vibrational modes is not specifically restricted to any single mode but generally possible. Although it has been stated that only the highly symmetric A_1' modes facilitate a DECP [22, 29], the broken inversion symmetry in 1L-TMDCs undermines this argumentation. However, the E' mode is expected to cause much weaker TA signals than A_1' [28]. Nevertheless, the amplitude of the oscillation is also influenced by the coupling strength of each phonon mode to the electronic system, which probably still depends on the pump wavelength. The underlying reason is that different photon energies excite different electronic states with correspondingly varying charge distributions. For instance, the absorption band of the B exciton lies around 530 nm in 1L-WS_2 and might couple strongly to E' as well. Classic Raman spectroscopy has similarly shown a strong spectral dependence of the ratio between E' and A_1': It so happens that in 1L-WS_2, the coupling for E' in relation to the A_1' mode reaches a maximum around 530 nm, giving rise to the observed peak [60]. Near 600 nm, in turn, A_1' prevails. Likewise, the E' mode plays at most a minor role in 1L-$MoSe_2$ for

IOP Publishing 2D Mater. 12 (2025) 035012 T Völzer et al

both excitation wavelengths [58, 59]. In 1L-WSe_2, as these two Raman bands lie too close to each other, we would not be able to distinguish them in the FFT spectra of the TA residue time curves. A contribution from other, close-lying modes cannot be fully excluded. In fact, we observe a slight spectral shift of the oscillation frequency in 2D FFT maps (SM, figure S10(b) and (e)). Here, the occurrence of a second frequency band with a possibly different spectral amplitude could provide an explanation. Concluding, we find a strong coupling between the electronic and phononic system that facilitates the coherent excitation of lattice vibration. Although the A_1' fingerprint prevails in the TA signal, the mechanism seems to apply to E' as well.

Now, we turn from the origin of the coherent phonons towards their effect on the TA spectrum. Figure 5(a) depicts the spectral distribution of the oscillation amplitude for all TMDCs, as obtained from integrating the 2D FFT spectra over the frequency interval of the peak. For comparison, the TA signal at a delay of 1 ps (b) as well as the 2D maps of the short-term TA fit residue (c)–(e) are shown. In general, the amplitude spectra illustrate a broad TA response to the oscillations, spanning almost the entire wavelength range. This unstructured, widespread imprint of the A_1' mode onto the TA signal rules out excitonic effects as the major cause for the spectral response, as they would emerge as defined bands in the spectrum. Yet, in agreement with the residue maps, the oscillations only weaken towards the rim of the spectral range. Even this might be an effect of the worse time resolution there, which smears out the sinusoidal characteristics. For the same reason, the oscillation amplitude is much weaker in 1L-WS_2 compared to the other two TMDCs (figures 5(c)–(e)). The higher oscillation frequency of ≈12.5 THz corresponds to a semi-period of 40 fs, which is close to our experimental time resolution of 45 fs. This confirms that we are able to resolve even this lattice vibration, albeit with a much lower TA signal amplitude than for the other two TMDCs.

In addition to their generally broad shape, the amplitude spectra exhibit certain modulations in the vicinity of the TA peaks. In fact, local minima in the oscillation strength coincide with zero crossings between the excitonic contributions in the TA. The maxima, accordingly, match the TA extrema. In this light, there seems to exist a—supposedly excitonic—mechanism that weakly couples the coherent phonons to the amplitude of the TA spectrum. All in all, we find a major TA response to the coherent phonons that is independent of specific electronic or excitonic transitions. On top of that, the lattice vibrations appear to have only a minor effect on the transient peaks. In previous theoretical attempts, the oscillation amplitude spectrum was approached by band structure calculations in dependence of the nuclei elongation following the A_1' Raman modes [28, 29, 34].

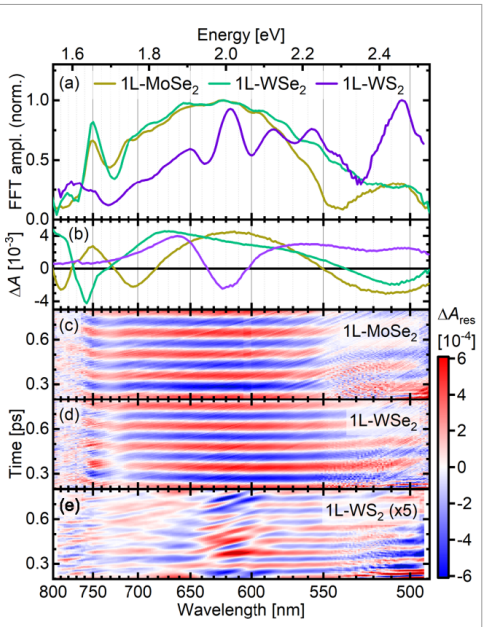

Figure 5. (a) Normalized FFT amplitude spectra integrated over the frequency band of the dominant oscillation for the three investigated TMDCs. They all show a broad contribution over the spectral region with modulations at or around the excitonic bands. At the rim of the investigated wavelength interval, the amplitude tends to drop. (b) TA spectra for the three monolayers at 1 ps and $F = 1000\ \mu J\ cm^{-2}$. (c)–(e) 2D TA fit residues (equivalent to figure 3(b)). The oscillations are in phase over a broad fraction of the visible spectrum. Phase changes towards the shortest/longest wavelengths proceed gradually, without any phase flips. The data in (e) was smoothed and scaled for clarity.

Here, the displacement of the atoms leads to a band gap renormalization that in turn causes a shift of the excitonic absorption bands. Hence, their peak positions would oscillate, manifesting in two key characteristics of the corresponding TA fingerprint. As a first point, this model predicts a characteristic spectral amplitude caused by the coherent lattice vibrations. In the flanks of the peak, where the slope is the steepest, the TA signal will change the strongest if the peak is shifted. In the center or far away from the flanks, however, a spectral displacement of the peak will barely alter the TA signal. As the second point, a periodically shifting peak would result in opposite phases of the signals on its two sides, respectively. When the absorption band spectrally moves from its original position towards higher energies, the signal will increase on its blue side while it is reduced on the red side. In total, for every absorption band that shifts periodically with the A_1' vibration, one would obtain two distinct peaks in the oscillation amplitude spectrum, which are characterized by opposite phases. While this phase flip was observed and accurately described for at least one absorption band in 1L-$MoTe_2$ [34], this model lacks accuracy in the case of 1L-MoS_2 [29]. Likewise, it

IOP Publishing 2D Mater. 12 (2025) 035012 T Völzer et al

does not account for the broad nature of the amplitude spectra we observe. Moreover, we do not find any phase flips associated with a periodic peak shift. Admittedly, the oscillation phase shifts close to the edges of the spectrum (see figures 5(c)–(e) and SM, figure S15). However, this proceeds continuously rather than abruptly. Consequently, the off-drifting phase is most probably caused by residual probe chirp owing to inaccuracies of the zero point correction employed in the TA analysis (discussed in detail in the SM, section 3.4). In the center of the investigated spectral range, both phase and amplitude are remarkably stable, in stark contrast to the aforementioned theoretical model. With this in mind, we rule out a periodic shift of the (excitonic) absorption bands as the dominating mechanism behind the oscillatory fingerprint on the TA signal.

These findings point towards a spectrally rather constant background being induced by the coherent lattice vibrations. Altogether, they indicate at most a minor contribution of band and peak shifts. To our best knowledge, a suitable model to describe such a broadband response is still missing. Thus, our results leave room for and encourage more comprehensive explanations of the mechanism that imprints the coherent phonons onto the transient signal and that defines their spectral signature.

Given the coherent nature of the excited phonons, we move on to investigate their behavior as a collective excitation whose effect on the material is tuned by varying the pump fluence. In order to quantify impact of the excited species density on the oscillation, we focused on spectrally averaged time traces as above. Fitting an exponentially decaying cosine, we extract the oscillation frequency, lifetime and amplitude, which are depicted in figure 6. To quantify their uncertainties, we varied one of the parameters, respectively, then kept it constant while fitting the others, to see when the fit quality decreases significantly. The details of this procedure can be found in the SM, section 3.3 and figure S12. For comparison, we also plot the maxima positions of the FFT peaks as a different approach to obtain the frequency. In this case, however, the peak width and thus the frequency resolution are essentially limited by the finite time interval, in which the oscillation does not decay completely. Ergo, a detailed discussion of the values obtained from the FFT does not appear reasonable and we focus on the fit results instead. For the sake of clarity, we restrain ourselves to the parameter values for 1L-$MoSe_2$, while findings for the tungsten-based materials can be found in the SM, section 3.3. and figure S13. To bring measurements at different excitation wavelengths into line, we plotted the parameters over the TA signal around 0.2 ps and from 500 nm to 520 nm as a measure of the excited species density. Here, the signal strength scales rather proportionally with the excitation fluence, as opposed to especially the $A^{\pm}$ and $B^{\pm}$ features, which saturate already

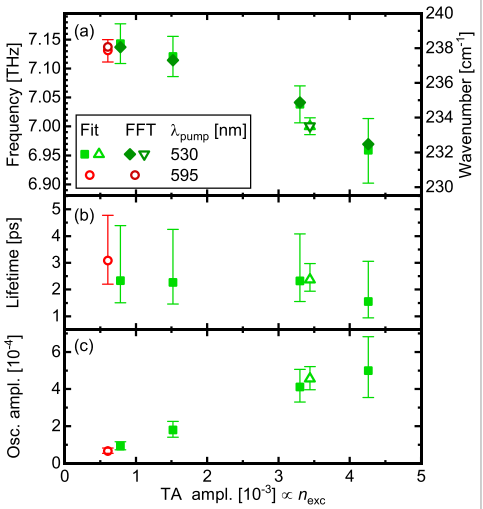

Figure 6. Excitation density dependence of oscillation frequency (a), lifetime (b), and amplitude (c) as obtained from fitting (and FFT) of the spectrally averaged 1L-$MoSe_2$ residue data. The *x*-axis shows the TA signal (500 nm to 520 nm at 0.2 ps) as a (pump wavelength-independent) measure for the excitation density. Solid symbols represent TA scans with a logarithmic time axis, while open symbols stem from scanning in small, equidistant time steps. The uncertainty bars are derived using the procedure described in the SM, section 3.3 and figure S12. Frequency and oscillation amplitude fall/rise almost linearly with signal strength and the results obtained from 595 nm excitation are in line with those yielded from pumping at 530 nm. The lifetime, in contrast, drops only at the highest fluence, while the long-wavelength excitation stands out with a significantly prolonged decay.

at the lowest fluences applied (see SM, figure S3 and S5). Likewise, the oscillation amplitude grows almost linearly with the excitation density (figure 6(c)). This observation holds for the other two TMDCs as well, see SM figure S13 (c) and (f).

The second consistent behavior is the decrease of the oscillation frequency at higher excitation density by 6 cm^{-1} to 8 cm^{-1} for all three TMDCs. Note that for the lowest fluence, the frequency discrepancy with respect to the Raman spectra (see figure 4) shrinks to no more than a few cm^{-1}. In other words, the $A_1^{'}$ mode softens at strong excitation compared to the quasi-zero fluence values in continuous wave experiments. We conclude that a high density of electronic excitations gives rise to a decelerated lattice vibration. This phenomenon can be understood in terms of the electronic states constituting the covalent bonds. As optical excitation lifts electrons into higher, i.e. antibonding orbitals, the bond strength weakens. On the one hand, this causes the DECP discussed above. On the other hand, a weak bond typically appears as a relatively flat energetic minimum. Thus, a high density of excitations will also globally lower the potential curvature around the equilibrium positions of the nuclei, manifesting in a softened vibrational mode with a reduced frequency. Alternatively,

IOP Publishing 2D Mater. 12 (2025) 035012 T Völzer et al

a similar effect could be induced by anharmonicities in the bonding potential [27]. However, they would cause higher harmonics emerging as additional bands in the FFT spectra, which we do not observe. All in all, regardless of the underlying mechanism, the present excitation density dependence provides another tunability of the vibrational modes, alongside temperature [32, 33] as well as doping, strain and layer number [31].

Finally, we turn to the oscillation lifetime plot of figure 6(b). Here, we generally find a tendency towards shorter lifetimes at higher excitation densities, albeit by far not as clear as for the previous parameters. For this parameter, the uncertainties appear to be rather overestimated, given that they drastically exceed the actual differences between the data points. In the case of 1L-$MoSe_2$, we note an acceleration of the oscillation amplitude decay only for the highest fluence. The data point originating from pumping at at 595 nm, in turn, protrudes with a clearly longer lifetime. Intuitively, this points towards a thermal effect, where a higher excitation excess energy or larger fluence result in a raised electronic temperature. Consequently, electron- or exciton-phonon scattering is enhanced, which promotes dephasing of the coherent phonons. However, the distinction between 595 and 530 nm does not remain as clear when looking at the other TMDCs (shown in the SM, figure S13 (b) and (e)). Hence, the nature and heterogeneity of the initially excited electronic states as well as how this translates to a broadening of the A_1' phonon peak appear to play the major role [27].

Concluding, the oscillations associated with the coherent lattice vibrations most notably undergo a deceleration with higher excitation density owing to an overall weakening of the covalent bonds. On top of that, the dephasing of the coherent phonons proceeds faster.

5. Conclusion

This work focuses on the TA changes in 1L-TMDCs induced by ultrashort optical excitation as well as the coupling of phonons to the electronically excited states. The TA spectra are characterized by a shift and broadening of the excitonic absorption bands. Additionally, we observe and discuss a broad, overlaying feature correlated to free carriers that emanate from the thermal dissociation of excitons. The following dynamics are governed by consecutive thermalization steps, first involving only the electronic system, then spreading to strongly coupled hot phonons and finally equilibrating the whole lattice. The limited availability of high-energy vibrational modes constitutes a phonon bottleneck decelerating the cooling at high fluences.

On top of these incoherent processes, coherent phonons are displacively excited, again proving a strong coupling to the electronic system. While the A_1' Raman mode dominates, we additionally find a contribution of E' in 1L-WS_2 exclusively. These coherent lattice vibrations cause a broad spectral response plus small modulations of the excitonic bands. Finally, especially the phonon frequency decreases while enhancing the excitation density, demonstrating a certain degree of tunability.

In summary, the electronic and phononic systems of monolayer TMDCs have been proven to be strongly coupled. On the one hand, their incoherent interactions govern the cascade-like cooling of excited species. On the other hand, exciton-phonon coupling during the optical excitation gives rise to coherent lattice vibrations, which in turn imprint a spectrally broad response onto the transient signal.

Data availability statement

The data that support the findings of this study are openly available at the following URL/DOI: https://doi.org/10.18 453/rosdok_id00004699.

Acknowledgments

This work was funded by the Deutsche Forschungsgemeinschaft (DFG, German Research Foundation) through SFB 1477 'Light-Matter Interactions at Interfaces', Project Number 441234705, as well as IRTG 2676/1 'Imaging of Quantum Systems', Project Number 437567992.

Author contributions

T V, J S, T K, and S L conceptualized and planned the project as well as contributed to writing the manuscript. T V and M K set up the transient absorption spectroscopy and performed the experiments. A B built and maintained the Raman spectroscopy, while J S and T V conducted the corresponding measurements. T V analyzed the data. S L and T K supervised the project.

ORCID iDs

T Völzer https://orcid.org/0000-0002-1085-9594
M Krupp https://orcid.org/0009-0006-8602-5445
J Schröer https://orcid.org/0000-0002-2990-2302
A Bergmann-Iwe https://orcid.org/0009-0007-4022-1536
T Korn https://orcid.org/0000-0003-4808-391X
S Lochbrunner https://orcid.org/0000-0001-9729-8277

IOP Publishing 2D Mater. 12 (2025) 035012 T Völzer et al

References

[1] Novoselov K S, Jiang D, Schedin F, Booth T J, Khotkevich V V, Morozov S V and Geim A K 2005 Two-dimensional atomic crystals *Proc. Natl Acad. Sci.* **102** 10451–3

[2] Novoselov K S, Mishchenko A, Carvalho A and Neto A H C 2016 2D materials and van der Waals heterostructures *Science* **353** 6298

[3] Mak K F, Lee C, Hone J, Shan J and Heinz T F 2010 Atomically thin MoS_2: A new direct-gap semiconductor *Phys. Rev. Lett.* **105** 136805

[4] Splendiani A, Sun L, Zhang Y, Tianshu Li, Kim J, Chim C-Y, Galli G and Wang F 2010 Emerging photoluminescence in monolayer MoS_2 *Nano Lett.* **10** 1271–5

[5] Cheiwchanchamnangij T and Walter R L L 2012 Quasiparticle band structure calculation of monolayer, bilayer and bulk MoS_2 *Phys. Rev. B* **85** 205302

[6] Mak K F and Shan J 2016 Photonics and optoelectronics of 2D semiconductor transition metal dichalcogenides *Nat. Photon.* **10** 216–26

[7] Rono N, Ahia C C and Meyer E L 2024 Recent advances in transition metal dichalcogenides-based materials for fourth-generation perovskite solar cell devices *AIP Adv.* **14** 070702

[8] Withers F *et al* 2015 Light-emitting diodes by band-structure engineering in van der Waals heterostructures *Nat. Mater.* **14** 301–6

[9] Lopez-Sanchez O, Lembke D, Kayci M, Radenovic A and Kis A 2013 Ultrasensitive photodetectors based on monolayer MoS_2 *Nat. Nanotechnol.* **8** 497–501

[10] Massicotte M, Schmidt P, Vialla F, Schädler K G, Reserbat-Plantey A, Watanabe K, Taniguchi T, Tielrooij K J and Koppens F H L 2015 Picosecond photoresponse in van der Waals heterostructures *Nat. Nanotechnol.* **11** 42–46

[11] Nazif K N *etal* 2021 High-specific-power flexible transition metal dichalcogenide solar cells *Nat. Commun.* **12** 7034

[12] Hein P, Stange A, Hanff K, Yang L X, Rohde G, Rossnagel K and Bauer M 2016 Momentum-resolved hot electron dynamics at the 2H-MoS_2 surface *Phys. Rev. B* **94** 205406

[13] Steinleitner P, Merkl P, Nagler P, Mornhinweg J, Schüller C, Korn T, Chernikov A and Huber R 2017 Direct observation of ultrafast exciton formation in a monolayer of WSe_2 *Nano Lett.* **17** 1455–60

[14] Shi H, Yan R, Bertolazzi S, Brivio J, Gao B, Kis A, Jena D, Xing H G and Huang L 2013 Exciton dynamics in suspended monolayer and few-layer MoS_2 2D crystals *ACS Nano* **7** 1072–80

[15] Sim S, Park J, Song J-G, In C, Lee Y-S, Kim H and Choi H 2013 Exciton dynamics in atomically thin MoS_2: interexcitonic interaction and broadening kinetics *Phys. Rev. B* **88** 075434

[16] Pogna E A A *et al* 2016 Photo-induced bandgap renormalization governs the ultrafast response of single-layer MoS_2 *ACS Nano* **10** 1182–8

[17] Vega-Mayoral V, Borzda T, Vella D, Prijatelj M, Pogna E A A, Backes C, Coleman J N, Cerullo G, Mihailovic D and Gadermaier C 2017 Charge trapping and coalescence dynamics in few layer MoS_2 *2D Mater.* **5** 015011

[18] Kulig M, Zipfel J, Nagler P, Blanter S, Schüller C, Korn T, Paradiso N, Glazov M M and Chernikov A 2018 Exciton diffusion and halo effects in monolayer semiconductors *Phys. Rev. Lett.* **120** 207401

[19] Völzer T, Fennel F, Korn T and Lochbrunner S 2021 Fluence-dependent dynamics of localized excited species in monolayer versus bulk MoS_2 *Phys. Rev. B* **103** 045423

[20] Völzer T, Lütgens M, Fennel F and Lochbrunner S 2017 Recombination dynamics of optically excited charge carriers in bulk MoS_2 *J. Phys. B: At. Mol. Opt. Phys.* **50** 194003

[21] Vialla F and Fatti N D 2020 Time-domain investigations of coherent phonons in van der Waals thin films *Nanomaterials* **10** 2543

[22] Zeiger H J, Vidal J, Cheng T K, Ippen E P, Dresselhaus G and Dresselhaus M S 1992 Theory for displacive excitation of coherent phonons *Phys. Rev. B* **45** 768–78

[23] Ishioka K and Oleg V M 2009 Coherent Lattice Oscillations in Solids and Their Optical Control: Part I *Fundamentals and Optical Detection Techniques* (Springer) pp 23–46

[24] Kumar N, Brian A R, Butch N P, Syers P, Kirshenbaum K, Paglione J and Zhao H 2011 Spatially resolved femtosecond pump-probe study of topological insulator Bi_2Se_3 *Phys. Rev. B* **83** 235306

[25] Wang Y, Xianfan X and Venkatasubramanian R 2008 Reduction in coherent phonon lifetime in Bi_2Te_3/Sb_2Te_3 superlattices *Appl. Phys. Lett.* **93** 113114

[26] Alexander Q W, Xianfan X and Venkatasubramanian R 2008 Ultrafast dynamics of photoexcited coherent phonon in Bi_2Te_3 thin films *Appl. Phys. Lett.* **92** 011108

[27] Bin H, Zhang C, Zhu W, Yufeng Li, Liu S, Zhu X, Xuewei W, Wang X, Wen H-hu and Xiao M 2016 Coherent optical phonon oscillation and possible electronic softening in WTe_2 crystals *Sci. Rep.* **6** 30487

[28] Jeong T Y *et al* 2016 Coherent lattice vibrations in mono- and few-layer WSe_2 *ACS Nano* **10** 5560–6

[29] Trovatello C *et al* 2020 Strongly coupled coherent phonons in single-layer MoS_2 *ACS Nano* **14** 5700–10

[30] Zou J, Zhu R, Wang J, Meng H, Wang Z, Chen H and Weng Y-X 2023 Coherent phonon-mediated many-body interaction in monolayer WSe_2 *J. Phys. Chem. Lett.* **14** 4657–65

[31] Iqbal M W, Shahzad K, Akbar R and Hussain G 2020 A review on Raman finger prints of doping and strain effect in TMDCs *Microelectron. Eng.* **219** 111152

[32] Zhang X, Qiao X-F, Shi W, Jiang-Bin W, Jiang D-S and Tan P-H 2015 Phonon and Raman scattering of two-dimensional transition metal dichalcogenides from monolayer, multilayer to bulk material *Chem. Soc. Rev.* **44** 2757–85

[33] Huang X, Gao Y, Yang T, Ren W, Cheng H-M and Lai T 2016 Quantitative analysis of temperature dependence of Raman shift of monolayer WS_2 *Sci. Rep.* **6** 32236

[34] Sayers C J *et al* 2023 Strong coupling of coherent phonons to excitons in semiconducting monolayer $MoTe_2$ *Nano Lett.* **23** 9235–42

[35] Castellanos-Gomez A, Buscema M, Molenaar R, Singh V, Janssen L, Herre S J van der Z and Steele G A 2014 Deterministic transfer of two-dimensional materials by all-dry viscoelastic stamping *2D Materials* **1** 011002

[36] Megerle U, Pugliesi I, Schriever C, Sailer C F and Riedle E 2009 Sub-50 fs broadband absorption spectroscopy with tunable excitation: putting the analysis of ultrafast molecular dynamics on solid ground *Appl. Phys. B* **96** 215–31

[37] Päpcke A, Friedrich A and Lochbrunner S 2020 Revealing the initial steps in homogeneous photocatalysis by time-resolved spectroscopy *J. Phys.: Condens. Matter* **32** 153001

[38] Riedle E, Beutter M, Lochbrunner S, Piel J, Schenkl S, Spörlein S and Zinth W 2000 Generation of 10 to 50 fs pulses tunable through all of the visible and the NIR *Appl. Phys. B* **71** 457–65

[39] Manzoni C and Cerullo G 2016 Design criteria for ultrafast optical parametric amplifiers *J. Opt.* **18** 103501

[40] Yilei Li *et al* 2014 Measurement of the optical dielectric function of monolayer transition-metal dichalcogenides: MoS_2, $MoSe_2$, WS_2 and WSe_2 *Phys. Rev. B* **90** 205422

[41] Hsu C, Frisenda R, Schmidt R, Arora A, de Vasconcellos S M, Bratschitsch R, van der Zant H S J and CastellanosGomez A 2019 Thicknessdependent refractive index of 1L, 2L and 3L MoS_2, $MoSe_2$, WS_2 and WSe_2 *Adv. Opt. Mater.* **7** 1900239

[42] Steinhoff A, Rösner M, Jahnke F, Wehling T O and Gies C 2014 Influence of excited carriers on the optical and electronic properties of MoS_2 *Nano Lett.* **14** 3743–8

[43] Chernikov A, Ruppert C, Hill H M, Rigosi A F and Heinz T F 2015 Population inversion and giant bandgap renormalization in atomically thin WS_2 layers *Nat. Photon.* **9** 466–70

IOP Publishing 2D Mater. 12 (2025) 035012 T Völzer et al

[44] Cunningham P D, McCreary K M, Hanbicki A T, Currie M, Jonker B T and Hayden L M 2016 Charge trapping and exciton dynamics in large-area CVD grown MoS_2 *J. Phys. Chem. C* **120** 5819–26
[45] Kang M, Jung S W, Shin W J, Sohn Y, Ryu S H, Kim T K, Hoesch M and Kim K S 2018 Holstein polaron in a valley-degenerate two-dimensional semiconductor *Nat. Mater.* **17** 676–80
[46] Thilagam A 2015 Excitonic polarons in low-dimensional transition metal dichalcogenides *Physica B* **464** 44–50
[47] Lorenc M, Ziolek M, Naskrecki R, Karolczak J, Kubicki J and Maciejewski A 2002 Artifacts in femtosecond transient absorption spectroscopy *Appl. Phys. B* **74** 19–27
[48] Borzda T *et al* 2015 Charge photogeneration in fewlayer MoS_2 *Adv. Funct. Mater.* **25** 3351–8
[49] Moody G *et al* 2015 Intrinsic homogeneous linewidth and broadening mechanisms of excitons in monolayer transition metal dichalcogenides *Nat. Commun.* **6** 8315
[50] Vega-Mayoral V *et al* 2016 Exciton and charge carrier dynamics in few-layer WS_2 *Nanoscale* **8** 5428–34
[51] Pötz W and Kocevar P 1983 Electronic power transfer in pulsed laser excitation of polar semiconductors *Phys. Rev. B* **28** 7040–7
[52] Chi Z, Chen H, Zhao Q and Weng Y-X 2020 Observation of the hot-phonon effect in monolayer MoS_2 *Nanotechnology* **31** 235712
[53] Wang W, Sui N, Chi X, Kang Z, Zhou Q, Li Li, Zhang H, Gao J and Wang Y 2021 Investigation of hot carrier cooling dynamics in monolayer MoS_2 *J. Phys. Chem. Lett.* **12** 861–8
[54] Wei X, Wang Z, Wang Z, Lu Y, Ji Q and Liu W 2024 Unveiling spatiotemporal diffusion of hot carriers influenced by spatial nonuniform hot phonon bottleneck effect in monolayer MoS_2 *Nano Lett.* **24** 9269–75
[55] Chen S-Y, Zheng C, Fuhrer M S and Yan J 2015 Helicity-resolved Raman scattering of MoS_2, $MoSe_2$, WS_2 and WSe_2 atomic layers *Nano Lett.* **15** 2526–32
[56] Shi W, Lin M-L, Tan Q-H, Qiao X-F, Zhang J and Tan P-H 2016 Raman and photoluminescence spectra of two-dimensional nanocrystallites of monolayer WS_2 and WSe_2 *2D Mater.* **3** 025016
[57] Lee D H, Choi S-J, Kim H, Kim Y-S and Jung S 2021 Direct probing of phonon mode specific electron-phonon scatterings in two-dimensional semiconductor transition metal dichalcogenides *Nat. Commun.* **12** 4520
[58] Soubelet P, Bruchhausen A E, Fainstein A, Nogajewski K and Faugeras C 2016 Resonance effects in the Raman scattering of monolayer and few-layer $MoSe_2$ *Phys. Rev. B* **93** 155407
[59] Nam D, Lee J-U and Cheong H 2015 Excitation energy dependent Raman spectrum of $MoSe_2$ *Sci. Rep.* **5** 17113
[60] del Corro E *et al* 2016 Atypical exciton-phonon interactions in WS_2 and WSe_2 monolayers revealed by resonance Raman spectroscopy *Nano Lett.* **16** 2363–8

Having a good vibe: Strong coupling to the electronic system creates incoherent and coherent phonons in 1L-TMDCs

Supporting Information

Tim Völzer[a,b], Marvin Krupp[a,b], Julian Schröer[a,b], Annika Bergmann-Iwe[a,b], Tobias Korn[a,b], and Stefan Lochbrunner[a,b,*]

a) Institute of Physics, University of Rostock, Albert-Einstein-Str. 23, 18059 Rostock, Germany

b) Department "Life, Light and Matter", University of Rostock, Albert-Einstein-Str. 25, 18059 Rostock, Germany

*stefan.lochbrunner@uni-rostock.de

Contents

1 Setup for transient absorption spectroscopy

Transient absorption (TA) spectroscopy forms the basis of our work. However, the investigation of ultrafast processes in atomically thin transition metal dichalcogenides (1L-TMDCs) poses particular requirements regarding time resolution and sensitivity. To achieve these, we modified the standard scheme for TA spectroscopy[1,2].

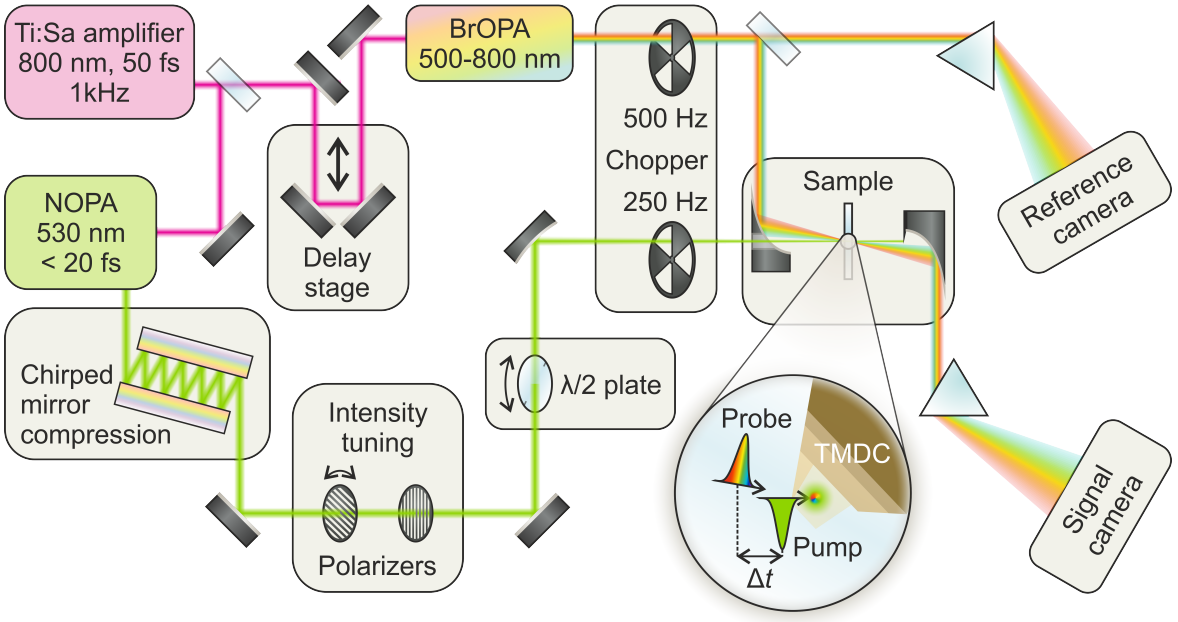

Figure S1: Schematic illustration of the experimental TA setup.

The schematic of the setup it depicted in figure S1. A titanium:sapphire (Ti:Sa) amplifier serves as the feed, emitting pulses with a duration of 50 fs at a rate of 1 kHz, centered around 800 nm. This fundamental near-infrared (NIR) beam is split up into two parts to generate pump and probe pulses independently, but from the same light source. Accordingly, the probe pulses are directed over a linearly movable delay stage that adds a defined length to the beam path, thus tuning its arrival time at the sample spot with reference to the pump pulses. The latter are created in a noncollinear optical parametric amplifier (NOPA)[3], converting the fundamental NIR light into visible laser pulses of 530 or 595 nm. They are subsequently compressed using ar pair of chirped mirrors, resulting in pulse lengths below 20 fs. Afterwards, the combination of one rotatable and one fixed wire grid polarizer provides the possibility to continuously tune the beam intensity while retaining the orientation of the linear polarization. The latter can then be adjusted with a half-wave ($\lambda/2$) plate. Finally, a spherical mirror focuses the pump beam onto the sample.

For the probe light, on the other hand, a broad spectrum is desired to investigate the absorption change of the sample over a large regime of the spectrum. Here, we use a broadband NOPA (BrOPA)[4], covering the range from 500 nm to 800 nm. This light is also focused onto the sample and its transmitted part is dispersed onto a camera, allowing for the spectrally resolved detection of the probe light. At this point, the distinctive features of this setup with respect to the typical ones come into play. Firstly, we use off-axis parabolic mirrors for the probe focusing, yielding $1/e^2$-spot sizes below 15 µm, which define the spatial resolution. Secondly, we chop both pump and probe beam at one quarter and one half of the laser repetition rate, respectively. This creates a period of four shots with different pulse configurations. In the case, where both beams are blocked, the detection measures only (electronic) background that can be subtracted from all other configurations' intensity. If only the pump pulse is transmitted, we detect the scattered excitation light. Transmitting solely the probe beam allows for measuring the static absorption

of the sample, that means in the unexcited state. Finally, when both pulses reach the sample, the pump will create an excitation while the probe arrives with a defined delay Δt. Therefore, it probes the absorption at that specific time after pumping the system. Here, the intensity measured in the pump-only configuration is subtracted to eliminate contributions that do not stem from the BrOPA light. At this point, the ratio of the probe intensities with versus without preceding excitation usually yields the change in the absorption/transmission of the sample. In this setup, however, we also track the intensity of the probe light separately from what happens in the sample, which constitutes the third and final modification of the setup. After the beam chopping, we split the probe beam using a wedge plate. While the reflected signal part proceeds as described above, the transmitted portion serves as a reference. Without any sample interaction, it is dispersed onto the reference camera and thus enables tracking the unaltered, original probe light intensity. In this way, any spectral fluctuations can be monitored and corrected before calculating the TA signal. It is expressed as the change in absorbance ΔA, that is the negative decadic logarithm of the ratio of the probe transmissions with (T^*) versus without (T_0) the pump pulse exciting the sample first:

$$\Delta A = -\log_{10} \frac{T^*}{T_0} \tag{1}$$

Since the time resolution of the experiment is of pivotal importance for the observation of ultrafast processes and especially the coherent phonons, we quantify it in the following. To this end, we take a closer look at the rising edge of the TA signal around time zero. However, for atomically thin TMDCs, the signal is relatively week and the zero point artifact prevails (see figure S6). To overcome this issue, we perform the technique on another sample with a stronger absorption. We use a thin membrane of polymethyl methacrylate (PMMA), in which molecules of the dye 1,6,7,12-tetraphenoxy-N,N'-bis(2,6-di-isopropylphenyl)-3,4,9,10-perylenedicarboximide (Perylene Red, PR) are incorporated.

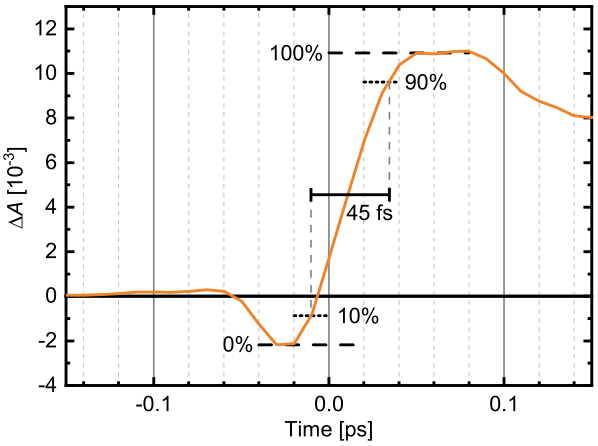

Figure S2: Rising edge of the TA time trace of a PR:PMMA thin film excited at 530 nm and probed at 585 nm. The horizontal dashed lines mark start and end level of the signal rise, the dotted ones represent the 10 and 90% completion of the build-up. The temporal distance between these two points amounts to 45 fs, serving as a measure for the time resolution of the setup.

Figure S2 depicts a time trace of this system, acquired at a probe wavelength of 585 nm in the middle of the BrOPA spectrum under similar conditions as the TMDC measurements. In fact, we observe an ultrafast signal rise that can be quantified to 45 fs, in terms of the duration from 10 % to 90 % of the rising edge. This demonstrates that the setup is indeed able to resolve oscillations like the coherent phonons with periods down to 80 fs.

2 TA dynamics of 1L-$MoSe_2$ and 1L-WSe_2

2.1 Fluence-dependent TA spectra

In the main body of this paper, we discuss the transient absorption (TA) signals of WS_2 and $MoSe_2$. We explicitly show the 2D TA maps for both materials as well as the fluence-dependent spectra for WS_2. Here, we present the complementing data for $MoSe_2$ as well as the measurements on WSe_2, which have not been discussed in detail yet.

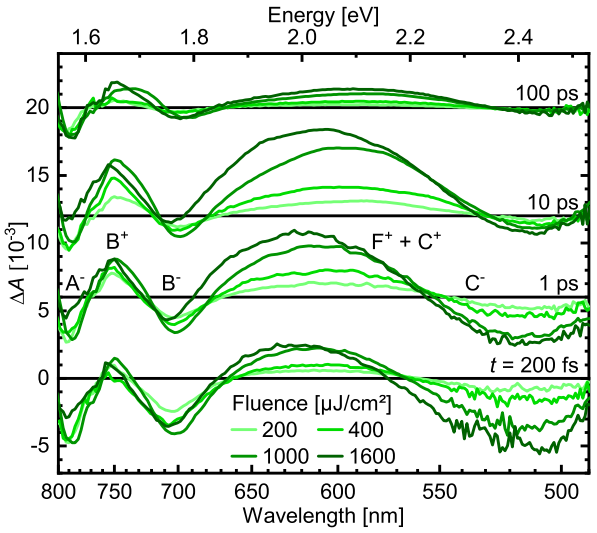

Figure S3: 1L-$MoSe_2$ TA spectra at characteristic probe delays for various pump fluences. The C^+- and F^+-features strongly overlap and therefore cannot be distinguished. Note that the different spectra are offset for clarity but share the same, original scaling.

Figure S3 shows the fluence-dependent TA spectra of 1L-$MoSe_2$ at various time delays. They exhibit similar features as for 1L-WS_2 (see figure 1 in the main body), especially the photoinduced shift of the static absorption bands. This manifests in pairs of a negative and red-shifted positive peak each. The major differences to WS_2 arise from the higher number of absorption bands in the examined wavelength range in $MoSe_2$[5,6]. Especially the excitonic A and B peaks lie close to each other, resulting in partial overlapping of the corresponding transient features. In combination with the presumed A^+ peak falling out of the spectrum, this arrangement largely veils all broadening and shifting dynamics of the positive peaks.
In contrast to the excitonic A and B contributions, the C peak originates from band nesting[7–9]. On top of that, the corresponding transient features $C^{\pm}$ scale relatively linearly with fluence at short times, while the excitonic contributions saturate already at the lowest fluences. Over time, C^- seems to shrink and C^+ to grow. In the light of what we learned from the spectra in WS_2, we suppose that this rather originates from the underlying and growing, broad F^+ feature than from actual dynamics of the $C^{\pm}$ peaks. F^+ is associated with free carriers and already emerged in the spectra of WS_2 as an unstructured feature covering most of the visible range (see figures 1 and two of the main body).

We now turn to the TA signal of 1L-WSe_2, as depicted in figure S4, that bears striking similarities to the data of 1L-$MoSe_2$. Again, the $A^{\pm}$ peak pair resides at the low-energy edge of the spectrum, while C^- marks its blue margin. Interestingly, we observe neither a clear C^+ nor some distinct $B^{\pm}$ contributions. However, literature shows that both the B exciton band as well as the band nesting absorption are less pronounced and sharp than in the other transition metal dichalcogenides (TMDCs)[10]. Consequently, the strong F^+ feature prevails in the center of the spectral range and even in its short-wavelength regime at longer times.
All in all, taking the different static absorption spectra of the three materials into account, the

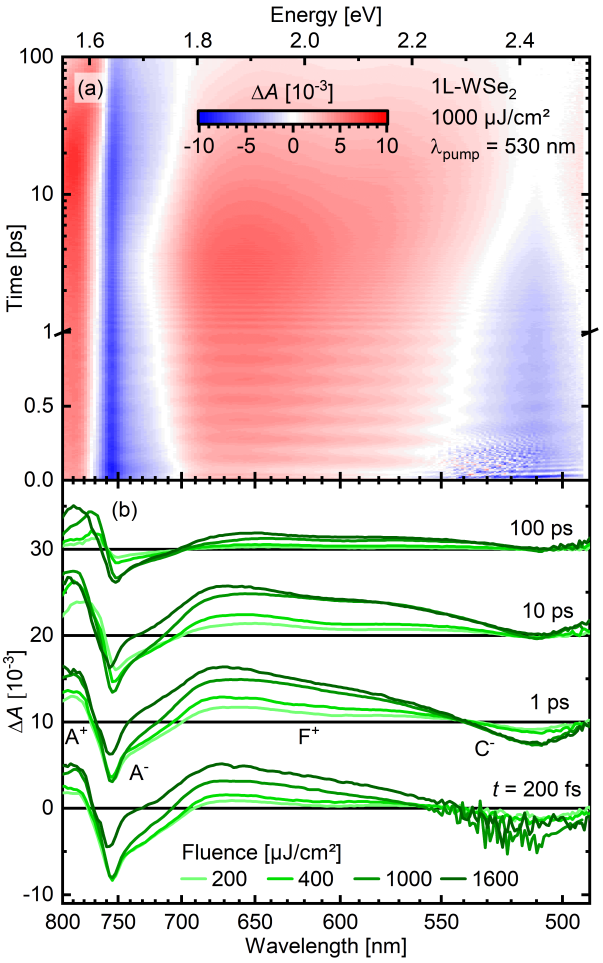

Figure S4: TA dynamics of 1L-WSe_2 (a) 2D TA map for a fluence of $1000\,\mu J\,cm^{-2}$. In addition to the rather monotonously proceeding signal decay as well as peak shifting and narrowing, there is a strong oscillatory contribution to the temporal evolution at short times. This component appears to be in phase over the whole spectral range. (b) Spectra at characteristic probe delays for various pump fluences. The $B^{\pm}$- and C^{+}-peaks are relatively weak in this material[10] and thus cannot be distinguished from the strong, spectrally constant F^{+}-feature. Note that the different spectra are offset for clarity but share the same, original scaling.

transient spectral features follow an identical pattern. They consist of pairs of positive and negative peaks due to the photoinduced red-shift of the original, static absorption bands plus a superposing broad contribution associated with free charge carriers.

2.2 TA signal linearity and saturation under varying pump fluence

For high excitation fluences, the TA signal of 1L-TMDCs may become subject to saturation effects. Most prominently, excitation in the range of or above the Mott density ($\approx 1 \times 10^{14}\,cm^{-2}$ [11,12], $\simeq 400\,\mu J\,cm^{-2}$ at 530 nm) will result in spatial saturation of the crystal with excitons. Hence, additional electron-hole pairs will dissociate, thus capping the amplitude of (transient) excitonic absorption bands. Peaks of other nature, in contrast, may continue to grow. However, as the ground state is significantly depopulated, the absorption of the material will bleach, constituting an upper limit for the excitation density and correspondingly for the TA signal strength as well. To investigate these effects, we take a closer look at the signal amplitude around characteristic excitonic versus non-excitonic features.

Table 1 lists the corresponding spectral regions and time ranges that were used to obtain

Table 1: Wavelength and time intervals used to evaluate TA signal strengths in figure S5.

Material	Peak	Wavelength range [nm]	Time range [ps]	Peak	Wavelength range [nm]	Time range [ps]
WS_2	F^+	500-550	1-2	A^-	600-640	0.19-0.21
WSe_2	F^+	650-680	0.2-0.5	A^-	600-640	0.19-0.21
$MoSe_2$	C^-	500-520	0.19-0.21	B^-	680-720	0.19-0.21

averaged values for the TA signal strength of the various contributions. In the case of the tungsten-based TMDCs, we choose the F^+ and A^- peaks as representatives of nonexcitonic and excitonic features, respectively. For $MoSe_2$, A^- resides already at the rim of the investigated spectral region, so we replaced it with B^-. Likewise, since F^+ is heavily superposed by other spectral components, we investigate C^- as a nonexcitonic band. The respective time intervals were selected based on the results of the dynamics evaluation (figures 2 in the main body as well as S7 and S8 in this SM). These spectral and temporal restrictions should ensure that the peaks are as isolated as possible and not overlayed by another feature.

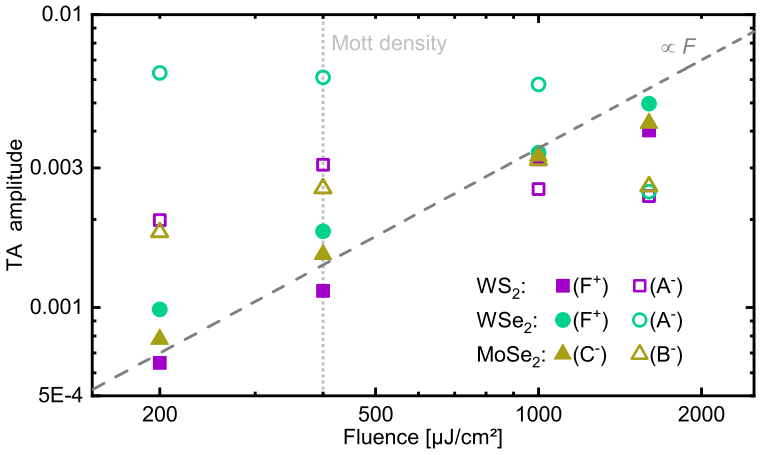

Figure S5: Scaling of excitonic (open symbols) and non-excitonic (solid symbols) TA contributions in 1L-TMDCs in dependence of the pump fluence for excitation at 530 nm. The corresponding wavelength and time intervals, in which the signal strength was extracted, are listed in table 1. The dashed line represents a perfectly linear relation for comparison, *i.e.* with a slope of 1. The Mott density is indicated by the vertical dotted line.

Based on aforementioned time and wavelength regions, figure S5 shows the TA amplitude of the above-named peaks in dependence of the pump fluence. As expected, the values for the excitonic peaks (open symbols) exhibit a clearly sublinear growth or even a reduction with rising fluence. The saturation results from strong excitation near or above the Mott density. The signal decrease at the highest fluences, on the other hand, presumably stems from superposition with the F^+ band, which is characterized by an opposite sign and a differing fluence dependence. Owing to the broad nature of F^+, this overlaying cannot be entirely circumvented.
The nonexcitonic features (solid symbols), in contrast, grow almost linearly with fluence, even far beyond the Mott density. Consequently, they provide a suitable measure for the excitation density. Their comparably weak saturation behavior at the highest fluences probably indicates the limit of how many photons the monolayer can absorb.

2.3 Decay processes and their spectral signatures

In the main body, we present a global fit to the dynamics of the WS_2 TA signal to separate and characterize the individual occurring processes (see main body, figure 2). Here, we apply

the same procedure to the remaining two TMDCs to compare the findings. The fitting function employs four exponential decays and one exponentially decaying cosine. It reads as follows:

$$\Delta A(\lambda,t) = \frac{1+\mathrm{erf}(\frac{t-t_0}{w_0})}{2}\left(\sum_{i=1}^{4} A_i(\lambda)\cdot \mathrm{e}^{-\frac{t}{\tau_i}} + A_{\mathrm{osc}}(\lambda)\cdot \mathrm{e}^{-\frac{t}{\tau_{\mathrm{osc}}}}\cdot\cos(2\pi\, f_{\mathrm{osc}}\cdot t-\alpha_{\mathrm{osc}})\right) \qquad (2)$$

with the four decay-associated amplitude spectra (DAS) $A_i(\lambda)$, the corresponding global time constants τ_i, and an oscillation with the amplitude spectrum $A_{\mathrm{osc}}(\lambda)$, a decay time τ_{osc} as well as a phase α_{osc}. The oscillatory part of the fit, however, is not discussed here but will be analyzed more thoroughly and by more precise means in section 3.
Around time zero, however, the coherent artifact prevails, see figure S6. It comprises various nonlinear interactions of pump and probe mediated by the optical nonlinearity of the sample and especially the substrate material. As a result, is exhibits a complex shape that is difficult to fit. Therefore, to avoid the results being distorted by the strong coherent artifact around time zero, we restricted the fit to probe delays beyond 0.2 ps. Hence, the signal rising edge around time zero plays only a minor role for the fit, so we fixed $t_0 = 0$ and assumed a FWHM time resolution of 40 fs, *i.e.* a Gaussian width of the error function of $w_0 = 24$ fs.

To gain an impression of the fit accuracy, data and fit for various wavelengths are compared in figure S6. Under this scope, all three TMDCs exhibit a similar behavior. The fit matches the data best in the spectral region where the broad F^+ feature dominates. For longer wavelengths, though, the spectra are largely shaped by the partially overlapping excitonic peaks. As the positive ones are subject to significant changes in width and even position, the resulting dynamics cannot be accurately described with the given exponential functions. Hence, the fit deviates significantly from the data, especially at longer times. Here, the saturation behavior of those peaks, their transforming shape and the presumably diffusion-mediated exciton recombination dynamics add up to a truly nonexponential time evolution of the signal.
Nevertheless, the fit largely yields a good agreement with the data. Albeit some aspects of the dynamics cannot be described in a quantitatively accurate fashion, the qualitative results still provide clear and valuable information on the different processes and mechanisms at play in these systems. They shall be thoroughly discussed in the following.

For 1L-$MoSe_2$, the dynamics start similarly to 1L-WS_2. Figure S7 (a) illustrate DAS 1 to be characterized by a spectrally broad, negative feature that actually describes the growth of the positive contribution F^+. Again, the amplitude scales more or less linearly with fluence while the corresponding time constant increases as well. However, in this case, the DAS 1 drops to zero beyond 550 nm, while in DAS 2, a complementary component appears in the exact same region. This suggests that F^+ is still broad in this material, yet the dynamics of its emergence depends on the probe wavelength. A retarded growth of C^+ might be possible. Simultaneously, the excitonic transitions do not leave any significant fingerprints in DAS 2. In WS_2, as opposed to this, strong changes of A^+ occurred on this timescale. There, we observe the coupling of carriers and hot phonons, drastically reducing the collisional broadening of the positive excitonic peak. However, since the $A^\pm$ and $B^\pm$ contributions heavily overlap in $MoSe_2$ and A^+ falls out of the investigated spectral range, these narrowing dynamics are largely concealed in these data sets. Correspondingly, the evolution of F^+ determines the time constant τ_2 as well. Here, we observe a deceleration of the process with increasing fluence. It appears that the two fastest processes tend to converge. Consequently, they may just represent a short- and long-term contribution to the same nonexponential dynamics, namely the thermalization of the electronic system after excitation.
DAS 3, in agreement with the analysis of the WS_2 data, embodies a partial decay of the F^+ feature plus a fluence-dependent shift of the positive peaks. We assign this signature to the cooling of the electronic system via coupling to low-energy phonons as well, as opposed to DAS 2. There is no consistent trend of τ_3 though, possibly arising from the strong overlap of multiple peaks with different saturation behavior. Finally, the mere signal decay is represented by DAS 4. Here,

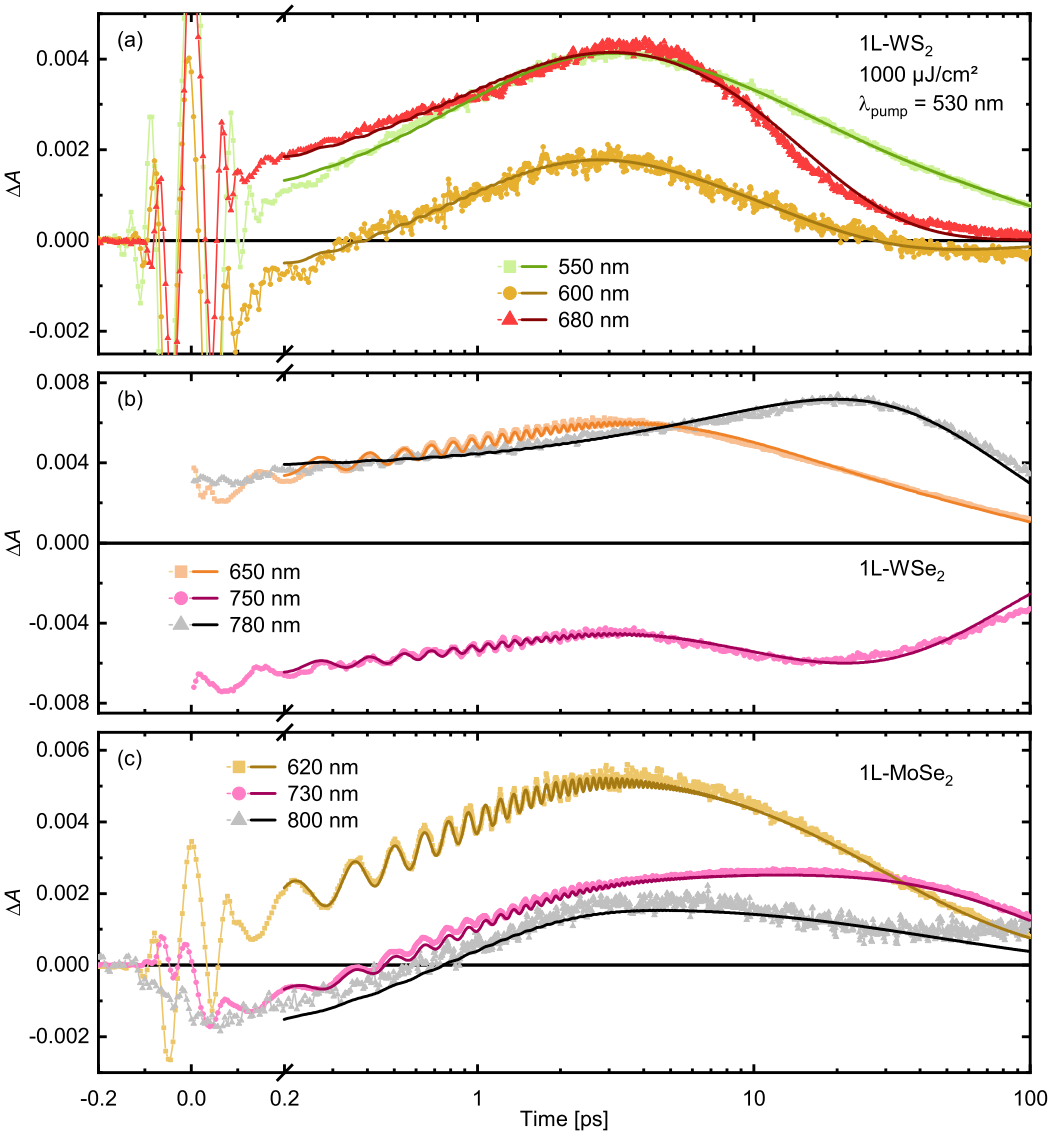

Figure S6: Comparison of measured (dots) and fitted (lines) time traces of monolayer WS_2 (a), WSe_2 (a), $MoSe_2$ (c) at characteristic wavelengths. The shortest wavelength each corresponds to a spectral region dominated by F^+, while the longest wavelength marks the high-energy side of the A^+ peak, respectively (see Figures S3, S4 as well as figure 1 of the main part for comparison.). Around time zero, the experimental data is dominated by the coherent artifact.

the spectral shape is essentially independent of the fluence, indicating a thermally equilibrated system. Due to the long-term inaccuracy of the global fit that was already discussed in the main body, the time constants do not follow a systematic trend.

For 1L-WSe_2, the third material, a global fit with 4 exponentials (plus the oscillation component reflecting the coherent phonon fingerprint) frequently ran into unstable results. We attribute this to the location of A^+ right at the low-energy edge of the spectrum, disguising most of the expected narrowing dynamics, similar to $MoSe_2$, as discussed above. We therefore removed one exponential decay to obtain a stable fit yielding consistent results.
Once more, the dynamics start with the emergence of the broad F^+ feature. Besides the value of τ_1 for the lowest fluence, this process slows down at higher excitation density. As mentioned above, the coupling of hot phonons to the electronic system, which would follow, leaves no clear trace in the investigated part of the spectra and is hence omitted in the fit. Subsequently, the DAS 2 represents the next step in the cooling cascade, namely the involvement of lower energetic

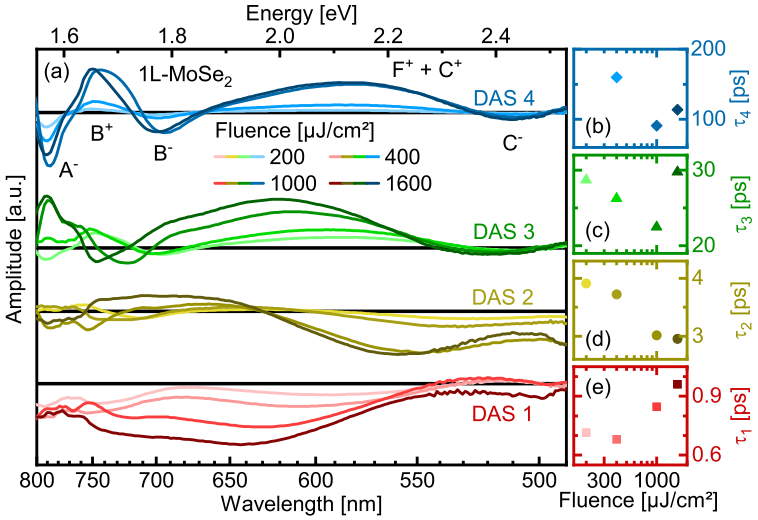

Figure S7: Global fitting analysis of $MoSe_2$. (a) Decay-associated spectra corresponding to four exponentials for various pump fluences. DAS 1 and 2 are dominated by spectrally broad, negative features and are consequently associated with the growth of the F^+-contribution. For DAS 3, the low-energy side of the spectrum is characterized by fluence-dependent shift signatures, similar to Figure 2 of the main body. Furthermore, F^+ starts to decay. In DAS 4, the peak positions are largely independent of the excitation density. Here, the signal simply decays. (b-e) Fluence dependence of time constants corresponding to the DAS, respectively. While the fastest process decelerates and the second one accelerates with rising fluence, there is no clear systematics for the two largest time constants. Note that the fitted τ_4 for the lowest fluence takes essentially infinite values and is therefore not depicted in (b).

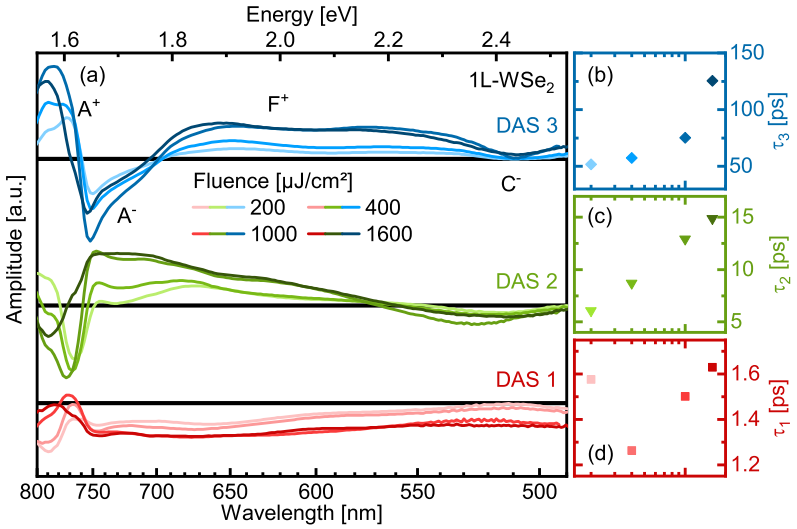

Figure S8: Global fitting analysis of WSe_2. (a) Decay-associated spectra corresponding to four exponentials for various pump fluences. All four DAS 1 are dominated by a spectrally broad, negative feature and are consequently associated with the growth of the F^+-contribution. For DAS 2, the low-energy side of the spectrum is characterized by fluence-dependent shift signatures, similar to Figure 2 of the main body. Furthermore, F^+ starts to decay. In DAS 3, the peak positions are largely independent of the excitation density. Here, the signal simply decays. (b-d) Fluence dependence of time constants corresponding to the DAS, respectively. While the slowest two processes decelerate with rising fluence, there is no systematics for τ_1.

phonons. This leads to a thermal equilibrium between lattice and excitons plus free carriers at a much lower temperature, hence causing a blue shift the A^+ peak and a partial decrease of F^+. Here, the phonon bottleneck effect prolongs the process. Finally, the recombination of the

excited species follows, leading to a decay of the signal, while the spectral shape is conserved. Consequently, DAS 3 simply grows with rising fluence. Simultaneously, the corresponding time constant τ_3 increases as well. In this case, such a decelerated decay may arise from the saturation of the $A^{\pm}$ peaks. When increasing the excited species density above a threshold, they quickly level at a certain saturated amplitude. In turn, as the excited species recombine, their density has to fall below that threshold again, before substantial changes in the amplitude can be observed. This process takes longer at higher initial densities, assuming an identical temporal evolution of the normalized excitation densities for different fluences[9]. Thus, the apparent decrease of the signal amplitude will be retarded, as observed.

3 Detailed analysis of transient oscillations

3.1 Oscillatory residue after multiexponential fitting of 1L-WSe_2 and 1L-WS_2 TA signal

To be able to analyze the oscillatory component of the TA signal separately from all other dynamics, we performed a multiexponential fit that was subsequently subtracted from the data. In contrast to section 2.3, where the interpretation of these monotonous dynamics formed the focus, we now aim at the highest accuracy in describing the non-oscillatory signal contributions. To that end, we increased the degrees of freedom for the fit, by replacing the single global time constants τ_i from equation 2 by a wavelength-dependent one $\tau_i(\lambda)$. Furthermore, we observe a second signal rise around 1 ps or 1.5 ps, depending on the sample substrate thickness. As these times exactly match the doubled light path through the substrate, we conclude a second excitation by the pump being reflected at the back of the cover slides that carry the TMDC flakes. To correct for this signal echo that supposedly follows a similar dynamics as that of the main excitation $\Delta A_0(\lambda, t)$, we added a shifted and attenuated replica of the original fit function. This means three more wavelength-dependent parameters, namely the time delay $t_{\mathrm{echo}}(\lambda)$, the temporal width $w_{\mathrm{echo}}(\lambda)$ of the rising edge $f_{\mathrm{re}}(\lambda, t)$ and the relative amplitude $a_{\mathrm{echo}}(\lambda)$ of the echo. To avoid disturbances by the coherent artifact, we again restricted the time interval to start only at 0.2 ps. Therefore, we omitted the original signal rise in the fit. On the other end of the time interval, we cut the data of the long-term measurements ($t_{\max} = 100$ ps) after 3 ps, as from this point, the time steps were too large to properly capture the oscillations. Due to this shorter time, we reduced the fitting function to three exponentials instead of four. All in all, we obtain the following formula:

$$
\begin{aligned}
\Delta A_0(\lambda, t) &= \sum_{i=1}^{3} A_i(\lambda) \cdot \mathrm{e}^{-\frac{t}{\tau_i}} \\
\Delta A(\lambda, t) &= \Delta A_0(\lambda, t) + a_{\mathrm{echo}}(\lambda) \cdot f_{\mathrm{re}}(w_{\mathrm{echo}}(\lambda), t - t_{\mathrm{echo}}(\lambda)) \cdot \Delta A_0(\lambda, t - t_{\mathrm{echo}}) \\
&= \left(\sum_{i=1}^{3} A_i(\lambda) \cdot \mathrm{e}^{-\frac{t}{\tau_i}} \right) + a_{\mathrm{echo}}(\lambda) \cdot \frac{1 + \mathrm{erf}(\frac{t - t_{\mathrm{echo}}(\lambda)}{w_{\mathrm{echo}}(\lambda)})}{2} \cdot \left(\sum_{i=1}^{3} A_i(\lambda) \cdot \mathrm{e}^{-\frac{t - t_{\mathrm{echo}}(\lambda)}{\tau_i}} \right) \qquad (3)
\end{aligned}
$$

with the error function erf that describes the rising edge for a presumably Gaussian temporal profile of the excitation pulse. Starting with this, all further analyses were performed using Matlab R2022a. In contrast to equation (2), this fit represents exclusively the monotonous contributions to the dynamics and contains no oscillatory part. Hence, to extract the latter from the data, we subtract the fit result from the measured signal.

Figure S9 shows the so-obtained residues for the two tungsten-based TMDCs. For WSe_2, we observe distinct temporal oscillations, similar to the case of $MoSe_2$ in the main body, figure 3 (b). They occur over almost the entire spectral region and start also in phase, with only minor drifts towards the rim of the spectrum. However, on a closer look on longer times, the quasi horizontal areas of positive and negative signal extrema at the beginning of the dynamics seem to slightly tilt or bend at longer times. This may indicate a possible, minimal frequency discrepancy between the green and red spectral region, which we will investigate in the next subsection.
The residue of the WS_2 data appears a bit more complex. Diagonal, curved bands of increased or reduced absorbance cross the 2D plot, superposing the oscillations. These features dominate especially at longer times and in the spectral region of the excitonic TA peaks, changing sign exactly at the zero crossing of the TA signal at 640 nm. Thus, they most probably arise from fluctuations of the pump intensity, resulting in modulations of the signal strength during the measurement. At this raw stage of the data, these fluctuations belong to one single spectrum that is assigned to one particular (measured) time point, hence lying horizontally in the plot. With the zero point correction of the 2D data (see section 3.4 for details) in the course of its

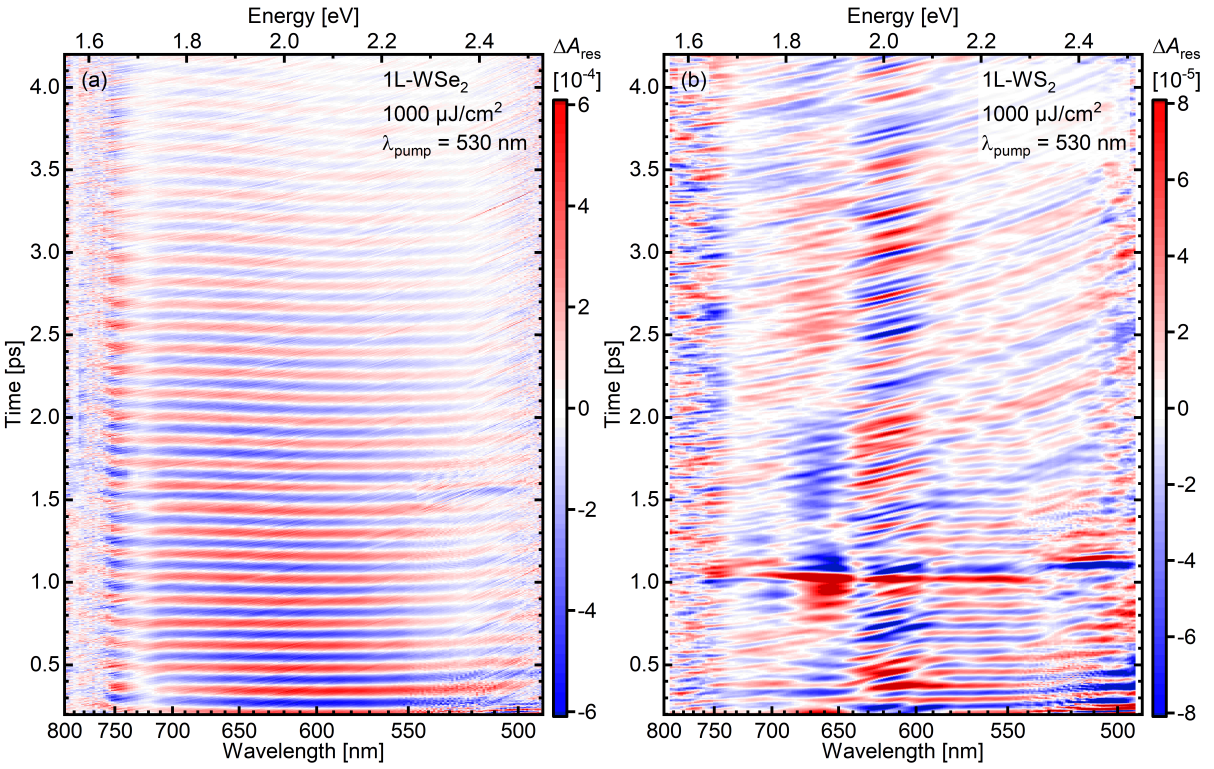

Figure S9: TA signal residue of WSe_2 (a) and WS_2 (b) after subtracting the result of a 4-exponential fit for each wavelength. The original scans were performed using equidistant time points. (a) The 2D map shows clear oscillations that start in phase over the whole investigated spectral range. Over time, a slight phase difference between the red and blue part of the spectrum seems to accumulate. (b) Note that the color scale spans one order of magnitude less than in (a), meaning that the oscillations are drastically weaker. Thus, signal fluctuations emerge (diagonal, curved features) and superpose the oscillations. Nevertheless, the latter seem to be in phase. The strong horizontal signal around 1 ps is a zero point echo originating from a second excitation by the back-reflected pump pulse. The data in (b) is smoothed to obtain a clearer picture.

processing, they get shifted or distorted, following the chirp of the probe pulse. On top, we find a strong horizontal feature at about 1 ps that is attributed to remains of the echo of the zero point coherent artifact.
Nevertheless, we clearly observe signatures of oscillations, in particular at short times, albeit roughly one order of magnitude weaker than in the other two materials (compare scales of figure S9 (a) and (b)). This attenuation likely arises from the higher oscillation frequency in WS_2. Generally, any finite experimental time resolution Δt will attenuate the observed oscillation amplitude. For a given Δt (approx. 40 fs in our experiments), this effect strengthens at higher oscillation frequencies. Thus, a lower observed amplitude for WS_2 does not necessarily imply an actually smaller elongation. In total, despite the superposed fluctuations and artifacts, the residue for WS_2 also exhibits consistent oscillations.

3.2 Fourier transform amplitude and phase

To obtain the wavelength-dependent frequency spectrum of the oscillations, we performed a fast Fourier transform (FFT) on the 2D residue data discussed in the previous subsection. As this results in generally complex numbers, we plotted their amplitude and phase separately in figure S10. For $MoSe_2$, the former was already shown in the main body, figure 3 (c). In comparison with the phase, we find that the relevant frequency band at about 7 THz manifests in an amplitude peak and a simultaneous sharp phase drop. In the closer environment of this major band, the

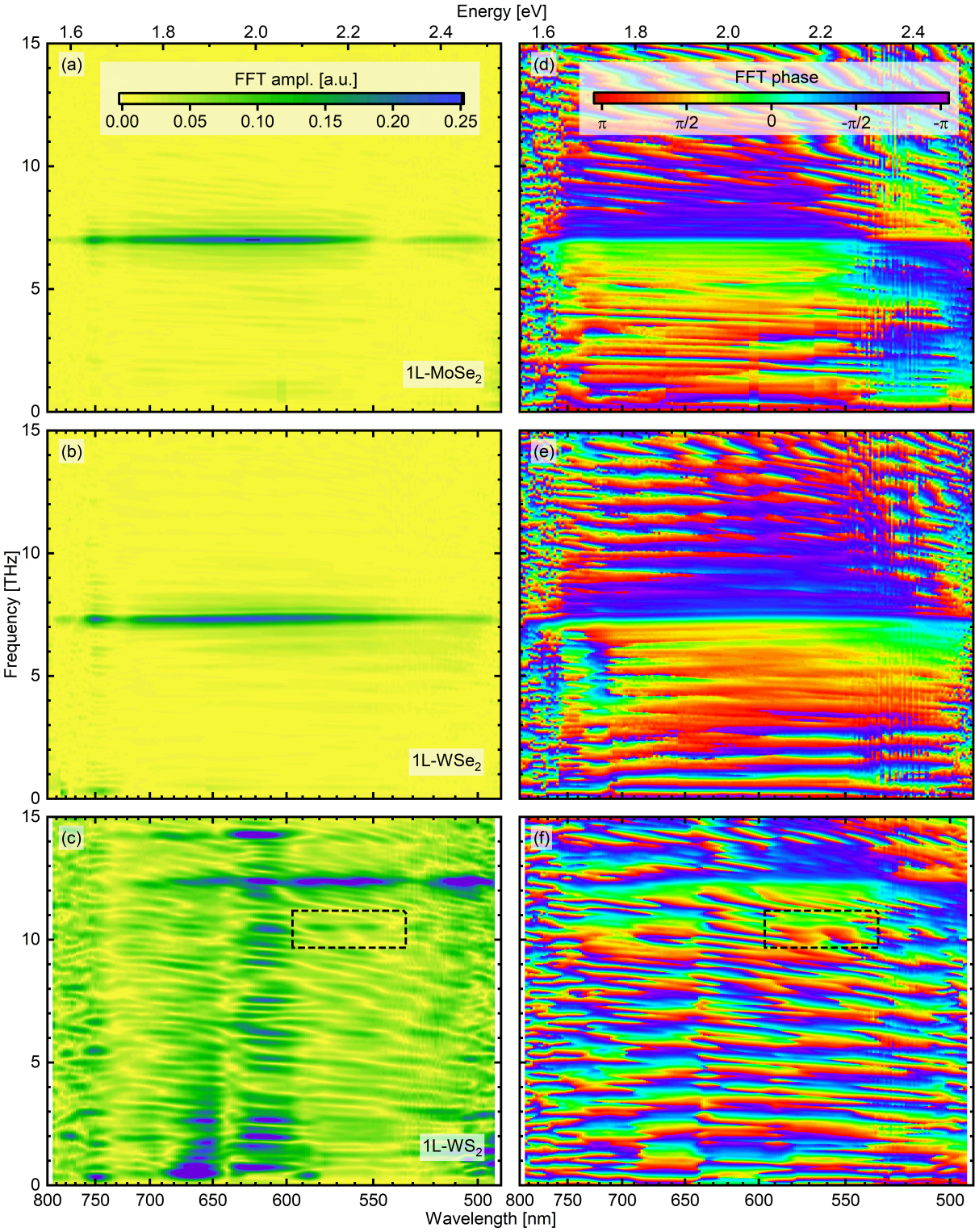

Figure S10: FFT amplitude (a-c) and phase (d-f) maps, obtained from the data shown in Figures 3(b) and S9. $MoSe_2$ and WSe_2 each exhibit one single frequency band near 7 THz marked by a striking amplitude feature and a spectrally stable phase, respectively. For WS_2, the background is much stronger in relation to the signal, especially around the positions of the excitonic TA peaks. Nevertheless, we observe a strong band around 12.5 THz. Additionally, a weak amplitude signature and a roughly stable phase counterpart can be found at 10.5 THz (dashed, rectangular outlines in (c) and (f)).

phase is rather constant with a slight wobble on it, which coincides with minor side peaks in the

amplitude FFT spectra. These two features stem from the limited time interval, where the data ends before the oscillation has fully faded away. They do not represent physical contributions to the spectrum.
For WSe_2, the FFT yields similar results, with a single band at slightly higher frequencies of 7.3 THz. However, it exhibits a weak curvature, *i.e.* a red-shift above 650 nm as well as on the high-energy end of the spectrum. In the case of WS_2, owing to the smaller measured oscillation amplitude, the FFT spectra are subject to strong noise, mostly induced by pump intensity fluctuations. These contributions, as already discussed for the TA residues in figure S9 (b), prevail in the range of the excitonic TA peaks from 590 nm to 690 nm. Nevertheless, we observe a clear band of an elevated amplitude as well as a spectrally stable phase feature with a frequency of 12.5 THz. On top of that, a close look reveals an area with a second phase drop and amplitude peak that spans from 540 nm to 590 nm at 10.5 THz (black, dashed box in figure S10 (c) and (f)). In contrast to the chaotic phase pattern that dominate the rest of the map, this one lies horizontally, *i.e.* stable in frequency over a larger spectral region. A clearer distinction from the background noise is also presented in figure S14. As we already discussed in the main body with reference to figure 4, we assign this second band in WSe_2 to the $E^{'}$ Raman mode. With this in mind, the apparent frequency shift in WSe_2 may result from a second vibrational mode as well. In this material, $A_1^{'}$ and $E^{'}$ lie close to each other, inhibiting a clear distinction between the two. If they now cause different impacts on the spectrum, *i.e.* different amplitude spectra, one or the other mode will prevail in a certain spectral region. Transitioning from one's dominance to the other's, the frequency would spectrally drift between the values for the two characteristic phonon modes.

3.3 Fourier transform and fitting of spectrally averaged residual time traces

In the following, we compare the oscillations at different measurement parameters, namely pump wavelength and fluence. To obtain a higher accuracy of the residual data that allows for such comparison, we start from spectrally averaged time traces. We aim to consider a wavelength region where the oscillations can be clearly seen and appear in phase for the given zero point correction. Thus, we calculated the mean time trace in the range from 550 nm to 700 nm for $MoSe_2$, 550 nm to 650 nm for WSe_2, and 540 nm to 590 nm for WS_2, respectively. The resulting, averaged curves were processed in terms of an FFT as well as fitting an exponentially decaying oscillation.

Figure S11 compares the averaged curves at different excitation wavelengths and fluences with the corresponding fits on the left side and depicts the equivalent FFT spectra on the right. The three panel rows correspond to the three different materials. Especially for the Se-based TMDCs, where the coherent phonons exhibit a lower frequency and their collective excitation is less smeared out, we observe clear oscillations. Consequently, the fits show a good agreement with the data, allowing for an analysis of the extracted parameters (see figures S13 and figure 6 of the main body). For the lowest two excitation fluences in WSe_2, however, we observe that between 1.5 ps to 2 ps, data and fit accumulate a phase mismatch which partially vanishes after some time. Since the fit - by definition - follows a constant frequency, this means that the data runs out of phase for a limited period of time. We conclude a lag by the delay stage that tunes the probe delay and therefore omit these two scans for further analysis.
In the case of WS_2, due to the lower oscillation amplitude, the curves are strongly superposed by fluctuations, especially for the lower fluences. Nevertheless, we can distinguish the oscillations at higher excitation density and especially for the more detailed, equidistant scans (upper two curves of each panel, see gray boxes). Here, the data is accurately fitted.
Regarding the FFT spectra of $MoSe_2$, we note a single, distinct peak that red-shifts with higher fluence. This shift is in line with the results from the curve fitting as depicted in the main body, figure 6. Minor side peaks that rather appear as a wobbly background result from the limited time window, within which the oscillation has not fully faded at the end of the scan. In WSe_2,

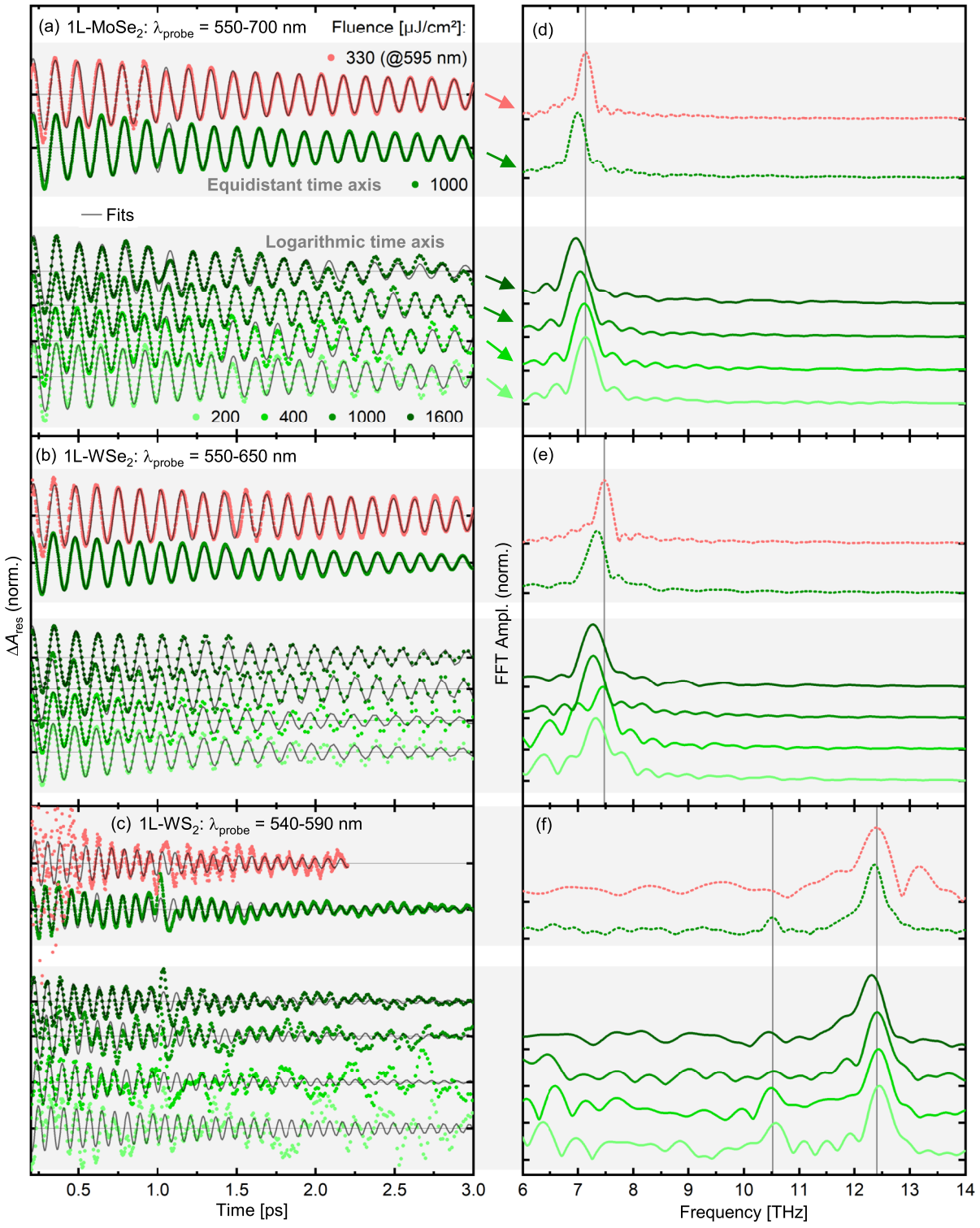

Figure S11: Analysis of spectrally averaged residual time traces for different fluences and pump wavelengths. As the gray boxes indicate, the upper two traces of each panel represent detailed scans with equidistant time points while the lower four stem from full-range scans that implemented a logarithmic time spacing. The latter were cut at 3 ps. If not noted otherwise, the excitation wavelength was 530 nm. (a-c) Spectrally averaged TA residues (dots) and corresponding fits (gray lines). For the two lowest excitation fluences applied to WSe_2, the data slowly dephased and then rephased again. (d-f) FFT spectra corresponding to the data shown left. Exclusively when exciting WS_2 at 530 nm, a second peak shows at a lower frequency than the major signature. The curves are offset for clarity.

the findings are similar. Yet, the phase drift from the averaged residue curves for the two lowest fluences translates into distorted peak shapes, so we discard those. Still, the red-shift from the (low-density) excitation at 595 nm to the higher pump fluences at 530 nm occurs here as well. For WS_2, the major FFT band again red-shifts at higher fluences. The thrilling feature, however, is the emergence of a second peak around 10.5 THz, as already discussed in the main body, figure 4. It is more or less present for all fluences when pumping at 530 nm, but appears neither in the other TMDCs, nor after long-wavelength excitation in WS_2. As already discussed in the main body, this is probably due to a different wavelength-dependent exciton-phonon coupling strength for the two Raman modes of the three materials[13–15].

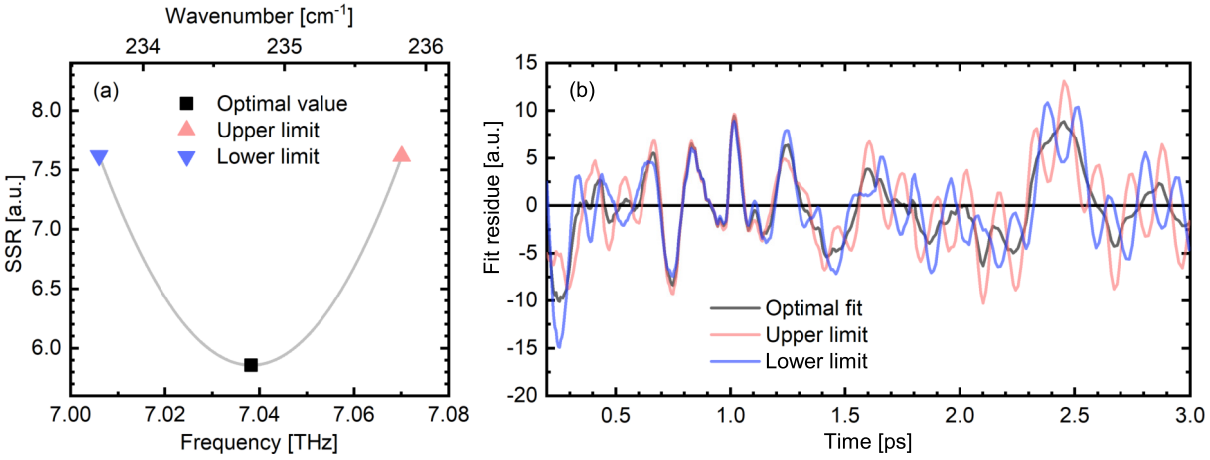

Figure S12: Determination of the uncertainty of the fitted frequency value for $MoSe_2$ excited at 530 nm with a fluence of 1000 µJ cm^{-2}, scanned using a logarithmic time axis. (a) SSR in dependence of the frequency, which is fixed, whereas all the other parameters are fitted. The black square marks the optimal values for frequency and SSR. The colored triangles represent the upper and lower limit, respectively. (b) Residual curves for the fits corresponding to the three constellations marked in (a). The limit cases exhibit oscillations around the curve for the optimum fit.

Based on the FFT spectra and fits of the averaged traces, we turn to the excitation density dependence of the oscillations, namely their frequencies, lifetimes and amplitudes. To quantify the uncertainties of the fitted parameters, we applied the following procedure. Even at their optimal values as obtained from the fit, there will still be some residual deviation of the fit from the data, which can be quantified in terms of the sum of the squared residuals (SSR). As this is the quantity optimized by the fit, it reaches its minimum at the corresponding optimum parameter set. Now, one chooses an element of the latter p_i, *e.g.* the frequency to investigate its uncertainty. To that end, the chosen parameter is increased (decreased) a little bit and then kept constant, while all the remaining parameters are fitted again. The SSR of this not quite optimal fit will lie a bit higher than the minimum one. Thus, one further raises (lowers) p_i and repeats the fit of the other $p_{j\neq i}$, until the SSR crosses a certain threshold. This means, that the fit result has moved away from the data that the quality of its result has diminished significantly compared to the original fit, where all parameters were fitted. The value of p_i at this threshold point represents the upper (lower) boundary for the confidence interval of this parameter. For illustration, the frequency dependence of the SSR plus the deduced upper and lower limit are depicted in figure S12 (a). The described procedure can be conducted for all other p_i as well to receive a complete set of uncertainties for the initial, optimal fit.
The crucial point for this analysis is a reasonable choice of the threshold. We used a 30% increase of the SSR compared to its minimum as a criterion. To confirm that this is a reasonable choice, we can take a look at the residuals that result from subtracting the fit from the data, *i.e.* the averaged time traces. These residue curves are plotted in figure S12 (b) for the optimum fit and the upper and lower limits concerning the frequency, as defined in the previous paragraph.

Even for the optimal parameters (black curve), the residual significantly deviates from the zero line. It most probably contains a track of the laser fluctuations. Yet, if we look at the two curves with an SSR right at the threshold - the upper and lower limit - we observe oscillatory components emerging especially at longer times. This indicates that for the corresponding frequency variations, the fit already starts to run out of phase with the data. Hence, we conclude that the corresponding boundaries extracted for the frequency parameter are a rather cautious measure for its uncertainty. Especially for the lifetime, the limits may lie far off the optimal value. This is due to the relatively short investigated time interval, in which the oscillations do not fully decay. Thus, the SSR is relatively insensitive to changes in the lifetime, in particular to an increase. For WS_2, the low signal-to-noise ratio even leads to constellations, where the SSR does not reach the threshold at all. In this case, the aforementioned approach to estimating the uncertainties seems to fail.

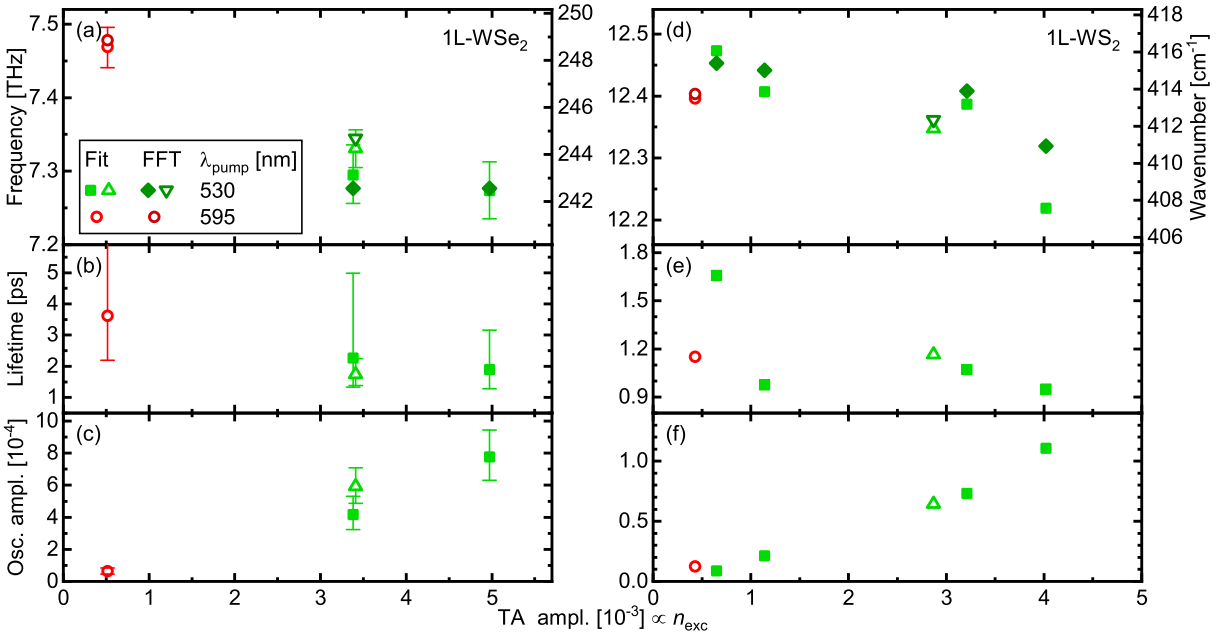

Figure S13: Fit and FFT peak parameters as extracted from figure S11 for WSe_2 (a-c) and WS_2 (d-f) in dependence of the excitation density, as represented by the TA amplitude. The frequency falls with rising fluence, the same tendentiously holds for the lifetime. The oscillation amplitude grows roughly linear with the strength of the TA signal. Generally, open symbols represent detailed scans with equidistant time points while solid dots stem from long-term scans that implemented a rather logarithmic time spacing. The uncertainty bars for WSe_2 stem from the procedure described in the previous paragraphs. For WS_2, they are omitted as they drastically exceed the variance between the different values. The WSe_2 results for lowest two fluences at 530 nm were excluded from this graph due to the phase drift.

The yielded confidence intervals are incorporated in the evaluation of the fit parameters. Similar to figure 6 of the main body, which shows the respective behaviors for $MoSe_2$, figure S13 depicts the same parameters for the tungsten-based materials. The measurements on WSe_2 (figure S13 (a-c)) essentially reproduce the trends already found in $MoSe_2$, despite the lacking data points for the two lowest fluences at 530 nm excitation. Here, as a measure for the excited species density, the x-axis represents the mean TA signal from 650 nm to 680 nm and 0.2 ps to 0.5 ps. This marks the C^- peak before the superposing F^+ contribution has gained a significant amplitude and therefore exhibits a relatively linear growth with fluence and mirrors the excitation density. The frequency decreases with rising TA amplitude, *i.e.* higher excitation density. Here, the FFT peak position (dark symbols) and fitted frequency (bright symbols) yield similar values. For the lifetime, we also observe a reduction from lower to higher fluence, albeit insignificant

given the large uncertainties. However, owing to the missing data points, we cannot conclude whether accelerated decay indeed originates from the increasing number of excitations or whether some effect may be attributed to the different pump wavelength. Nevertheless, the normalized time traces in figure S11 (b) show a rather long-living oscillation for 595 nm excitation compared to all curves for the green pump pulses. This observation is in line with the behavior in $MoSe_2$. Finally, the oscillation amplitude exhibits a rather linear growth parallel to the TA signal, both showing only weak saturation even at the highest fluences.
For WS_2, in turn, the trends are less distinct owing to the unfavorable signal-to-noise ratio, see figure S13 (d-f). Here, we used the TA signal from 500 nm to 550 nm and 1 ps to 2 ps, i.e. the fully grown F^+ feature to mirror the excitation density given on the x-axis. In this case, the uncertainties exhibit values far beyond the variance between the individual data point and are therefore omitted. Nevertheless, one can find some of the general tendencies discussed in the two selenides. Again, the frequency falls with increasing fluence, albeit less clearly than for the selenides. Moreover, the discrepancy between the data points obtained from the FFT peaks and those from the fits is significantly enhanced. The tendencies in the lifetime observed in the other materials can barely be found here, most probably due to the strong fluctuations in the time traces for the lowest fluences. At least, the roughly proportional scaling between excitation density in terms of TA signal versus oscillation amplitude holds in this case as well.
Summing up, the two tungsten dichalcogenides essentially confirm the fluence-dependent parameter trends originally described in $MoSe_2$. However, the findings are less clear, taking the measurement uncertainties into account.

After focusing on the fit results, we now dive into a feature specific to the complex FFT analysis, namely the phase spectrum as the counterpart to the amplitude that was already thoroughly analyzed in the main body figure 4 as well as figure S11 (d-f). We now directly compare phase and amplitude spectra, *i.e.* the two polar coordinates of the complex FFT values calculated from the averaged time traces in figure S14. Here, we choose the detailed, linear scans after excitation at 530 nm, as they offer a maximum signal-to-noise ratio. For the two selenides, one single amplitude peak dominates the spectrum. At the exact same positions, the FFT phase undergoes a sudden drop, while beyond that narrow frequency interval, it changes only gradually plus exhibiting some minor fluctuations. Thus, this phase drop serves as a second marker of

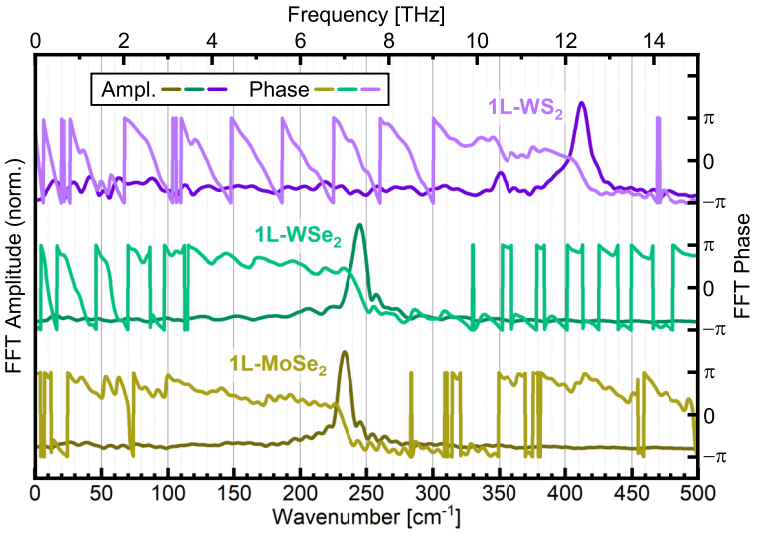

Figure S14: Normalized FFT amplitude and phase spectra obtained from high resolution time scans with equidistant time points, employing a pump fluence of 1000 µJ cm^{-2} (see figures 3 (b) and S9). The dominant amplitude peaks are each accompanied by a downward step in the phase spectrum, respectively. Likewise, the second, smaller peak at 10.5 THz in the WS_2 spectrum exhibits a corresponding phase feature. The curves for the different materials are offset for clarity.

relevant frequency bands. Turning to WS_2, we now observe a second, smaller amplitude peak at approximately 10.5 THz in addition to the main signature. The former was already assigned to the $E^{'}$ Raman mode in the main body, figure 4. To prove a real contribution as opposed to background wobbles, we check the phase trend at this frequency. Indeed, a small but distinct sudden reduction of the phase occurs. Aside from these two frequency bands, in contrast, the phase changes rather continuously. Ergo, we conclude that the second peak exhibits a true physical origin and confirm the attribution to the $E^{'}$ vibrational mode.

3.4 Phase spectra

Although the FFT phase serves as a second marker for frequency bands to distinguish them from background artifacts, its intuitive translation to the overall observed oscillation appears difficult. A fit, in contrast, provides a more direct manner to determine its phase, also in dependence of the probe wavelength. Thus, we separately fitted each time trace for all three materials with an exponentially decaying phase-shifted cosine.

The so-obtained phase spectra are displayed in figure S15. Again, the results for the Se-based TMDCs match each other quite well, showing a relatively flat phase curve in the center of the spectral range. Here, where the oscillation is strongest and the zero point determination most reliable, the phase levels approximately at π. Given the input cosine function, this corresponds to the oscillations starting at maximum negative elongation. This points towards a displacive excitation of the coherent phonons, as discussed in the main body. Towards the rim of the spectrum, however, the phase falls continuously. We suppose that this phase shift originates from inaccuracies in the zero point determination. In TA spectroscopy, a chirped probe pulse means that its various colors arrive at the sample at different times. Ergo, the time zero, *i.e.* the starting point of any TA dynamics, shifts over the spectrum. To correct this, all time traces have to be corrected to match a unified time-axis with only one single time zero. To define a common reference point, one uses a characteristic flank, maximum or zero crossing of the zero point artifact that is created where and when pump and probe pulse overlap temporally. However, this artifact exhibits varying shapes at different wavelengths. Eventually, this may cause a drift in the zero point correction, which would in turn manifest in a spectrally changing phase for the oscillations, even if they are actually in phase over the whole wavelength range. Given the coherent lattice vibrations as the underlying mechanism for the oscillations, it seems reasonable that the time traces are indeed strictly in phase. Any deviations probably result from

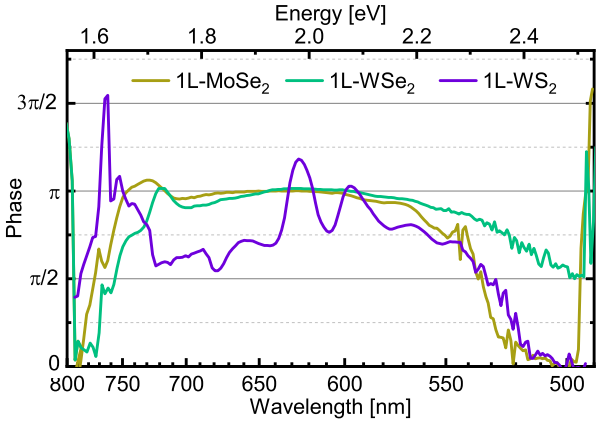

Figure S15: Oscillation phase spectra for different TMDCs as obtained from fitting the respective 2D residues (figures 3 (b) and S9) pixel-wise with an exponentially decaying cosine. For $MoSe_2$ and WSe_2, where the oscillations are strongest, the phase levels at π in the middle of the spectrum. In the case of WS_2, the curve is strongly modulated near the excitonic TA peaks. Generally, the phase decreases towards the rim of the investigated wavelength range.

the discussed zero point corrections.
For WS_2, the phase behavior seems unfortunately more chaotic, experiencing strong modulations in the spectral region of the excitonic TA peaks from 1.9 eV to 2.1 eV. They probably result from the superposition of the actual oscillations with the TA signal fluctuations associated with a slightly volatile pump fluence during the experiment.

References

[1] U. Megerle, I. Pugliesi, C. Schriever, C. F. Sailer, and E. Riedle. Sub-50 fs broadband absorption spectroscopy with tunable excitation: putting the analysis of ultrafast molecular dynamics on solid ground. *Applied Physics B*, 96(2–3):215–231, June 2009.

[2] Ayla Päpcke, Aleksej Friedrich, and Stefan Lochbrunner. Revealing the initial steps in homogeneous photocatalysis by time-resolved spectroscopy. *Journal of Physics: Condensed Matter*, 32(15):153001, January 2020.

[3] E. Riedle, M. Beutter, S. Lochbrunner, J. Piel, S. Schenkl, S. Spörlein, and W. Zinth. Generation of 10 to 50 fs pulses tunable through all of the visible and the NIR. *Applied Physics B*, 71(3):457–465, September 2000.

[4] C Manzoni and G Cerullo. Design criteria for ultrafast optical parametric amplifiers. *Journal of Optics*, 18(10):103501, August 2016.

[5] Yilei Li, Alexey Chernikov, Xian Zhang, Albert Rigosi, Heather M. Hill, Arend M. van der Zande, Daniel A. Chenet, En-Min Shih, James Hone, and Tony F. Heinz. Measurement of the optical dielectric function of monolayer transition-metal dichalcogenides: MoS_2, $MoSe_2$, WS_2, and WSe_2. *Physical Review B*, 90(20):205422, November 2014.

[6] Chunwei Hsu, Riccardo Frisenda, Robert Schmidt, Ashish Arora, Steffen Michaelis de Vasconcellos, Rudolf Bratschitsch, Herre S. J. van der Zant, and Andres Castellanos-Gomez. Thickness-dependent refractive index of 1L, 2L, and 3L MoS_2, $MoSe_2$, WS_2, and WSe_2. *Advanced Optical Materials*, 7(13), May 2019.

[7] P. Hein, A. Stange, K. Hanff, L. X. Yang, G. Rohde, K. Rossnagel, and M. Bauer. Momentum-resolved hot electron dynamics at the 2H-MoS_2 surface. *Physical Review B*, 94(20):205406, November 2016.

[8] Yuanzheng Li, Jia Shi, Yang Mi, Xinyu Sui, Haiyang Xu, and Xinfeng Liu. Ultrafast carrier dynamics in two-dimensional transition metal dichalcogenides. *Journal of Materials Chemistry C*, 7(15):4304–4319, 2019.

[9] Tim Völzer, Franziska Fennel, Tobias Korn, and Stefan Lochbrunner. Fluence-dependent dynamics of localized excited species in monolayer versus bulk MoS_2. *Physical Review B*, 103(4):045423, January 2021.

[10] Daichi Kozawa, Rajeev Kumar, Alexandra Carvalho, Kiran Kumar Amara, Weijie Zhao, Shunfeng Wang, Minglin Toh, Ricardo M. Ribeiro, A. H. Castro Neto, Kazunari Matsuda, and Goki Eda. Photocarrier relaxation pathway in two-dimensional semiconducting transition metal dichalcogenides. *Nature Communications*, 5(1), July 2014.

[11] Tawinan Cheiwchanchamnangij and Walter R. L. Lambrecht. Quasiparticle band structure calculation of monolayer, bilayer, and bulk MoS_2. *Physical Review B*, 85(20):205302, May 2012.

[12] Alexey Chernikov, Claudia Ruppert, Heather M. Hill, Albert F. Rigosi, and Tony F. Heinz. Population inversion and giant bandgap renormalization in atomically thin WS_2 layers. *Nature Photonics*, 9(7):466–470, June 2015.

[13] Dahyun Nam, Jae-Ung Lee, and Hyeonsik Cheong. Excitation energy dependent Raman spectrum of $MoSe_2$. *Scientific Reports*, 5(1), November 2015.

[14] P. Soubelet, A. E. Bruchhausen, A. Fainstein, K. Nogajewski, and C. Faugeras. Resonance effects in the Raman scattering of monolayer and few-layer $MoSe_2$. *Physical Review B*, 93(15):155407, April 2016.

[15] E. del Corro, A. Botello-Méndez, Y. Gillet, A. L. Elias, H. Terrones, S. Feng, C. Fantini, Daniel Rhodes, N. Pradhan, L. Balicas, X. Gonze, J.-C. Charlier, M. Terrones, and M. A. Pimenta. Atypical exciton–phonon interactions in WS_2 and WSe_2 monolayers revealed by resonance Raman spectroscopy. *Nano Letters*, 16(4):2363–2368, March 2016.

Acknowledgements

As this thesis stands on the shoulders of giants, or - specifically - of many scientific and personal mentors and companions, I would like to take the opportunity to express my cordial gratitude to all those who supported me throughout the last years.

First of all, I thank Prof. Lochbrunner for providing me with the opportunity of conducting this project. He was always there to lend a sympathetic ear when I was dealing with problems, be it scientifically or organizationally. Moreover, I greatly benefited from his experience in and passion for scientific storytelling, which he gladly passes on to his mentees. I am truly grateful to him for granting me a huge amount flexibility and freedom, especially during the last year, when I frequently worked remotely from Brussels and attended language courses during the daytime.

Next, I would like to highlight the role of Prof. Korn as my second supervisor. I particularly appreciate his vast TMDC knowledge, which he is always willing to share and spread. Furthermore, he substantially aided me with the anticipation and translation of the community's ways, conventions and language. In that respect, I equally thank both of my supervisors for their guidance and support in partially difficult peer review processes.

However, even the professors represent just the tip of the iceberg that is their research groups and the institute as a whole. Here, I always encountered a genuinely friendly and supportive atmosphere and a lot of constructive feedback, leaving an overwhelmingly positive impression on the personal level. Similarly, I acknowledge all the cooperation partners that I had the privilege to work with, both from physics and other disciplines beyond my own focus. This insight into various scientific branches felt thoroughly enriching.

At this point, I would like to mention several specific groups and persons who particularly contributed the the advancement of my projects. I am grateful to the team of the institute's workshop for their proficiency and creativity with which they designed and fabricated crucial parts for several of my experimental setups. Likewise, the teaching team of the laboratory courses helped me by regularly granting me access to their soldering tools to build or fix the TVD chamber. Additionally, I would like to express my gratitude for their passion for teaching, which I had the opportunity to be a part of during multiple semesters.

For individual support, I would like to begin by acknowledging Franziska for the years that we shared an office and the time she supervised me as a student. She taught me some of the unspoken ways and soft skills of science, be it the design of figures or the subtleties of scientific writing, especially in English.

In light of the experimental challenges, I owe Marvin a special gratitude for his tireless dedication for the ongoing development and maintenance of the optical part of the TA setup. His improvements enabled the high-quality measurements of coherent phonons in the first place.

I very much appreciate Julian for breaking the loneliness of the everyday work as he joined the hybrid project. Besides his profound overview of the TMDC field and community, it was always equally fun and productive to collaborate with him. On the other hand, as a sorrow shared is a sorrow halved, his company and humor eased the numerous experimental setbacks and disappointments inherent to the quotidian laboratory life.

On the institutional and financial side, I would like to acknowledge the funding by the university of Rostock in terms of its PhD scholarship.

Furthermore, an intense project such as a dissertation requires spaces low in distraction to unfold one's productivity. On that account, I would like to highlight and appreciate the often accursed German railway company, in whose trains I produced a significant portion of the text that constitutes my last major publication as well as this thesis.

Last but not least, I turn to those who laid the mental and emotional foundation for any of my accomplishments, namely my friends and family. They form my balance to retain or reestablish the contact to reality, especially after diving into intense periods of measurement series or writing, and put any troubles into perspective. Among them, my girlfriend Sonja deserves a special mention, as we shared the ups and downs of doing a PhD and she uplifted me through all of the latter.